

Development of a PET radioligand targeting angiogenesis for oncology applications

Kayleigh Louise Brocklesby BSc (Hons)

Submitted towards the degree of Doctor of Philosophy

The University of
Hull

and

University of York

Hull York Medical
School

March 2016

Grandad,

This is for you!

Love always and forever

The memories of you never fade

ABSTRACT

All tumours must become vascularised in order to survive and metastasise, and initiate angiogenesis through the dysregulated and uncontrolled release of pro-angiogenic factors. Such uncontrolled angiogenesis leads to highly disordered and abnormal vasculature and is widely recognised as a hallmark of cancer. The major angiogenic pathway hyper-activated in cancer is the VEGF-VEGFR₂ signalling system. Anti-angiogenic therapies have been developed, but there is no accepted way of determining which patients will respond. The development of a molecular imaging probe targeting VEGFR₂ through the use of PET represents one way to achieve this. Currently, there are no PET imaging probes which exhibit the required characteristics. Therefore, the initial focus of this project was to synthesise novel probes based around existing suitable pharmacophores. Initial libraries focusing on urea or indole motifs, lacked either routes to a radiolabelling precursor or selectivity on biological testing, and were abandoned. A third library based around the only known selective VEGFR₂ inhibitor 5-((7-benzyloxyquinazolin-4-yl)amino)-4-fluoro-2-methylphenol **98**, ZM323881, was developed. Synthesis of **98** proceeded via the Dimroth rearrangement in three steps, with a shorter synthesis time, use of less toxic reagents and easier purification than published methods. Initial kinase profiling revealed **98** also targeted closely related kinases; VEGFR₁, VEGFR₃, RET, PDGFR α . Known inhibitor **98** and closely related analogue 4-fluoro-5-((7-(4-fluorobenzyl)oxy))quinazolin-4-yl)amino)-2-methylphenol **101** exhibited activity against VEGFR₂, 4.75 nM and 7.5 nM respectively. The quinazoline focused library was selected for radiolabelling. Initial radiolabelling revealed a debenzylation reaction occurring, to produce 4-(2-fluoro-5-hydroxy-4-methylphenyl)amino quinazolin-7-ol **166** during the radiolabelling reaction. Radiolabelling analogue 7-(benzyloxy)-N-(4-bromo—fluorophenyl)quinazolin-4-amine **123**, via the Dimroth rearrangement was troublesome and requires more optimisation, due the presence of the de-cyanation by-product. Initial biological testing presented in this thesis does not rule out the quinazoline library from its use as a PET imaging agent and further *in vitro* characterisation is required.

Table of Contents

Chapter One	1
Literature Review	1
1.1. Angiogenesis	2
<i>1.1.1. Physiological angiogenesis</i>	3
1.1.1.1. Vasculogenesis	3
1.1.1.2. Sprouting angiogenesis.....	4
1.1.1.3. Non-sprouting angiogenesis	4
1.1.1.4. Lymphangiogenesis.....	5
1.1.1.5. Key molecular players in physiological angiogenic signalling.....	6
<i>1.1.2. Oncological angiogenesis</i>	10
1.1.2.1. Dysregulation of signalling in oncological angiogenesis.....	11
<i>1.1.3. The VEGF-VEGFR signalling system - The key mediator of angiogenesis</i>	13
1.1.3.1. Role of VEGF in cancer	13
1.1.3.2. Role of VEGFR ₂ in cancer	16
1.1.3.3. Expression of VEGFR ₂ in cancer	19
1.2. Therapeutic intervention of the VEGF-VEGFR ₂ signalling system.....	20
<i>1.2.1. Molecular targeted VEGF/VEGFR₂ therapies</i>	21
<i>1.2.2. Inhibitors targeting VEGF_A</i>	22
1.2.2.1. Bevacizumab	22
1.2.2.2. Aflibercept.....	22
<i>1.2.3. Tyrosine kinase inhibitors targeting VEGFR₂</i>	23
1.2.3.1. Sunitinib 1	25
1.2.3.2. Sorafenib 2	25
1.2.3.3. Pazopanib 3	26
1.2.3.4. Vandetanib 4	26
<i>1.2.4. Summary of current therapies targeting the VEGF-VEGFR₂ signalling system</i> ..	26
<i>1.2.5. Biomarkers for the VEGF-VEGFR₂ signalling system</i>	28
1.2.5.1. Predictive biomarkers.....	29

1.2.5.2.	Pharmacodynamic biomarkers	30
1.2.	Molecular imaging of the VEGF-VEGFR ₂ signalling system	33
1.2.1.	<i>What is molecular imaging?</i>	33
1.2.2.	<i>Use of molecular imaging to visualise the VEGF-VEGFR₂ signalling system</i>	34
1.2.2.1.	Ultrasound	34
1.2.2.2.	Magnetic Resonance Imaging	36
1.3.	Nuclear medicine imaging of the VEGF-VEGFR ₂ signalling system	39
1.3.1.	<i>What is nuclear medicine?</i>	39
1.3.1.1.	Single photon emission computed tomography	39
1.3.2.	<i>Introduction to PET</i>	40
1.3.2.1.	Positron emission and annihilation.....	40
1.3.3.	<i>Development of a VEGFR₂ specific PET probe</i>	42
1.3.3.1.	High affinity for VEGFR ₂	42
1.3.3.2.	High contrast ratio	43
1.3.3.3.	High selectivity for VEGFR ₂ over other kinases	43
1.3.3.4.	Lipophilicity	43
1.3.3.5.	High metabolic stability	44
1.3.3.6.	Adequate half-life	44
1.3.3.7.	Toxicity.....	45
1.3.3.8.	Ease of radiolabelling.....	45
1.3.4.	<i>PET imaging in cancer</i>	45
1.3.4.1.	Imaging the VEGF-VEGFR ₂ signalling system.....	45
1.3.4.2.	Imaging VEGF _A	45
1.3.4.3.	Imaging angiogenesis with RGD targeting PET probes.....	48
1.3.4.4.	Imaging expression of the VEGF receptor using TKI-PET	54
1.3.4.5.	Monitoring treatment response to VEGF-VEGFR ₂ targeted therapies – using PET pharmacodynamic biomarkers.....	59
1.3.5.	<i>Use of fluorine-18 in the development of a PET probe</i>	64
1.3.5.1.	Electrophilic radiolabelling	65

1.3.5.2. Nucleophilic radiolabelling	65
1.3.1.1. Novel approaches to fluorine-18 radiolabelling	66
1.4. Summary	72
1.5. Aims and Objectives	73
Chapter Two.....	74
Urea focused library	74
2.1 Ureas in medicinal chemistry	75
2.1.1. VEGFR ₂ inhibitors possessing a urea functional group	77
2.2 Rationale	79
2.2.1. Design of a urea focused library	80
2.2.2. Considerations of the urea focused library for developing a successful candidate	
81	
2.3 Synthesis of urea homologues.....	83
2.3.1. Isocyanates	83
2.3.2. Phosgene.....	83
2.3.3. Curtius Rearrangement	84
2.3.4. 1,1'-Carbonyldiimidazole 25	85
2.4 Results and discussion.....	86
2.4.1. Synthesis of the core scaffold	86
2.4.2. Synthesis of ureas via 1,1'-carbonyldiimidazole 25	89
2.4.3. Synthesis via 4-nitrophenyl chloroformate.....	91
2.4.4. Synthesis of fluoroalkylamines	93
2.4.5. Synthesis of fluoromethyl tosylate 52	95
2.5 Conclusions	100
Chapter Three.....	101
Indole focused library	101
3.1 Indoles in medicinal chemistry	102
3.1.1. Indoles as VEGFR ₂ inhibitors	103
3.1.2. Indoles as PET imaging agents	105

3.2 Rationale	107
3.2.1. <i>Design of an indole focused library</i>	108
3.2.2. <i>Considerations of the indole focused library for developing a successful PET candidate</i>	110
3.3 Synthesis of Indoles	111
3.3.1. <i>Fischer indole synthesis</i>	111
3.4 Results and discussion.....	113
3.4.1. <i>Chemistry of the indole series</i>	113
3.4.1.1. Synthesis of 4-fluoro-2-methyl-1 <i>H</i> -indol-5-ol 64	113
3.4.1.2. Synthesis of 2-trifluoromethyl-1 <i>H</i> -indol-5-ol 65	119
3.4.1.3. Synthesis of 5-hydroxy-1 <i>H</i> -indole-2-carbonitrile 66	120
3.4.1.4. Synthesis of the indole core scaffold	121
3.4.2. <i>Biology of the indole series</i>	124
3.4.2.1. Cellular proliferation assay	125
3.4.2.2. Evidence of non-specific toxicities	128
3.4.2.3. Evidence of the indole as mitotic inhibitors	130
3.5 Summary	133
Chapter Four.....	135
Quinazoline focused library	135
4.1 Quinazolines in medicinal chemistry	136
4.1.1. <i>Quinazoline as VEGFR₂ inhibitors</i>	137
4.1.2. <i>Quinazolines as PET imaging agents</i>	139
4.2 Rationale	140
4.2.1. <i>Selection of the target compounds</i>	140
4.2.2. <i>Design of an quinazoline focused library</i>	141
4.2.3. <i>Considerations of the quinazoline focused library for developing a successful PET candidate</i>	141
4.3 Results and discussion.....	143
4.3.1. <i>Chemistry of the Quinazoline series</i>	143
4.3.1.1. Synthesis via Quinazlinone.....	143

4.3.1.2. Synthesis via PyBOP coupling	145
4.3.1.3. Synthesis via the Dimroth rearrangement.....	149
4.3.1.4. Benzylic fluorination	154
4.3.2. <i>Screening of the quinazoline focused library</i>	155
4.3.2.2. Kinase based screening.....	155
4.3.2.1. Development of tools for evaluation of radiolabelled compounds.....	158
4.4 Conclusions	160
Chapter Five	162
Radiochemistry	162
5.1 Selection of the library for radiochemical evaluation	163
5.2 Results and discussion.....	163
5.2.1. <i>Chemistry</i>	163
5.2.1.1. Synthesis of a precursor for 98	163
5.2.1.2. Synthesis of a precursor for 101	166
5.2.1.3. Synthesis of the radiochemical precursor to 123	168
5.2.1.4. Synthesis of NOTA-ZD-G2 125	169
5.2.2. <i>Radiochemistry</i>	176
5.2.2.1. Synthesis of [¹⁸ F]- 101	176
5.2.2.2. Synthesis of [¹⁸ F]- 123	183
5.3 Conclusions	188
Chapter Six.....	190
Summary	190
6.1 Summary	191
Chapter Seven	194
Experimental	194
7.1 Chemistry	195
7.1.1. <i>General Comments</i>	195
7.2 Biology.....	269
7.2.1. <i>Table of standard solutions</i>	269

7.2.3. <i>Culture of cell lines</i>	270
7.2.3. <i>Cell proliferation assay</i>	271
7.2.4. <i>Nuclear Staining</i>	271
7.2.5. <i>Protein preparation and Western blot analysis</i>	272
7.2.5.1. <i>Protein extraction from cells</i>	272
7.2.5.2. <i>Determination of protein content</i>	272
7.2.5.3. <i>Sample preparation for SDS polyacrylamide gel electrophoresis</i>	272
7.2.5.4. <i>SDS polyacrylamide gel electrophoresis</i>	272
7.2.5.5. <i>Coomassie staining of SDS gels</i>	272
7.2.5.6. <i>Protein transfer</i>	273
7.2.5.7. <i>Immunoblotting</i>	273
7.2.5.8. <i>Enhanced Chemi-Luminescence (ECL) detection of HRP-conjugated secondary antibody binding</i>	273
7.3 <i>Radiochemistry</i>	275
7.3.1. <i>Production</i>	275
7.3.2. <i>Manual Radiolabelling</i>	275
7.2.3. <i>Automated Radiolabelling</i>	276
Chapter Eight	277
References and Appendix	277
8.1 <i>References</i>	278
8.2 <i>Appendices</i>	300
8.2.1. <i>Appendix One</i>	300
8.2.2 <i>Appendix Two</i>	302
8.2.3. <i>Appendix Three</i>	311
8.2.4. <i>Appendix Four</i>	314

List of Abbreviations

AcOH	Acetic Acid
ADP	Adenosine Diphosphate
AIBN	Azobisisobutyronitrile
ANG	Angiopoietin
ATP	Adenosine Triphosphate
B _{max}	maximum density of receptors
BOC	<i>tert</i> -Butyloxycarbonyl
BOC ₂ O	Di- <i>tert</i> -butyl dicarbonate
BOLD	Blood oxygen level dependent
BOP	(Benzotriazol-1-yl-oxo)tris(dimethylamino)phosphonium hexafluorophosphate
CDI	1,1'-Carbonyldiimidazole
CHK	Checkpoint Kinase
cKIT	stem cell growth factor receptor
CNS	Central Nervous System
COX	Cyclooxygenase
CRC	Colorectal cancer
CT	Computed Tomography
CuAAC	Copper Azide Alkyne Cycloaddition
DAPI	4',6-diamino-2-phenylindole
DBU	1,8-Diazabicycloundec-7-ene

DCE	Dynamic Contrast Enhanced
DCM	Dichloromethane
DLL4	Delta like ligand
DMA	<i>N,N</i> -Dimethylacetamide
DMAP	4-Diemthylaminopyridine
DMEM	Dulbecos Modified Eagles Medium
DMF	<i>N,N</i> -Dimethylformamide
DMF-DMA	<i>N,N</i> -Dimethylformamide dimethyl acetal
DMSO	Dimethylsulfoxide
DOTA	1,4,7,10-tetraazacyclododecane-1,4,7,10-tetraacetic acid
dppf	1,1'-Bis(diphenylphosphino)ferrocene
ECL	Enhanced chemiluminescence
ECM	Extracellular Matrix
EDCI	1-Ethyl-3-(3-dimethylaminopropyl)carbodiimide
EGF(R)	Epidermal Growth Factor (Receptor)
EORTC	European Organisation for Research and Treatment of Cancer
EPC	Endothelial Progenitor Cells
ERK	Extracellular signal-regulated kinase
ESI	Electron spray ionisation
ESS	Extravascular space
EtOAc	Ethyl Acetate

EtOH	Ethanol
EWG	Electron Withdrawing Group
FAK	Focal Adhesion Kinase
FCH	Flourocholine
FDA	Food and Drug Administration
FDG	2-deoxy-2-fluoro-D-glucose
(b)FGF(R)	(basic)-Fibroblast Growth Factor (Receptor)
FLT	3'-deoxy-3'-fluorothymidine
FMISO	1-(2-Nitro-imidazolyl)-3-fluoro-2-propanol
FP	Fluticasone propionate
FRET	Fluorescence Resonance Energy Transfer
GAPDH	Glyceraldehyde-3-Phosphate Dehydrogenase
GBM	Glioblastoma multiforme
GIST	gastrointestinal stromal tumour
HB	Heating block
HBA	Hydrogen bond acceptor
HBD	Hydrogen bond donor
HGF	Hepatocyte growth factor
HIF	Hypoxia inducible factor
HMBC	heteronuclear multiple bond correlation
HPLC	High Performance Liquid chromatography

HRP	Horseradish peroxidase
HUVEC	Human umbilical vein endothelial cells
IAUC	Initial Area under the Contrast agent concentration
Id	DNA-binding protein inhibitor
Ig	Immunoglobulin
IHC	Immunohistochemistry
IL	Interleukin
INF	Interferon
IP	C-X-C motif chemokine
IR	Infrared
Kd	Dissociation constant
Kep	rate constant
Ki	Unidirectional influx constant
K^{trans}	volume transfer constant between plasma and ESS
LCMS	Liquid Chromatography Mass Spectrometry
LEC	Lymphatic Endothelial Cells
LOR	Line Of Response
LPA	Lipoprotein
MeCN	Acetonitrile
MEK	Mitogen-activated protein kinase kinase
MeOH	Methanol

MMP	Matix metallproteins
MAPK	Mitogen-activated protein kinases
MRI	Magnetic Resonance Imaging
MTS	3-(4,5-dimethylthiazol-2-yl)-5-(3-carboxymethoxyphenyl)-2-(4-sulfophenyl)-2H-tetrazolium,
MW	Microwave
NAD(PH)	Nicotinamide adenine dinucleotide (phosphate)
NMP	N-Methyl-2-pyrrolidone
NO	Nitrous Oxide
NOTA(-NHS)	2,2'-(7-(2-((2,5-dioxopyrrolidin-1-yl)oxy)-2-oxoethyl)-1,4,7-triazonane-1,4-diyl)diacetic acid – (N-hydroxysuccinimide)
NP or NRP	Neuropilin
NS	Not Significant
(N)SCLC	(Non) Small Cell Lung Carcinoma
OS	Overall Survival
PBS	Phosphate buffered saline
PDGF(R)	Platelet Derived Growth Factor (Receptor)
PERCIST	PET response criteria in solid tumours
PES	phenazine ethyl sulfate
PET	Positron Emission Tomography
PFS	Progression free survival

Pi3K	Phosphoinositide 3-kinase
PIDA	(Diacetoxyiodo)benzene
PKB	Protein Kinase B
PKC	Protein Kinase C
PLC	Phospholipase C
PIGF	Placental Growth Factor
PSMA	Prostrate specific membrane antigen
PTC	Phase transfer catalyst
PTEN	Phosphatase and tensin homolog
PVDF	Polyvinyl
PyBOP	benzotriazol-1-yl- oxytripyrrolidinophosphonium hexafluorophosphate
rBV	Regional Blood Volume
RCC	Renal Cell carcinoma
RECIST	Response Evaluation Criteria in Solid Tumours
RET	Rearranged during Transfection
RGD	Arginine-Glycine-Aspartamine
ROI	Region of Interest
RTK	Receptor tyrosine kinase
SAR	Structure activity relationship
S _N Ar	Nucleophilic substitution
SNP	Single Nucleotide Polymorphism

SPECT	Single Photon Emission Computed Tomography
SUV	Standardised Uptake Value
T _b	biological half-life
TBAC	Tetrabutyl ammonium chloride
TBAF	Tetrabutyl ammonium fluoride
Teff	half-life of potential PET candidate
TFA	TriFluoroAcetic acid
TGF	Tumour Growth Factor
THF	Tetrahydrofuran
TIE	Angiopoietin receptor
TIPS	TriIsoPropylSilyl
TK	Thymidine Kinase
TKI	Tyrosine Kinase Inhibitor
TLC	Thin Layer Chromatography
TMEDA	Tetramethylethylenediamine
TMS	Tetramethyl silane
T _p	physical half-life
TTP	Time to progression
TSP	Thrombospondin
TSPO	Translocator protein
US	UltraSound
UV	UltraViolet

Ve	Volume of ESS per unit volume of tissue
VEGF(R)	Vascular Endothelial Growth Factor (Receptor)
vHL	von Hippel-Lindau

List of Figures

Figure 1: Mechanisms of tumour vascularisation. This figure highlights the six prominent types of vascularisation seen in physiologically and solid tumours.	2
Figure 2: Recruitment of endothelial progenitor cells (EPC - mesoderm cells) are differentiated into haemangioblasts which form the primitive blood vessels.....	3
Figure 3: Sprouting angiogenesis. A) activation of quiescent cells through the change in balance of pro and anti-angiogenic factors B) The growing spout is control through a gradient of growth factors C) The primitive lumen is formed through polarisation of the migrating endothelial cells D) Stabilisation of the immature blood vessels.....	4
Figure 4: Non-sprouting angiogenesis – splitting of the blood vasculature through the insertion of tubular tissue pillars which leads to degradation of the ECM with endothelial cell proliferation, leading to the splitting of the parent blood vessel.	5
Figure 5: Development of the lymphatic system. LECs are formed during the formation of the lymphatic network, expression of transcription factors in the first LECs occurs in the embryonic veins. The assembly of the lymphatic sacs and sprouting leads to the formation of the lymphatic plexus, which expands into the highly branched lymphatic system.....	6
Figure 6: Angiogenic signalling. This figure highlights some of the pathways involved in angiogenesis and the upregulation of pro-angiogenic factors through the recruitment of various growth factors and cytokines, showing the crosstalk between tumour cells and endothelial cells.....	8
Figure 7: The angiogenic switch. A) The tumour vasculature network is minimal and suffers from depleted oxygen levels and a lack of essential nutrients, triggering the angiogenic switch. B) Triggering the angiogenic switch causes the tumour to become more vascularised, however it is dysregulated.....	11
Figure 8: The key molecular players involved in tumour angiogenesis. a) HIF1- α expression is induced due to a state of hypoxia which triggers the release of pro-angiogenic factors b) Tip cells elongate and migrate towards higher VEGF gradients c) Resulting vasculature is abnormal and prone to cell extravasation.....	13
Figure 9: VEGF _A isoforms and the exons required to the respective isoform.....	14
Figure 10: Family of VEGF proteins and their corresponding receptors located on either the vascular or lymphatic endothelium	15
Figure 11: Factors responsible for VEGF production and subsequent VEGFR ₂ activation on the vascular endothelium, thus activating the signalling cascade which results in the sustained angiogenesis observed in cancers.....	16

Figure 12: Simplified structure of VEGF receptor 2. VEGFR ₂ consisting of both an intracellular and extracellular portions, whilst highlighting the important tyrosine residues involved in activating the signalling cascade.....	17
Figure 13: Dimerisation of VEGFR ₂ . Simplified representation of ligand binding, dimerisation and consequently receptor activation initiating a signal cascade.....	18
Figure 14: Cascade of signalling activated from VEGF binding to VEGFR ₂ . Initiation of the downstream signalling pathway after the activation of VEGFR ₂ leading to sustained angiogenesis	19
Figure 15: Therapeutic strategies of anti-angiogenic agents. The specific mechanism of actions of generic classes of inhibitors which target either VEGF _A , VEGFR ₂ or neuropilin could result in tumour regression or enhancing clinical response	21
Figure 16: Aflibercept – A simplified representation. The protein highlighted in green is from the FC domain of IgG, the purple domain is the VEGF binding domain of VEGFR ₂ and the blue portion is the VEGF binding domain of VEGFR ₁	23
Figure 17: Structures of four clinically relevant TKIs	24
Figure 18: Relative sensitivity of medical imaging techniques	33
Figure 19: Radioactive decay of the unstable, neutron poor ¹¹ C to the more stable ¹¹ B via the release of a positron, followed by the collision of the positron with an electron producing two γ photons	41
Figure 20: Calculating the effective half-life of the potential candidate	44
Figure 21: Structure of three RGD PET candidates (7-9) and their positioning of fluorine-18 highlighted in red	49
Figure 22: Time activity curves of [¹⁸ F]- 7 in the different malignancies investigated when compared to normal kidney, muscle and blood	53
Figure 23: Analogues of 4 which have shown some promise in the development of a VEGFR ₂ specific PET probe.....	54
Figure 24: Structure of target DOTA-ZDG2 which showed enhanced binding to VEGFR ₂	57
Figure 25: A) Uptake of [⁶⁴ Cu]-DOTA-ZDG2 in cell lines which minimal expression of VEGFR ₂ (MDA-MB-231) or overexpression of VEGFR ₂ (HUVEC); b) Saturation curve for [⁶⁴ Cu]-DOTA-ZDG2 in U87 cells	57
Figure 24: Positions of fluorine-18 tried on 10a and 10b and the final radiolabelled compound 11	59
Figure 25: [¹⁸ F]- 12	60
Figure 26: [¹⁸ F]- 13	61
Figure 27: [¹⁸ F]- 14	63

Figure 28: Different urea classes targeting the cancer genome	75
Figure 29: Structure of 15 and 16 , urea containing VEGFR ₂ inhibitors that have progressed to clinical trial, urea moieties are highlighted in pink.....	76
Figure 30: Interactions of urea containing inhibitors with VEGFR ₂ . A) The typical binding modes of urea containing VEGFR ₂ inhibitors, showing binding via the urea to both the Glu885 and Asp1046 residues, with 1 as a comparison B) VEGFR ₂ in complex with 2 , showing binding interactions. Docking studies performed using Schrödinger Gold (2014-2) and visualised on Chemical Computing Group MOE (2013-8802). PDB code: 4ASD	77
Figure 31: VEGFR ₂ inhibitor 17 demonstrating the importance of the urea moiety	78
Figure 32: Left: the core structure in which this study is based 18 . Right: Structure of adenine 19 . Bottom: Hydrogen bonding formed within the core structure 20 (shown in red)	79
Figure 33: Structure of scaffold 21 developed by Connolly <i>et al.</i> Urea highlighted in pink, with the ether bridge highlighted in red	80
Figure 34: Docking studies of 21f (shown in blue – area highlighted by yellow circle), the receptor binding pocket is highlighted in grey. Docking was performed using Schrödinger Gold (2014-2) and visualised on Chemical Computing Group MOE (2013-8802).PDB code: 3VHE.....	81
Figure 35: SAR to be explored in this urea focused library.....	81
Figure 36: Different methods used for the synthesis of urea moieties.....	83
Figure 37: Phosgene mediated synthesis of isocyanates.....	84
Figure 38: Curtius rearrangement of 24 to 23	84
Figure 39: Conversion of 25 into a urea derivative	85
Figure 40: Positions of the protons of interest on 31e for HMBC analysis	87
Figure 41: HMBC analysis of 31e	88
Figure 42: Resonance stabilisation of aniline systems.....	91
Figure 43: Structure of the product observed by LCMS.....	93
Figure 44: Positioning of PET tag on the urea scaffold.....	93
Figure 45: Structures of two common monofluoromethylated drugs ([¹⁸ F]-FP and [¹⁸ F]-FCH).....	95
Figure 46: Caesium fluoride equivalent dependant conversion of ditosylate 51 to 52 over six hours using <i>t</i> -amyl alcohol (N=3), under conventional heating at 100 °C. Reported as average, with error bars indicating standard deviation. ^ No standard deviation calculated for these bars	97
Figure 47: Use of indole core in drug therapies.....	102
Figure 48: Structure of various indoles (pink) and indol-2-ones	104

Figure 49: Binding modes of AZD2171 58 , AG-028262 and 1 with VEGFR ₂	105
Figure 50: Structures of some experimental PET candidates containing fluorine, the indole fragment is highlighted in pink and the positioning of fluorine-18 in red.....	105
Figure 51: New molecular architecture, with the indole fragment highlighted in pink and the previous pyrimidine highlighted in black, with some VEGFR ₂ affinity data from the literature	107
Figure 52: A) expected binding mode, based on the predicted binding mode of the urea focused compounds B) Predicted binding mode provided by <i>in silico</i> docking using Schrödinger Gold (2014-2) and visualised on Chemical Computing Group MOE (2013-8802). (PDB: 2OH4).....	108
Figure 53: Structure of the molecular architecture showing the positions in which the library can be diversified from the original structure described by Connolly <i>et al</i>	110
Figure 54: Common methods utilised to synthesise indole 54 , also highlighting the conventional numbering system of indoles.....	111
Figure 55: Mechanism of Fischer indole synthesis.....	112
Figure 56: Structures of the indoles required 64-66	113
Figure 57: Identification of the protons likely to cause a signal on NOESY NMR evaluation of the isomers of 68b , a signal is seen in the area circled.....	114
Figure 58: The transformation of 68a into 71 over a 72 hour time period; Pure ¹ H NMR of 71 (bottom) indicates a pure sample after column chromatography. The aromatic region (6.5ppm – 8.2 ppm) is represented as these highlight the marked differences in the aromatic regions and the transformations can be followed.....	117
Figure 59: Mechanism for the conversion of 72 to 64	118
Figure 60: Mechanism for the conversion of 74 to 75	120
Figure 61: POCl ₃ mediated dehydration of 5-methoxy-1 <i>H</i> -indole-2-carboxamide to 77	121
Figure 62: Mechanism for the condensation of the carbaldehyde and <i>O</i> -methylhydroxylamine hydrochloride	122
Figure 63: Catalytic cycle of Copper catalysed azide alkyne cycloaddition	123
Figure 64: Effects of different lysis buffers on VEGFR ₂ pulldown in either normoxic or hypoxic conditions.s A) A549 B) HCT116 C) HUVEC. Cells were harvested by scraping and lysed in the different bussfers. 50 µg of lysate was loaded onto the 6% acrylamide gel and separated by SDS-PAGE.....	125
Figure 65: Reduction of tetrazolium salt 84 to the formazan product 85 by the mitochondria - the main principle of an MTS assay	126
Figure 66: IC ₅₀ data for two developed VEGFR ₂ inhibitors.....	128

Figure 67: DAPI staining of A549 (A-C) and HCT116 (D-F). Cells were treated for 16 hours, on coverslips, before being fixed for staining. DMSO concentration 0.2%. A and D) Vehicle (DMSO) treated B and E) Treatment with 78a at 452 nM C and F) Treatment with 78c at 66 nM. Blue channel only	129
Figure 68: Treatment of A549, HCT116 and HEK293 cells causes a dose dependent decrease in beta tubulin protein expression. A549, HCT116 and HEK293 cells were cultured in DMEM + 10% FCS until 60% confluent. Media was then removed and replaced with fresh media containing 0-1000 nM of indole compound 78a (panel a) or 78c (panel b) for 24 h.....	130
Figure 69: Structures of three dual VEGFR ₂ , tubulin inhibitors.....	131
Figure 70: Structures of mitotic/tubulin inhibitors	132
Figure 71: Structure of quinazoline 94 , 4(3 <i>H</i>)-quinazolinone 95 , adenine 19 , purine 96 and pteridine bases 97	136
Figure 72: Common quinazoline based kinase inhibitors.....	137
Figure 73: Common VEGFR ₂ inhibitors A) Structures of three relevant quinazoline (highlighted in purple) TKIs B) The typical binding mode of these VEGFR ₂ inhibitors with 1 as a comparison	138
Figure 74: Three fluorine-18 containing PET probes containing the quinazoline core....	139
Figure 75: Docking pose of 98 in VEGFR ₂ Docking was performed using Schrödinger Gold (2014-2) and visualised on Chemical Computing Group MOE (2013-8802). PDB code: 3VHE.....	140
Figure 76: Identification of possible fluorine-18 positions on the scaffold of 98	141
Figure 77: cLogP* values (highlighted in red) for some quinazoline based PET candidates (* calculated using ACD Chem Sketch V12.01)	142
Figure 78: Structures of three proposed compounds and cLogP based around 98 (* calculated using ACD Chem Sketch V12.01).....	143
Figure 79: Niementowski mechanism for the synthesis of 104	143
Figure 80: Structure and mechanism of product 107 - identified by LCMS	145
Figure 81: Structures of coupling reagents BOP 108 and PyBOP 109	146
Figure 82: Structure of 111 , the product of the PyBOP 109 mediated synthesis and ¹ H NMR identifying the aniline protons	147
Figure 83: Initial attack of PyBOP on 105a	147
Figure 84: Second half of the PyBOP mediated synthesis of 98 and 111	148
Figure 85: Structures of Gefitinib 99 and Erlotinib 116 synthesised via the Dimroth rearrangement.....	149
Figure 86: ¹ H NMR for 119 , highlighting the NH and OH proton.....	150

Figure 87: Mechanism of the Dimroth rearrangement, as highlighted by Asgari <i>et al.</i> ...	151
Figure 88: Structural similarities of 98 and 4 , leading to the hybrid compound 123	152
Figure 89: Z-LYTE kinase assay - The principles. The investigated kinase transfers the γ -phosphate to the tyrosine/serine/threonine residue on the FRET peptide.....	156
Figure 92: Structure of target 125	159
Figure 93: Proposed compound which should be synthesised to determine where the selectivity for VEGFR ₂ arises from	161
Figure 94: Envisaged strategies for the radiochemical synthesis of [¹⁸ F]- 98	163
Figure 95: Proposed structures of the precursors 126 and 127 for 98	164
Figure 96: Proposed radiochemical strategies for the synthesis of [¹⁸ F]- 101	166
Figure 97: Plausible side reaction - resulting in the synthesis of 146	167
Figure 98: Approaches utilised for the synthesis of a precursor to 123	168
Figure 99: Structure of target NOTA-ZD-G2 125	169
Figure 100: Structure of key intermediate 146	170
Figure 101: A) Radiochromatogram for entry J of Table 25, showing excess fluoride streaking the column with the peak at approximately eight minutes. B) HPLC chromatogram demonstrating by-product 166 at approximately four minutes, with UV detection.	178
Figure 102: Structure of the identified by-product 166 by mass spectrometry.	178
Figure 103: A) Programme used for the attempted fluorination B) Picture of the TRASIS Allinone synthesiser used.....	180
Figure 104: A) UV trace for the crude reaction mixture from TRASIS labelling B) Fluorine-18 trace for the radioactivity for the crude reaction C) Spike sample for synthesis confirmation using the same crude reaction mixture D) Fluorine-18 trace for the spike sample (approximately 10 second delay from UV detection to radio-detection)	181
Figure 105: Proposed mechanism for the fluorination of boronic species, postulated by Sanford's group	182
Figure 106: A) HPLC radiochromatogram for the radiosynthesis of [¹⁸ F]- 168 , showing a minimum radiochemical purity of 95%. B) Reduction of [¹⁸ F]- 168 to [¹⁸ F]- 155 (region 4). Regions 1-3 can be seen upon expansion of the top chromatogram	185
Figure 107: Schematic showing the position of the cartridges to identify where the activity would be trapped. The blue arrow indicates where the radioactivity was trapped	186
Figure 108: Possible by-product obtained during the Dimroth rearrangement as indicated by LCMS.....	187
Figure 109: IC ₅₀ curves for 78a	302
Figure 110: IC ₅₀ curves for 78b	303
Figure 111: IC ₅₀ curves for 78c	304

<i>Figure 112:</i> IC ₅₀ curves for 78d	305
<i>Figure 113:</i> IC ₅₀ curves for 78e	306
<i>Figure 114:</i> IC ₅₀ curves for 78f	307
<i>Figure 115:</i> IC ₅₀ curves for 78g	308
<i>Figure 116:</i> IC ₅₀ curves for 78h	309
<i>Figure 117:</i> IC ₅₀ curves for 78i	310
<i>Figure 118:</i> VEGFR ₂ IC ₅₀ curve for 98	311
<i>Figure 119:</i> VEGFR ₂ IC ₅₀ curve for 101	311
<i>Figure 120:</i> VEGFR ₂ IC ₅₀ curve for 123	312
<i>Figure 121:</i> VEGFR ₃ IC ₅₀ curve for 101	312
<i>Figure 122:</i> RET IC ₅₀ curve for 101	313
<i>Figure 123:</i> ¹ H NMR and HPLC chromatogram for 98	314
<i>Figure 124:</i> ¹ H NMR and HPLC chromatogram for 101	315
<i>Figure 125:</i> ¹ H NMR and HPLC chromatogram for 123	316
<i>Figure 126:</i> ¹ H NMR and HPLC chromatogram for 136	317
<i>Figure 127:</i> ¹ H NMR and HPLC chromatogram for 166	318

List of Tables

Table 1: Pro- and anti-angiogenic factors involved in physiological angiogenesis	7
Table 2: List of antiangiogenic agents.....	27
Table 3: DCE-MRI predictive or pharmacodynamic biomarkers of antibody based therapy	37
Table 4: DCE-MRI predictive or pharmacodynamic biomarkers of TKI based therapy	38
Table 5: Common radionuclides used in PET imaging	41
Table 6: Examples of radioligands and radiotracers used in clinical practice.....	42
Table 7: VEGFR ₂ IC ₅₀ data for the urea scaffold 21 with modifications of the R position	80
Table 8: Summary of conditions attempted for the synthesis of ureas via 25 , reactions were monitored by TLC	90
Table 9: Summary of attempted conditions for the fluorination of 43	94
Table 10: Initial attempts for the fluorination of ditosylate 51	96
Table 11: Microwave assisted synthesis of 52	98
Table 12: Scale up conditions ^a A) <i>t</i> -amyl alcohol removed under reduced pressure then extracted with stated solvent; B) poured onto water extracted with stated solvent; C) solvent added to microwave vial then sonicated to break up the reaction mixture then filtered and washed with the solvent. The filtrate was concentrated under reduced pressure; D) <i>t</i> -amyl alcohol removed under reduced pressure and the solid was triturated with stated solvent and filtrate concentrate under reduced pressure.....	99
Table 13: Impact of the position of the functional group on cLogP ¹	109
Table 14: Attempts at the introduction of the benzyloxy moiety to 69	115
Table 15: Structures of the final compounds synthesised for this indole focused library (78a-i)	123
Table 16: IC ₅₀ data for the indole library (DMSO final concentration 0.0002%).....	127
Table 17: The known selectivity profile for 98	138
Table 18: Attempts at the introduction of a suitable leaving group (X) on 106	145
Table 19: Quinazoline library for biological evaluation.....	153
Table 20: Heat map for the data obtained from the Z-LYTE assay (% inhibition against a panel of kinases at 1 μM. ATP concentration is K _{mapp} . *ATP 100 μM).....	157
Table 21: Activity against VEGFR ₂ for 98 , 101 and 123 (ATP concentration is at K _{mapp})	157
Table 22: Activity against VEGFR ₃ and RET for 101 (ATP concentration is at K _{mapp})...	158
Table 23: Summary of the attempts to introduce the boronic pinacol ester on 129	165
Table 24: Attempts at the conjugation of NOTA-NHS with 160	174

Table 25: Summary of the conditions utilised for the attempted fluorination of 136 , using 2 mg of precursor with a 300 μ L reaction volume.....	177
Table 26: Attempts at the synthesis of [^{18}F]- 101 from 136 using the TRASIS allinone synthesiser	181
Table 27: Investigation of the amount of base used in the initial fluorination attempts, using 5 mg of 138	184
Table 28: Summary of the Dimroth rearrangement conditions used to synthesise [^{18}F]- 123	187
Table 29: General stock solutions.....	269
Table 30: Western blotting antibodies and conditions used	274
Table 31: Optimised radiolabelling conditions.....	275
Table 32: Identification of successful conditions. (^a microwave heating).....	300
Table 33: Use of a phase transfer catalyst for the fluorination of 51 with KF with a reaction time of one hour	300
Table 34: Time course conversion of 51 to 52 using differing equivalents of CsF using <i>t</i> -amyl alcohol whilst heating at 100 °C. Aliquots taken at the allotted time, solvent removed and conversion judged by ^{19}F NMR.....	301

List of Schemes

<i>Scheme 1:</i> Positioning and <i>N</i> -Methyl carbon-11 radiolabelling of 2	58
<i>Scheme 2:</i> Electrophilic radiolabelling of [¹⁸ F]- 12	65
<i>Scheme 3:</i> Nucleophilic radiolabelling of [¹⁸ F]- 12	66
<i>Scheme 4:</i> Traditional methods of trifluoromethylation, with two examples of drug candidates (CCT245737 and Enzalutamide) containing the CF ₃ group (highlighted in red)	67
<i>Scheme 5:</i> Copper mediated fluorination of aryl and heteroaryl iodides	68
<i>Scheme 6:</i> Examples of fluorination with iodonium salts	68
<i>Scheme 7:</i> Radiosynthesis of Rotstein spirocyclic hypervalent iodonium compounds	69
<i>Scheme 8:</i> Ritter's Pd mediated fluorination	69
<i>Scheme 9:</i> Copper mediated fluorination	70
<i>Scheme 10:</i> Aryl boron derivatives for fluorination.....	71
<i>Scheme 11:</i> Gouverneur fluorination of phenols.....	71
<i>Scheme 12:</i> Synthesis of the core scaffold 28a and 28b	86
<i>Scheme 13:</i> Attempted isocyanate mediated synthesis of final compounds	87
<i>Scheme 14:</i> Synthesis of urea derivatives, the via use of coupling reagent 25	89
<i>Scheme 15:</i> Attempted synthesis of 31b using 36	91
<i>Scheme 16:</i> Attempted synthesis of 31b and 40 using 4-nitrophenyl carbamate analogues	92
<i>Scheme 17:</i> Proposed synthesis of 3-fluoropropan-1-amine 46 , with the envisaged synthesis of isocyanate 47	94
<i>Scheme 18:</i> Alternative proposed fluorination method using the Gabriel synthesis	95
<i>Scheme 19:</i> Synthesis fluoromethyl tosylate 52	96
<i>Scheme 20:</i> Synthesis of 68a and 68b	113
<i>Scheme 21:</i> Attempted introduction of the benzyl moiety to 69	115
<i>Scheme 22:</i> Attempts at protecting the ketone functionality	116
<i>Scheme 23:</i> Attachment of the methoxy group to form 71	116
<i>Scheme 24:</i> Remaining steps towards the synthesis of 2-methyl-1 <i>H</i> -indol-5-ol 64	118
<i>Scheme 25:</i> Full synthesis of target indole 65	119
<i>Scheme 26:</i> Synthesis target indole 66	120
<i>Scheme 27:</i> Synthesis of the final compounds 78a-i	121
<i>Scheme 28:</i> Click synthesis of 78e from alkyne 78d	122
<i>Scheme 29:</i> Synthesis of quinazolinone intermediate 105a and 105b	144
<i>Scheme 30:</i> Rearomatisation of 106 , for the introduction of a suitable leaving group	144

<i>Scheme 31:</i> PyBOP mediated synthesis of target compound 98	146
<i>Scheme 32:</i> TIPS protection of 110 and subsequent PyBOP mediated coupling with 105a	149
<i>Scheme 33:</i> Synthesis of 119 , a trial Dimroth rearrangement.....	150
<i>Scheme 34:</i> Synthesis of formimidamides 122a and 122b	151
<i>Scheme 35:</i> Synthesis of final compounds 98 , 101 and 123	153
<i>Scheme 36:</i> Attempts to fluorinate the benzylic position of 102 from 98	154
<i>Scheme 37:</i> Synthesis of 129 for further diversification for an appropriate precursor	164
<i>Scheme 38:</i> Attempted synthesis of 132a and 132b	167
<i>Scheme 39:</i> Alternative strategy to synthesise 132a	167
<i>Scheme 40:</i> Synthesis of the precursor 136	168
<i>Scheme 41:</i> Attempted synthesis of precursor 137	169
<i>Scheme 42:</i> Initial attempted synthesis of 4 , via quinazoline 144	170
<i>Scheme 43:</i> Synthesis of <i>N, N</i> -dimethylformamidine 151 – the key intermediate for the Dimroth mediated synthesis	171
<i>Scheme 44:</i> Synthesis of 154 via the Dimroth rearrangement	172
<i>Scheme 45:</i> Synthesis of tosylate 156	172
<i>Scheme 46:</i> TFA deprotection of the piperidine to reveal 146	173
<i>Scheme 47:</i> Synthesis of linker 158	173
<i>Scheme 48:</i> Synthesis of 125	174
<i>Scheme 49:</i> Alternative strategies for NOTA-NHS conjugation	175
<i>Scheme 50:</i> Attempts at the NOTA conjugation with a chromophore	175
<i>Scheme 51:</i> Radiosynthesis of [¹⁸ F]- 101	176
<i>Scheme 52:</i> Reduction conditions utilised in order to purify the reaction, producing by- product 166	179
<i>Scheme 53:</i> Synthesis and structure of [¹⁸ F]- 167 , synthesised via the Dimroth rearrangement	183
<i>Scheme 54:</i> Radiosynthesis of the aniline fragment required for the Dimroth rearrangement	184
<i>Scheme 55:</i> Incorporation of fluorine-18 to afford [¹⁸ F]-Afatinib, via BOP coupling.....	189

Acknowledgments

Firstly, I would like to thank my supervisors for their continued support: Dr Graham Smith for allowing me to spend two thirds of my PhD at The Institute of Cancer Research, Dr Jenny Waby for your continued support with the biology of this thesis and making me think about how to make my chemistry biology friendly, Dr Chris Cawthorne for his thought provoking discussions whilst writing this thesis and taking role of my supervisor when Jenny left Hull for greener pastures.

I owe a massive gratitude of thanks to The Institute of Cancer Research for allowing me to work in their labs for two thirds of my PhD when Graham relocated from Hull. A massive thanks to everyone in Room 24 and Lab 4 for all their support and laughter when needed; Leo, Hannah, Liam, Gabor, Deb and Gary. Without Graham's team I would never have known how to use the HPLCs and learn the radiochemistry I did, thank you!

I will be forever in debt to my London family who adopted me as one of their own, especially when I was meant to be there for six months and left two years later. Thank you to Carolyn, Dimitrie, Tom, Will, Emily and Kate. I miss you guys so much and Northern will be coming to visit you!

Anna thank you for putting up with all the messages and for the support you offer continually, with all the 'I will make sure you finish' and to your sister who provided so many journal articles. A massive thanks to Ash who stopped me from going mad during the write-up and became my write-up buddy for those epic long days!

Dougie, thank you for all those trips to come and visit where I ended up working and when I moved back up north – all those weekends and evenings when I was working on this thesis, it's worth it now. I love you! Thank you to Caroline for reading this thesis and for your expert teaching skills in helping with the writing up.

Finally, a big thank you to my mum and sister (aka ratbag) without whom I would not be in the position I am today, writing this thesis. Who says one parent families amount to nothing! I hope this makes you proud.

Authors Declaration

I confirm that this work is original and that if any passage(s) or diagram(s) have been copied from academic papers, books, the internet or any other sources these are clearly identified by the use of quotation marks and the reference(s) is fully cited. I certify that, other than where identified, this is my own work and does not breach the regulations of HYMS, the University of Hull or the University of York regarding plagiarism or academic conduct in examinations. I have read the HYMS Code of Practice on Academic Misconduct, and state that this piece of work is my own and does not contain any unacknowledged work from any other sources.

Chapter One

Literature Review

1. Introduction

1.1. Angiogenesis

In humans, all cells are supported through the development of a blood vasculature network. Organisms do this through three primary routes; vasculogenesis, sprouting angiogenesis and non-sprouting angiogenesis (intussusception).¹ Vasculogenesis is important in the *de novo* development of a blood vasculature network. Angiogenesis is defined as the development of new blood vasculature from pre-existing vessels. Figure 1 highlights the different types of blood vessel development, with each being discussed briefly below in the context of the normal physiological development of vasculature networks or tumour vascularisation.

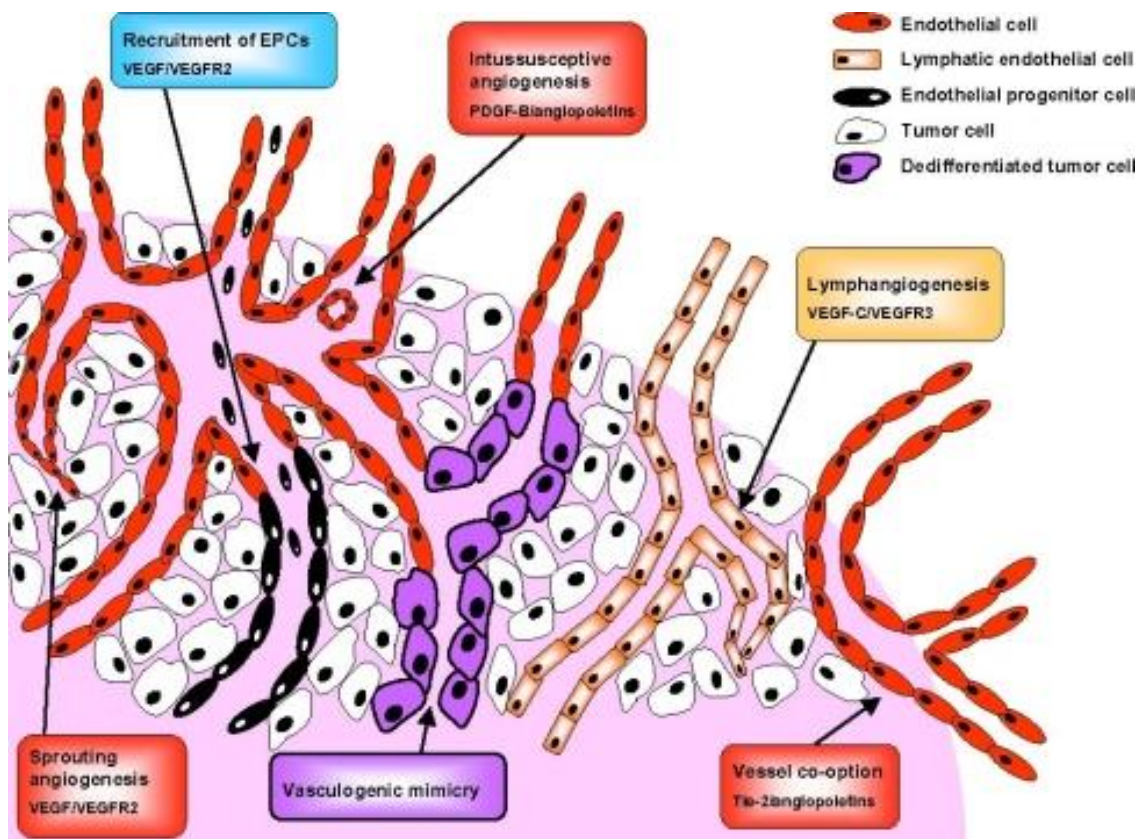


Figure 1: Mechanisms of tumour vascularisation. This figure highlights the six prominent types of vascularisation seen in physiologically and solid tumours.²

1.1.1. Physiological angiogenesis

Physiological angiogenesis is a highly regulated process and is limited in the adult, occurring mainly during embryogenesis.^{3,4} Examples of physiological angiogenesis are menstruation and wound healing. In adult vasculature there is very little proliferation of the endothelial cells, due to the decreasing need for new blood vessel formation in healthy tissue.³ Physiological angiogenesis involves the activation of quiescent endothelial cells to form ordered new vasculature and is controlled by the release of both pro-angiogenic and anti-angiogenic factors.^{5,6}

1.1.1.1. Vasculogenesis

Vasculogenesis is the first process in which blood vessels are formed *in utero* during embryonic development.⁷ As shown in Figure 2, endothelial progenitor cells differentiate and proliferate *in situ*, occurring in an avascular tissue to form primitive tubular networks. These primitive tubular networks form the major vessels including; the aorta, the major veins and honeycomb-like plexus which connects the major vessels.⁷ These initial primitive tubular networks then undergo angiogenic remodelling, through vessel enlargement and pruning to form the interconnecting branching patterns characteristic of mature vasculature.

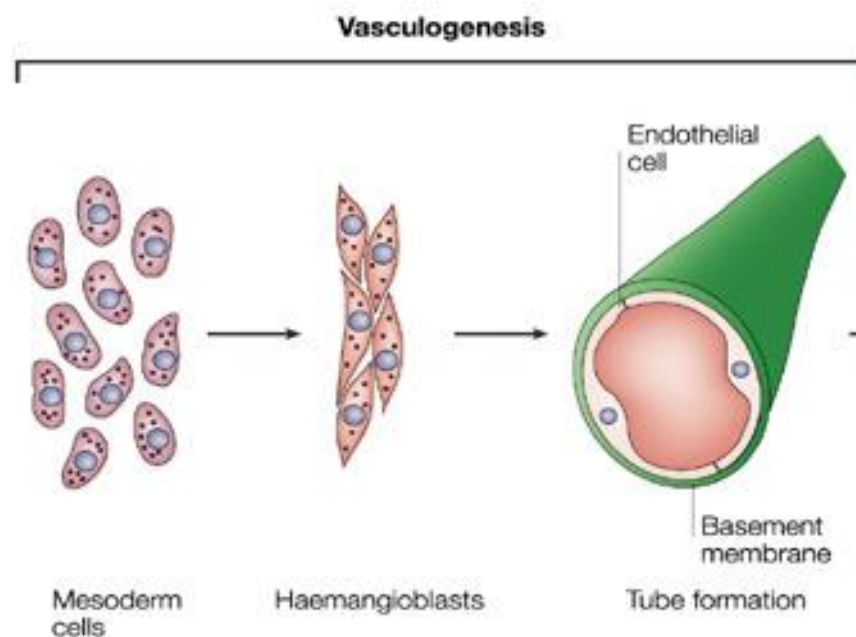


Figure 2: Recruitment of endothelial progenitor cells (EPC - mesoderm cells) are differentiated into haemangioblasts which form the primitive blood vessels⁸

1.1.1.2. Sprouting angiogenesis

Sprouting angiogenesis was first described by Folkman and is defined as the development of a new blood vasculature from pre-existing vessels, involving several steps.^{2,9} First is the activation of endothelial cells by growth factors binding to their respective receptors. Consequently, the extracellular matrix (ECM) and the basement membrane surrounding the newly activated endothelial cells are degraded by proteases (Figure 3). This allows the endothelial cells to invade the surrounding matrix, promoting proliferation and migration.¹⁰ Polarisation of the migrating endothelial cells forms a lumen, creating an immature blood vessel. These immature blood vessels are stabilised through the recruitment of mural cells and the regeneration of the ECM.¹¹

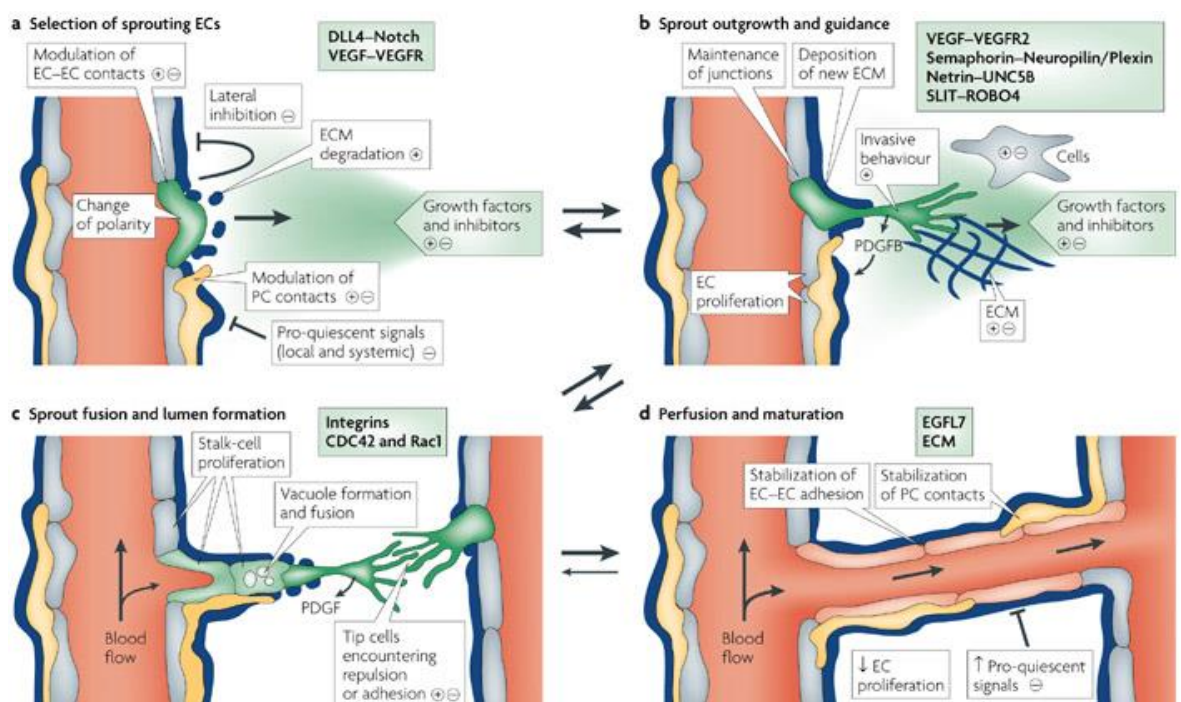


Figure 3: Sprouting angiogenesis. A) activation of quiescent cells through the change in balance of pro and anti-angiogenic factors B) The growing spout is control through a gradient of growth factors C) The primitive lumen is formed through polarisation of the migrating endothelial cells D) Stabilisation of the immature blood vessels.¹²

1.1.1.3. Non-sprouting angiogenesis

Non-sprouting angiogenesis, or intussusception, is defined as the process of splitting pre-existing blood vessels by transcapillary pillars, a process first described in the lungs of rabbits and rats.¹³ It is less well studied compared to sprouting angiogenesis and is known to occur when transluminal tissue pillars develop within capillaries or small arteries and vein (Figure 4). Subsequently, the newly formed transluminal tissue pillars create new

vasculature or remodelling of existing vasculature.¹⁴ Non-sprouting angiogenesis has two main advantages over sprouting angiogenesis. First is the development of vasculature which occurs with a lower rate of endothelial cell proliferation. Secondly, it is accomplished in a shorter space of time, with minimal tissue degradation.¹⁴ This type of vascular development occurs normally during physiological angiogenesis during embryonic development and can be stimulated through either changes in blood flow or upregulation in the expression of specific genes transcribing endothelial growth.¹⁴

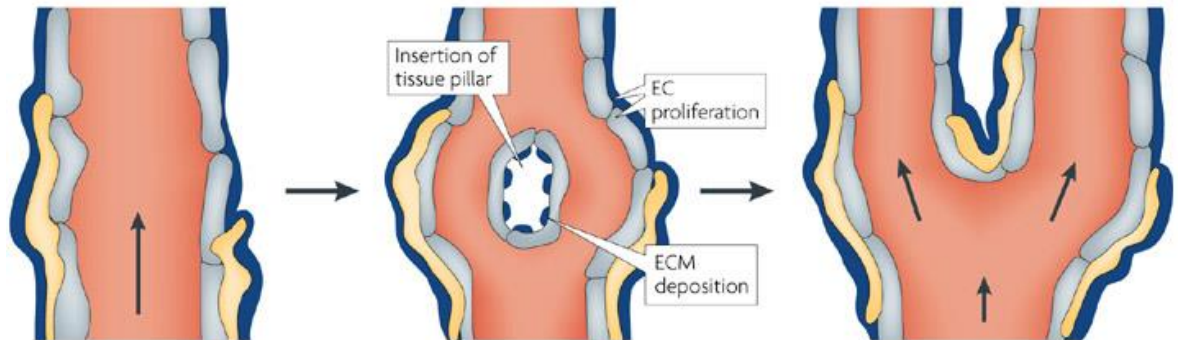


Figure 4: Non-sprouting angiogenesis – splitting of the blood vasculature through the insertion of tubular tissue pillars which leads to degradation of the ECM with endothelial cell proliferation, leading to the splitting of the parent blood vessel.¹²

1.1.1.4. Lymphangiogenesis

The lymphatic system is involved in the drainage of lymph fluid from extracellular spaces and is important in normal cellular function, as well as disease associated pathologies.⁸ It is developed after the blood vasculature and consists of unidirectional blind-ended, thin-walled capillaries, indicating a blood vasculature origin from embryonic veins.¹² The lymphatic system is not commonly found in avascular tissue, such as hair, nails, cartilage, cornea and epidermis.⁸ Lymphatic endothelial cells (LEC) differentiate, migrate and proliferate to form a lymphatic plexus. Sprouting and expansion of the lymphatic plexus creates the lymphatic system (Figure 5).¹²

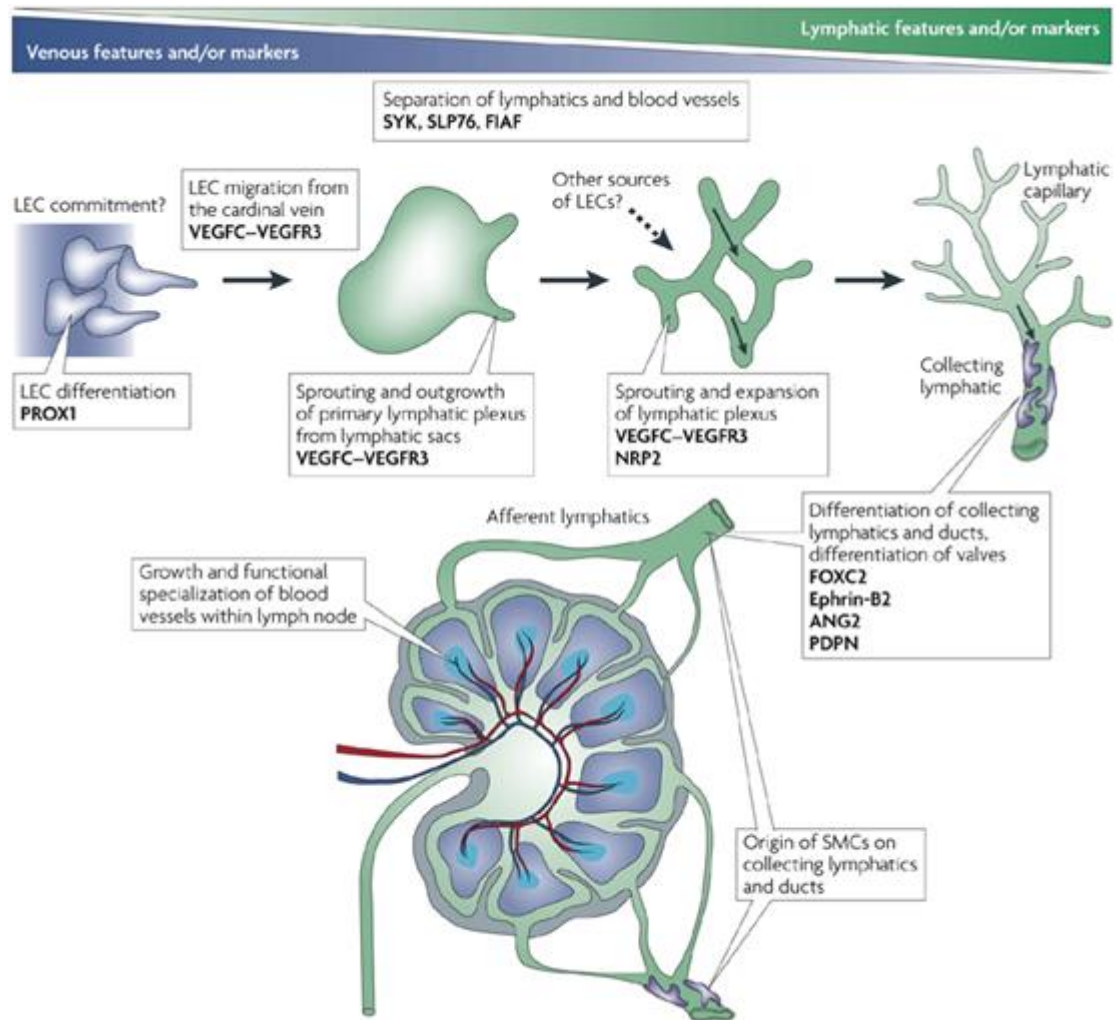


Figure 5: Development of the lymphatic system. LECs are formed during the formation of the lymphatic network, expression of transcription factors in the first LECs occurs in the embryonic veins. The assembly of the lymphatic sacs and sprouting leads to the formation of the lymphatic plexus, which expands into the highly branched lymphatic system¹²

1.1.1.5. Key molecular players in physiological angiogenic signalling

The process of angiogenesis is tightly controlled via the release of pro- and anti-angiogenic factors. These pro-angiogenic factors are summarised in Table 1. The release of these pro- or anti-angiogenic factors is controlled through the induction by hypoxia of hypoxia inducible factor 1 α (HIF-1 α) and the subsequent downregulation of this molecule when the areas of hypoxia have been resolved through vascularisation.⁴

Table 1: Pro- and anti-angiogenic factors involved in physiological angiogenesis^{15, 16}

Pro-angiogenic	Anti-angiogenic
VEGF (vascular endothelial growth factor)	Endostatin
FGF	Angiostatin
LPA	Tumstatin
S1P	Canstatin
EGF	TIMP1
PDGF- β	Interferon
HGF	IL-4 and IL-12
PIGF	IP-10
IL-8	Vasostatin
TGF	TSP-1 and TSP-2
TIE	Id1 and Id3
angiopoietins	INF γ and INF β

The upregulation or downregulation of either pro- or anti-angiogenic factors tightly controls angiogenesis in physiological angiogenesis. The signalling pathways involved in angiogenesis are shown in Figure 6 (in the context of cancer). These include VEGF-VEGFR₂, NOTCH, ANG-TIE2 signalling pathways, each of these will be described briefly and the respective signalling pathways shown in Figure 6.

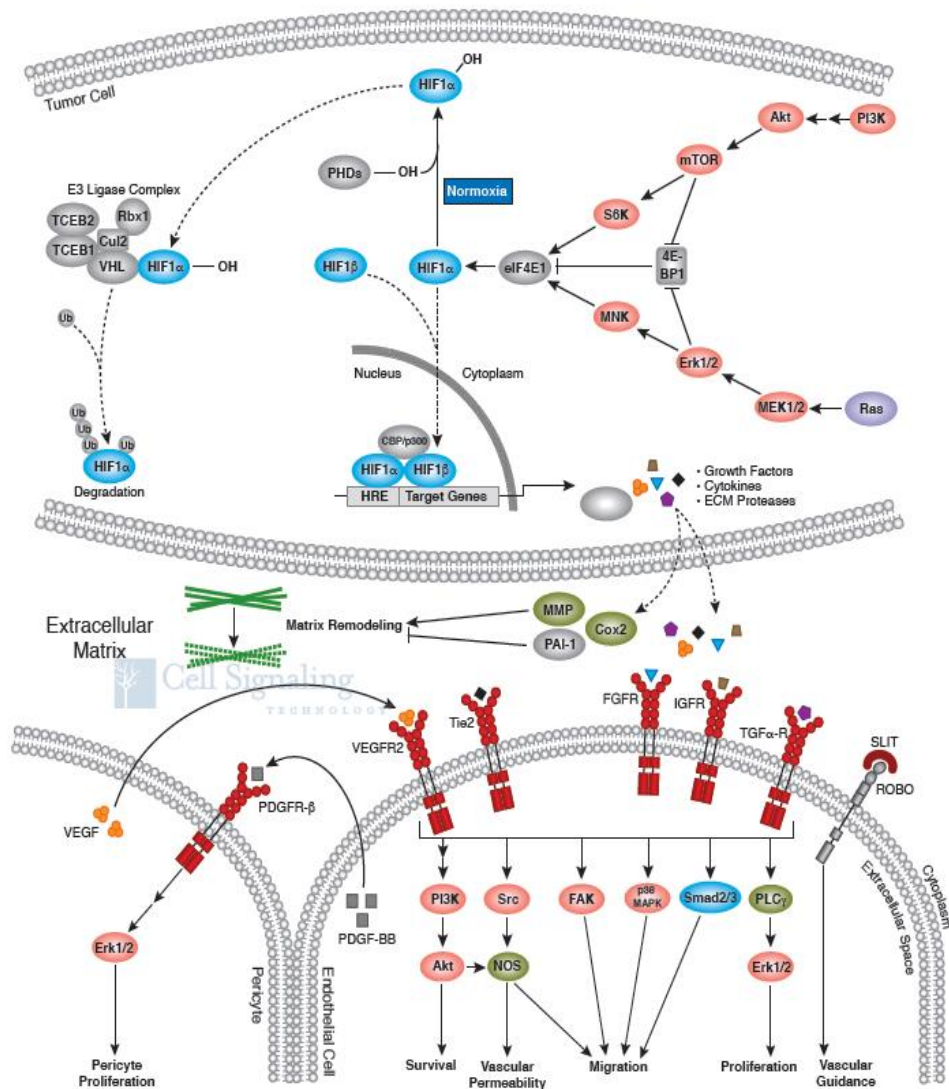


Figure 6: Angiogenic signalling. This figure highlights some of the pathways involved in angiogenesis and the upregulation of pro-angiogenic factors through the recruitment of various growth factors and cytokines, showing the crosstalk between tumour cells and endothelial cells¹⁷

VEGF-VEGFR₂ signalling

Activation of the VEGF-VEGFR₂ signalling pathway (Figure 6 and 11) induces proliferation, sprouting and tubular formation of endothelial cells and is considered the key mediator of angiogenesis.¹⁸ Activation of this particular pathway upregulates PDGF β which is known to recruit mural cells.⁴ VEGFR₂ signalling is heavily implicated in embryonic vasculogenesis and angiogenesis, with high levels of expression during these processes. VEGFR₂ deficient mice are embryonic lethal at day E8.5-9.5, and exhibit defective blood-island formation and vasculogenesis. Importantly, yolk-sac blood islands were absent and organised blood vessels were not present in the yolk-sac or embryo, with a reduction of hematopoietic progenitors.¹⁹⁻²¹ Further consequences of activating this signalling system are

an increase in vascular permeability and the suppression of apoptosis during vessel stabilisation.²⁰

NOTCH signalling

The NOTCH signalling pathway is responsible for a negative feedback system for VEGF mediated vessel sprouting through downregulating their corresponding receptors and is also responsible for determining fate of arterial vessels.^{4, 22}

Ang-TIE signalling

Angiopoietins are known to be critical in the formation of vascular networks in developmental angiogenesis (Figure 6). Activation of this system results in endothelial cell apoptosis when VEGF is not present. Activation also results in interactions of the matrix and mural cells with the endothelial cells.^{4, 23}

1.1.2. *Oncological angiogenesis*

The importance of angiogenesis, for the development and survival of tumours, was first recognised by Judah Folkman who made the following observations:

- Implanting patient tumours into isolated perfused organs, where there is limited blood vessel proliferation, led to tumours that were limited in size (approximately 1-2 mm³). In contrast, when the xenograft is implanted into mice the tumour rapidly expanded (10-20mm³)²⁴
- Tumours implanted into subcutaneous transparent chambers demonstrated slow growth before exponential growth after vascularisation, this is also apparent when tumours were implanted into the cornea (pre-vascularisation)^{25, 26}
- Tumours suspended in the aqueous fluid of the eye remain viable but small in size. When implanted into the vascular rich iris, the tumours grow exponentially (16000 times the original volume in two weeks)²⁷

Once a tumour reaches approximately 2 mm in size, without establishing an adequate blood supply, the interstitial pressure can increase. This impacts on the diffusion of metabolites and nutrients, essential for growth and survival.³ Due to the tumours increased demand for oxygen and glucose, and for the evacuation of all waste material, all viable tumour cells are located within 100-200 µm of vasculature network.²⁸ Initial tumour growth occurs with minimal support from surrounding vasculature; when nutrients and oxygen become depleted the process of angiogenesis is stimulated, a well-established hallmark of cancer.^{4, 29} The point at which tumours begin to undergo vascularisation is called the “angiogenic switch” (Figure 7), a term first coined over 30 years ago, and is defined as the transition of the tumour from the latent to the invasive phase.³⁰ Activation of the angiogenic switch is associated with the expression and excretion of pro-angiogenic factors, such as basic fibroblast growth factor (bFGF), VEGF and various other growth factors, from both the tumour and the tumour microenvironment.^{3, 4, 30, 31} From the tumour microenvironment pro-angiogenic factors can be secreted by stromal cells, pericytes, cancer associated fibroblasts and tumour associated macrophages and are reported to correlate with disease staging, as well as overall patient survival.³²

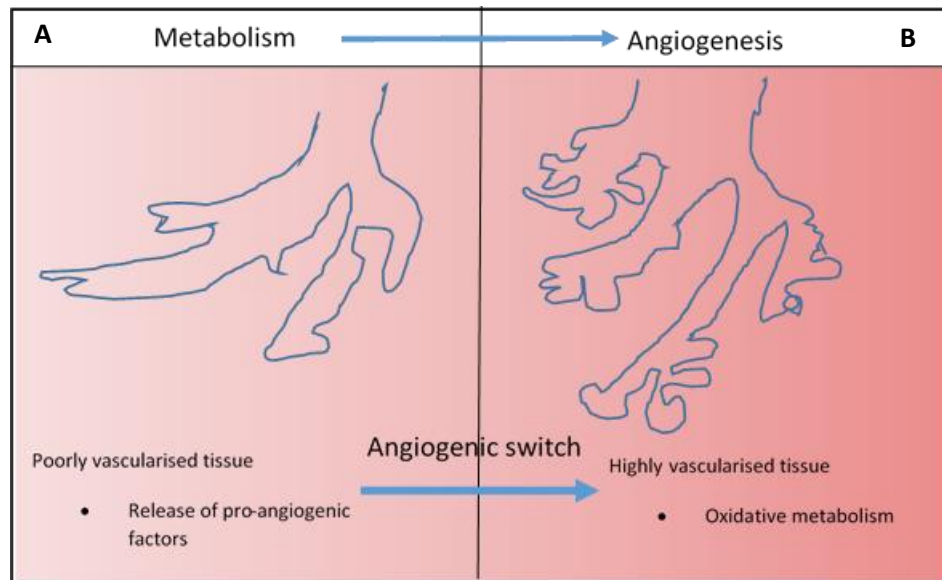


Figure 7: The angiogenic switch. A) The tumour vasculature network is minimal and suffers from depleted oxygen levels and a lack of essential nutrients, triggering the angiogenic switch. B) Triggering the angiogenic switch causes the tumour to become more vascularised, however it is dysregulated (adapted from³³)

The tightly controlled angiogenic process observed in physiological angiogenesis is not apparent in oncological angiogenesis. Typically, oncological angiogenesis is persistent and unresolved which is fuelled by tumour hypoxia and the dysregulation of pro-angiogenic factors.⁴ Genetic instability may also contribute to the uncontrolled angiogenesis observed in tumours.⁴ The blood vasculature of tumours are extremely disordered, irregular, inadequately differentiated and abnormal in both structure and function, unlike that of normal vasculature.³⁴ This favours primary tumour growth, a requirement for metastatic spread, through dissemination of tumour cells through the abnormal vasculature.^{29, 35} In addition to angiogenesis described in 1.1.1, tumours also utilise the following methods of vascular growth: vessel co-option (growth of tumours alongside pre-existing vasculature with invasion of host tissue)³⁶ and vascular mimicry (formation of channels by aggressive and genetically deregulated cancers) to obtain adequate blood supply. The ability to control tumour growth through inhibition of angiogenesis has been extensively researched as a therapeutic target.^{37, 38}

1.1.2.1. Dysregulation of signalling in oncological angiogenesis

Due to depleted oxygen levels as a consequence of the lack of vasculature, a state of hypoxia is induced within the tumour causing the production of HIF-1 α .³⁹ HIF-1 α may also be upregulated by mutations in the vHL gene or upregulation in normoxic states, so called

hypoxic mimicry. The production of HIF-1 α induces the upregulation of pro-angiogenic factors such as VEGF.^{28, 40} The state of hypoxia produced within the tumour itself is caused by the less effective nature of the tumour vasculature. Therefore to circumvent this, VEGF production is upregulated in order to re-vascularise the hypoxic areas (Figure 8).³⁹ Metastatic spread is favoured through uncontrolled release of pro-angiogenic factors and the altered regulation of natural, biological tumour suppressors, such as PTEN through loss of gene function.⁴¹ The major signalling pathways dysregulated in oncological angiogenesis are:

- VEGF-VEGFR₂ – This system is implicated in the recruitment of immune cells which suppress the anti-tumour immune response or those immune cells which promote tumour growth and sustained angiogenesis.⁴ The VEGF pathway plays a significant role in the regulation of tumour angiogenesis and development through the following mechanism.³¹ In response to increasing levels of hypoxia, increased transcription of VEGF is initiated. This leads to increased secretion of VEGF into the stroma and the ECM. Thus allowing receptor activation of the VEGF signalling system and upregulation of MMP, leading to vascular permeability. This initiates the migration of the vascular endothelial cells towards the cancer cells, followed by the formation of new blood vasculature.³¹
- NOTCH-DLL4 - expression upregulated and inhibition of DLL4 *in vivo* results in inadequate vasculature and inhibits tumour growth
- PDGF-PDGFR β – tumour survival and recruitment of vasculature associated stromal cells
- Ang-TIE2 – recruitment of tumour associated TIE2-expressing monocytes which promotes VEGF mediated tumour vascularisation
- TGF-TGFR – promotes angiogenesis through inducing VEGF expression and pro-tumorigenic phenotypes in associated stromal cells

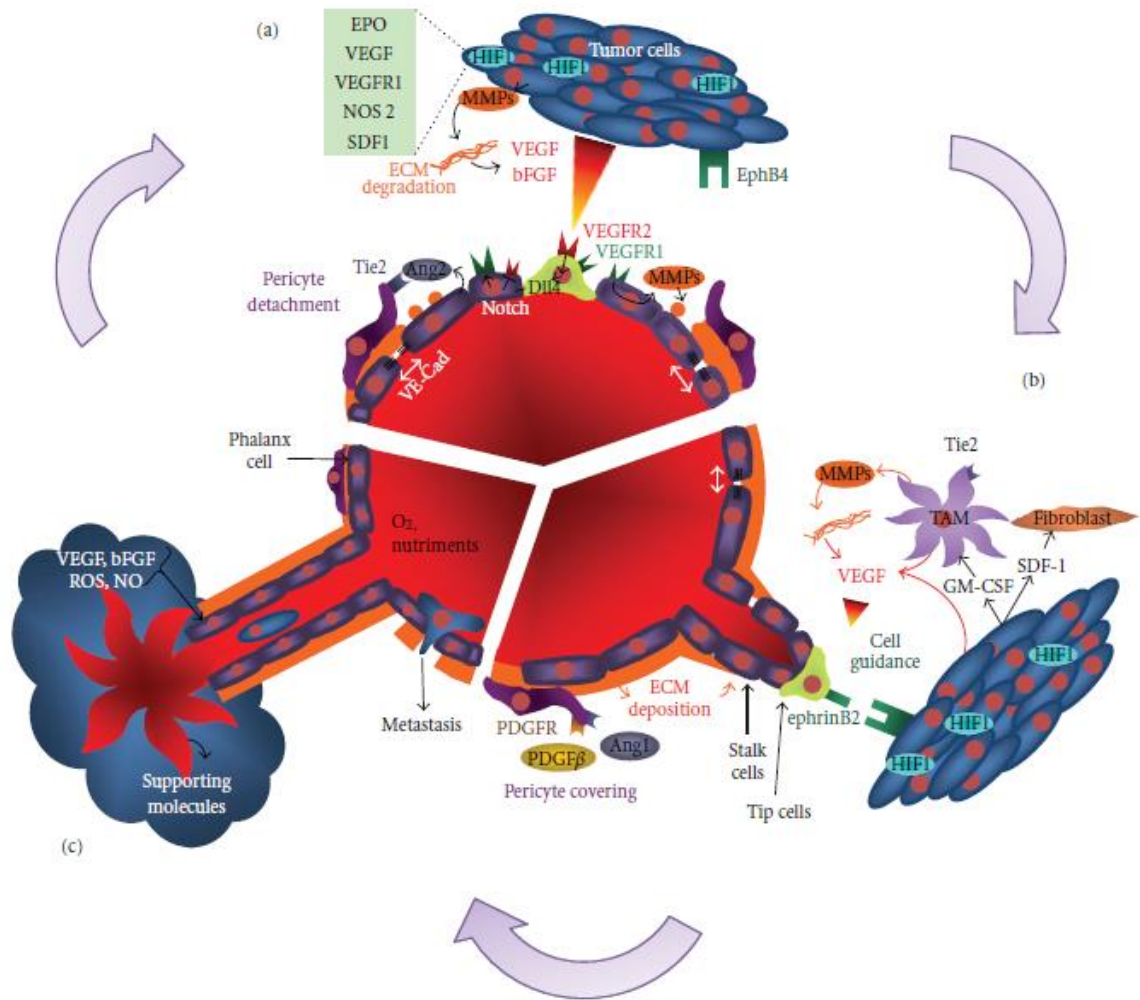


Figure 8: The key molecular players involved in tumour angiogenesis. a) HIF1- α expression is induced due to a state of hypoxia which triggers the release of pro-angiogenic factors b) Tip cells elongate and migrate towards higher VEGF gradients c) Resulting vasculature is abnormal and prone to cell extravasation¹⁵

1.1.3. The VEGF-VEGFR signalling system - The key mediator of angiogenesis

This section will describe the role of VEGF and its receptor in the initiation, progression and metastatic spread of cancer as the key mediator of angiogenesis.

1.1.3.1. Role of VEGF in cancer

VEGF is considered the main inducer of angiogenesis and lymphangiogenesis in cancer cells.^{28,31} VEGF is known to be highly conserved between species, with an 85% homology between both human and rat VEGF.⁴² Currently seven different isoforms of VEGF (VEGF_{A-F}) have been identified, each with different characteristics,⁴³ including solubility, receptor binding characteristics and the ability to be excreted into the ECM.⁴⁴ The VEGF gene is located on the short arm of chromosome six. Native VEGF (VEGF_A) is a basic, homodimeric, 45 kDa glycoprotein which is specific for receptors expressed on vascular

endothelial cells.⁴² VEGF_A is commonly interchanged with VEGF in literature, as this is the key mediator for the receptor activation in angiogenesis.⁴⁵ There are seven sub-isoforms of VEGF_A, each differing in conformation at the 121, 145, 165, 183, 189 and 206 amino acid (Figure 9).

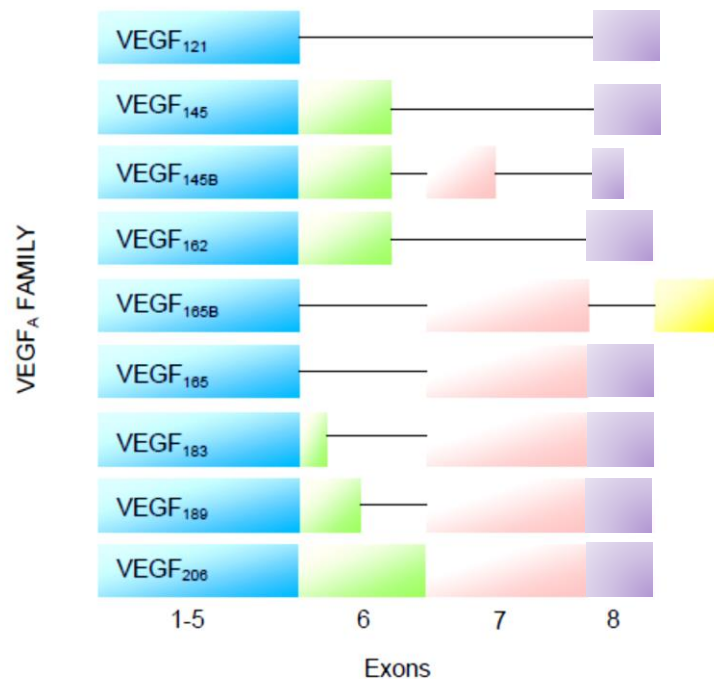


Figure 9: VEGF_A isoforms and the exons required to form the respective isoform; Key blue) exons 1-5; Green) exon 6; Pink) exon 7; Purple) exon 8; Yellow) exon 9 (adapted from²⁸)

The sub-isoforms of VEGF_A are created by alternative splicing of mRNA and proteolytic processing. VEGF₁₂₁ differs from the other high molecular weight VEGF isoforms, as VEGF₁₂₁ lacks the heparin binding domain, encoded by exon 7 which binds to neuropilin-1 (NP-1). VEGF₁₆₅ is cleaved by matrix metalloproteinases (MMPs) and plasmin, creating VEGF₁₁₀ and VEGF₁₁₃ which both contain two biologically active amino terminal groups.⁴⁵ VEGF_A expression is regulated by hypoxia, pH, oncogenes and the concentration of glucose within the cell.⁴⁶ Despite each VEGF_A isoform having independent functions, VEGF_{A165} is responsible for the sustained angiogenesis observed in tumours (Figure 10). VEGF_A binds to VEGF receptor 1, 2 and also NP-1, 2. VEGF_A is not involved in any heparin or matrix binding, and is highly angiogenic in tumours and associated with vascularisation of organs during development.⁴⁶ VEGF_C and VEGF_D bind to VEGF receptor 3 and are involved in the growth and maintenance of lymphatic vessels (lymphangiogenesis).⁴⁷

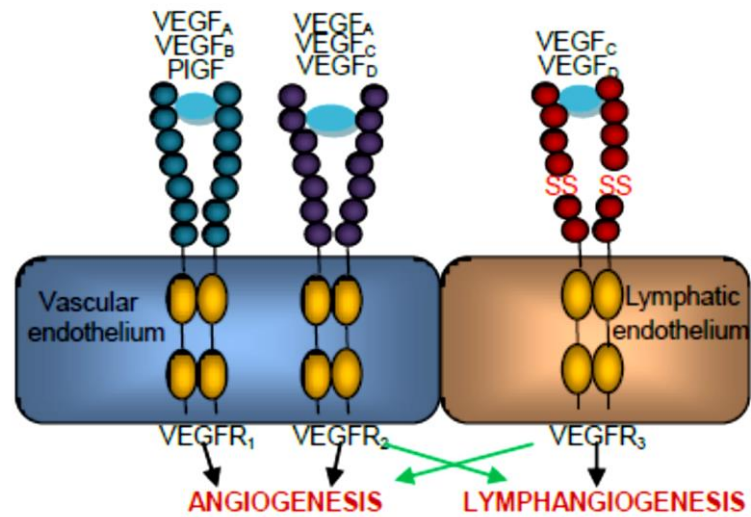


Figure 10: Family of VEGF proteins and their corresponding receptors located on either the vascular or lymphatic endothelium (adapted from⁴⁸)

The VEGF signalling pathway was previously discussed in this Chapter (1.1.2.1) and the activation is initiated through the increased production of VEGF_A. Although hypoxia is a major factor in the upregulation of VEGF, other growth factors and nitric oxide also results in the increased VEGF_A production (Figure 11).³²

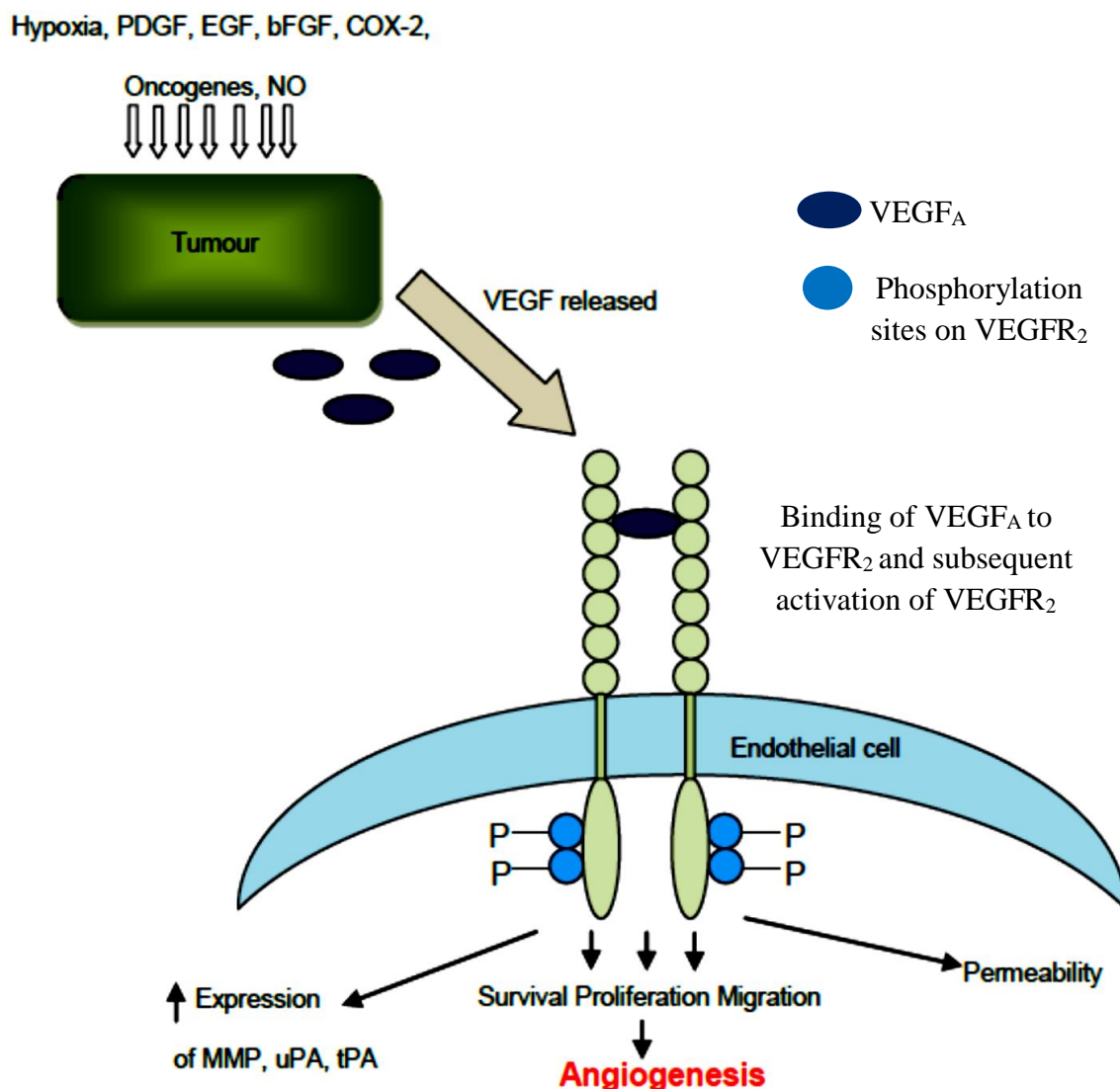


Figure 11: Factors responsible for VEGF production and subsequent VEGFR₂ activation on the vascular endothelium, thus activating the signalling cascade which results in the sustained angiogenesis observed in cancers (adapted from⁴⁹)

1.1.3.2. Role of VEGFR₂ in cancer

There are three different VEGF receptor tyrosine kinases, VEGFR1, 2 and 3.⁵⁰ These are transmembrane receptors, exhibiting tyrosine kinase activity and are permanently expressed on the vascular endothelium, independently of proliferation.³¹ The VEGF receptors are type III transmembrane kinase receptors, sharing a common structure.⁵⁰ As shown in Figure 12, there is an extracellular portion of the receptor, consisting of an N-terminal signalling sequence and seven Ig-like domains, followed by a singular transmembrane segment.⁵⁰ The intracellular portion of the receptor consists of a juxtamembrane segment and a tyrosine kinase domain. The tyrosine kinase segment is divided into the distal and proximal kinase domains. The proximal and distal kinase domains are separated by a 70 amino acid sequence

and the tail of the VEGF receptor is terminated by a carboxy group, as depicted in Figure 12.⁵⁰

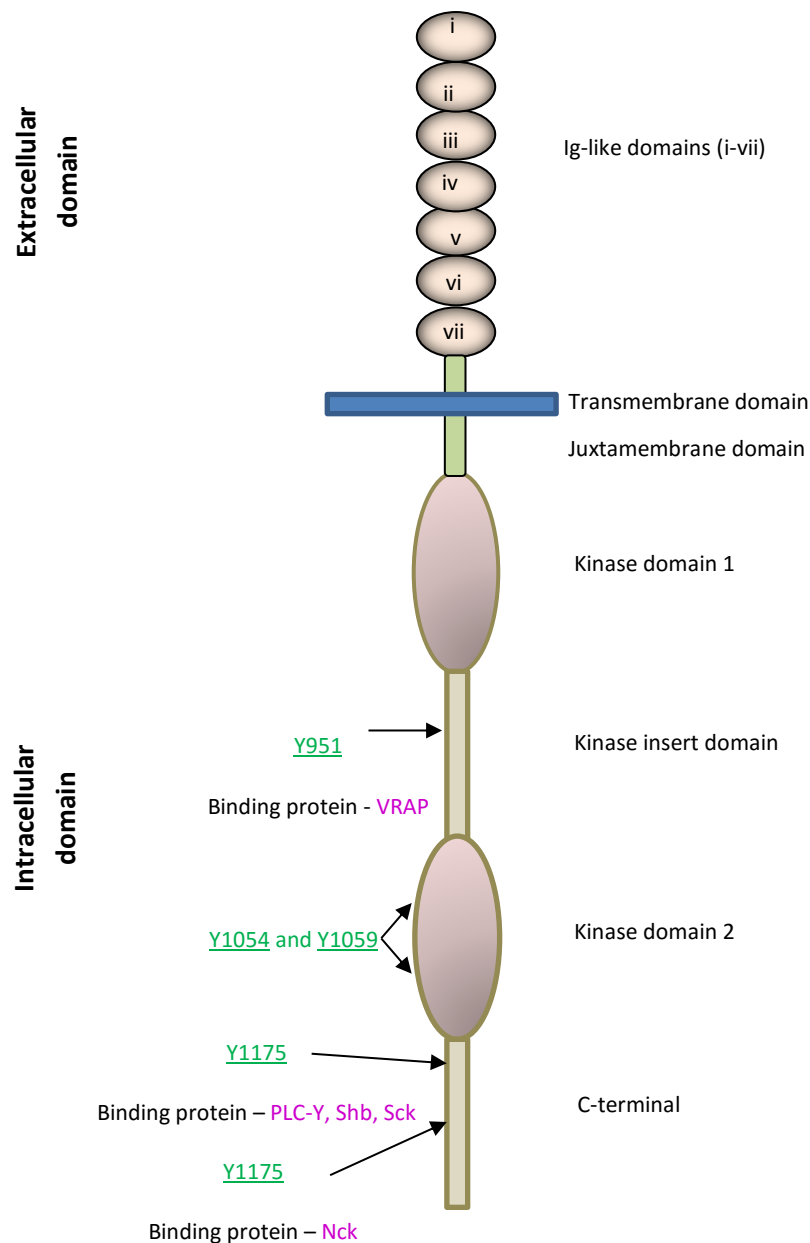


Figure 12: Simplified structure of VEGF receptor 2. VEGFR₂ consisting of both an intracellular and extracellular portions, whilst highlighting the important tyrosine residues involved in activating the signalling cascade (adapted from⁵¹)

The VEGF ligand binds in an overlapping fashion to VEGFR₁₋₃, each with different functions. VEGFR₁ is crucial for haematopoietic cell development and acts as a decoy receptor for VEGFR₂.^{31, 50} VEGFR₂ modulates vascular endothelial cell development, which

binds VEGF in a tenfold lower affinity than VEGFR₁, but with higher mitogenic potential. VEGFR₃ is associated with lymphatic endothelial cell development and the expression is limited to the lymphatic endothelium.⁵⁰

VEGFR₂ (also known as Flk-1/ KDR) is expressed on endothelial cells of both the vascular and lymphatic system, and is 1356 amino acids in length.⁵² When VEGFR₂ is not activated, it exists as a monomer (Figure 13). When VEGF binds to one monomer, another VEGFR₂ monomer unit binds to VEGF. The extracellular binding causes a change in conformation of the intracellular portion, which is responsible for the signalling activity observed.

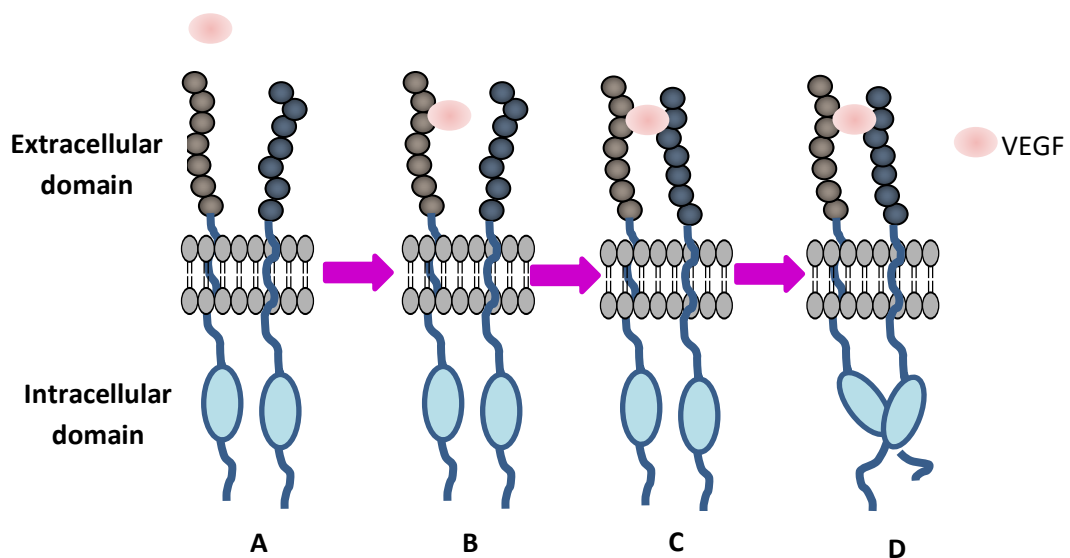


Figure 13: Dimerisation of VEGFR₂. Simplified representation of ligand binding, dimerisation and consequently receptor activation initiating a signal cascade. (adapted from⁵³)

This ligand dependent activation, described above, exposes a site which favours ATP binding.⁵⁰ Once ATP binding has occurred, two key tyrosine residues (Tyr1054 and Tyr1059) are phosphorylated and the signalling cascade is activated for the recruitment of intracellular proteins (Figure 14). This signalling cascade results in the activation of p38MAPK, Pi3K/PKB and RAF/MEK/ERK pathways, which are frequently hyperactivated in cancer cells. Research indicates that NP-1 enhances the mitogenic effects of VEGFR₂ signalling in endothelial cells, although the exact role of NP-1 in angiogenesis is not fully understood. However it is thought that VEGF upregulates NP-1 expression through VEGFR₂ dependant pathways,³⁷ forming a complex with VEGFR₂ to attenuate its mitogenic potential.¹³

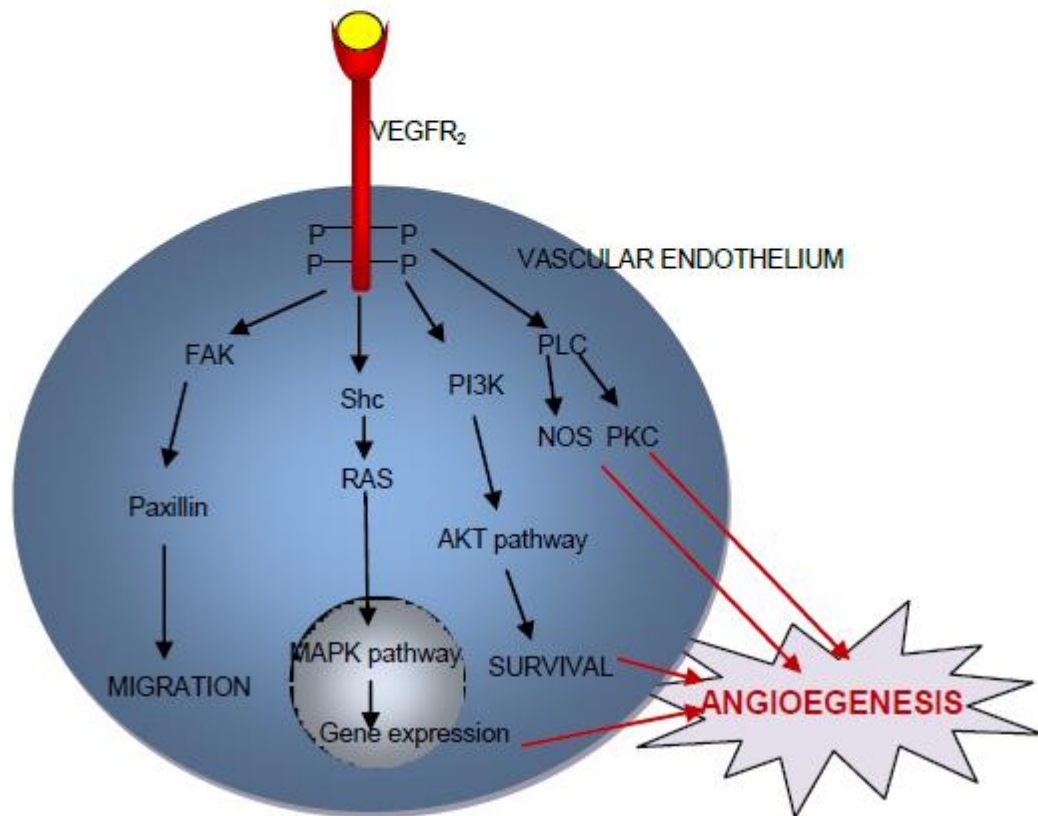


Figure 14: Cascade of signalling activated from VEGF binding to VEGFR₂. Initiation of the downstream signalling pathway after the activation of VEGFR₂ leading to sustained angiogenesis (adapted from⁵⁴)

1.1.3.3. Expression of VEGFR₂ in cancer

Recent publications suggest that expression of VEGFR is not solely limited to the vascular endothelium, but expressed, in varying levels, across the surface of tumour cells.⁵⁵ Data suggests VEGFR₂ is found on the surface of brain, breast, colon, cervical, lung and pancreatic tumours, although this is highly disputed within the field.⁵⁵ Smith *et al.* suggest this discrepancy is due to non-specific binding of anti-VEGFR₂ antibodies. They suggest antibody 55B11 should be standardised as it produced consistent results for the correct identification of VEGFR₂ positive cells.⁵⁶ It is well-known that sustained angiogenesis is considered a hallmark of cancer progression and an attractive target for chemotherapeutic intervention. Therefore inhibiting the VEGF-VEGFR₂ signalling system may produce clinical benefit.²⁹ The rest of this literature review will focus solely on targeting the VEGF-VEGFR₂ signalling system for therapeutic effect.

1.2. Therapeutic intervention of the VEGF-VEGFR₂ signalling system

Targeting angiogenesis as a strategy in treating cancer is highly attractive due to its involvement in tumour growth and metastatic spread. Due to the highly complex nature of the angiogenic signalling system, there are many targets available to achieve therapeutic inhibition of angiogenesis.⁵⁷ In 1971, Folkman first proposed that preventing tumour growth by blocking angiogenesis in microscopic tumours, was the key to maintaining stable disease.⁵⁸ Anti-angiogenic therapies are thought to work by ‘normalising’ the vasculature supporting the tumours which can aid the delivery of other chemotherapeutic agents.¹⁹ Anti-angiogenic therapy can also minimise tumour growth of well-established tumours. This can enhance the effects of conventional chemotherapy or radiotherapy, by causing the tumour cells to become stressed.¹⁹ As previously highlighted, the key mediator of angiogenesis is the VEGF-VEGFR₂ signalling system, therefore this section will discuss its role in angiogenesis.

Thereafter, research has focused on the development of anti-angiogenic therapies, with therapeutic inhibition of VEGF-VEGFR₂ pathways being the most investigated approach for the treatment of cancer. Strategies for targeting the VEGF-VEGFR₂ pathway are based on either neutralisation of VEGF by antibodies or traps or the direct targeting of VEGFR₂ (Figure 15).⁵⁹

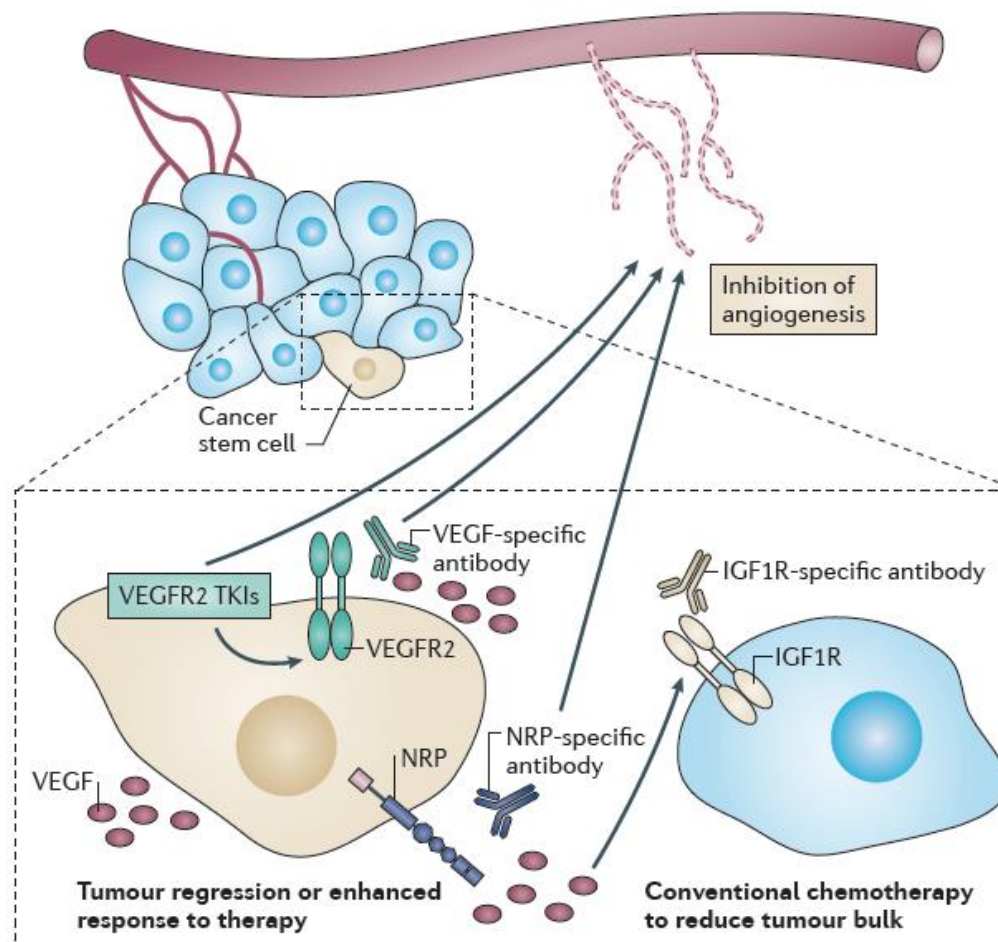


Figure 15: Therapeutic strategies of anti-angiogenic agents. The specific mechanism of actions of generic classes of inhibitors which target either VEGF_A, VEGFR₂ or neuropilin could result in tumour regression or enhancing clinical response⁵⁵

As previously highlighted anti-angiogenic therapies are split into two distinct categories, either targeting VEGF_A or VEGFR₂, each of the therapeutic strategies will be discussed briefly.

1.2.1. Molecular targeted VEGF/VEGFR₂ therapies

Targeted therapies are those therapies which have the capability to target a specific biological process, whereas cytotoxic chemotherapies target all rapidly growing cells. The transition from traditional cytotoxic chemotherapy to molecularly targeted therapy has led to the development of personalised therapy. This is focused on the premise that molecularly targeted therapies focus on pathways which tumours commonly exploit, such as VEGF-VEGFR₂ signalling. However due to the lack of biomarkers assessing treatment efficacy, anti-angiogenic agents cannot be classed as targeted therapy, and it is frequently used in

combination with conventional cytotoxic therapies. This is not to say anti-angiogenic therapy will not become targeted therapy upon discovery of specific biomarkers. Biomarkers will be discussed later in this Chapter (1.2.5).

1.2.2. Inhibitors targeting VEGF_A

Ferrara *et al.* highlighted that neutralising antibodies bound to VEGF slowed tumour growth and also demonstrated the limited side effects associated with antibody use.⁶⁰ This next section will discuss the two main strategies for targeting VEGF_A.

1.2.2.1. Bevacizumab

The first anti-angiogenic agent to be FDA approved in 2004 was Bevacizumab (tradename Avastin).⁶⁰ It is a humanised monoclonal antibody which neutralises VEGF, preventing receptor activation. Like the murine parent antibody, Bevacizumab binds to all sub-isoforms of human VEGF_A including any bioactive proteolytic fragments.⁶¹ Importantly, the pharmacokinetics of Bevacizumab were consistent with other humanised monoclonal antibodies.⁶² Genentech conducted phase I clinical trials in 1997, which demonstrated the single agent use of Bevacizumab was relatively non-toxic and the addition to conventional chemotherapy did not increase the toxicities observed using conventional chemotherapy.⁶³ ⁶⁴ Furthermore, phase II clinical trials comparing the use of Bevacizumab as a single agent or in combination with fluorouracil and leucovorin, revealed single agent use demonstrated greater clinical benefit in non-small cell lung cancer (NSCLC) and combined use with the fluorouracil and leucovorin in colorectal cancer (CRC) was beneficial.⁶⁵ Bevacizumab is currently approved for use in lung and renal cancers and glioblastoma multiforme of the brain.^{66, 67}

1.2.2.2. Aflibercept

The soluble VEGFR decoy Aflibercept (Figure 16) is commonly known as a VEGF trap. Its proposed mechanism of action is to bind to excess VEGF_A, thus preventing VEGFR₂ activation and subsequent initiation of the signalling cascade.⁶⁸ Aflibercept is a fusion protein, which contains the Fc region of IgG and the extracellular binding domains of VEGFR₁ and VEGFR₂. Therefore, it should be capable of binding VEGF_A with the same potencies as previously described, for the respective VEGFR, earlier in this chapter. Aflibercept is also known to target VEGF_B and PlGF, both known to be activators of

angiogenesis.^{69, 70} This could potentially overcome any resistance mechanism sought by the tumours through alternative pro-angiogenic factors. Aflibercept is currently involved in phase III clinical trials to assess its therapeutic efficacy in metastatic (CRC), pancreatic, metastatic androgen-independent prostate cancers and NSCLC.^{71, 72, 73, 74}

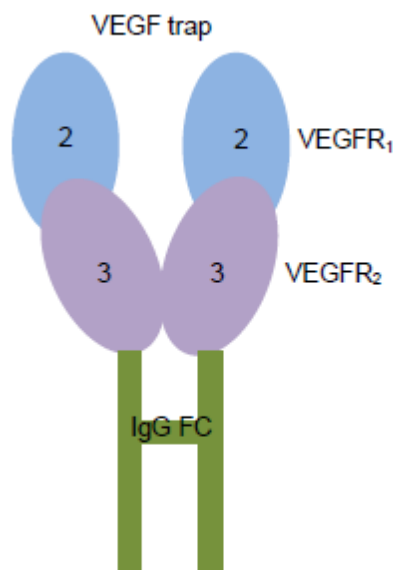


Figure 16: Aflibercept – A simplified representation. The protein highlighted in green is from the FC domain of IgG, the purple domain is the VEGF binding domain of VEGFR₂ and the blue portion is the VEGF binding domain of VEGFR₁. (adapted from⁷⁵)

1.2.3. Tyrosine kinase inhibitors targeting VEGFR₂

There have been several tyrosine kinase inhibitors (TKI) which demonstrate the ability to inhibit VEGFR₂ signalling. Structural similarity of VEGFR₁₋₃ often causes a lack of specificity of the TKI.⁵⁰ This lack of specificity between VEGFR₁₋₃ allows simultaneous inhibition of VEGFR₁ and VEGFR₂, which may be required for the prevention of metastatic disease.⁷⁶ These TKIs include Sunitinib **1**, Sorafenib **2**, Pazopanib **3** and Vandetanib **4** (Figure 17). TKIs which target VEGF receptors aim to reduce angiogenesis and lymphangiogenesis have been extensively investigated as potential targeted therapies. TKI are typically small molecules, which compete with ATP by binding inside the ATP pocket.⁵⁰

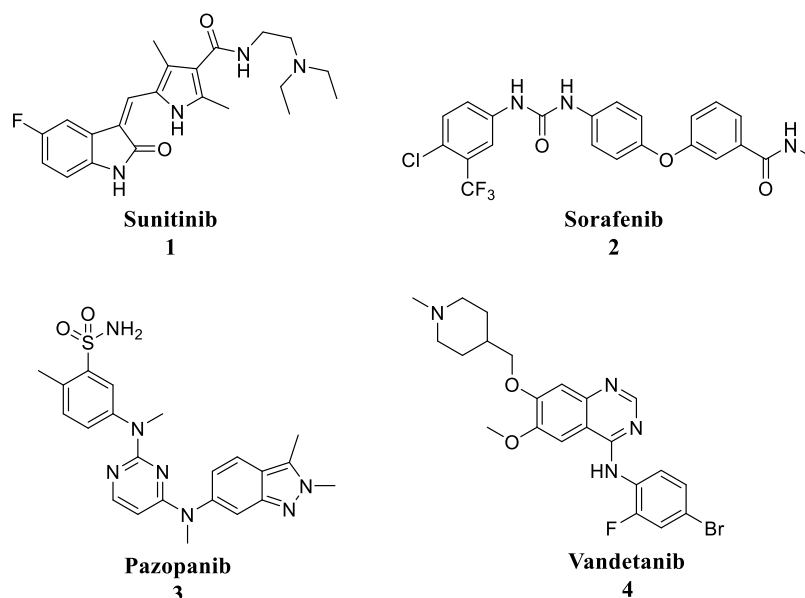


Figure 17: Structures of four clinically relevant TKIs

Multi-targeted therapeutic strategies are employed in cancer treatment, as VEGFR₂ inhibition alone may promote overexpression of angiogenic factors and hypoxic tumour cell survival the development of resistance.⁵⁰ Consequently, this may select for cells that use alternative pro-angiogenic pathways, such as MET signalling.⁵⁰ Anti-cancer therapies based on anti-angiogenic agents are, in theory, less toxic than other chemotherapeutic strategies, with the most common adverse events being thromboembolic event, gastrointestinal perforation and hypertension.⁷⁷ Those heavily pre-treated patients with ovarian cancer can be at higher risk of these adverse events and are therefore not suitable for anti-angiogenic therapy.⁷⁸ This makes the administration of anti-angiogenic therapies potentially more suitable for long-term administration, due to their limited side effects. However they are associated with some adverse events which is dependent on associated comorbidities.⁵⁰

Some drug discovery programmes favour lead candidates which exhibit a lack of selectivity for one target, this is termed polypharmacology or promiscuity.⁷⁹ This can include a single candidate acting on multiple targets of a particular pathway or a single drug acting on multiple independent targets of multiple pathways.⁷⁹ Interestingly, an up-side to polypharmacologic candidates could be the discovery of therapeutic agents which exhibit activity for more than one target. The highly conserved nature of the ATP binding site of kinases means any type I inhibitor can bind inside the ATP of the active kinase, therefore exhibiting wide promiscuity.⁸⁰ Whereas, most type II inhibitors bind to the inactive kinase, occupying a hydrophobic pocket adjacent to the ATP pocket. Despite this, type II inhibitors still exhibit some promiscuity between the kinases and many TKIs exhibit different degrees

of selectivity for a broad range of targets.⁸⁰ One postulated mechanism to explain this promiscuous nature of some TKIs suggest that functional groups of the TKIs may covalently bond with proteins forming an irreversible bond. Alternatively the TKI may contain a privileged scaffold which has the capacity to bind to several tyrosine kinase families.⁸¹ Promiscuous inhibitors may be of clinical value when a tumour may contain overexpression of a range of kinases or mutations in several signalling pathways. This can be troublesome when developing an inhibitor which targets a singular kinase for the development of an imaging probe.

1.2.3.1. Sunitinib **1**

In 1994, Sugen identified the indolin-2-one scaffold to target VEGFR₂ whilst testing against PDGFR.⁸² The promiscuous inhibitor Sunitinib **1** (also known as SU11248 or Sutent) exhibits both anti-tumour and anti-angiogenic properties and is known to inhibit tumour cells which are dependent on either PDGFR or VEGFR signalling.⁸³ Importantly, neither PDGFR or VEGFR were required for **1** to exhibit anti-tumour properties.⁸³ It was first approved for use in the clinic, by the FDA in 2006, as first line therapy for advanced renal cell carcinoma and Imatinib-resistant gastrointestinal stromal tumours (GIST).^{84, 85} Sunitinib highlights the use of the indol-2-one core and is known to target VEGFR₁, VEGFR₂, FLT-3, cKIT, PDGFR α and PDGFR β . *In vitro* studies demonstrated that **1** can inhibit growth of VEGF, PDGF and KIT driven cell lines. It is also known to induce apoptosis in human umbilical vein endothelial cells (HUVEC).⁵⁰

1.2.3.2. Sorafenib **2**

Sorafenib **2** is a urea based kinase inhibitor initially developed as BAY 43-9006 by Bayer Pharmaceuticals in 2001, and was identified from a library of 1000 compounds, via a high throughput screen.^{77, 86} Preclinical data revealed **2** to inhibit VEGF_A induced phosphorylation of both VEGFR₁ and VEGFR₂ in HUVECs, and is also known to be active against the V600E mutation commonly found in RAF driven cancers. Dual RAF and VEGFR₂ inhibitor **2** is a small molecule tyrosine kinase inhibitor which has been shown to inhibit cellular proliferation and angiogenesis in different tumours, including RCC, hepatocellular carcinoma, NSCLC, ovarian, CRC and differentiated thyroid cancers.^{84, 86}

1.2.3.3. Pazopanib **3**

The second generation indazole based small molecule TKI, Pazopanib **3**, is a multi-targeted inhibitor which gained FDA approval in 2009, demonstrating activity against RCC, NSCLC, pancreatic islet cell tumours, ovarian, breast tumours and sarcomas.⁸⁷ On a kinase level, **3** is known to target all VEGFRs and PDGFR β as well as other essential proteins involved in angiogenesis and improves PFS in metastatic RCC.^{45, 87}

1.2.3.4. Vandetanib **4**

Small-molecule quinazoline based TKI Vandetanib **4**, targets VEGFR₂, RET, VEGFR₃, FLT-1, PDGFR β , Tie-2, FGFR1 and EGFR with potencies less than 2 μ M and was initially developed by Astrazeneca.^{54, 88} FDA approval of **4** was achieved in 2011 and was the first TKI to gain approval for treatment against symptomatic or progressive medullary thyroid cancer in patients with localised or metastatic cancer.^{89, 90} Greater potential for anti-tumour efficacy of **4** has been achieved as it has the ability to simultaneously target both VEGFR₂ and EGFR, in high expressing cell lines.⁹⁰ Proliferation in breast, lung, melanoma, CRC and prostate cell lines is known to be inhibited on treatment with **4**.⁹⁰

1.2.4. Summary of current therapies targeting the VEGF-VEGFR₂ signalling system

Anti-angiogenic approaches which inhibit blood vessel growth in cancer, have led to FDA approval of VEGFR inhibitors (Table 2).³³ These therapies can be a source of controversy, as resistance to the inhibition of the VEGF-VEGFR₂ pathway can develop, which can allow the tumour activate alternative angiogenic signalling pathways.³³ As a result, it is unclear which cohorts of patients will benefit from therapies targeting the VEGF-VEGFR₂ signalling system. Some cohorts of patients, with advanced disease, initially show response to anti-angiogenic therapy quickly show progressive disease despite aggressive therapy.^{91, 92} A biomarker may have use in the identification of those patients which are most likely to respond to anti-angiogenic therapy. This could be achieved by identifying a dependence in the VEGF-VEGFR signalling pathway, with higher or lower levels of VEGFR₂ expression.

Table 2: List of antiangiogenic agents (adapted from^{93,94})

Drug	Pharmacophore	Mode of Action	Targets	Cancer targeted	Clinical status
Bevacizumab	-	MAB	VEGF	colorectal, NSCLC, ovarian,	approved
Afilbercept	-	VEGF-Trap	VEGF	metastatic breast cancer	phase III
Axitinib	indazole	RTK	VEGFR ₁₋₃ , PDGFR and c-KIT	RCC, ovarian, NSCLC, GIST	phase III
Cediranib	quinazoline/indole	RTK	VEGFR ₁₋₃ , PDGFR- β and c-Kit	NSCLC, RCC, CRC, CNS	phase III
Motesanib	indoline	RTK	VEGFR ₁₋₃ , PDGFR and c-kit	breast, thyroid	phase III
Pazopanib	indazole	RTK	VEGFR ₁₋₃ , PDGFR alpha and beta and c-kit	metastatic RCC	approved
Regorafenib	urea	RTK	VEGFR ₂	CRC	unknown
Sorafenib	urea	RTK	Raf, VEGFR ₂ and -3, PDGFR, and c-kit	RCC, heptalocarcoma	approved
Sunitinib	indolin-2-one	RTK	VEGFR, PDGFR, Flt-3, c-kit, RET, and CSF-1R	RCC, GIST	approved
Vandetanib	quinazoline	RTK	VEGFR-2, PDGFR-, EGFR, and RET	metastatic thyroid cancer	phase III
Vatalanib	phthalazine	RTK	VEGFR ₁₋₃ , PDGFR-, and c-kit	multiple tumour	phase II

1.2.5. Biomarkers for the VEGF-VEGFR₂ signalling system

Given the varying degrees of response or non-response seen in the clinic from the use of the clinically available anti-angiogenic treatments, biomarkers are an important tool for predicting probable treatment response and also quantifying treatment response. Identification of a VEGF-VEGFR₂ specific biomarker is of utmost importance as inhibition of this pathway can be associated with serious adverse events, some of which are fatal. Therefore, identifying patients with a dependence on this pathway could potentially improve patient outcomes, whilst minimising the risk of adverse events from unwarranted anti-angiogenic therapy.^{95, 96} Biomarkers can be defined as cellular, molecular or functional parameters which can be indicative of genetic or the functional status of a biological system. Biomarkers are identified through pre-clinical, epidemiological or clinical trials. Biomarkers can be utilised for staging, prognosis, diagnosis, receptor expression status and treatment prediction.⁹⁷ Biomarkers can be split into three distinct categories, as defined below:

- Predictive biomarker - *Predictive biomarkers allow the identification of a smaller subset of patients where this line of therapy is most likely to be beneficial. Predictive markers such as hypertension, circulating markers and single nucleotide polymorphisms (SNPs)*⁹⁷
- Prognostic biomarkers - *Prognostic biomarkers have the ability to predict the overall survival of a patient, regardless of the line of therapy, but not therapeutic response. Either the presence or absence of prognostic biomarkers can be used to select patients for therapy, therefore, it is closely linked with the predictive biomarker*⁹⁸
- Pharmacodynamic biomarker - *Pharmacodynamic biomarker allows the identification of biomarkers which change in response to therapy. Monitoring these biomarkers can give an indication to potential long term success. The identification of a pharmacodynamic biomarker is dependent on the treatment given*⁹⁷

Currently in the literature both predictive and prognostic biomarkers are used interchangeably, however as described above there are differences between both types of biomarkers.⁹⁸ Therefore for the purpose of this project, the literature review will be focused on discussing either predictive or pharmacodynamic biomarkers.

1.2.5.1. Predictive biomarkers

Predictive biomarkers are important for identifying smaller cohorts of patients which share similar biological characteristics. These characteristics can be detected by molecular, biochemical methods or via imaging. Predictive biomarkers allow appropriate treatment to be selected based on the characteristics of interest.

The next section will briefly highlight potential predictive biomarkers measured via *ex vivo*, non-imaging based, methods.

Circulating (or blood-borne) biomarkers

Although less invasive than tissue based biomarkers, circulating biomarkers provide systemic information and are arguably less informative about tumour biology.⁹⁹ Circulating markers such as baseline VEGF have yielded disappointing and, often, contradictory results. High basal levels of VEGF can indicate survival benefit in some cancers, whilst being indicative of poor prognosis in others. These differing levels of baseline VEGF can be seen as a prognostic biomarker, as they are not predictive of response to anti-angiogenic treatment.^{97,100} In a randomised phase II clinical trial with Vandetanib, lower baseline VEGF levels were correlated to an improved progression free survival (PFS) in advanced NSCLC patients. Lower basal levels of VEGF also correlated with a longer time to progression (TTP) with metastatic breast carcinoma when treated with Bevacizumab and chemotherapy and PFS with HCC treated with Sunitinib.¹⁰¹ Ko *et al.* investigated the use of VEGF_A as a circulating biomarker when 46 patients were treated with gemcitabine, cisplatin and Bevacizumab for pancreatic changes. Whilst the amount of circulating VEGF increased during treatment, it was found that this was not of prognostic value.¹⁰² Dowlati *et al.* investigated the predictive value of VEGF_A levels at baseline and found a correlation with low levels and enhanced PFS, in NSCLC patients treated with Bevacizumab, carboplatin and paclitaxel.¹⁰³ Dreves *et al.* also confirmed low basal levels of VEGF_A were associated with low risk of disease progression in Vandetanib treated NSCLC.¹⁰⁴ A phase II clinical trial confirmed higher basal levels of serum VEGFR₂ was correlated with longer PFS in Apatinib treated advanced breast cancer.¹⁰⁵ Therefore, higher pre-treatment levels of VEGFR₂, predicts clinical benefit upon treatment with Sunitinib.¹⁰⁶

Tissue based biomarkers

Tissue based biomarkers are important as they can indicate any changes occurring within the tumour during treatment.⁹⁹ However, in practice this is difficult to achieve due to the invasiveness of biopsy procedures and the heterogeneity of the samples acquired. On acquiring biopsy samples, immunohistochemistry (IHC) could be performed to assess the expression or phosphorylation of VEGFR₂ or of VEGF_A. Other hurdles for IHC of biopsies are the lack of agreement in the literature as to which antibody is the gold standard and the requirement of repeat biopsies. However, thus far no conclusive evidence has been obtained to predict treatment outcome of anti-angiogenic behaviour.⁹⁹ A recent study by Wilson *et al.* highlighted that upon treatment with oxaliplatin-based chemotherapy with either additional Vatalanib or placebo treatment (CONFIRM-1 trial), a higher basal intra-tumour gene expression level of VEGFR₂ corresponded to a longer progression free survival. The primary endpoint in both arms of the trial, however did not correlate with overall survival.¹⁰⁷

There are some research groups currently investigating the predictive nature of tumour microvascular density.¹⁰⁸ Two independent studies found when treating with Bevacizumab, in conjunction with radiation therapy and fluorouracil, there was a decrease in microvascular density in CRC, although other studies could not support the findings of the previously described studies.¹⁰⁹⁻¹¹¹ However, an increase in apoptosis was observed with no change in the proliferation rate.¹¹¹ It could be postulated that any remaining vasculature has been 'normalised' by the anti-VEGF therapy, though this needs more thorough investigation.

1.2.5.2. Pharmacodynamic biomarkers

Given the transient responses seen to either anti-VEGF_A or anti-VEGFR₂ therapy, the identification of a pharmacodynamic biomarker is required to monitor therapeutic response. Currently response to personalised therapy is monitored by the Response Evaluation Criteria in Solid Tumour (RECIST), published in 2000. The RECIST criteria states that the number of lesions assessed should be no more than ten, with a limit of five per organ. With CT or MRI imaging, transaxial imaging is usually used to determine the longest dimension of the neoplasm for RECIST evaluation of therapeutic response.¹¹²

RECIST response criteria is split into four categories:

- Complete response – *disappearance of tumour lesions for a minimum of four weeks*
- Partial response – *decrease in tumour volume of at least 30% for a minimum of four weeks*

- Stable disease – *no change in tumour dimensions*
- Progressive disease – *a minimum of 20% increase in the sum of all tumour dimensions*

Concerns were raised regarding the RECIST criterion which is based around anatomic response, especially where cytostatic therapies (newer therapies) are utilised where stable disease would be the ideal endpoint. An example of this is in GIST tumours, Imatinib treated, where tumour lesions decrease in size slowly but the patients live for extended periods with stable disease.¹¹² However, a pharmacodynamic biomarker may distinguish those patients with stable disease resulting from treatment and stable disease resulting from ineffective treatments.

Pharmacodynamic biomarkers are currently being investigated to study anti-angiogenic treatment efficacy, as a companion to the RECIST criteria described above. This next section will discuss both tissue and circulating biomarkers investigated to meet this clinical need.

Circulating (or blood-borne) biomarkers

Siegel *et al.* discussed the use of monitoring changes in VEGF_A levels in response to therapy as a pharmacodynamic biomarker.¹¹³ The study found that an increase in VEGF_A levels was associated with disease progression in Bevacizumab treated unresectable hepatocellular carcinoma. In a phase I clinical trial, Stopeck *et al.* concluded an increase in urine VEGFA was associated with responders in Semaxinib treated advanced cancer.¹¹⁴

Burstein *et al.* studied changes in soluble-VEGFR₃ (s-VEGFR₃) in respect with Sunitinib treated metastatic breast cancer, concluding decreases in s-VEGFR₃ is linked with a decreased overall survival.¹¹⁵ Duda *et al.* investigated changes in s-VEGFR₁ when advanced CRC is treated with Bevacizumab.¹¹⁶ The study concluded monitoring s-VEGFR₁ levels could be a pharmacodynamic biomarker.

Tissue based biomarkers

As discussed previously in this Chapter, clinical data making use of tissue based biomarkers is limited due to the invasive and repetitive nature of biopsy. Fountzilias *et al.* highlighted the clinical significance of high initial intra-tumoural VEGFR₃ expression and subsequent changes in VEGFR₃ expression post-treatment were linked with clinical response.¹¹⁷ Whereas a general overexpression of VEGFR₁ at baseline was linked with poor OS.¹¹⁷ The AVAGAST clinical trial to identify suitable tissue based biomarkers, found no significance in the expression of VEGFR levels and outcome with Bevacizumab and chemotherapy.¹¹⁸ Interestingly, a strong correlation with low NP-1 expression and overall survival was observed but not statistically significant.¹¹⁸ This is particularly interesting, as previously discussed, NP-1 is involved in forming heterodimers with VEGFR₂, possibly highlighting the use of NP-1 as a predictive biomarker.¹¹⁸

Hypertension

Hypertension is a common side-effect during treatment with a VEGF-VEGFR₂ targeting agent, seen in approximately 20% of patients with grade three hypertension. Although the exact mechanism is not fully understood, it is postulated that VEGF dependant signalling activation influences NO-synthase activity. This reduces NO production resulting in increased vasoconstriction and ultimately hypertension.¹⁰⁰ Monitoring blood pressure may give an early indication of therapeutic response, as shown by Hanvick *et al.* who conclude blood pressure should be monitored for the first month following initiation of anti-VEGFR₂ therapy.¹¹⁹

It is clear from examining the literature there is no single pharmacodynamic or predictive biomarker available to be standardised across the multitude of cancers for anti-VEGF or VEGFR₂ targeted therapies. However, recently molecular imaging has been used to image the VEGF-VEGFR₂ signalling system as a replacement of the more traditional biomarkers.

1.2. Molecular imaging of the VEGF-VEGFR₂ signalling system

1.2.1. What is molecular imaging?

Molecular imaging can be defined as the non-invasive characterisation, visualisation and measurement of biological processes, both at molecular and cellular level.¹²⁰ Since its first conception, it has supported improvements in early diagnosis and therapeutic monitoring in oncology, cardiology and neurology. Molecular imaging also has place in advancing drug discovery and development, understanding protein-protein interactions and enzymatic conversions.¹²¹

Modern oncology now requires precise information about the location and size of the tumour and possible involvement of lymph nodes.¹²¹ This information can be obtained through both structural imaging (computed tomography (CT), magnetic resonance imaging (MRI) and ultrasound (US)) and molecular imaging (positron emission tomography (PET) and single photon emission computed tomography (SPECT)). Figure 18 highlights the sensitivity of imaging techniques towards different aspects of a biological system.

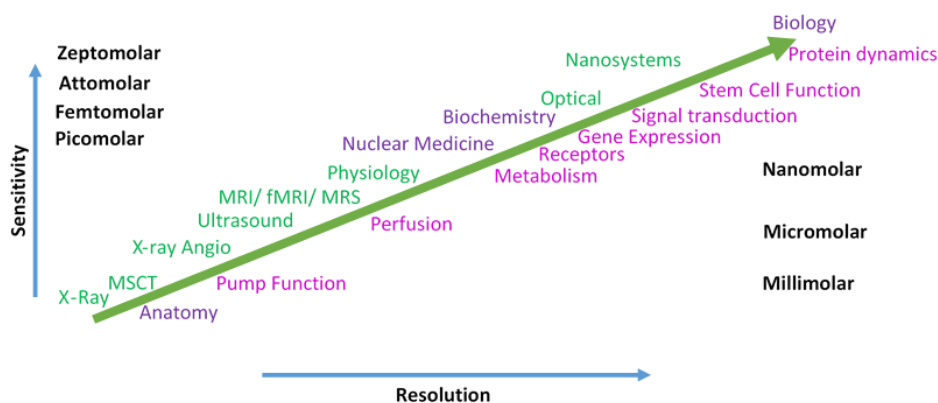


Figure 18: Relative sensitivity of medical imaging techniques (adapted from ¹²²)

Molecular imaging techniques can provide information on metabolic and physiological processes within the target tissue. These techniques include PET and SPECT which allow the monitoring of different metabolic processes, such as angiogenesis. They also allow monitoring within the same biological system over time, supporting repeated *in vivo* measurements of different critical pathways occurring in the neoplasm.^{122, 123} These critical pathways include: metabolism, proliferation, apoptosis and angiogenesis.⁴⁴ All these

pathways are exploited in order to quantify therapeutic responses or stratify patients according to receptor expression status.

Molecularly targeted therapies often result in cytostasis rather than cytoreduction. A prime example of this is Bevacizumab which, as previously discussed, targets VEGF_A.¹²⁴ Consequently, anatomical imaging modalities such as CT and MRI have limited scope to assess early treatment response, therefore a lack of disease progression cannot be used as a response measure for early detection.¹²⁵ Therefore, the development of molecular imaging biomarkers are important as these can provide information on a cellular and molecular level regarding changes in target expression, altered cellular signalling, alterations in metabolism and differences in molecular characteristics can be detected.¹²⁵ Due to the lack of circulating and tissue based biomarkers being consistently identified, an imaging based biomarker or the VEGF-VEGFR₂ signalling system is essential.¹⁰¹ Identification of an imaging based biomarker may prevent patients from receiving potentially toxic treatment if it would make no difference to overall patient outcome. Therefore developing a molecular imaging probe which is capable of assessing the tumours dependence on the VEGF-VEGFR signalling pathway, or assessing the expression level of VEGFR₂ is key. The imaging approach is desirable due to the non-invasive nature of this system, negating the need for repeated invasive biopsies.

1.2.2. Use of molecular imaging to visualise the VEGF-VEGFR₂ signalling system

Molecular imaging has been used to either quantify treatment response or visualisation of VEGFR₂ expression. The current approaches for imaging this system are described in the sections below.

1.2.2.1. Ultrasound

An Austrian neurologist, Karl Theo, was the first clinician to apply US as a medical diagnostic tool for imaging the brain.¹²⁶ US is the most widely utilised medical imaging technique to provide real time quantification.¹²⁷ US is a safe imaging technique not involving the use of ionising radiation and is relatively low cost in comparison to other imaging techniques.

Modern medical US is primarily performed using a pulse-echo approach with brightness-mode (B-mode) displays. This displays the acoustic impedance of a two-dimensional cross-

section of the imaged tissue. Despite its great clinical utility, US has pitfalls depending on the acoustic impedance of the tissue imaged. Imaging lung tissue is problematic for US due to the low acoustic impedance generated. Recently, US can be used as a source for cancer therapy. US is used in sonodynamic therapy, enhancing the activity of chemotherapy regimens and sonoporation to induce apoptosis and necrosis.

Dynamic contrast-enhanced ultrasound (DCE-US) has been developed for non-invasive imaging of monitoring anti-angiogenic treatment response.¹²⁸ Contrast agents for US are encapsulated in microbubbles at a similar size to red blood cells, thus restricting their distribution to the vasculature. The encapsulated gas microbubbles exhibit high echogenicity, thus providing real-time assessment of the tumour vasculature and microvasculature.¹²⁸ Modifications of these encapsulated gas microbubbles to include additional ligands have been developed to target specific receptors expressed on the vascular endothelium. A prime example of a receptor expressed on the vascular endothelium is VEGFR₂.

BR55 is a VEGFR₂ targeting microbubble developed by Bracco Suisse and has been shown to be specific for VEGFR₂ imaging and monitoring therapeutic response.¹²⁹ Upon testing BR55 against two treatments which are known to either target VEGFR₂ or not (Sunitinib or Imatinib), it was found that BR55 was selective in showing differences between the treatments, through targeting VEGFR₂.¹²⁸ A lower level of VEGFR₂ expression as well as a reduction of tumour mass, was observed after Sunitinib therapy. Therefore, BR55 is capable of detecting the early changes associated with anti-angiogenic treatment in CT26 tumours (mouse colon cancer).¹²⁸ When BR55 microbubbles are used to monitor Sorafenib therapy, changes in differential targeted enhancement (dTE) were compared for the responders and non-responder group (as assessed by increases in tumour volume). dTE is representative of a numerical value which is directly proportional to the amount of microbubbles bound to VEGFR₂.¹²⁹ In Huh7 xenografts (hepatocyte cell carcinoma) at baseline those in the non-responding group had higher dTE levels.¹²⁹

1.2.2.2. Magnetic Resonance Imaging

MRI involves the use of radiowaves and a strong magnetic field creating detailed images of soft tissue. The principle of MRI is similar to NMR involving the protons in the water which generate the signal for MRI imaging. MRI can be used in cancer detection, staging, therapy response and biopsy guidance.¹²²

MRI used to image malignancies is focused on relaxivity-based imaging, both with and without contrast, and blood oxygen determination (BOLD) imaging.¹²² There are several techniques which can be utilised to image perfusion and diffusion, cellular surface targets, enzyme activity and ultimately intracellular events, such as dynamic contrast enhanced-MRI (DCE-MRI).¹³⁰ DCE-MRI is a quantitative method of studying microvasculature structure and function by monitoring the pharmacokinetics of the low-weight contrast agents.¹³¹ This technique is highly sensitive towards changes in vascular permeability, extracellular extravascular and vascular volumes, in blood flow.^{130, 131} The images of DCE-MRI are T1-weighted and the concentration of the contrast agent is measured when it passes from the vasculature into the extracellular space, and whether it goes back into the blood vessels. The contrast agent used on DCE-MRI is typically a gadolinium based small molecule.¹³² Parameters which describe the shape of the contrast agent concentration-time curve are a combination of blood flow, volume, vascular permeability and extracellular extravascular leakage space (ESS). The initial area under the contrast agent (IAUC) is easy to calculate, reproducible and is routinely used as a biomarker in clinical trials monitoring therapeutic efficacy.¹³¹ Table 3 summarises the use of DCE-MRI to identify biomarkers for the VEGF-VEGFR₂ signalling system. As shown in Table 3, no imaging DCE-MRI biomarker was identified when investigating antibody based VEGF therapy for either a predictive or pharmacodynamic biomarker.

Table 3: DCE-MRI predictive or pharmacodynamic biomarkers of antibody based therapy

Trial Phase	Number of patients	Drug (cancer)	DCE-MRI biomarker	Drug induced changes	Predictive or pharmacodynamic	Ref
phase I	31	CDP791 (advanced cancer)	K_{ep}	no DCE-MRI change	no significant value	Ton <i>et al.</i> ¹³³
phase I	20	HuMV833 (advanced cancer)	K_{ep} , K^{trans} , rBV	$\downarrow K_{ep}$	no significant value	Jayson <i>et al.</i> ¹³⁴
phase II	20	Bevacizumab (breast cancer)	K^{trans} , V_e	$\downarrow K^{trans}$	no significant value	Wedam <i>et al.</i> ¹¹¹
phase II	26	Docetaxel and Bevacizumab	K_{ep}	$\downarrow K_{ep}$	no significant value	Overmoyer <i>et al.</i> ¹³⁵

K^{trans} volume transfer constant between plasma and EES; V_e volume of ESS per unit volume of tissue; K_{ep} rate constant; rBV regional blood volume; ESS extravascular space;

Table 4 highlights the attempts to identify a suitable DCE-MRI biomarker based around TKI therapy. As clearly demonstrated there is a lack of agreement for a suitable biomarker when treating with the same therapy. Although DCE-MRI is advantageous for targets of some patient stratification and monitoring treatment efficacy, it is not of any valuable use in developing a molecular imaging biomarker for the VEGF-VEGFR₂ signalling system. Thus strengthening the need to identify a suitable alternative imaging technique to develop a molecular imaging biomarker.

Table 4: DCE-MRI predictive or pharmacodynamic biomarkers of TKI based therapy

Trial Phase	Number of patients	Drug (cancer)	DCE-MRI biomarker	Drug induced changes	Prognostic and Predictive value	Ref
phase I	11	Semaxinib	K_{ep}	NS	no significant value	Dowlati <i>et al.</i> ¹³⁶
phase I	14	Vatalanib (advanced cancer)	K_i , rBV	$\downarrow K_i$	change in K_i predicts progression pharmacodynamic	Conrad <i>et al.</i> ⁸³
phase II	27	Vandetanib (breast cancer)	IAUC, K^{trans}	\downarrow IAUC	no significant value	Miller <i>et al.</i> ¹³⁷
phase II	20	Sorafenib (renal)	K^{trans}	$\downarrow K^{trans}$	high baseline, change in % of K^{trans} predicts PFS both predictive and pharmacodynamic	Flaherty <i>et al.</i> ¹³⁸
phase II	24	Semaxinib	K^{trans}	NS	no significant value	O'Donnell <i>et al.</i> ¹³⁹
phase II	27	SU6668	IAUC	NS	no significant value	Xiong <i>et al.</i> ¹⁴⁰

K_{ep} rate constant; rBV regional blood volume; IAUC initial area under the contrast agent concentration; K_i unidirectional influx constant

1.3. Nuclear medicine imaging of the VEGF-VEGFR₂ signalling system

1.3.1. What is nuclear medicine?

Nuclear medicine provides unique opportunities to image the pathophysiology of cell processes.¹⁴¹ Conventional nuclear medicine involves the use of radioisotopes for SPECT and PET imaging. Hybrid techniques, such as PET/CT, are commonly used for dual functional/anatomical assessment of solid tumours.¹⁴¹ This next section will highlight the use of SPECT and PET in imaging the VEGF-VEGFR₂ signalling system.

1.3.1.1. Single photon emission computed tomography

SPECT is a tomographic technique based on acquiring γ emissions from varying projections, which are then reconstructed into three-dimensional images.¹⁴² Radioisotopes used in SPECT imaging decay through the release of a single photon, resulting in limited sensitivity. The most commonly used radioisotope in SPECT is ^{99m}Tc, with a half-life of six hours. SPECT is widely used in clinical practice and due to the wide availability in hospitals.¹⁴³

VEGF₁₂₁ and VEGF₁₆₅, the two most mitogenic VEGF_A isoforms, have been assessed for their potential use in SPECT.¹⁴⁴ Both isoforms have been radiolabelled with iodine-123 and the binding properties assessed against a panel of cell lines. Biological activity of both the radiolabelled VEGF isoforms was identical to non-radiolabelled isoforms in human umbilical vein endothelial cells (HUVECs), this showed promise due to low immunogenicity and exhibited activity in a wide range of cell lines.¹⁴⁵ Both ¹²³I-VEGF₁₆₅ and ¹²³I-VEGF₁₂₁ demonstrated specific binding sites, however ¹²³I-VEGF₁₂₁ bound to more tumour types.¹⁴⁵ Another study involved the use of PAE/VEGFR₂ cell lines which express roughly 2×10^5 VEGFR₂/cell.¹⁴⁶ scVEGF was radiolabelled with ^{99m}Tc-tricine and was found that Sunitinib does reduce uptake of ^{99m}Tc-scVEGF in MDA-231/luc xenografts, with a decrease in VEGFR₂ immunostaining after four days of Sunitinib treatment. Interestingly, the Sunitinib treated xenografts promoted decrease in VEGFR₂ immunostaining was lower than the decrease in CD31 immunostaining. This could indicate endothelial cells with increased VEGFR₂ expression are more resistant to Sunitinib therapy. The decrease in ^{99m}Tc-scVEGF could be reversed after a three day holiday from the treatment regime.¹⁴⁶ This particular approach would be most useful as a pharmacodynamic biomarker, monitoring treatment efficacy though monitoring changes in VEGFR₂ expression.

1.3.2. Introduction to PET

Positron emission tomography (PET) is a tomographic technique which a 3D picture can be built up according to the distribution of radioactivity can be considered as the most sensitive, non-invasive imaging technique.^{88, 147} The next section will describe the use of radionuclides and their decay in PET imaging.

1.3.2.1. Positron emission and annihilation

Positron emitting radionuclides are typically prepared via cyclotrons, which propel protons to high speeds to bombard the stable nuclei of nitrogen, oxygen and carbon atoms. This produces an unstable isotope, which undergoes positron emission (release of a positron (β^+) and a neutrino) as shown in Figure 19. The highly energetic positron formed has a short lifetime in electron rich matter. When travelling through human tissue, the positron gives up their kinetic energy through Coulomb interactions with electrons, following random paths through tissue. When the positron reaches thermal energies, they interact with electrons through annihilation or via forming hydrogen-like orbitals named the positronium. However the positronium formed only lasts for 10^{-10} seconds before annihilation occurs, releasing two γ -photons at almost 180° apart. This opposite trajectory is also known as the line of response (LOR), vital for tomography that allows for electronic collimation, resulting in the higher sensitivity for PET over SPECT.¹⁴⁸ These photons are highly energetic, therefore there is a high probability these photons will be detected externally. The photons which are emitted in a same geometry are detected, the line joining the two trajectories are joined and this gives precise information about the point of annihilation. This point of annihilation coincides with the location of the PET probe. This image reconstruction can be used to evaluate the bio-distribution of the PET probe, providing cross-sectional images which can be done via a number of methods.¹⁴⁸

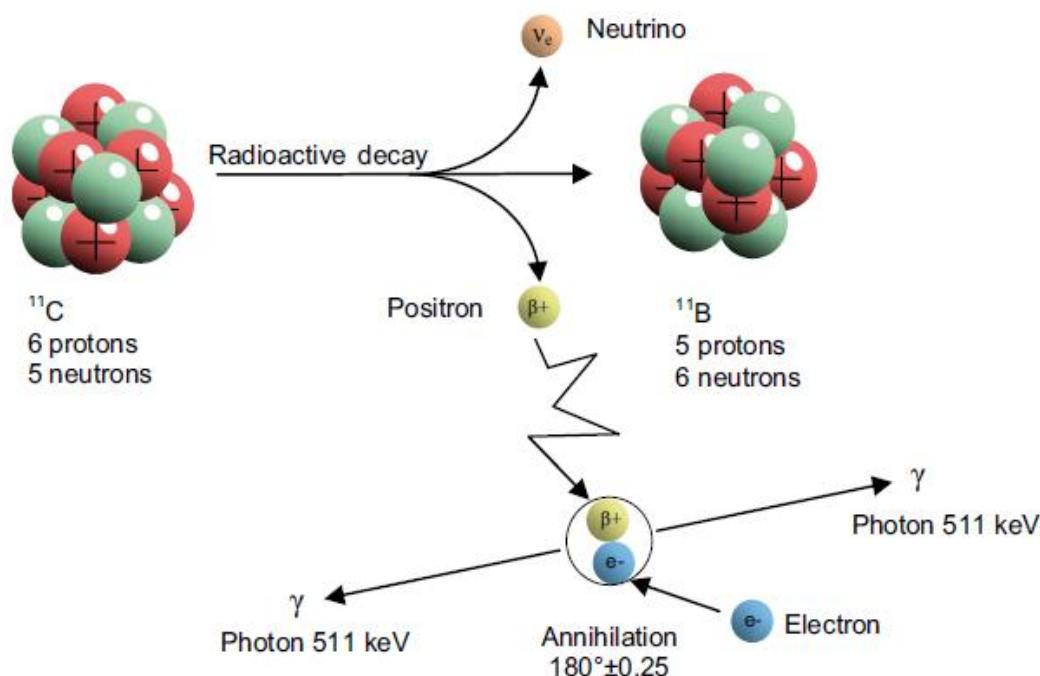


Figure 19: Radioactive decay of the unstable, neutron poor ^{11}C to the more stable ^{11}B via the release of a positron, followed by the collision of the positron with an electron producing two γ photons

PET requires minimal concentrations of the radiolabelled probe for efficient imaging, the common radionuclides used in PET imaging are shown in the Table 5.¹⁴⁹

Table 5: Common radionuclides used in PET imaging (adapted from¹⁴⁹⁻¹⁵¹)

Radionuclide	Half-life	% Positron emission	Mean range in water (mm)
^{11}C	20.4 min	99.7	1.1
^{15}O	2.03 min	99.9	1.5
^{18}F	109.8 min	97	0.6
^{68}Ga	68 min	88	2.9
^{82}Rb	75 sec	96	1.7
^{89}Zr	3.3 days	22.8	1.2

The radioactive probes commonly used in PET imaging can be either specific to a particular metabolic process or bind to a target of interest, a radiotracer or a radioligand respectively (Table 6). These probes provide a detailed image of the biological process of targeted tissue structure.⁸⁸

Table 6: Examples of radioligands and radiotracers used in clinical practice (adapted from¹⁵²)

Probe	Biological Target	Type of cancer
[¹⁸ F] or [¹¹ C]-Choline	Lipid metabolism	prostate
[¹¹ C]-Methionine	Amino acid metabolism	brain tumours
[¹⁸ F]-Fluoromisoindazole	Hypoxia	lung, head and neck
[¹⁸ F]-FDG	Metabolism	variety
[⁶⁸ Ga]-PSMA	PSMA	prostrate
[¹⁸ F]-FLT	Proliferation	rapidly growing sarcomas

1.3.3. Development of a VEGFR₂ specific PET probe

The development of a PET probe is typically in response to an unmet clinical need with the potential to increase the standard of care for patients. The following are typically considered:

- specific targets for common diseases¹⁵³
- specific targets for uncommon diseases¹⁵³
- a probe which could target processes in multiple diseases (e.g. [¹⁸F]-FDG)¹⁵³
- use of the probe which can offer advantages over other imaging techniques¹⁵³

There are several criteria a new potential PET probe must satisfy and the next section will discuss these features in the context of the development of a PET probe for VEGFR₂.

1.3.3.1. High affinity for VEGFR₂

Molecular targets are often expressed in varying levels, therefore the affinity of the PET candidate must satisfy the density of the target. For example, as VEGFR₂ is expressed at low levels, its detection requires a probe with a high affinity. Expression levels of VEGFR₂ in HUVECs is 5800 ± 300 receptors/cell.¹⁵⁴ This receptor density for VEGFR₂ in HUVECs is relatively low in comparison to EGFR which has a receptor density of 3.3×10^6 receptors/cell.¹⁵⁵ Ideally the optimal target to non-target ratio is the maximum target density (B_{\max}) divided by the affinity of the probe. B_{\max}/K_d can be used to calculate maximum theoretical contrast for potential labelled antagonists and inhibitors before commencing further *in vivo* studies.^{120, 153} The dissociation constant (k_d) of the ligand-target complex is typically in the nM range, for when the B_{\max} of a target is low.¹⁵⁶ For example, β -amyloid has a B_{\max} of 1000-2000 nM which therefore requires a K_d of 2 nM to obtain sufficient binding potential.¹⁵⁷ There are some cases in which the affinity for the target is too high,

which causes the limiting factor to be the delivery time of the tracer, although in some cases this is an ideal feature.¹⁵⁸ Therefore a lower affinity probe would be acceptable, which eases the dissociation of the ligand from the target through displacement with the endogenous or exogenous ligand. This achieves a pseudo-equilibrium in a shorter timeframe.¹⁵⁹ VEGFR₂ is expressed at a lower level than VEGFR₁ (1800 ± 300 receptors/cell in HUVECs and VEGFR₃ is approximately 2900 receptors/cell in HUVECs).^{154, 160} Therefore PET probe must exhibit a greater affinity for VEGFR₂. As previously mentioned VEGFR₁ acts as a decoy receptor, thus self-regulating angiogenesis.

1.3.3.2. High contrast ratio

Conclusions drawn from low quality images can be confusing and misleading. High resolution images, with high signal-to-noise ratio, are required for adequate interpretations. Preferably a tracer will have high uptake with slow wash-out from the target tissue and low uptake with fast clearance from normal organs.¹²⁰ Therefore the PET candidate must accumulate within the target or ROI and clear low affinity binding within the half-life of the tracer.

1.3.3.3. High selectivity for VEGFR₂ over other kinases

The potential candidate must be selective for the target to avoid confounding the PET image, thus avoiding misinterpretation. This includes preferential binding for one target if there is more than one sub-type. Typically, it is acceptable for the potential probe to exhibit 100 times stronger binding between the target and non-targets.¹⁵⁶ As previously discussed, there are three potential targets in the VEGFR family. Although VEGFR₃ is not structurally similar, there are structural similarities between VEGFR₁ and VEGFR₂ (43.2% overall sequence homology for VEGFR₁ and VEGFR₂).¹⁶¹ As TKIs mainly target the ATP binding pocket, this introduces the lack of selectivity observed in the clinic which is a great challenge in meeting this criteria when developing a novel PET candidate. Competition with ATP could be an important factor to consider, especially if the candidate could be a type I inhibitor, as previously discussed.

1.3.3.4. Lipophilicity

Lipophilicity is fundamental when predicting the physicochemical properties of a compound. It also plays a pivotal role in absorption, distribution, metabolism and elimination of the PET

candidate. Very polar compounds (low cLogP) are highly soluble in water, exhibit fast clearance in by the kidneys and often contain easily ionisable functional groups. High lipophilicity is associated with increased nonspecific binding, therefore for successful PET imaging an ideal logP should be around 1-4, which is the typical range for previous successful small-molecule radiotracers.¹⁴⁹ Typically scaffolds which target VEGFR₂ are bicyclic structures which increases logP, there are several strategies to circumvent this. These strategies include isosteric replacement or hydrogen bonding which has the capability of mimicking a bicyclic structure.

1.3.3.5. High metabolic stability

Image quality and associated quantitative analysis relies heavily on the stability of the tracer. Any radiometabolites entering the ATP binding site of VEGFR₂ can complicate the quantification of changes in binding density. Consequently, the potential candidate should not generate problematic metabolites.^{120,162} Therefore, in cases where uptake and washout of the parent drug is faster than production and accumulation of radio-metabolites in the plasma, radio-metabolites may not reach sufficient concentration to confound PET images.¹⁶³

1.3.3.6. Adequate half-life

The half-life of a potential candidate (T_{eff}) is defined as the time required to reduce the radioactivity in an organ or the whole body to half its original value due to both elimination and decay. Therefore, it is the function of both its physical half-life (T_p) and its biological half-life (T_b), this described by Figure 20.¹⁶⁴

$$\frac{1}{T_{\text{eff}}} = \frac{1}{T_p} + \frac{1}{T_b}$$

Figure 20: Calculating the effective half-life of the potential candidate

It can, therefore, be surmised that if $T_p > T_b$ then $T_{\text{eff}} \approx T_b$ and if $T_b > T_p$ then $T_{\text{eff}} \approx T_p$. It can be inferred here that the effective half-life of the radiotracer is dependent on the half-life which is lesser in value. The effective half-life ideally should match the time window required to image the biological process. For example the effective half-life should allow accumulation

in the ATP binding site of VEGFR₂, allowing equilibrium to be reached. However, the effective half-life should be short to avoid extended exposure to radiation.¹⁶⁴

1.3.3.7. Toxicity

Despite the PET probes being administered below the therapeutic level, close monitoring is required for any potential biological effect. A potential imaging probe should have a minimal level of immunogenicity and toxicity before it would be available for clinical use.¹²⁰

1.3.3.8. Ease of radiolabelling

Due to the relative short half-life of fluorine-18 (109.7 minutes), incorporation of the radionuclide must be achieved within two synthetic steps prior to scanning. For routine clinical use of a successful candidate, the radiolabelling must be adapted for automated synthesis.^{120, 165} The radiosynthesis must be achieved in sufficient yields (5-40% non-decay corrected), with high radiochemical purity (<95%) and with high specific activity.¹⁶⁶

1.3.4. *PET imaging in cancer*

PET in oncology has several important roles including: diagnosis, staging, stratification of patients with receptor expression status and monitoring treatment efficacy. This next section will focus on current strategies targeting the VEGF-VEGFR₂ signalling system in the development of either a predictive or pharmacodynamic biomarker.

1.3.4.1. Imaging the VEGF-VEGFR₂ signalling system

The two main approaches for imaging the VEGF-VEGFR₂ signalling system can be split into the two main categories highlighted in the therapeutic intervention section; either targeting VEGF_A or targeting the ATP binding pocket of VEGFR₂. This next section will discuss both these strategies for predictive biomarker discovery.

1.3.4.2. Imaging VEGF_A

Any bio-molecule radiolabelling strategy must not alter the binding or pharmacokinetic profile of the parent compound. The choice of radionuclide is an important factor, as the half-life of the isotope must be compatible with the biological half-life of the parent compound. Typically mABs are larger in size, up to 150 kDa and PET isotopes commonly

used in mAB-PET imaging are ^{124}I , ^{89}Zr and for fragments of mAB, ^{68}Ga , ^{64}Cu , ^{86}Y . ^{68}Ga is of particular interest due to the isotope as it can be produced from a gallium generator, or a cyclotron.¹⁶⁷

Bevacizumab

Bevacizumab can be radiolabelled with zirconium-89 and can be used to visualise tumour levels of VEGF_A, and quantify the efficacy of treatments.¹⁶⁸ A recent study by van der Bilt *et al.* demonstrated a correlation between [^{89}Zr]-Bevacizumab uptake, in three different ovarian cancer xenografts, and treatment with everolimus. A correlation was found between [^{89}Zr]-Bevacizumab uptake and levels of VEGF_A, with decreased uptake observed in treated tumours.¹⁶⁸

Targeting heat shock protein 90 (HSP90) with NVP-AUY922 has been shown to down-regulate VEGF_A expression, through HIF and NF κ B dependent pathways.^{169, 170} Nagengast *et al.* highlighted higher uptake of [^{89}Zr]-Bevacizumab was observed in pre-treated A2780 xenografts compared to CP70 xenografts. Following two weeks treatment with NVP-AUY922, a 44% decrease in [^{89}Zr]-Bevacizumab uptake was observed in the A2780 xenografts, whilst no change in uptake was observed in the CP70 xenografts.¹⁷⁰ *Ex vivo* studies were performed to determine if the decrease in [^{89}Zr]-Bevacizumab uptake was driven by a treatment induced change in VEGF_A levels. ELISA studies determined a decrease, in VEGF_A levels, of 69% and 20% for the A2780 and CP70 xenografts respectively. Haematoxylin and eosin staining showed after two weeks of treatment increased tumour necrosis was not present. Thus indicating the decreased uptake of the tracer was not due to tumour necrosis, but decreasing levels of VEGF_A, highlighting its potential use as a pharmacodynamic biomarker.¹⁷⁰

The first clinical study of [^{89}Zr]-Bevacizumab, in breast cancer patients, showed an excellent correlation with VEGF_A expression and uptake. [^{89}Zr]-Bevacizumab also positively identified 25 out of 26 patients, with a higher uptake in tumours than surrounding normal tissue and no adverse events reported.¹⁷¹ This is important as it has potential to be a predictive biomarker. Although no findings were reported on treatment outcome [^{89}Zr]-Bevacizumab was able to distinguish between different levels of VEGF_A expression.¹⁷¹ A further study by Gaykema *et al.* evaluated the clinical utility of [^{89}Zr]-Bevacizumab in evaluating changes in VEGF_A expression after treatment with the HSP90 inhibitor NVP-AUY922.¹⁷² Unfortunately, no correlation was seen between [^{89}Zr]-Bevacizumab uptake, 5.7% average increase post NVP-AUY922 therapy, and anatomical changes observed by

CT. This 5.7% increase in [^{89}Zr]-Bevacizumab uptake could be due to the presence of bone metastases, which could not be identified by CT due to the small size of the tumour.¹⁷² Oosting *et al.* performed a pilot clinical study evaluating [^{89}Zr]-Bevacizumab use in metastatic RCC. The 22 patients were enrolled and split into two groups receiving either Bevacizumab/interferon- α or Sunitinib therapy.¹⁷³ VEGF_A plasma levels were determined at baseline, 11 and 19 days into the study, with a view to correlate with [^{89}Zr]-Bevacizumab uptake. Unfortunately no correlation between plasma VEGF_A levels and [^{89}Zr]-Bevacizumab uptake was found. Interestingly, this study found significant differences in [^{89}Zr]-Bevacizumab uptake between the two therapies. From baseline to the first scan at week two, [^{89}Zr]-Bevacizumab uptake was decreased by 47%, with Bevacizumab/interferon α therapy. The Sunitinib treated arm had an average decrease 14% of [^{89}Zr]-Bevacizumab uptake, however this dramatically increased by 73% after a therapy holiday of two weeks.¹⁷³ This increase in [^{89}Zr]-Bevacizumab uptake for the Sunitinib arm can be explained by a release of VEGF_A by normal cells. An elevated uptake of [^{89}Zr]-Bevacizumab at baselines was found to correlate with a longer time to progression (TTP). Uptake of [^{89}Zr]-Bevacizumab was found to be heterogeneous intra and inter patient. Although further studies are required to confirm whether [^{89}Zr]-Bevacizumab can be used as a predictive biomarker due to time constraints taken for mABs to localise in the tumour.

VG76e

VG76e is an IgG₁ monoclonal antibody radiolabelled with ^{124}I which directly targets human VEGF.¹⁷⁴ VG76e has been used in PET imaging of solid tumour xenografts in immune deficient mice.¹⁷⁴ Collingridge *et al.* developed [^{124}I]-SHHP-VG76e to quantify biodistribution in HT1080 subclones (26.6 or 1/3C respectively). Immunoreactivity of this radioligand was poor. Three different attempts at radiolabelling VG76e all resulted in a maximum bound activity of 34% in comparison with the unlabelled VG76e. Although it was confirmed that [^{124}I]-SHHP-VG76e did bind to VEGF_A, a large amount of non-specific binding was observed when challenged with unlabelled VG76e. This radioligand exhibited time-dependant accumulation in the tissues, peaking at 24 and 48 hours respectively in the tumour region.¹⁷⁵ No further studies have been published using this mAB.

^{64}Cu -DOTA-VEGF₁₂₁

PET imaging of VEGFR expression, *in vivo*, was first conducted using a ^{64}Cu radiolabelled probe, ^{64}Cu -4,7,10-tetraazacyclododecane-*N,N',N'',N'''*-tetraacetic acid (^{64}Cu -DOTA-

VEGF₁₂₁).¹⁷⁶ Radiolabelling of the complex was achieved through the chelation of the ⁶⁴Cu to the DOTA-VEGF₁₂₁ conjugate. Evaluation of the ⁶⁴Cu-DOTA-VEGF₁₂₁, *in vivo*, with U87MG human glioblastoma xenografts showed rapid and specific accumulation of the radioligand in the smaller tumours 4 hours post-injection.¹⁷⁶ In comparison, larger tumours exhibited a slower radioligand uptake, with the differences accounting for the expression of VEGFR₂, mainly due to the differences in tumour localisation.¹⁷⁶

1.3.4.3. Imaging angiogenesis with RGD targeting PET probes

$\alpha_v\beta_3$ is a dimer belonging to the integrin family of cell adhesion molecules, consisting of noncovalent transmembrane bound molecular subunits, that play a vital role in angiogenesis.¹⁷⁷ $\alpha_v\beta_3$ acts as a receptor for proteins which express the Arg-Gly-Asp (RGD) tripeptide sequence, such as collagen, von Willebrand Factor, fibrinogen and osteoponin.¹⁷⁸ Normally $\alpha_v\beta_3$ is expressed at relatively low levels on the surface of normal endothelium; however, $\alpha_v\beta_3$ is overexpressed on the activated vascular endothelium of a range of tumours, thus making it a candidate target for a PET imaging agent for the imaging of angiogenesis.¹⁷⁹ Several RGD based probes have been described, each with different structures and all exhibit similar *in vivo* pharmacokinetic properties.¹⁸⁰⁻¹⁸⁴ The next section will briefly discuss each of the RGD radioligands as a predictive or pharmacodynamic biomarker, and are shown in Figure 21.

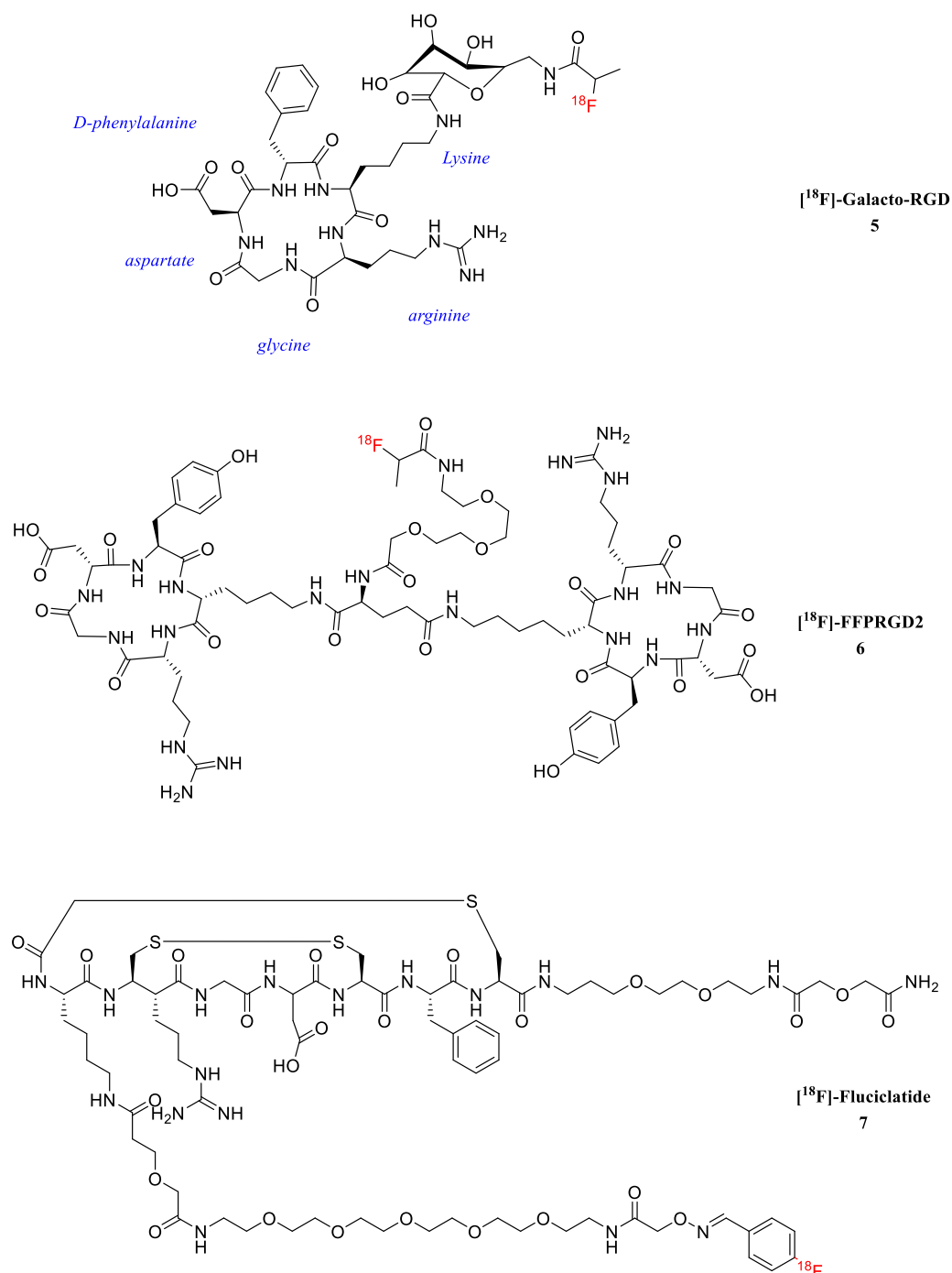


Figure 21: Structure of three RGD PET candidates (7-9) and their positioning of fluorine-18 highlighted in red.^{185, 186}

$[^{18}\text{F}]\text{-Galacto-RGD}$

Galacto-RGD **5** (Figure 21) is based on the cyclic peptide c(RGDfK) and allows for radiolabelling with fluorine-18, via the prosthetic group 2- $[^{18}\text{F}]\text{-fluoropropionate}$. Thus far clinical studies of $[^{18}\text{F}]\text{-5}$ have been conducted with the following tumour types: glioblastoma multiforme (GBM), NSCLC, breast cancer, melanoma, RCC, CRC, sarcoma and squamous cell carcinoma of the head and neck.¹⁷⁹

With an affinity of approximately 5 nM, **5** exhibits high affinity for $\alpha_v\beta_3$. Biodistribution studies demonstrated its primary excretion route is via the kidneys, with fast clearance from the blood and muscle tissue.¹⁸⁷ Enhanced tracer uptake of [^{18}F]-**5** in tumours expressing $\alpha_v\beta_3$ has been observed, but is also found to accumulate in the colon, liver as well as the kidneys.¹⁸⁷ In A431 xenograft models, [^{18}F]-**5** was found to localise on the endothelium expressing $\alpha_v\beta_3$.¹⁸⁸ Although A431 do not express $\alpha_v\beta_3$ themselves, they do significantly induce angiogenesis.¹⁸⁹

The first clinical use of [^{18}F]-**5** was in 2005, with variable tumour uptake in nine patients with melanoma, sarcoma, villonodular synovitis and renal cell carcinoma, although the tracer was well tolerated with no notable side-effects. In this study, [^{18}F]-**5** uptake correlated significantly with $\alpha_v\beta_3$ expression.¹⁸⁵ This was further confirmed by a later study which showed the same correlation between [^{18}F]-**5** uptake and $\alpha_v\beta_3$ expression.¹⁸¹ Another clinical study compared the uptake of [^{18}F]-**5** with [^{18}F]-FDG (discussed in detail further in this Chapter (1.3.4.5)) in 18 patients with metastatic disease.¹⁹⁰ Out of 59 lesions, uptake of [^{18}F]-**5** was observed in 76%; missed lesions were located in the liver, bone, lung, lymph node, soft tissue and the adrenal gland.¹⁹⁰ Also the SUV for [^{18}F]-**5** was significantly lower than [^{18}F]-FDG, with the exception of one patient with bronchus carcinoid. Importantly there was no correlation with either primary tumour or secondary tumours and uptake of either [^{18}F]-**5** or [^{18}F]-FDG. This is suggestive of no correlation between $\alpha_v\beta_3$ expression and metabolism. [^{18}F]-FDG exhibited superior uptake in tumour cells in comparison to [^{18}F]-**5**, which can be explained to their mechanism of action. The mechanism of [^{18}F]-FDG will be discussed in more detail later in this Chapter (1.3.4.5), but briefly [^{18}F]-FDG accumulates inside the tumour cell. Whereas, [^{18}F]-**5** localises on the surface of endothelial cells which are not as abundant as the number of tumour cells, which potentially accounts for the differences in uptake.¹⁹⁰ Also [^{18}F]-FDG is also a radioligand, therefore the equilibrium level will be higher than the radiotracer [^{18}F]-**5**. This study concluded that [^{18}F]-FDG is superior in the detection of lesions (i.e. staging of the cancer) and [^{18}F]-**5** could provide superior information on treatment planning and response, a pharmacodynamics biomarker, though further extensive evaluation is required. The clinical use of [^{18}F]-**5** is limited owing to its difficult radiolabelling and challenging automated synthesis.¹⁹¹ Despite this, [^{18}F]-**5** has a reasonable detection rate of 59-94%, however this was not superior to [^{18}F]-FDG.^{192, 193} Therefore it can be concluded that [^{18}F]-**5** can be used as a companion to [^{18}F]-FDG for the management of oncological disease.

[¹⁸F]-FPPRGD₂

$\alpha_v\beta_3$ expression has also been quantified using a dimeric RGD peptide, [¹⁸F]-FPPRGD₂ ([¹⁸F]-**6**, Figure 21).¹⁹⁴ Dimer [¹⁸F]-**6** has a higher binding affinity than the monomeric equivalents, potentially this could be due to the multi-valency effects of binding to $\alpha_v\beta_3$. In H460-bearing mice with HCT116 xenografts treated with Bevacizumab, preliminary work demonstrated significant uptake of [¹⁸F]-**6** occurred prior to notable significant changes in the tumour size occurred.¹⁹⁵ Preclinical studies demonstrate good signal-to-background ratios and reproducibility between subject, with limited toxicities observed.¹⁹⁴

An initial pilot study evaluating the use of [¹⁸F]-**6** in eight breast cancer patients, revealed favourable localisation in both primary and secondary tumours. Three lesions were identified in one patient which were not identified by a [¹⁸F]-FDG scan. In this first pilot study, no adverse events were reported involving the use of [¹⁸F]-**6**.¹⁹⁶ Minamimoto *et al.* conducted a clinical study comparing [¹⁸F]-**6** with [¹⁸F]-FDG in six patients with either cervical or ovarian cancers, with a total of 52 lesions.¹⁹⁷ In this study both pre- and one week post-treatment scans were conducted for [¹⁸F]-**6** and the standard of care six weeks post-treatment [¹⁸F]-FDG scan, treatment of Bevacizumab. As noted with [¹⁸F]-**5**, there was also no correlation between [¹⁸F]-**6** uptake and [¹⁸F]-FDG uptake.¹⁹⁷ This strengthens the theory that metabolism and angiogenesis are not linked. No changes in the uptake of [¹⁸F]-**6** were seen in normal organs after anti-angiogenic treatment, however changes were observed in as little as one week post-treatment in tumour uptake. Interestingly, a decrease in [¹⁸F]-**6** uptake was seen in those patients who exhibited responses. Whereas, in one patient who had progressive disease an increase in [¹⁸F]-**6** uptake was observed. Importantly, this demonstrates [¹⁸F]-**6** use as a potential pharmacodynamic biomarker for monitoring anti-angiogenic therapy.¹⁹⁷

[¹⁸F]-Fluciclatide

[¹⁸F]-Fluciclatide ([¹⁸F]-**7**, Figure 21) is a small radiolabelled peptide developed by GE Healthcare which contains the RGD terminal sequence and is capable of binding to $\alpha_v\beta_3$ and to $\alpha_v\beta_5$ (11 nM and 0.1 nM respectively).^{178, 191} In comparison to [¹⁸F]-**5**, [¹⁸F]-**7** radiosynthesis is simpler through the reaction of the aminoxy precursor with [¹⁸F]-4-fluorobenzaldehyde.^{180, 186} Total synthesis time is shorter in comparison to [¹⁸F]-**5** (170 v 200 minutes respectively) with less reaction steps, although a hit in specific activity is observed.^{180, 185, 186} Pharmacological properties of [¹⁸F]-**7** are enhanced through the introduction of PEG groups, disulfide bridges and cyclisation.¹⁹¹

RGD containing peptide, [^{18}F]-7 exhibits high affinity for $\alpha_v\beta_3$ and has been employed to monitor the treatment efficacy of anti-angiogenic treatment using PET.¹⁷⁸ Preclinical studies monitoring the efficacy of Sunitinib against glioblastoma xenografts showed significant decreases in radiotracer uptake in the treated group versus the untreated.¹⁷⁸ Despite showing a decrease in tracer uptake at day two, no significant change was observed after day two of treatment. Potentially, this could indicate the inadequacies of either the radiotracer or treatment regime. In another study, conducted by Morrison *et al.* [^{18}F]-7 was used to monitor the efficacy of ZD4190 against Calu-6 xenografts (lung adenocarcinomas), and a marked decrease in tracer uptake in the tumours of the treated population was observed, although treatment outcomes were not reported.^{178, 198} Both of these pre-clinical studies confirm the ability of [^{18}F]-7 to differentiate between differences in levels of $\alpha_v\beta_3$ expression and monitoring $\alpha_v\beta_3$ levels *in vivo*. However, this also may indicate the inability to differentiate between tumour cells and inflammatory cells.¹⁹⁸

In the first clinical study of [^{18}F]-7, Kenny *et al.* explored the distribution, stability and the ability of the radiotracer to localise in the tumour site, along with evaluation as a biomarker tool.¹⁹³ Seven patients were injected with [^{18}F]-7 with no adverse events reported. [^{18}F]-7 was able to locate all 18 tumours, as observed by CT, and was also able to find a lesion which was not detected by CT. Distribution of [^{18}F]-7 was found to be localise to the tumours or the tumour periphery. This study also concluded the radioligand exhibited fast clearance from the blood and normal lung tissue. Both primary and secondary tumours exhibited preferential uptake with respect to the surrounding tissue. Although some heterogeneous localisation of radioligand was observed, but this could be due to the heterogeneous nature of angiogenesis which required further investigation.¹⁹³

A clinical study of 18 patients with either chromophobe, non-chromophobe and oncocyte renal cancer or melanoma, demonstrated no correlation between tumour size and [^{18}F]-7 uptake. Interestingly, [^{18}F]-7 was able to differentiate between the different types of renal malignancies, with greater uptake seen in chromophobe malignancy than the non-chromophobe malignancy. The time activity curves are shown in Figure 22, where a rapid localisation of [^{18}F]-7 in the tumours is observed, followed by a plateau and quick clearance from the blood and normal tissue. Due to the plots becoming linear, this could be suggestive of irreversible binding kinetics.¹⁹²

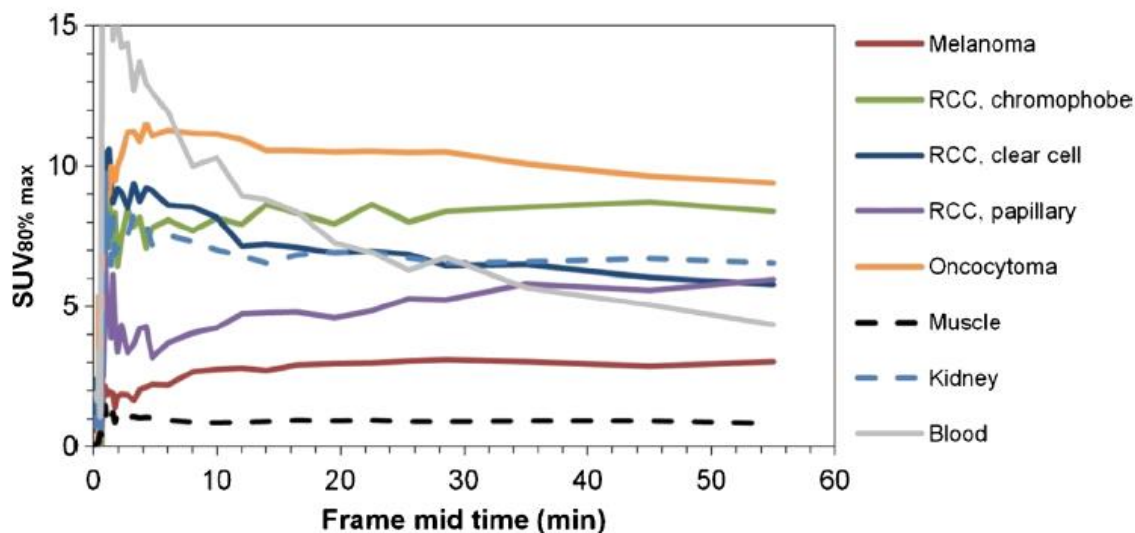


Figure 22: Time activity curves of $[^{18}\text{F}]\text{-7}$ in the different malignancies investigated when compared to normal kidney, muscle and blood¹⁹²

Limitations of this study were: only one tumour was evaluated in those patients with metastatic disease; differences in tumour uptakes between malignancies could be due to the small size of the study.¹⁹² Despite these limitations, $[^{18}\text{F}]\text{-7}$ was able to distinguish between the highly vascularised tumours and those which are not (chromophobe and non-chromophobe respectively). Determining the vascular nature of renal malignancies is of vital importance and could be predictive of treatment response, influencing therapeutic options. This is an example of $[^{18}\text{F}]\text{-7}$ being evaluated as a stratification marker, through evaluating the expression status of either $\alpha_v\beta_3$ or $\alpha_v\beta_5$.¹⁹²

In a recent publication, Sharma *et al.* investigated the reproducibility of $[^{18}\text{F}]\text{-7}$ in the following cancers; NSCLC, breast, ovarian, CRC, melanoma, pancreatic, head and neck, cervical, GBM, mesothelioma, sarcoma and neuroendocrine.¹⁹⁹ Eligibility criteria for the study stipulated the patients were not to receive current treatment, avoiding any bias from previous treatment through interfering with levels of $\alpha_v\beta_3$. PET scans with $[^{18}\text{F}]\text{-7}$ were obtained ten days apart and assessed for the reproducibility. Importantly the SUV_{peak} was not significantly different for each $[^{18}\text{F}]\text{-7}$ acquisition in the two sessions, on a lesion by lesion basis (0-2% difference). Moreover, the reproducibility seen in this study is consistent with the reproducibility data of $[^{18}\text{F}]\text{-FDG}$ obtained in large, multi-centre studies, which is important for the development of an *in vivo* biomarker.²⁰⁰

1.3.4.4. Imaging expression of the VEGF receptor using TKI-PET

Imaging with small radiolabelled inhibitors has the potential to offer a more sensitive and direct approach to assessing the expression status of a specific receptor and monitoring treatment efficacy without requiring multiple invasive biopsies, which are complementary to the imaging approaches described previously. This enhances the potential for more personalised therapies, optimising doses and increasing the awareness of early responders.²⁰¹ Intracellular protein kinase PET imaging is focused on the radiolabelling of known TKI, and related compounds currently involved in clinical trials, with either carbon-11 or fluorine-18. In the last ten years, seven clinically relevant kinase inhibitors have been assessed for their potential use in PET, most of these have failed due to a lack of inherent selectivity of the parent inhibitor. The following section will review the literature pertaining to the development a VEGFR₂ specific TKI-based PET probe.

PAQ

An analogue of **4**, PAQ **8** (Figure 23) has an IC₅₀ for VEGFR₂ of 10 nM and 1 nM for the *S* and *R* enantiomer respectively.²⁰² This analogue also achieved better selectivity for VEGFR₂ over VEGFR₁ (both *S*- and *R*- 500 nM) and EGFR (*S*- 100 nM and *R*- 200 nM),²⁰³ crucial in the development of a PET probe.

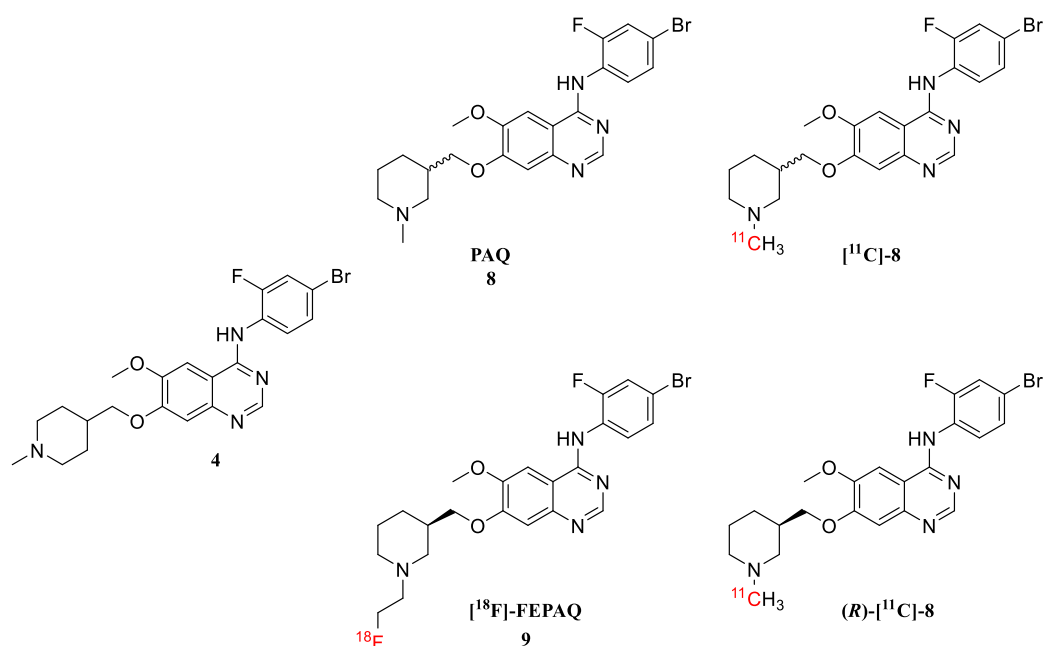


Figure 23: Analogues of **4** which have shown some promise in the development of a VEGFR₂ specific PET probe

Synthesised from the desmethylated via the wet carbon-11 method, [^{11}C]-**8** exhibited high metabolic stability, with less than 1% metabolised over a 30 minute period by liver microsomes.²⁰² Biodistribution in healthy mice revealed [^{11}C]-**8** was rapidly distributed into the tissue from the blood. Despite the rapid distribution, clearance from the blood was slow, the activity remaining stable between 10-40 minutes. Initial distribution occurred in the lungs, then the kidneys and liver where levels of radioactivity plateaued over 30 minutes. Attempts to block [^{11}C]-**8** uptake in these VEGFR₂ rich organs with the unlabelled **8**, resulted in a decrease in radioligand uptake in the specific organs, cold **8** was injected 15 minutes post injection with [^{11}C]-**8**. This is suggestive of saturation of the ATP binding sites, which could not be displaced with [^{11}C]-**8**, revealing a potential irreversible binding or very slow dissociation.²⁰² Radiolabelled quinazoline, [^{11}C]-**8** demonstrated an ability to detect VEGFR₂ expression around the tumour periphery, although uptake was heterogeneous. Both TUBO and B16F10 demonstrated variable uptake of [^{11}C]-**8**, which could be suggestive of the heterogeneous nature of angiogenesis, location of xenograft or a lack of selectivity.²⁰² Due to the varied nature of [^{11}C]-**8** uptake, further development of this radioligand in more extensive xenograft studies is required before it can enter the clinic, as either a predictive or pharmacodynamic biomarker. However, it demonstrates potential as a companion to [^{18}F]-FDG.

Samén *et al.* presented a follow-up study evaluating the use of (*R*)-[^{11}C]-**8** uptake, as a predictive biomarker to stratify levels of VEGFR₂ expression in a MMTV-PyMT cell line.²⁰⁴ This study used MMTV-PyMT (polyoma middle T antigen), an oncoprotein which is controlled by mouse mammary tumour virus, as it is known that invasive mammary tumours with pulmonary metastases develop around 12-15 weeks in this model. The MMTV-PyMT model has been shown to be dependent on endothelial progenitor cell infiltration and forms highly vascularised tumours, ideal for studying VEGFR₂ expression.²⁰⁴ As previously mentioned, (*R*)-[^{11}C]-**8** has an affinity for VEGFR₂ of approximately 1 nM, whilst demonstrating a 200 fold selectivity over EGFR. Biodistribution studies for (*R*)-[^{11}C]-**8** were conducted and compared to the racemic [^{11}C]-**8** for both mice and rats. Uptake in the VEGFR₂ rich organs (liver, lung and kidney) remains high, this could demonstrate specificity due to the relatively high levels of VEGFR₂ expression in these organs. In comparison to the racemic [^{11}C]-**8**, there was a lower uptake of (*R*)-[^{11}C]-**8** in the kidney in mice, whilst similar levels of uptake in the liver and enhanced uptake in the lungs are evident.²⁰⁴ In mice, the uptake of both the racemic [^{11}C]-**8** and (*R*)-[^{11}C]-**8** decreased from ten minutes to one hour. Potentially this distribution profile of (*R*)-[^{11}C]-**8** in mice is advantageous, minimising any background signals. This higher uptake of (*R*)-[^{11}C]-**8** in the

liver, lungs and kidneys of mice is not surprising as it is well-known that VEGFR₂ is abundantly expressed in the vasculature of adult mice.²⁰⁴ Interestingly, uptake of (**R**)-[¹¹C]-**8** in tumours was proven to be associated with VEGFR₂ and a higher microvascular density, as confirmed by IHC and immunofluorescence.²⁰⁴ [¹⁸F]-FDG were performed in conjunction with (**R**)-[¹¹C]-**8** to discern if any additional information could be obtained over [¹⁸F]-FDG. Interestingly, (**R**)-[¹¹C]-**8** was able to identify a site of lung metastases which was missed by [¹⁸F]-FDG, further *ex vivo* immunofluorescence confirmed the uptake of (**R**)-[¹¹C]-**8** with a high area of angiogenic activity and, therefore, could be used in conjunction with the $\alpha_v\beta_3$ imaging probes described in this Chapter (1.3.4.3). This is the first demonstration that a VEGFR₂ specific radioligand has the potential be more specific for the detection of tumours which express VEGFR₂ than [¹⁸F]-FDG. However, further investigations with a range of xenografts are needed before (**R**)-[¹¹C]-**8** can be put forward for clinical trials as a predictive biomarker.

Similar to [¹¹C]-**8**, (**R**)-[¹⁸F]-**9** has the same core scaffold with the exception of the *N*-methyl switched for a fluoroethyl group (Figure 23).²⁰⁵ After the synthesis of (**R**)-[¹⁸F]-**9**, studies were performed using glioblastoma tissue samples. Autoradiography was performed to determine if (**R**)-[¹⁸F]-**9** binds to VEGFR₂ and also blocked with either (**R**)-**8** or ZM323881, known selective inhibitors of VEGFR₂. Autoradiography did demonstrate specific binding of (**R**)-[¹⁸F]-**9** to VEGFR₂, although no follow-up work has been published.²⁰⁵

DOTA-ZDG2

Recently published by Li *et al.* was the development of a dimeric probe based around a Vandetanib analogue (DOTA-ZDG2), showing preferential uptake in U87-MG xenografts (Figure 24).²⁰⁶ Despite Vandetanib targeting EGFR and RET, DOTA-ZDG2 was shown to selectively target VEGFR₂ with higher affinity than the monomeric equivalent.

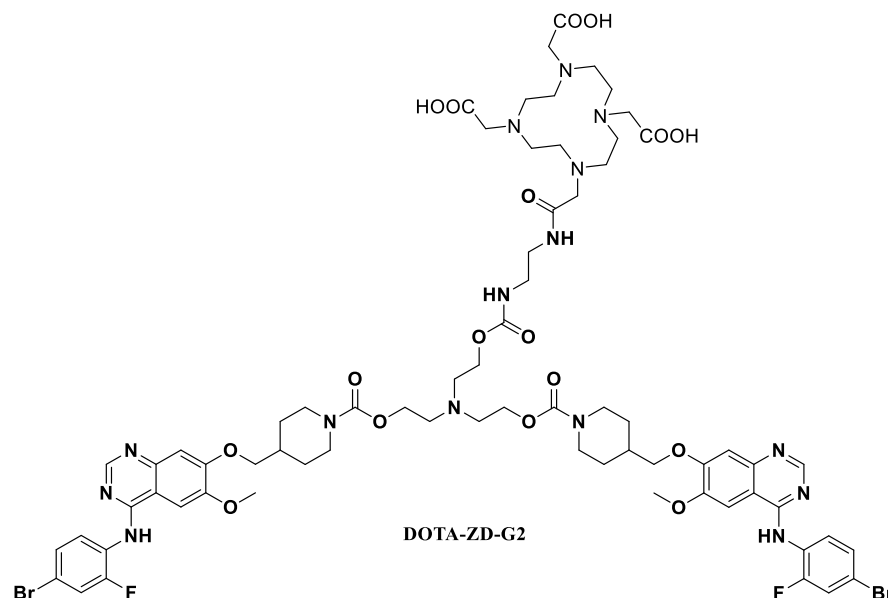


Figure 24: Structure of target DOTA-ZDG2 which showed enhanced binding to VEGFR₂

DOTA-ZDG2 was found to have a K_d value of 0.45 nM, when [⁶⁴Cu]-DOTA-ZDG2 was evaluated in a competition assay with **4** in U87 cells. In U87 xenograft studies, [⁶⁴Cu]-DOTA-ZDG2 localised within the tumour tissue (Figure 25).

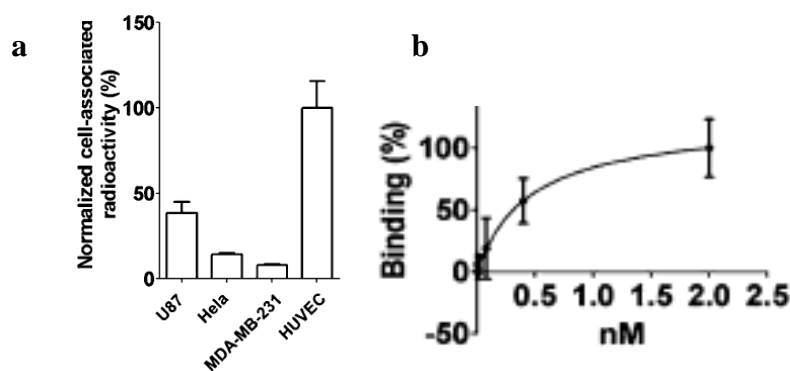
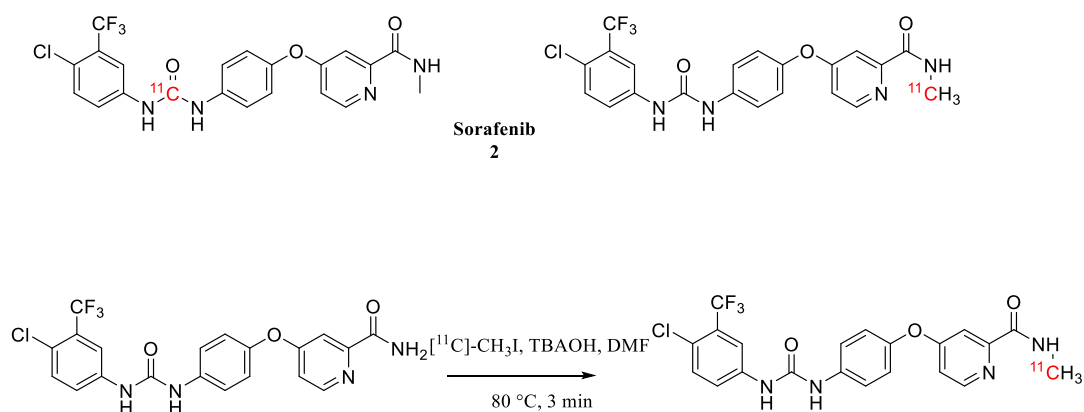


Figure 25: A) Uptake of [⁶⁴Cu]-DOTA-ZDG2 in cell lines which minimal expression of VEGFR₂ (MDA-MB-231) or overexpression of VEGFR₂ (HUVEC); b) Saturation curve for [⁶⁴Cu]-DOTA-ZDG2 in U87 cells²⁰⁶

Dota-labelled [⁶⁴Cu]-DOTA-ZDG2 was identified to have superior binding kinetics and specificity for VEGFR₂. This is an interesting development and requires follow-up studies from the Li group to further verify this as a specific VEGFR₂ PET radioligand for potential clinical applications.

Sorafenib 2

Sorafenib **2** has been radiolabelled with [^{11}C] at both the urea position and the amide position (Scheme 1). Poot *et al.* studied mouse xenograft models using MDA-MB-231 (breast), RXF393 (renal) and FaDu (head and neck) cell lines.²⁰⁷ These cell lines overexpress Raf-1 kinase, with RXF393 and FaDu expressing high concentrations of Raf-1 kinase, whilst MDA-MB-231 did not express Raf-1 kinase.²⁰⁷



Scheme 1: Positioning and *N*-Methyl carbon-11 radiolabelling of **2**

PET imaging of these xenograft models showed the RXF393 cell line revealed enhanced uptake in the tumours compared to the reference tissue, with a maximum tracer uptake in the ROI at approximately 7.5 minutes after radioligand injection. In comparison, MDA-MB-231 and FaDu cell lines showed much slower radioligand uptake, also tumour uptake was not significantly different to the uptake in the reference tissue.²⁰⁷ Biodistribution of [^{11}C]-**2** showed increased levels of uptake in the liver, when *ex vivo* studies were conducted, which slowly decreased over longer time periods. This shows the vulnerability of [^{11}C]-**2** towards different levels of expression of Raf-1 kinase. This PET imaging technique would require the standard IHC techniques in order to quantify levels of kinase expression prior and during treatment to assess the [^{11}C]-**2** of suitability towards predicting treatment outcome, however may show great clinical utility for determining response to Sorafenib.

3(4'-[^{18}F]fluorobenzylid-ene)indolin-2-one **11**

A Semaxinib **10a** derivative, [^{18}F]-**11** (3(4'-[^{18}F]fluorobenzylid-ene)indolin-2-one) was developed to image VEGFR₂ *in vivo*, when attempts to introduce fluorine-18 onto the scaffold of **10a** and **10b** were unsuccessful (Figure 26).²⁰⁸ Biodistribution of [^{18}F]-**11**

revealed a high and sustained uptake in adipose tissue and well-perfused organs. Although [^{18}F]-**11** exhibited high metabolic stability *in vitro*, *in vivo* stability was a major problem as after 20 minutes post injection only 12% of [^{18}F]-**11** remained; there was no detectable accumulation of [^{18}F]-**11** in the tumour.²⁰⁸

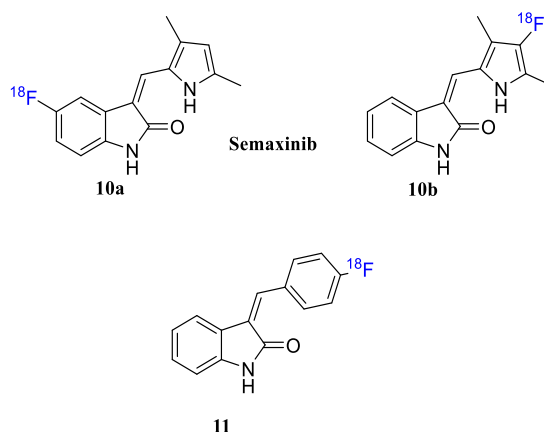


Figure 26: Positions of fluorine-18 tried on **10a** and **10b** and the final radiolabelled compound **11**²⁰⁸

1.3.4.5. Monitoring treatment response to VEGF-VEGFR₂ targeted therapies – using PET pharmacodynamic biomarkers

As discussed earlier in this Chapter (1.2.5.2), the RECIST criteria is used as the benchmark for monitoring response to therapy. PET based methods, i.e. PET Response Criteria in Solid Tumours (PERCIST) have also been developed in order to combat some of RECISTs deficiencies.¹¹² PERCIST operates on the premise that cancer response evaluated by PET is a time-dependant variable and metabolic response criteria could have a greater predictive value over anatomical response criteria. PET is capable of highlighting detecting early response or non-response to therapy. There are three PET probes routinely used in the clinical setting to either monitor anti-angiogenic treatment response and these radiotracers will be discussed.

Imaging metabolism with [¹⁸F]-FDG 12

The glucose analogue, [¹⁸F]-2-Fluoro-2-deoxyglucose (**12**, FDG -Figure 27) is currently widely used in a clinical setting for the detection of tumours.^{150, 209} The use of [¹⁸F]-**12** to detect glucose metabolism, due to the higher metabolic demands of the tumour cells for glycolysis under aerobic conditions, is known as the Warberg effect.²¹⁰ PET imaging using [¹⁸F]-**12** has proven clinical utility for detection and staging in a wide range of cancers; including CRC, lymphoma, breast cancers and head and neck cancers.¹⁵⁰

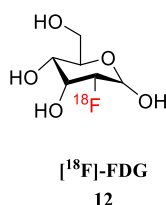


Figure 27: [¹⁸F]-**12**²¹¹

With a detection rate of approximately 90%, regardless of tumour origin, [¹⁸F]-**12** is highly sensitive in the detection of malignancy.^{212, 213} It is used to provide details on the progression of the disease, *i.e.* staging and has also found application in the detection of therapy response in lymphoma.²¹⁴ It has also been used to monitor therapeutic response to either VEGF_A or VEGFR₂ inhibitors.^{212, 213} Post TKI treatment, [¹⁸F]-**12** has been used to monitor treatment efficacy, through comparison of pre- and post-treatment scans. A decrease in radioactivity in the tumour due to the decreased metabolic demands, is expected.²¹¹ This approach has been adopted for use in the monitoring of treatment efficacy in patients with GIST, previously treated with Imatinib or Sunitinib.²¹¹ Novello *et al.* conducted a study in which 22 chemotherapy naïve patients, diagnosed with stage IIIB/IV NSCLC, were subjected to an initial [¹⁸F]-**12** PET scan, with another PET scan performed two weeks into the treatment cycle with Sorafenib or placebo. According to the European Organisation for Research and Treatment of Cancer (EORTC) criteria progressive disease is determined if SUV increases by approximately 25% within the tumour region.²¹⁵ An increase in SUV of less than 25% or a marked decrease in SUV of less than 15% indicates stable disease. Complete metabolic response is considered if tumour uptake is indistinguishable from the surrounding tissue.²¹⁵ Results of this study conclude that 13 patients showed a degree of metabolic response after two weeks of treatment, whilst nine patients showed stable or progressive metabolic disease. The nine patients who received Sorafenib, a marked change in SUV ($\Delta 37.2\%$) compared to

the 13 patients who received placebo ($\Delta 14.2\%$) was observed. This study demonstrates the metabolism within the tumour changes dramatically during treatment, of those tumours which responded to anti-angiogenic treatment which might also indicate survival benefit. It also demonstrates early identification of metabolic changes, from anti-angiogenic therapy, can identify responders from non-responders and, therefore, increase patient outcomes through switching the ineffective therapy regimes to more effective regimes.²¹⁵

Imaging proliferation with [¹⁸F]-FLT 13

Increased cellular proliferation is a hallmark of cancer, changes in response to therapy is a decline in proliferation.²⁹ Therefore, efforts were focused on the development of a PET candidate capable of imaging proliferation, as [¹⁸F]-12 is not a marker specific for cancer. Shields developed a fluorine-18 radiolabelled 3'-deoxy-3'-fluorothymidine **13** ([¹⁸F]-13 - Figure 28) which is a thymidine analogue used to measure proliferation *in vivo*.²¹⁶ Uptake of [¹⁸F]-13 by cancer cells is driven by the hENT1 transporter and subsequently phosphorylated by thymidine kinase 1 (TK1);²¹⁷ this modification leads to intracellular trapping and accumulation of FLT and consequent detection via PET.²¹⁷ Thymidine analogue [¹⁸F]-13 has been used to monitor the efficacy of growth factor receptor inhibitors and is capable, along with [¹⁸F]-12, of detecting early changes in cell biochemistry *in vivo*.²¹⁷

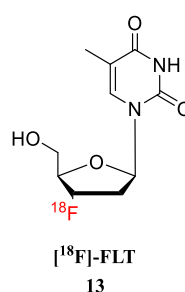


Figure 28: [¹⁸F]-13²¹⁶

There is limited evidence for the use of [¹⁸F]-13 in monitoring anti-angiogenic therapy however; Kenny *et al.* described a pioneering study showing the use of [¹⁸F]-13 in detecting proliferation changes in 5-Fluorouracil, epirubicin and cyclophosphamide treated breast cancers.²¹⁸ Interestingly, this early response seen after one week correlated with long-term

outcomes.²¹⁸ Despite the clinical utility of [¹⁸F]-**13** PET, imaging lesions in the liver, kidneys, bladder and bone marrow is difficult due to physiological retention.²¹⁹ Uptake of [¹⁸F]-**13** is observed in the following organs for the following reasons; liver due to it being heavily glucuronidated, kidneys and bladder due to the mode of excretion, and the bone marrow due to the highly proliferating nature of the tissue.²¹⁹ Whilst [¹⁸F]-**12** and [¹⁸F]-**13** PET exploit characteristics of most tumours, it is important to develop a PET candidate which images a single characteristic of a specific tumour, such as the development of a PET candidate capable of either predicting or monitoring therapeutic response targeting the VEGF-VEGFR₂ signalling system. In a pre-clinical study, xenograft studies using SW480 and SW620 (CRC cell lines) both known to express VEGFR₂ found no correlation between expression and [¹⁸F]-**13** uptake.²²⁰ Bao *et al.* also investigated the utility of [¹⁸F]-**13** in detecting changes in Sunitinib treated U87MG xenografts. Uptake of [¹⁸F]-**13** was decreased in the Sunitinib treated xenografts, although as expected this was not correlated to VEGFR₂ expression, but to a general decrease in proliferation (evidenced by Ki67).²²¹ Whilst [¹⁸F]-**13** has great clinical utility in imaging proliferation of tumours, there is limited evidence showing its use for monitoring anti-angiogenic therapy for changes specific to differences in VEGFR₂ expression.

Imaging hypoxia with [¹⁸F]-FMISO 14

As previously discussed in this chapter, hypoxia is one of central causes for upregulation of VEGF_A, therefore it is pertinent to discuss the use of PET in imaging hypoxia. Tumour hypoxia has been extensively studied in a variety of imaging modalities, such as MRI, BOLD and SPECT.²²² However, several PET probes have been reported as providing a readout of intracellular hypoxia.^{222, 223} Nitroimidazole based hypoxia PET probes were developed in the 1970s and are known to enter the cell by passive diffusion.²²² Upon entry to the cell, the nitroimidazole tracers undergo reduction to form a reactive intermediate. This reduction can be completed by nitroreductase, including lipoxygenases, NADPH oxidases and xanthine oxidases. In normoxic conditions, the reactive intermediate is oxidised back to the parent compound where diffusion out of the cell occurs. However, in hypoxia further reduction of the reactive nitro-radical occurs. This radical is not able to diffuse back out the cell, becoming trapped within the cell forming the principle of hypoxia imaging.²²³ This reduction requires metabolically active cells and therefore does not occur in necrotic or apoptotic cells, therefore the accumulation of the radiotracer is directly proportional to the pO_2 .²²²

A classical nitroimidazole PET radiotracer is [^{18}F]-Fluoromisonidazole **14** ([^{18}F]-FMISO – Figure 29) and is the most extensively studied hypoxia radiotracer. The lipophilic nature of [^{18}F]-**14** ensures it is cell penetrable. An oxygen level of 10 mmHg is required for hypoxia related retention of [^{18}F]-**14** in gliomas, head and neck, breast, lung and renal cancers.²²² Despite its use in the aforementioned cancers, clinical use of [^{18}F]-**14** is limited due to its slow pharmacokinetic profile and slow clearance.²²² Preclinically, [^{18}F]-**14** uptake has been shown to be dependent on the choice of anaesthesia.²²⁴

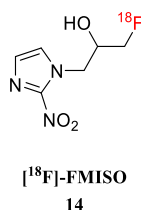


Figure 29: [^{18}F]-**14**

Interestingly, some recent studies have revealed a correlation between [^{18}F]-**14** uptake and VEGF_A expression, which was heterogeneously expressed within the tumour of 19 soft tissue sarcoma patients.²²⁵ Cher *et al.* also observed a positive correlation between [^{18}F]-**14** uptake and VEGFR₁ expression but no correlation with VEGF_A expression in high-grade gliomas.²²⁶ In another clinical study of malignant gliomas, both newly diagnosed and recurrent (grade III and above), 32 patients were evaluated to determine a correlation between hypoxia, HIF-1 α and VEGF_A expression.²²⁷ The study determined a weak correlation between VEGF_A expression (judged by IHC) and [^{18}F]-**14** uptake of newly diagnosed gliomas, but not recurrent gliomas.²²⁷

Despite the limitations described above with using [^{18}F]-**14**, further investigations into its use as a clinical predictive biomarker for the VEGF-VEGFR₂ signalling system are required. Due to the strong indicators of the involvement of hypoxia in the activation of the VEGF-VEGFR₂ signalling cascade, the development of a companion tool for the direct imaging of VEGFR₂ expression is required.

1.3.5. Use of fluorine-18 in the development of a PET probe

The purpose of this project is to develop a small molecule kinase inhibitor analogue radiolabelled with fluorine-18, with the necessary affinity and specificity for the ATP binding pocket of VEGFR₂.

The following characteristics of fluorine-18 make this positron emitting isotope attractive for radiolabelling of the VEGFR₂ targeting PET candidate developed during this project:

- Fluorine-18 allows for multistep synthesis, off-site transportation and with a half-life of 110 minutes avoids overnight hospitalisation of patients following radiotracer injection¹⁵¹
- Fluorine-18 has a low positron energy (0.64 MeV) with a short range in tissue, providing high resolution images^{151, 228}
- Fluorine-18 containing radiopharmaceuticals can be produced with high specific activity and in high yields (20-40%)^{151, 228}
- Fluorine-18 can be produced in large quantities (> 370 GBq)¹⁵¹
- Fluorine-18 has acceptable dosimetry for multiple studies in patients¹⁵¹

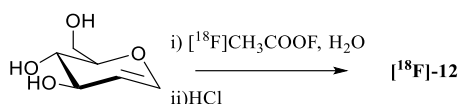
Fluorine-18 is generated in a cyclotron in two forms: nucleophilic ¹⁸F⁻ ions or electrophilic F₂ gas.^{88, 151} The cyclotron accelerates a 20 MeV beam of protons which bombard the target, creating unstable isotopes. The most common target, used in fluorine-18 generation, is highly enriched oxygen-18 water. This produces fluorine-18 ion in the nuclear reaction known as ¹⁸O(p,n)¹⁸F. Alternatively, bombarding a neon-20 target with a 25 MeV deuteron beam produces fluorine-18 with low activity (<37 GBq). This generation of ¹⁸F is from the ²⁰Ne(d,α)¹⁸F reaction.¹⁵¹ The ¹⁸O(p,n)¹⁸F is the superior method for fluorine-18 generation as it sticks to the target walls. Oxygen-18 can then be removed and replaced with argon and cold F₂ gas (1%). A short irradiation will result in the generation of [¹⁸F]-F₂ gas, this process is considered the “double shoot”.⁸⁸

The ability to generate both electrophilic and nucleophilic fluorine-18 allows for a wide range of reactions to radiolabel the PET probe. The radionuclide can be introduced into the molecule through direct fluorination or through the use of a prosthetic group. There are many different examples of radiolabelling for aromatic versus aliphatic and organometallic

reactions⁸⁸. The next section will discuss the differences in radiolabelling techniques and will include; nucleophilic, electrophilic and novel methods of fluorine-18 radiolabelling.

1.3.5.1. Electrophilic radiolabelling

Electrophilic radiolabelling is conducted by the introduction of either [¹⁸F]-F₂ gas or less reactive reagents derivative of [¹⁸F]-F₂ gas, such as xenon difluoride ([¹⁸F]-XeF₂). As electrophilic radiolabelling involves the use of [¹⁸F]-F₂ gas, the maximum radiochemical yield is limited to 50%.^{229, 230} Consequently, electrophilic radiolabelling is limited to radiopharmaceuticals which do not require high specific activity. Another negative of electrophilic radiolabelling is the generation of side-products, which requires extensive purification. An example of electrophilic radiolabelling is shown through the radiolabelling of [¹⁸F]-**12** (Scheme 2).



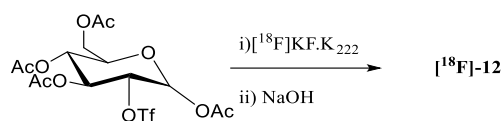
Scheme 2: Electrophilic radiolabelling of [¹⁸F]-**12**²³¹

[¹⁸F]-XeF₂ is typically prepared through isotopic exchange of a fluorine-19 with [¹⁸F]-fluoride. As described previously, this is known as the double shoot method and makes use of excess [¹⁸F]-fluoride production. There is a wealth of precedence in the literature describing the use of XeF₂ for the fluorination of organic molecules under mild conditions, however is rarely used in research.²³²⁻²³⁴

1.3.5.2. Nucleophilic radiolabelling

Nucleophilic radiolabelling typically begins with a drying step, to remove any hydrogen bonding with water which decreases the nucleophilicity of the [¹⁸F]-fluoride ion. After washing from the target, the aqueous [¹⁸F]-fluoride is passed through an ion exchange target, removing bulk H₂¹⁸O. The trapped fluoride is released from the ion exchange cartridge using acetonitrile, potassium carbonate and Kryptofix_{2.2.2}[®] (K_{2.2.2}), a crown ether which complexes potassium ions increasing the nucleophilicity of the naked [¹⁸F]-fluoride ion. Acetonitrile is used to in the removal of excess water, due to azeotrope formed between acetonitrile and water. The removal of water is generally conducted in vial which is placed

under a stream of nitrogen and heated, ensuring complete dryness of the fluoride.²³⁵ This step is repeated a further two times, an example of nucleophilic radiolabelling of [¹⁸F]-**12** is presented below in Scheme 3.



Scheme 3: Nucleophilic radiolabelling of [¹⁸F]-**12**^{88, 236}

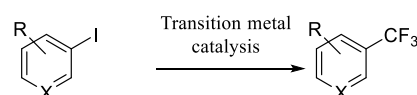
This type of radiolabelling is normally conducted in polar aprotic solvents such as acetonitrile, DMSO or DMF. This is due to the ease of ionic dissociation of K_{2.2.2}. The reactivity of the leaving group depends largely on its ability to stabilise the negative charge from the [¹⁸F]-fluoride attack. Consequently, in aliphatic radiolabelling a triflate group is the most reactive. However, mesylates or tosylates are more commonly used due to increased precursor stability compared to the triflate. For an aromatic systems, nitro or trimethyl ammonium groups are the most common prosthetic groups for radiolabelling. This is due to nucleophilic substitutions being more successful when the ring system is activated with a negative inductive or a negative mesomeric effect from ortho-para substituents. Leaving groups ideal for aliphatic radiolabelling are generally not suitable for aromatic radiolabelling. Fluorine itself is an excellent leaving group, however only low specific activity is generated. This is due to requiring large excesses of precursor in comparison to [¹⁸F]-fluoride.²³⁵

1.3.1.1. Novel approaches to fluorine-18 radiolabelling

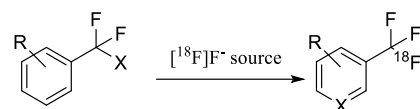
Traditional nucleophilic radiolabelling of both aromatic with electron neutral and electron rich systems typically results in low yields, there are a variety of novel fluorination methods which have been published to avoid this problem.²³⁷ The next section will highlight a few of these methods relevant to this project.

Trifluoromethylation

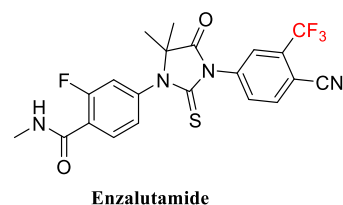
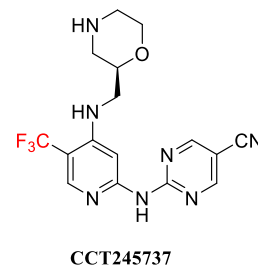
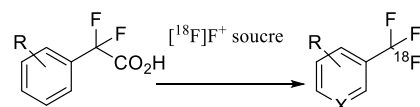
A trifluoromethyl group is incorporated into the scaffold of important pharmacophores, such as Enzalutamide and CCT245737, used in the treatment of prostate cancer and a novel CHK1 inhibitor respectively.^{238, 239} However, there is no general method for the preparation of radiolabelled trifluoromethyl groups in both arene and heteroarene scaffolds. Past methods have included the use of pre-generated [¹⁸F]-CuCF₃ complexes, halix exchange and halodecarboxylation with reagents such as [¹⁸F]-Selectfluor.^{240, 241} Each of the trifluoromethylation techniques are limited in scope or require multistep syntheses (Scheme 4).

A) CF₃ source

B) Halix exchange

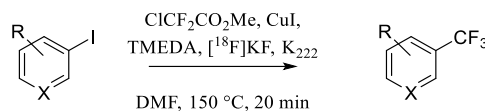


C) Fluorodecarboxylation



Scheme 4: Traditional methods of trifluoromethylation, with two examples of drug candidates (CCT245737²³⁹ and Enzalutamide²³⁸) containing the CF₃ group (highlighted in red)

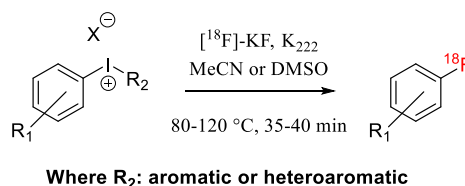
Huiban *et al.* presented an elegant method for the trifluoromethylation of aryl and heteraryl iodides using methyl chlorodifluoroacetate in a copper catalysed cross-coupling reaction (Scheme 5).²⁴² A wide substrate scope is presented, ranging from nitro to phenols, involving the use of commercially available reagents which can be used in air.²⁴²



Scheme 5: Copper mediated fluorination of aryl and heteroaryl iodides²⁴²

Iodonium salts

An efficient alternative to the traditional radiochemistry, is the use of diaryliodonium salts. Nucleophilic attack of the fluorine-18 usually occurs on the most electron deficient ring, also an ortho-effect is observed (Scheme 6). The ortho-effect describes the most favourable site off attack due to the iodine-centred trigonal bipyrimidal intermediate.²⁴³ This places the sterically more hindered ortho-substituted ring at an equatorial position. One major disadvantage of this radiochemistry, is the preparation of the precursor. The precursors usually have a short shelf-life, and the electron rich ring system requires extreme conditions for radiolabelling. Another disadvantage is the solubility of the compounds when the anion is a halide. However this is overcome through the use of triflate or tetraborate salts.²⁴³ The fluorination of these iodonium salts exhibit a lack of regioselectivity and, at best, provide modest yields.

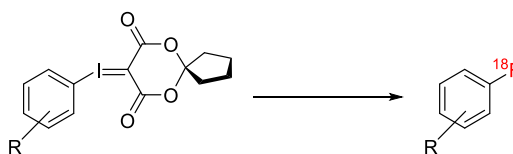


Scheme 6: Examples of fluorination with iodonium salts²⁴³

Iodonium Ylides

Coenen *et al.* developed iodonium ylides to improve on the fluorination of the iodonium salts described above.²⁴⁴ Iodonium ylides allow the fluorination of the electron rich rings highlighted above. However stability of the ylides was still an issue. Rotsetin *et al.* have developed the use of hypervalent iodonium spirocyclic compounds for the use in PET precursors, which demonstrated superior stability to those developed by Coenen (Scheme 7).²⁴⁵ These spirocyclic hypervalent iodonium salts have proven to be able to direct the fluorine-18 in a regioselective manner. This new methodology can be used to radiolabel both

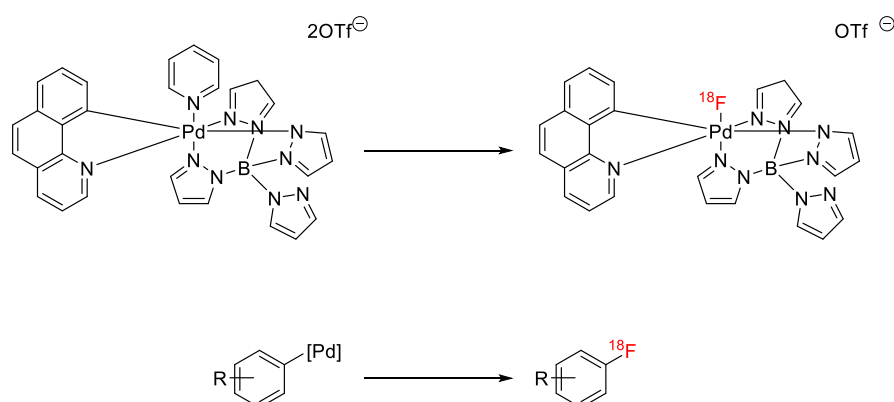
electron neutral and sterically challenged arene. The spirocyclic hypervalent iodonium precursor is also capable of fluorinating a wide range of precursors, isolatable in high radiochemical yields and specific activities.²⁴⁵



Scheme 7: Radiosynthesis of Rotstein spirocyclic hypervalent iodonium compounds²⁴⁵

Palladium mediated fluorination

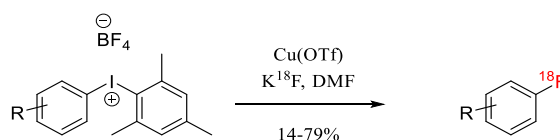
Palladium mediated fluorination has been developed for the electron rich scaffold, with the potential to enhance reactivity, selectivity and reaction times. The Ritter group have developed an *in situ* fluorophilic Pd(IV) with $K[^{18}F]$, forming an intermediate capable of reacting with Pd(II) arenes. This forms Pd(IV) aryl fluoride complexes (Scheme 8), which undergo C-F coupling to yield the fluorinated products in reasonable yields.⁸² Pitfalls to this method include the need for a two-step synthesis and the air sensitive nature of the first intermediate.



Scheme 8: Ritter's Pd mediated fluorination

Copper mediated fluorination

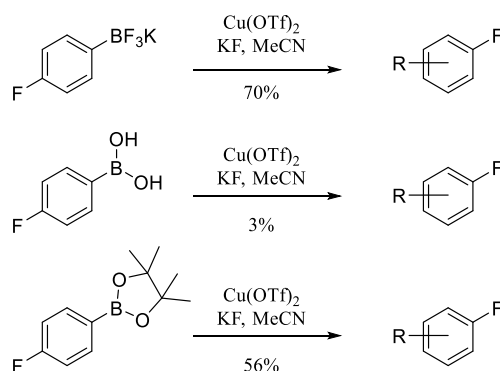
The Sanford group have developed methods which mesityl substituted diaryliodonium or arenes were fluorinated mediated by copper (Scheme 9). In cold chemistry Cu(II) catalysts give high yields, however this is over a longer time period.²⁴⁶ In the radiochemistry setting, Cu(I) catalysts are preferred as a much shorter time period is required for the fluorination, giving higher radiochemical yields. Limitations of the Sanford copper mediated fluorination is the multistep synthesis of the radiochemical precursors, transfer to an automated system and low isolated radiochemical yields.^{246, 247}



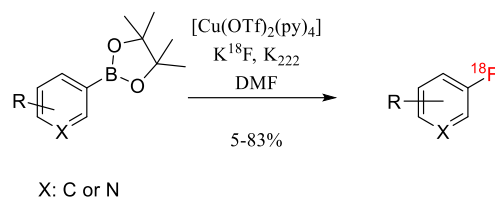
Scheme 9: Copper mediated fluorination²⁴⁶

Preliminary cold work from Sanford demonstrated that aryl fluorides can be generated from aryl boron salts and pinacol esters, catalysed by copper (Scheme 10).²⁴⁸ The Gouverneur group applied this work for radiolabelling with fluorine-18, showing that both aryl and heteroaryl boronic pinacol esters undergo radiolabelling with fluorine-18 (Scheme 10b).²⁴⁹ Limitations of the Gouverneur fluorination are the expensive nature of the copper catalyst, incompatibility with boronic acids and its inability to translate well on an automated system. Recently, Mossine *et al.* have published a method in which they displace a boronic acid with fluorine-18, whilst addressing the limitations of the Gouverneur method (Scheme 10c).²⁵⁰

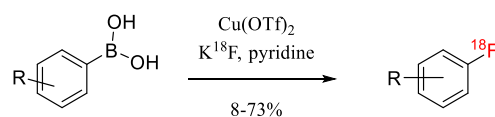
A) Sanford cold chemistry



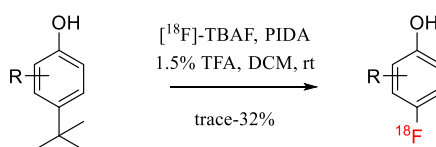
B) Gouverneur radiochemistry



C) Sanford and Scott radiochemistry

**Scheme 10:** Aryl boron derivatives for fluorination²⁴⁸⁻²⁵⁰Fluorination of phenols

Occasionally there is the need to radiolabel a phenol. Conventionally this has been achieved through radiolabelling the corresponding aldehyde or ketone, Baeyer-villiger oxidation of the ester and the saponification of the ester.²⁵¹ This is low yielding, with two steps required after radiolabelling. Gouverneur's group developed a metal free method to directly access the fluorine-18 labelled arenes (Scheme 11). This reaction is based on umpolung chemistry; requiring the presence of phenyliodine diacetate (PIDA) and TBAF. This methodology requires further optimisation but is showing promise.²⁵¹

**Scheme 11:** Gouverneur fluorination of phenols²⁵¹

1.4. Summary

Angiogenesis is a tightly control process under normal physiological conditions where endothelial cells are quiescent unless activated. However, cancer angiogenesis is pathogenic and central for both tumour growth and metastatic spread. Upregulation of pro-angiogenic factors and activation of the central VEGF-VEGFR₂ signalling axis results in the development of a disordered and chaotic vascular network, substantial efforts have been made to develop therapies that target this system. Ensuring the correct patient receives the appropriate therapy, maximises therapeutic benefit whilst minimising the risk of unwarranted adverse events.

Responses observed in the clinic for VEGF-VEGFR₂ targeted therapies for some patients are transient at best. Therefore, establishing a biomarker which could either predict who may benefit from anti-angiogenic treatment or monitor responses of anti-angiogenic treatment would be ideal. Tissue and circulating biomarkers have been extensively evaluated with conflicting results. VEGF_A levels pre-treatment have correlated with shorter PFS and OS in some studies. Tissue based biomarker evaluation is limited due to the requirement for repetitive invasive biopsies. Imaging of the VEGF-VEGFR₂ signalling system is ideal owing to its non-invasive nature. Current imaging based strategies have been focused on either DCE-US or DCE-MRI. DCE-US has been focused on BRR5 microbubble which has been shown to distinguish between VEGFR₂ and non-VEGFR₂ specific treatment response. Various DCE-MRI parameters, such as K^{trans} , K_{ep} and rBV, have been investigated but no agreement has been reached in the literature on a single biomarker.

Nuclear molecular imaging techniques PET and SPECT are ideal as non-invasive imaging techniques. [¹⁸F]-Fluciclatide, an RGD based probe which targets $\alpha v \beta 3$ and $\alpha v \beta 5$, has shown the most clinical promise, but is incapable of imaging VEGFR₂ expression. PET imaging of the VEGF-VEGFR₂ signalling system has been approached using two different strategies, i.e. developing a probe targeting VEGF_A or a probe targeting VEGFR₂. PET strategies based on VEGF_A imaging have focused on radiolabelling Bevacizumab with ⁸⁹Zr, VG76e with ¹²⁴I or radiolabelling VEGF₁₂₁ with the chelating group DOTA. However this strategy of targeting VEGF_A leads extended exposure to radiation due to longer-lived radioisotopes and longer biological half-lives. Efforts to develop a VEGFR₂ specific PET probe focused around known clinical candidates have been confounded by a lack of inherent selectivity.

1.5. Aims and Objectives

Amongst the pro-angiogenic factors upregulated in response to tumour hypoxia, activation of the VEGF-VEGFR₂ signalling pathway is the key mediator of angiogenesis. Response to anti-angiogenic treatment is transient for some cohorts of patients. No single biomarker, predictive or pharmacodynamic currently exists, for delivering on the goal of personalised therapy. A VEGFR₂ targeted imaging agent would allow the selection of patients for anti-angiogenic therapy. The use choice of PET for this task will negate the need for repeated invasive biopsies, due its capability of imaging processes such as angiogenesis.

Previous efforts to develop a PET imaging agent targeting VEGFR₂ have failed, due to the lack of selectivity exhibited by clinically relevant kinase inhibitors. Therefore, the probe must be selective for VEGFR₂ only. The potential PET imaging probe will be heterocyclic in nature, enhancing binding to VEGFR₂ through interaction with Cys919 at the kinase active site. Motifs shown to achieve this are a urea, indole or a quinazoline. Although not a major consideration, the candidate libraries will be designed with a focus to keep lipophilicity low to avoid high non-specific binding to plasma proteins, but high enough to allow diffusion across the cellular membranes. The candidates will also be designed to allow incorporation with fluorine-18, the preferred PET radioisotope for small molecule radiotracers.

Ideally the libraries will be assessed for non-specific off-target effects, by a proliferation assay using cell lines known not to express VEGFR₂. The initial screening for off-target effects will be a crude assessment for a larger library of candidates. The lead candidate(s) identified after screening for non-specific off-target effects will be assessed for the presence of a lack of selectivity between the kinases closely related to VEGFR₂, through the use of kinase assays.

Finally, radiolabelling with fluorine-18 of the lead candidate(s) will be attempted. After the identification of the optimal radiolabelling conditions, stability studies of the radiolabelled lead candidate(s) will be carried out, followed by evaluation in VEGFR₂ positive xenografts (U87) to determine biodistribution and the ability of the lead candidate to localise in the VEGFR₂ xenografts.

Chapter Two

Urea focused library

2. Urea Focused Library

2.1 Ureas in medicinal chemistry

Kinase inhibitors are an important class of effector for targeted therapy strategies in different cancers, and have the potential to be adapted for PET imaging of therapeutic response or evaluating receptor expression status (the main focus of this project).²⁵² Amongst the varied structures identified from drug discovery programmes, urea moieties have emerged as a chemical building block which has shown inhibitory activity towards kinases that play important roles in angiogenesis, metastasis and survival.²⁵² Figure 30 highlights different urea scaffolds having different targets within the cancer genome.²⁵³

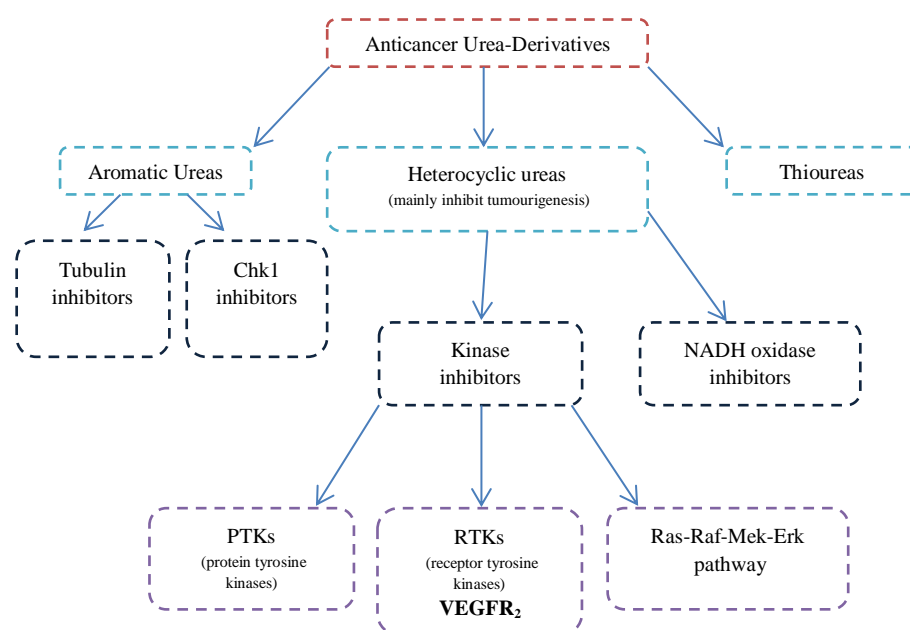


Figure 30: Different urea classes targeting the cancer genome (Adapted from²⁵³)

The properties which make the incorporation of urea into medicinal chemistry scaffolds attractive are:

- High aqueous solubility²⁵⁴
- Powerful hydrogen bond donors-from the NH in the urea scaffold²⁵⁵
- Hydrogen bond accepting nature of the urea carbonyl – allowing for more interactions with the target

Of the kinases possessing urea moieties to undergo clinical trials (ABT-869 **15** and KRN-951 **16** –Figure 31), Sorafenib was FDA approved in 2005, as previously discussed in Chapter One (1.2.3.2).²⁵⁶⁻²⁵⁸

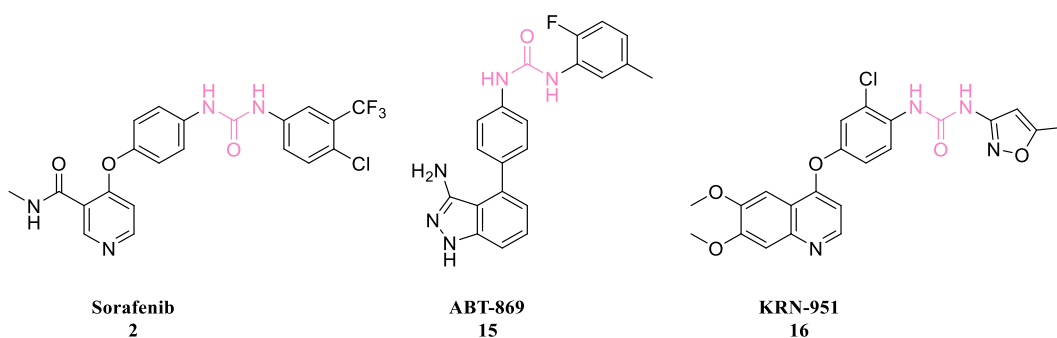


Figure 31: Structure of **15** and **16**, urea containing VEGFR₂ inhibitors that have progressed to clinical trial, urea moieties are highlighted in pink.

Adverse events exhibited by **15** include several non-haematologic adverse events, including hypertension, occurring at an elevated level compared to **16**. A lack of selectivity between VEGFR family and PDGFR α and PDGFR β is exhibited by **15**, with similar affinities for each target.²⁵⁹ However, **15** does exhibit dose dependant inhibition of VEGF-induced proliferation *in vitro*, whilst also showing activity against a broad spectrum of xenograft models.²⁶⁰ No selectivity is demonstrated by **16** for the VEGFR family, exhibiting affinity for PDGFR α , PDGFR β , TIE-2, cKIT and the FGF family.²⁵⁷ A study by Eskins *et al.* highlighted the most frequently observed adverse event was dose-dependent hypertension, which can be attributed to pharmacological response. The study also highlighted favourable oral bioavailability, slow absorption and a half-life appropriate for once daily dosing with a recommended dose of 1.5 mg.²⁶¹ Despite this study initially highlighting favourable pharmacological properties, it is not suitable for a PET imaging probe due to its non-selective behaviour.

2.1.1. VEGFR₂ inhibitors possessing a urea functional group

The urea-possessing inhibitors typically form hydrogen bonds with the Asp1046 and Glu885 residues of VEGFR₂, developing the same critical hydrogen bonds as the adenine ring of ATP as shown in Figure 30a.²⁶² Importantly all the inhibitors also bind to Cys919, which is key for VEGFR₂ inhibition. These type II kinase inhibitors also incorporate large, hydrophobic groups to occupy the hydrophobic pocket observed in the inactive conformation, unlike that of **1**. This prevents the DFG (Asp – Phe – Gly) motif from moving to its ‘in’ position and binding to metal ions for stability in the active state, thus blocking receptor activation of VEGFR₂.^{256, 262} As shown in Figure 32b, the DFG group is prevented from moving to its ‘in’ position due to a binding interaction, in the form a hydrogen bond, to Asp1046, the first amino acid of the DFG complex in VEGFR₂, and therefore signal transduction.²⁶³

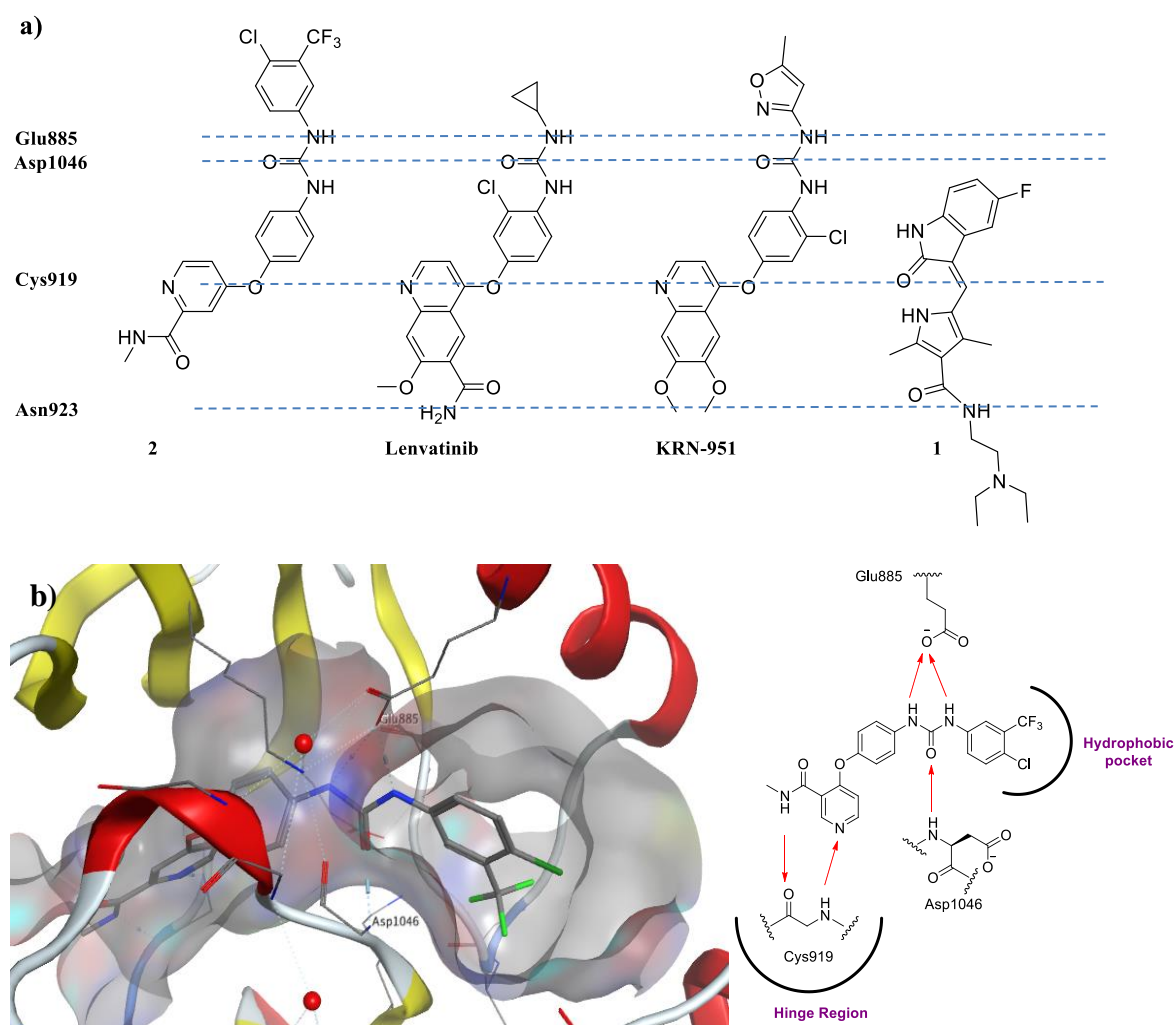


Figure 32: Interactions of urea containing inhibitors with VEGFR₂. A) The typical binding modes of urea containing VEGFR₂ inhibitors, showing binding via the urea to both the Glu885 and Asp1046 residues, with **1** as a comparison (adapted from²⁶⁴) B) VEGFR₂ in complex with **2**, showing binding interactions. Docking studies performed using Schrödinger Gold (2014-2) and visualised on Chemical Computing Group MOE (2013-8802). PDB code: 4ASD

Miyamoto *et al.* explored the significance of the urea group in **17a-c** and the resultant effects on activity.²⁶⁵ As shown in Figure 33, the presence of the urea moiety is crucial for potency and removal of nitrogen **Z** in **17b** results in very little loss of potency, thus demonstrating this nitrogen is not necessary for creating interactions with the receptor. This is due to the binding of one of the amino groups forming the hydrogen bond in the correct orientation. Moreover, the additional amino group **17a** facilitates increasing binding affinities for this class of molecules. Removal of nitrogen **X** in **17c** is extremely detrimental to potency, resulting in a 12 fold loss of activity. The extra nitrogen the urea provides, allows easy access to the hydrophobic back pocket that could allow for more interactions with VEGFR₂ which could increase selectivity.

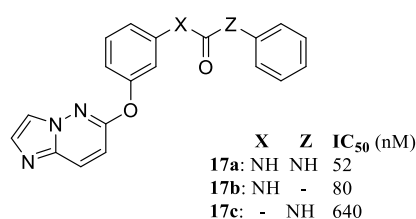


Figure 33: VEGFR₂ inhibitor **17** demonstrating the importance of the urea moiety²⁶⁵

2.2 Rationale

A literature search for current and experimental VEGFR₂ inhibitors, possessing the urea moiety, concluded that most scaffolds are based on a bicyclic structure. Despite offering modest to excellent potencies and affinities towards VEGFR₂, these compounds are often extremely lipophilic and are thus less suitable for PET imaging. High plasma protein binding confounds data acquisition by increased non-specific binding of highly lipophilic compounds, as well as cross activity confounding the obtained image. Currently, there are limited examples in the literature of small-molecule TKI targeted PET radiotracers, radiolabelled with fluorine-18, which have the required specificity and do not have close affinities for other kinase targets. However, increased lipophilicity of the PET candidate will not preclude its use as a tracer if the selectivity and affinity requirement is fulfilled. The aim of this chapter has to determine whether the urea-based scaffold retains its inherent selectivity, after the synthesis of a small library of urea based compounds.

Huang *et al.* proposed a monocyclic core structure **18**, having the capability of mimicking the adenine ring of ATP **19**, through the formation of a hydrogen bond **20** (Figure 34).²⁶⁶ This offers cLogP values more suitable for PET imaging, whilst retaining hydrogen bond donor (HBD) and hydrogen bond acceptor (HBA) in the scaffold required for binding, as well as being a unique urea-containing fluorine-18 scaffold for PET imaging.

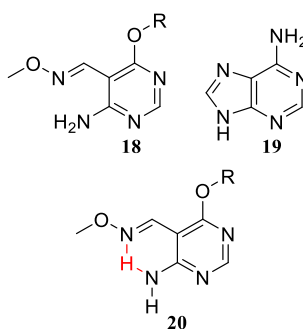


Figure 34: Left: the core structure in which this study is based **18**. Right: Structure of adenine **19**. Bottom: Hydrogen bonding formed within the core structure **20** (shown in red)

This monocyclic core structure **21** was taken as the basis for a novel VEGFR₂-binding PET radiotracer. Huang *et al.* also explored the urea moiety attached to the pyrimidine-5-oxime (highlighted in red) via an ether link, as shown in Figure 35.²⁶⁶

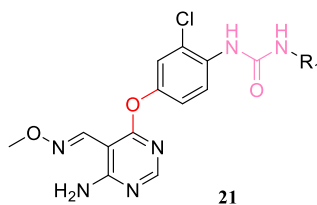


Figure 35: Structure of scaffold **21** developed by Huang *et al.*²⁶⁶ Urea highlighted in pink, with the ether bridge highlighted in red

Initial SAR studies from this scaffold revealed bulkier substituents, at the R₁ position, were well tolerated, which can be attributed to the increased electron density being able to access the hydrophobic pocket, thus increasing the potency of the compounds (Table 7).²⁶⁶

Table 7: VEGFR₂ IC₅₀ data for the urea scaffold **21** with modifications of the R position²⁶⁶

Entry	Compound	R	VEGFR ₂ IC ₅₀ (nM)
a	21a	Methyl	25
b	21b	Ethyl	11
c	21c	Propyl	28
d	21d	Cyclohexyl	6.5
e	21e	Phenyl	3.0
f	21f	2-chlorophenyl	2.6

2.2.1. Design of a urea focused library

It was envisaged, informed by the data discussed above, the library would be focused on the synthesis of aromatic homologues around the urea core, whilst also including the synthesis of a small library of fluorinated aliphatic analogues. This is to exploit the hydrophobic back binding pocket of VEGFR₂ in the inactive state. As Figure 36 highlights, the back pocket occupied by the phenyl still has space for modifications which could be explored in the synthesis of this library.

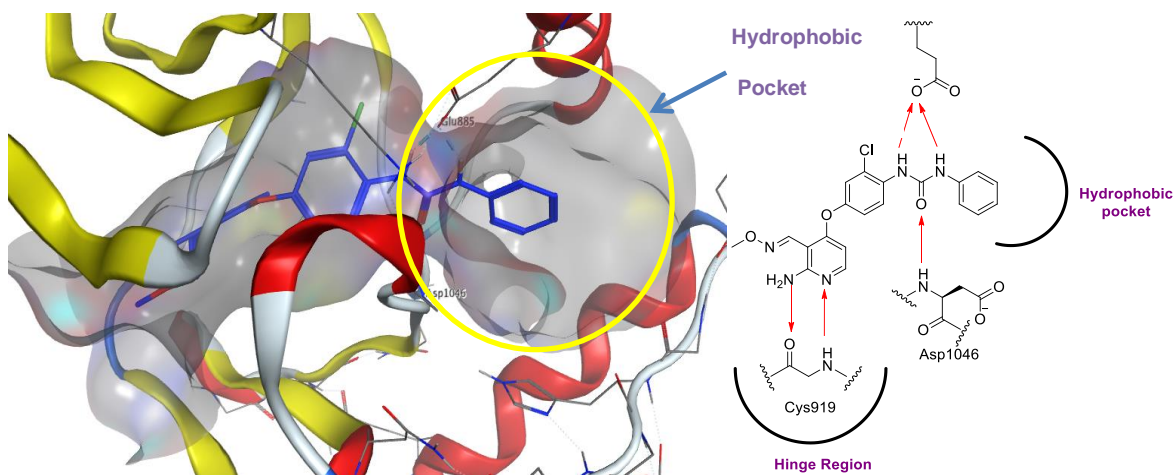


Figure 36: Docking studies of **21f** (shown in blue – area highlighted by yellow circle), the receptor binding pocket is highlighted in grey. Docking was performed using Schrödinger Gold (2014-2) and visualised on Chemical Computing Group MOE (2013-8802). PDB code: 3VHE

It is expected that, based around initial docking, modifications would occur pendant to the urea moiety, as shown in Figure 37. With smaller substitutions pendant to the oxime, to occur after preliminary SAR has been performed at the urea moiety.

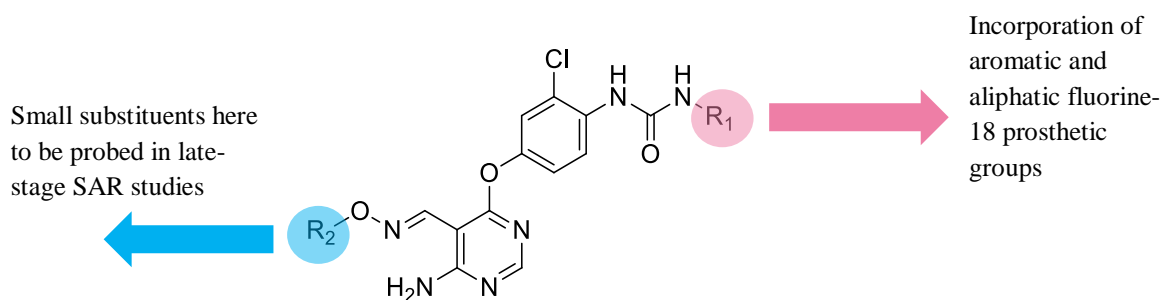


Figure 37: SAR to be explored in this urea focused library

2.2.2. Considerations of the urea focused library for developing a successful candidate

Figure 37 shows modifications which aid the development of the scaffold highlighted by Huang *et al.*²⁶⁶ Incorporation of a prosthetic group pendant to the urea allows for quick radiolabelling, an essential characteristic required for PET imaging due to the half-life of fluorine-18 (109.7 minutes). The PET tag at this position could be easily accessed through direct labelling of a prosthetic group (a tosylate for aliphatic groups, a nitro or trimethyl ammonium for aromatic), or through the synthesis of a radiolabelled amine which could be converted to either an isocyanate or directly coupled to the core scaffold. Typically urea scaffolds are radiolabelled with carbon-11 due to the wide range of radiochemistry available.

However due to its short half-life of 20 minutes this makes it less than ideal for quantifying VEGFR₂ expression, as rapid radiolabelling and injection into the patient is required, followed by rapid equilibrium at the receptor site. As previously discussed the highlighted scaffold is known to achieve the affinity required for a PET imaging agent. Therefore this scaffold is ideal for the development of a PET imaging agent incorporating the urea functionality, radiolabelled with fluorine-18, and is the focus of this Chapter.

2.3 Synthesis of urea homologues

There are many methods which are utilised for synthesising urea derivatives, including reacting amines with isocyanates, reacting amines with phosgene to produce isocyanates *in situ* followed by a second equivalent of an amine, and the direct coupling of two amines using a coupling reagent (Figure 38).

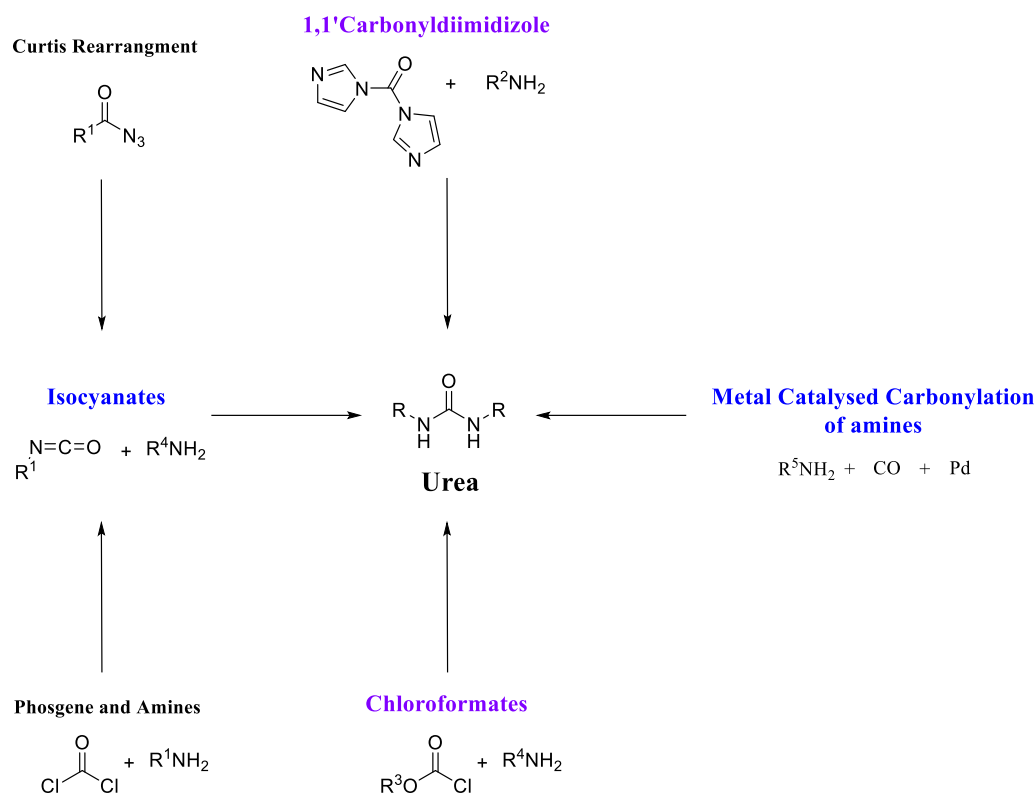


Figure 38: Different methods used for the synthesis of urea moieties

2.3.1. Isocyanates

Isocyanates were first identified by Wurtz in 1849. With 20 methods describing their preparation to date, a few of these methods will be discussed below.²⁶⁷ Isocyanates are used in the manufacture of adhesives, agrochemicals, thermoplastic foams as well as the pharmaceutical industry. Isocyanates are widely used as precursors to pharmaceuticals containing either carbamate or urea moieties.²⁶⁷

2.3.2. Phosgene

Phosgene **22** and its equivalents, diphosgene and triphosgene, are extremely toxic and mostly used for industrial scale synthesis of isocyanates **23**.²⁶⁸ Phosgene is reacted with primary amines, under anhydrous conditions, which ultimately releases two equivalents of

hydrochloric acid, as depicted in Figure 39.²⁶⁸ Therefore this method is less than ideal for small scale laboratory synthesis, due to the associated toxicities. Ultimately the elevated temperatures required for phosgene mediated synthesis of **23**, this rules out the use of phosgene mediated synthesis of smaller molecules required for this project.²⁶⁷

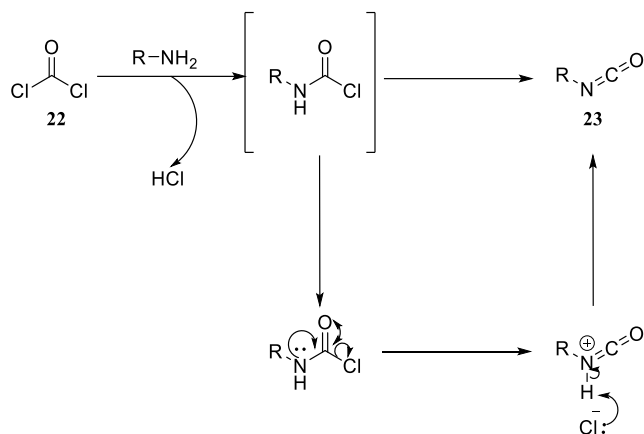


Figure 39: Phosgene mediated synthesis of isocyanates

2.3.3. Curtius Rearrangement

The Curtius rearrangement converts acyl azides **24** to **23** and is a classical reaction in organic chemistry. It is one of a few methods which does not involve the use of phosgene in the production of **23**.²⁶⁹ The acyl azide **24** is produced through the reaction of an acyl chloride with sodium azide and then heating the reaction to facilitate the rearrangement to the isocyanate. Although the exact mechanism has not been elucidated, it is generally accepted that the mechanism is a concerted process or through the loss of nitrogen first as shown in Figure 40.²⁶⁹ However this reaction is not utilised on an industrial scale due to the explosive nature of **24** and the associated toxicities, although it is employed on a small laboratory scale.

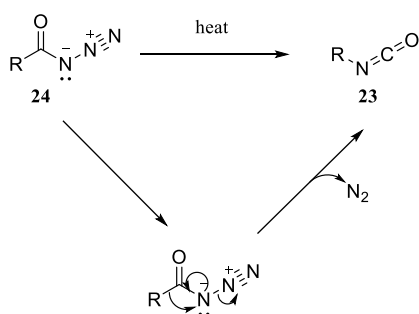


Figure 40: Curtius rearrangement of **24** to **23**

2.3.4. 1,1'-Carbonyldiimidazole **25**

1,1'-Carbonyldiimidazole **25** (CDI) is a mild reagent in comparison to phosgene and its derivatives. Due to the hygroscopic nature of **25**, all reactions involving its use are performed under nitrogen, utilising DCM, THF or acetonitrile as the solvent of choice.²⁷⁰ This route can also utilise amines where the corresponding isocyanates are not commercially available, or contain functional groups which are sensitive to the formation of isocyanates, to afford otherwise inaccessible ureas analogues (Figure 41). The use of **25** as a very mild reagent is widespread and has no known effect on human health, is widespread in coupling reactions.

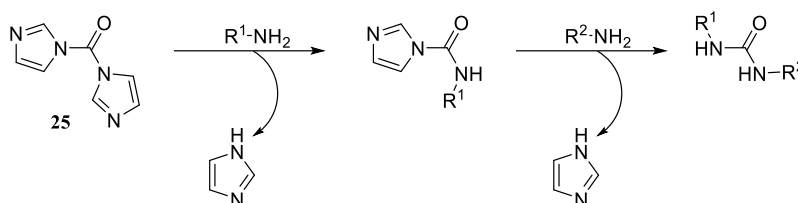
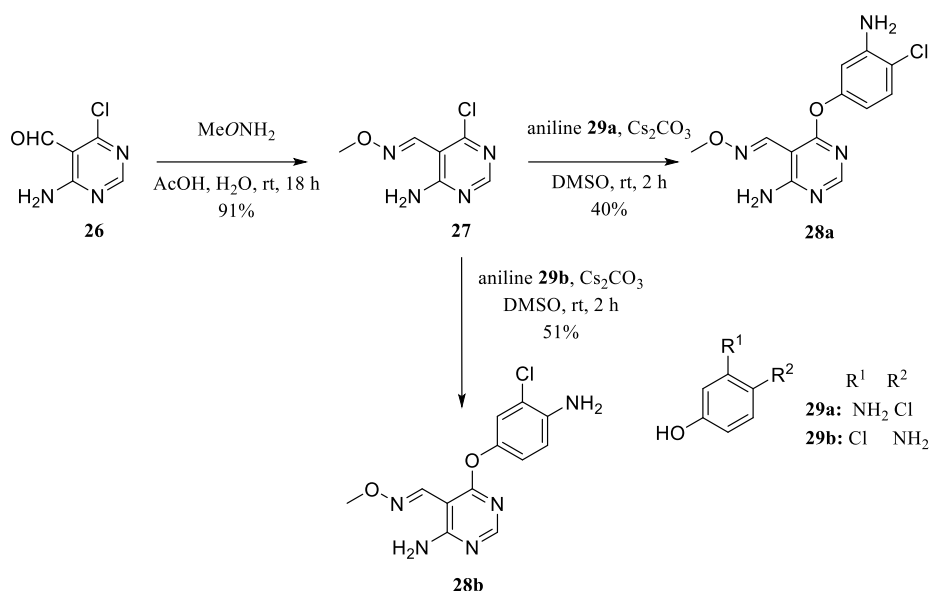


Figure 41: Conversion of **25** into a urea derivative

2.4 Results and discussion

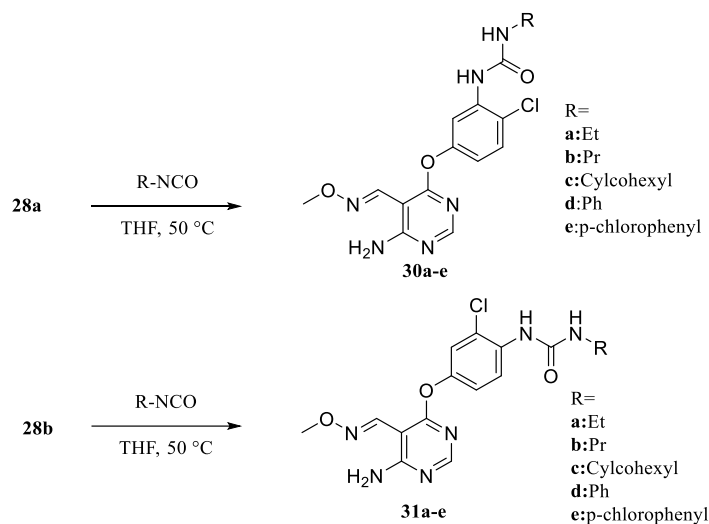
2.4.1. Synthesis of the core scaffold

The first step in the synthesis towards the core structure is the simple condensation of the aldehyde **26** with methoxyamine hydrochloride salt in a 91% yield requiring no further purification. Displacement of the chlorine in **27** with the appropriate aminophenol, resulted in the formation of the biaryl ether **28a** and **28b** in a 40 and 51% yield respectively, after column chromatography purification (Scheme 12).



Scheme 12: Synthesis of the core scaffold **28a** and **28b**

The resulting amine precursors **28a** and **28b** were reacted with various isocyanate analogues resulting in the suspected formation of the urea analogues (**30a-e** and **31a-e**). These reactions were monitored by TLC until the consumption of the amine starting material was observed at which point the reactions were considered complete (Scheme 13).



Scheme 13: Attempted isocyanate mediated synthesis of final compounds

Although the formation of these urea moieties should be relatively straightforward, proton NMR highlighted a different species to the aniline precursor and mass spectrometry analysis confirmed the urea was not formed. Further 2D experiments were deployed in order to solve this problem and heteronuclear multiple bond correlation (HMBC) was used. HMBC analysis was undertaken on **31e** (Figure 42), to find a 4J coupling between the urea carbonyl carbon and protons H_g or H_k , from **31e**, as this would confirm the presence of the urea moiety.

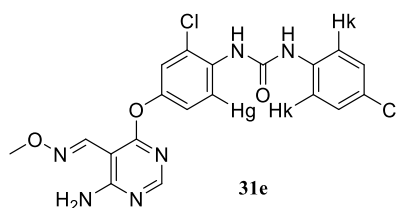


Figure 42: Positions of the protons of interest on **31e** for HMBC analysis

As Figure 43 demonstrates, there is no coupling between the carbon of interest, at approximately 155 ppm, and the protons of interest. However as shown in Figure 43 no coupling is seen between the carbon of interested and H_g or H_k , perhaps due to the weak 4J coupling.

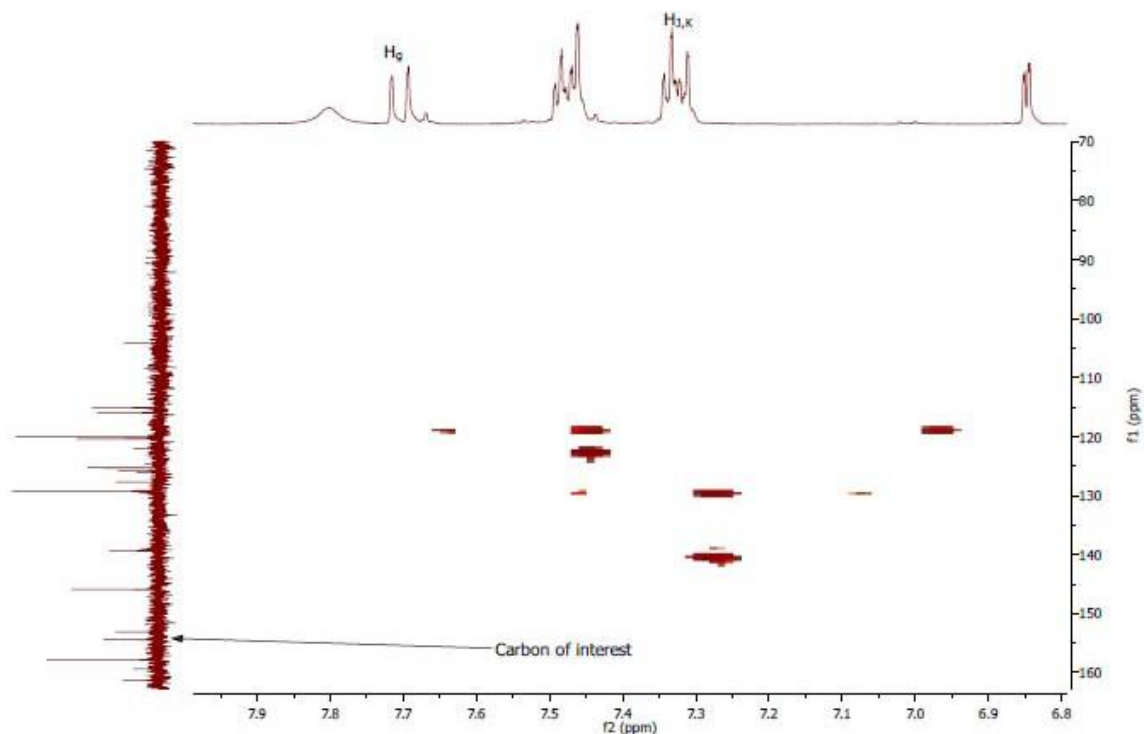


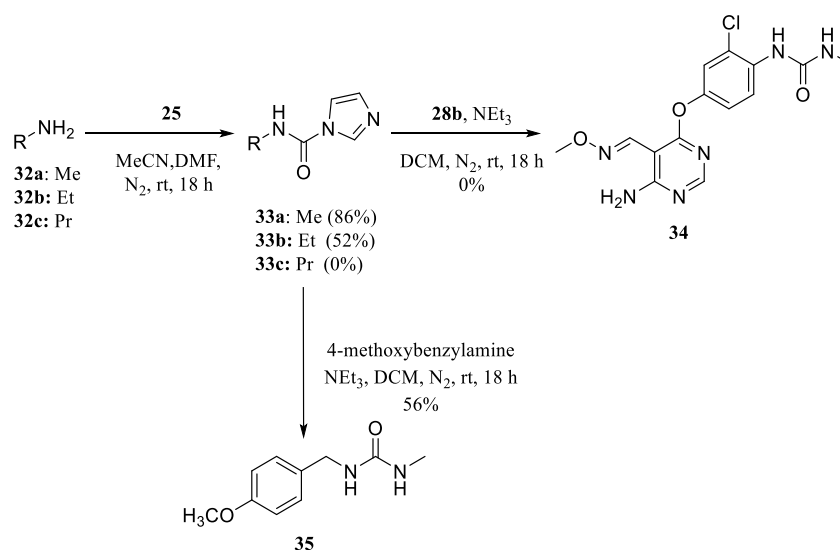
Figure 43: HMBC analysis of **31e**

Owing to the inconclusiveness of the HMBC analysis and the negative mass spectrometry results, the reactions were conducted again in the presence of 3 Å molecular sieves. This removes water produced in the reaction, driving the reaction forward towards the urea homologues, following Le Chatelier's principle. Despite the removal of water, the isocyanate mediated synthesis of urea moieties was unsuccessful, as judged by both NMR and TLC. Consequently, alternative methods were investigated to synthesise these urea compounds.

2.4.2. Synthesis of ureas via 1,1'-carbonyldiimidazole **25**

Duspara *et al.* published a method which accessed methyl urea analogues through the use of less toxic reagents in a milder fashion.²⁷¹ Coupling reagent **25** was used under more facile, environmentally friendly conditions which could give access to the methyl previously inaccessible due its highly toxic nature, difficulty in handling and shipping restrictions associated with methyl isocyanate.²⁷² Its toxicity is best exemplified by the Bhopal disaster in 1984 in which 3800 people died.²⁷² The methyl analogue is particularly important due to its small size, fitting inside the hydrophobic pocket of VEGFR₂. Although not a requirement for this fluorine-18 driven project, there is the opportunity to radiolabel this compound with carbon-11.

Scheme 14 highlights the synthetic route utilised to access the urea analogues, involving the condensation of amine analogues with one equivalents of **25**. *N*-methyl carbamoylimidazole **33a** was synthesised in an 86% yield after column chromatography, identical to that reported.²⁷¹ The next corresponding reaction with the amine precursor **28b** was not successful and resulted in the decomposition to unidentifiable by-products, with several spots seen on the TLC plate.



Scheme 14: Synthesis of urea derivatives, the via use of coupling reagent **25**

Several alternative conditions were attempted to obtain **34**, as summarised in Table 8. The addition of DMAP (entry **a**) as a catalyst also proved unsuccessful, whether the DMAP was present at the start or added after a period of time. To ascertain whether this is a result of deactivated scaffold or whether the conditions reported were inaccurate, a direct comparison reaction from the article was undertaken which was successful. Upon reaction of *N*-methyl

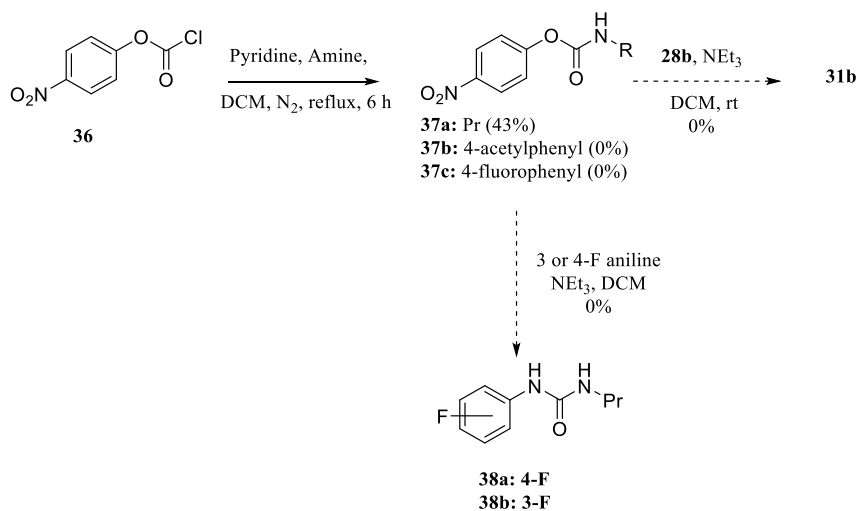
carbamoylimidazole **33a** with 4-methoxybenzylamine and subsequent column chromatography this yielded **35** in a 56% yield. This confirmed the scaffold is inactive for these milder conditions for the synthesis of the urea moiety. This led to a literature search to find more vigorous methods to form the urea from the aniline.

Table 8: Summary of conditions attempted for the synthesis of ureas via **25**, reactions were monitored by TLC

Entry	Conditions	Catalyst	Time	Outcome
a	1 eq of 33a 1 eq of 28b	none	3-48 h	No reaction
b	1 eq of 33a 2 eq of 28b	none	3-48 h	Breakdown products
c	1 eq of 33a 1 eq of 28b	DMAP (0.05 eq)	3-48 h	No reaction
d	1 eq of 33a 1 eq of 28b	DMAP (0.05 eq) then a further 0.05 eq after 24 hours	3-72 h	No reaction

2.4.3. Synthesis via 4-nitrophenyl chloroformate

The use of chloroformates has been noted in the synthesis of ureas and carbamates moieties. In particular, 4-nitrophenyl chloroformate **36** is highlighted as a suitable alternative. Scheme 15 highlights the reaction of 4-nitrophenyl chloroformate with an amine in the presence of pyridine, as a base, in refluxing DCM. The vast majority of amines tested using these reported conditions were successful reactions. 4-Nitrophenyl propyl carbamate **37a** was synthesised in modest yields (43%) after column chromatography purification.



Scheme 15: Attempted synthesis of **31b** using **36**

In the case of 4-fluoroaniline and 4-aminoacetophenone these reactions with chloroformate **36** were unsuccessful, as evidenced by TLC and ¹H NMR. This is postulated due to the presence of weakly and strongly deactivating functional groups attached to the aniline. Therefore, it was envisaged that the aforementioned functional groups withdraw electron density from the aniline, which deactivates the system through the resonance and inductive effects. The lone pair on the aniline acts to alleviate the lack of electrons in the system, thus preventing the aniline functional group from reacting (Figure 44).

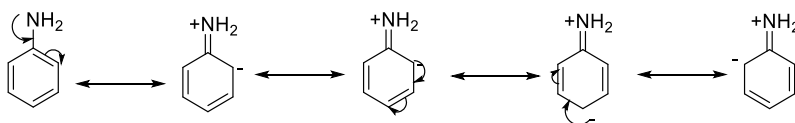
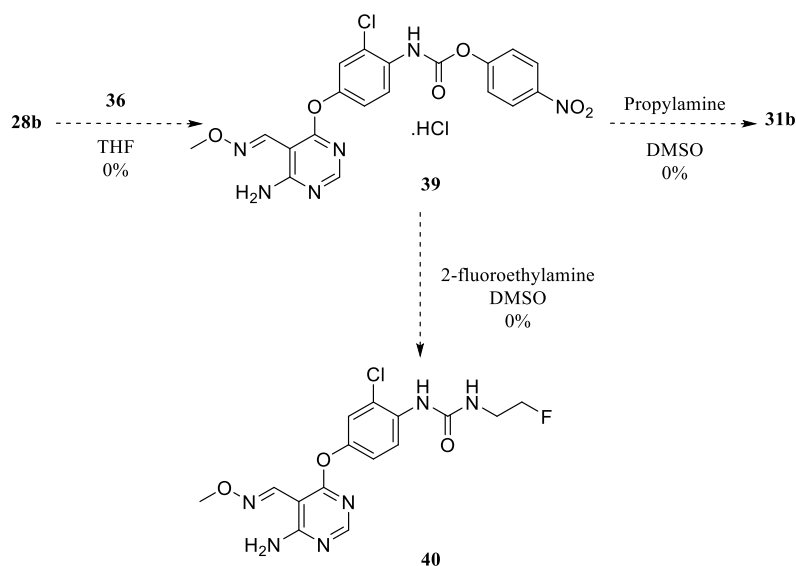


Figure 44: Resonance stabilisation of aniline systems

As 4-nitrophenoxide is an excellent leaving group, the 4-nitrophenyl *N*-propyl carbamate **37a** was reacted in the presence of the aniline **28b** and triethylamine (Scheme 15). Regardless of the excellent leaving ability of the 4-nitrophenoxide, these reactions were not successful even when probed in model systems **37a** and **37b**. This can be attributed to the large bulky nature of the scaffold, nucleophilic attack is hindered by both the large bulky nature of the adjacent chlorine atom, and the deactivating nature of the ether linkage and, again, the chlorine. Both these factors together force the electrons from the aniline to stabilise the ring system, thus deactivating the aniline from successful nucleophilic attack.

Consequently, the synthesis was attempted in reverse (Scheme 16), resulting in a precipitate unable to be dissolved in any appropriate NMR solvent. Despite initially appearing successful, through a change in R_f value on TLC and disappearance of starting material, mass spectrometry analysis concluded the absence of the key mass or any possible breakdown fragments.



Scheme 16: Attempted synthesis of **31b** and **40** using 4-nitrophenyl carbamate analogues

This finding was later confirmed through the attempt of the second step with propylamine in DMSO. ^1H NMR and mass spectrometry analysis both concluded that 4-amino-6-propylaminopyrimidine-5-carbaldehyde *O*-methyl oxime **41** was produced as a by-product (Figure 45). Despite all the conditions described the urea moiety could not be synthesised for the continuation of this project.

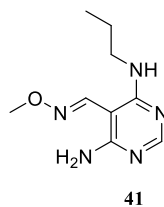


Figure 45: Structure of the product observed by LCMS

2.4.4. Synthesis of fluoroalkylamines

In order to address the need to incorporate a PET radionuclide, it was envisaged this would occur pendant from urea of **21** at the R¹ position, as shown in Figure 46.

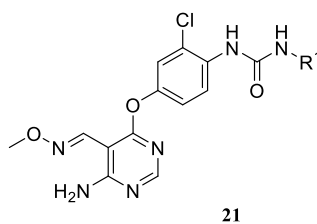
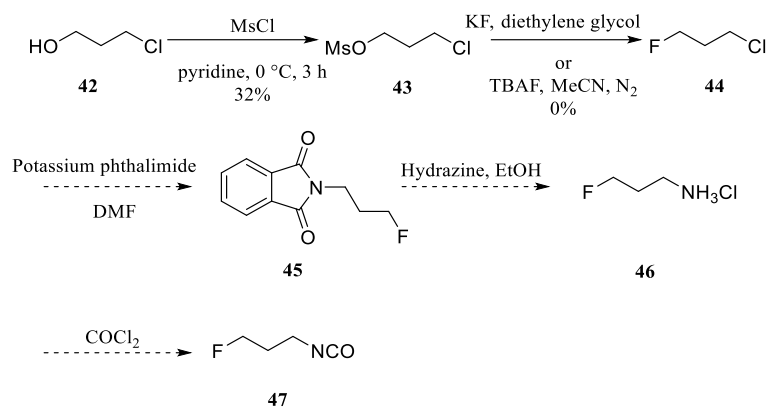


Figure 46: Positioning of PET tag on the urea scaffold

The incorporation of the PET tag would take place in the form of a fluoroalkyl amine, to be synthesised in the manner shown in Scheme 17, or as a fluorobenzyl analogue. Therefore in conjunction with the synthesis of the scaffold, synthesis of a fluorinated isocyanate was attempted.

This reaction began with the reaction of one equivalents of 3-chloropropan-1-ol **42** with one equivalent of methanesulfonyl chloride, resulting in the formation of the mesylate **43**, which is considered an ideal leaving group for the fluoride displacement, after column chromatography purification on a neutral alumina column in high purity and yield (78%).



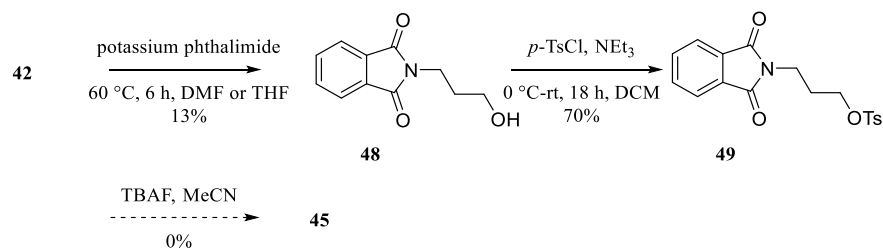
Scheme 17: Proposed synthesis of 3-fluoropropan-1-amine **46**, with the envisaged synthesis of isocyanate **47**

Several attempts were made to displace the mesylate **43** for the fluorine moiety, as summarised Table 9. The attempted fluorination with KF in diethylene glycol, disappointingly, did not result in the distillation of **44**.

Table 9: Summary of attempted conditions for the fluorination of **43**

entry	Fluoride Source	Solvents	Conditions
a	KF	Diethylene glycol	Kugelrohr
b	TBAF	MeCN	90 °C
c	TBAF	MeCN	50 °C
d	TBAF	MeCN	reflux

The fluorination attempts with TBAF were also unsuccessful regardless of the conditions used and excess of the reagents used. These failures lead to the reconsideration of the most practical synthetic methods to synthesise the cold compounds for *in vitro* evaluation. The direct alkylation of potassium phthalimide with **42** was a low yielding reaction in DMF and was unsuccessful in THF, owing to the lower temperatures required for this solvent (Scheme 18). Further fluorination attempts to displace this tosylate group were unsuccessful, therefore a literature search was performed to identify suitable aliphatic fluorination techniques.



Scheme 18: Alternative proposed fluorination method using the Gabriel synthesis

2.4.5. Synthesis of fluoromethyl tosylate 52

There are several examples in the literature highlighting the importance of fluoromethyl tosylate involved in both medicinal chemistry scaffolds and in PET imaging. Introduction of monofluoromethyl groups to drug candidates can offer enhanced biological properties; bioavailability, higher lipophilicity and metabolic stability.²⁷³ These fluoromethyl tosylates could be used in the synthesis of a cold standard for both the urea library discussed in this chapter and the indole library discussed in Chapter Three. Examples of monofluoromethylated drugs are shown in Figure 47. Fluticasone propionate (FP) is a synthetic anti-inflammatory steroid used in the treatment of asthma.²⁷⁴ Choline is an essential nutrient phosphorylated by choline kinases. Its derivative [¹⁸F]-FCH is used as a potential biomarker for cancer diagnosis.²⁷⁵

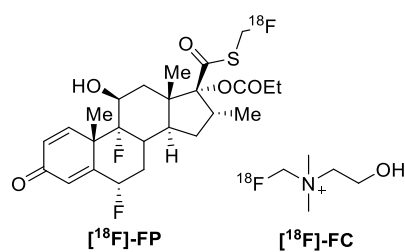
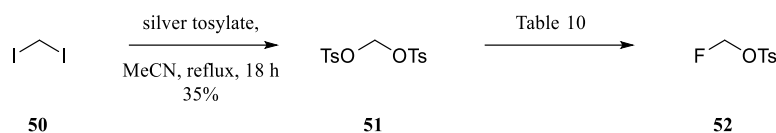


Figure 47: Structures of two common monofluoromethylated drugs ([¹⁸F]-FP and [¹⁸F]-FCH)

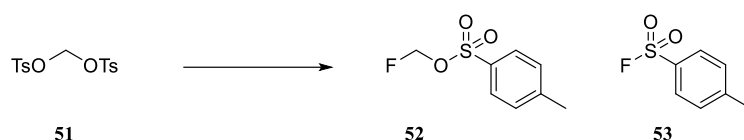
Scheme 19 highlights the synthesis of methylene ditosylate **51**, from diiodomethane in a 35% yield, and subsequent fluorination to synthesise **52**, a suitable prosthetic group.



Scheme 19: Synthesis fluoromethyl tosylate **52**

Literature precedence for aliphatic radiolabelling is typically low yielding, involving a wide variety of fluorinating agents, phase transfer catalysts and catalysts. Table 10 summarises a some of the literature conditions applied to the fluorination of **51** (See Appendix One (7.2.1) for a full list of attempted conditions)

Table 10: Initial attempts for the fluorination of ditosylate **51**



Entry	Solvent	F source/ PTC ^c (eq)	Temp (°C)	Time (h)	Conversion (%) ^b			Methodology Ref [*]
					51	52	53	
a ^c	MeCN	TBAF	110	0.5	100	-	-	This work
b ^c	MeCN	CsF	110	0.5	95	5	-	This work
c	MeCN	KF/K ₂₂₂ (1.4)	reflux	1	85	15	-	275
d	DMF	CsF	120	24	75	5	20	This work
e	DMSO	CsF	120	24	100	-	-	This work
f ^c	THF	TBAF	110	0.5	100	-	-	276
g ^d	<i>t</i> -amyl alcohol	CsF	80	6	-	100	-	277
h ^d	<i>t</i> -BuOH	CsF	80	6	57	43	-	277

^aUnless otherwise stated, all reactions were carried out with 20 mg of **51**, 2 equivalents of the fluoride source in 1 mL of stated solvent. ^bconversion identified by ¹H NMR. ^cmicrowave irradiation. ^d3 equivalents of CsF were used. ^ephase transfer catalyst (PTC) * these yields were determined experimentally using the literature methods

As shown in Table 10, there is a wide variety of fluorination methods available utilising a wide variety of fluoride sources and solvents. In Table 10, entry **g** highlights conditions which provided adequate fluorination of **51** to investigate further. It is well-known that the partial positive charge of polar protic solvents can aid the fluoride ion by increasing its nucleophilicity and by also enhancing the leaving group ability of the tosylate through hydrogen bonding.^{277, 278}

To optimise the identified conditions further, reactions were conducted to investigate the effect of the equivalents of caesium fluoride, length of reaction and microwave conditions. Initial investigations into a time dependence and equivalents of caesium fluoride were conducted. Figure 48 clearly demonstrates using one equivalent of caesium fluoride is not sufficient in adequate radiolabelling, only achieving a maximum 16%. Two equivalents achieves an 87% conversion after six hours, however using five equivalents achieves maximum conversion after one hour (For the full table see Appendix One (7.2.1)).

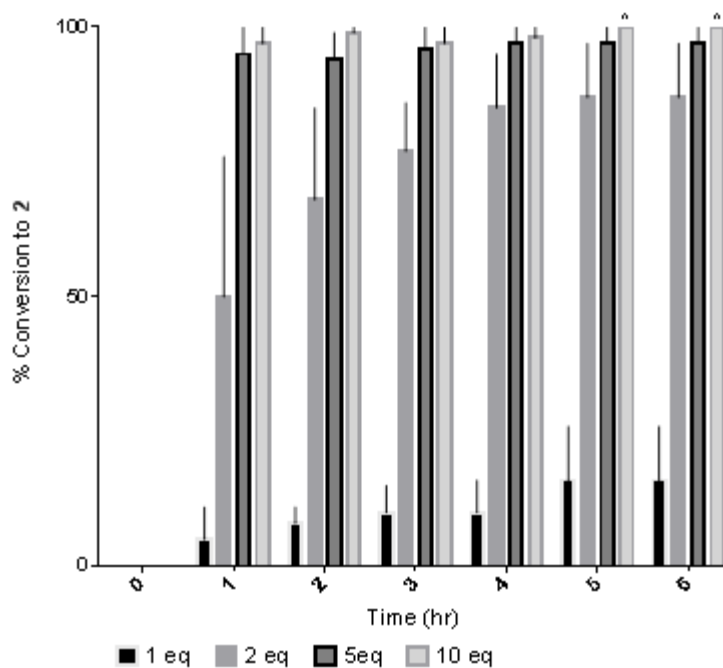
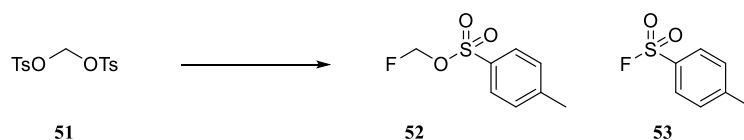


Figure 48: Caesium fluoride equivalent dependant conversion of ditosylate **51** to **52** over six hours using *t*-amyl alcohol (N=3), under conventional heating at 100 °C. Reported as average, with error bars indicating standard deviation. ^ No standard deviation calculated for these bars

Despite one hour being an excellent time for a reaction, the half-life of fluorine-18 is 109 minutes, therefore shortening the reaction further would be highly beneficial.²⁷⁷ Conducting the identified conditions (five equivalents of caesium fluoride in *t*-amyl alcohol) in the microwave significantly shortened the reaction times, which can be easily applied to

radiochemistry (Table 11). However also shown in the below table is the introduction of *p*-tosyl fluoride impurity **53**, which can be tolerated due to the decreased reaction time and should be easily separated from the target complex by semi-preparative radio-HPLC or SPE purification.²⁷⁹

Table 11: Microwave assisted synthesis of **52**^a



Entry	Temp. (°C)	Time (min)	Conversion(%) ^b		
			51	52	53
a	80	30	-	95	5
b	80	15	45	55	-
c	90	15	-	95	5

^a Reactions conducted in 1 mL of *t*-amyl alcohol, using 20 mg of **51** and 5 eq of CsF (n=3) ^b conversion identified by ¹H NMR

With the reaction times now shortened to 15 minutes, attention was focused to isolating **52**. Larger scale reactions (~500 mg of **51**) afforded unexpected problems. A yield of 37%, which is still greatly improved than the literature conditions shown in Table 10. Table 12 summarises work-up conditions attempted to achieve an adequate isolated yield. Entry **h** highlights the conditions identified which gave the highest yield of **52**. It should be noted complete removal of all residual solvent was required as ¹H NMR evaluation was difficult, due to overlapping peaks.

Table 12: Scale up conditions^a A) *t*-amyl alcohol removed under reduced pressure then extracted with stated solvent; B) poured onto water extracted with stated solvent; C) solvent added to microwave vial then sonicated to break up the reaction mixture then filtered and washed with the solvent. The filtrate was concentrated under reduced pressure; D) *t*-amyl alcohol removed under reduced pressure and the solid was triturated with stated solvent and filtrate concentrate under reduced pressure

Entry	Work Up	Solvent	% Yield of 52 ^b	% impurity of 53 ^c
a	A	EtOAc	37	5
b	B	Et ₂ O	36	5
c	C	EtOAc	38	5
d	C	Et ₂ O	88	2
e	C	DCM	40	5
f	D	Et ₂ O	60	5
g	D	DCM	42	5
h	D	Et ₂ O	65	3

^a Reactions conducted in 5 mL of *t*-amyl alcohol, using 100 mg of **51** and 5 eq of CsF. ^b isolated yield ^c determined by ¹⁹F NMR. ^d reaction conducted with 500 mg of **51**, 5 mL of *t*-amyl alcohol and 5 eq of CsF

2.5 Conclusions

Despite initial publications by Huang *et al.* offering a scaffold which favours decreased cLogP values with a monocyclic structure capable of offering a pseudo-bicyclic structures, synthesis of the scaffold following the published procedure could not be achieved. The oxime core was predicted to form the hydrogen bond, as shown through primitive docking studies, and docking in a position which would classify this library as type II inhibitors. This urea focused library would have been interesting to biologically evaluate, owing to their predicted binding interactions being similar to Sunitinib.

Although the reported synthesis from the original published method was not successful, literature searches highlighted other potential methods in order to synthesise this library. Alternative methods include; the Curtius rearrangement, the use of phosgene (to generate *in situ* isocyanates), the use of coupling reagents (**25**) and the use of 4-nitrophenyl chloroformates **36**. These synthetic procedures were attempted, as discussed in this Chapter (2.4.3), but unfortunately did not yield the expected ureas.

Also discussed in this Chapter (2.4.5) is the synthesis of fluoromethyl tosylate **52** in a yield and conversion greater than published literature. All aspects of the reaction were optimised to give ideal conditions: 15 minutes in the microwave using five equivalents of caesium fluoride, followed by complete removal of solvent and trituration with cold ether.

Owing to the inaccessible nature of this library, a literature search was performed to identify a new scaffold, keeping the monocyclic nature of this library. Chapter Three will discuss the design rationale and identification of the new library of compounds.

Chapter Three

Indole focused library

3. Indole focused library

3.1 Indoles in medicinal chemistry

Indoles are typically colourless, crystalline solids which are an important constituent in a variety of natural products.²⁸⁰ These indole containing natural products are alkaloid based, and small-molecule derivatives are known to bind to a range of cancer-associated therapeutic targets. This has led to an explosion of incorporating indoles into small-molecule inhibitors (Figure 49). An example of this is indol-3-carbinol which has potential use in targeting multiple pathways in cancer including; cell cycle regulation, caspase activation, cyclin-dependant kinases activities, oestrogen metabolism and signalling and BRCA gene expression.²⁸¹

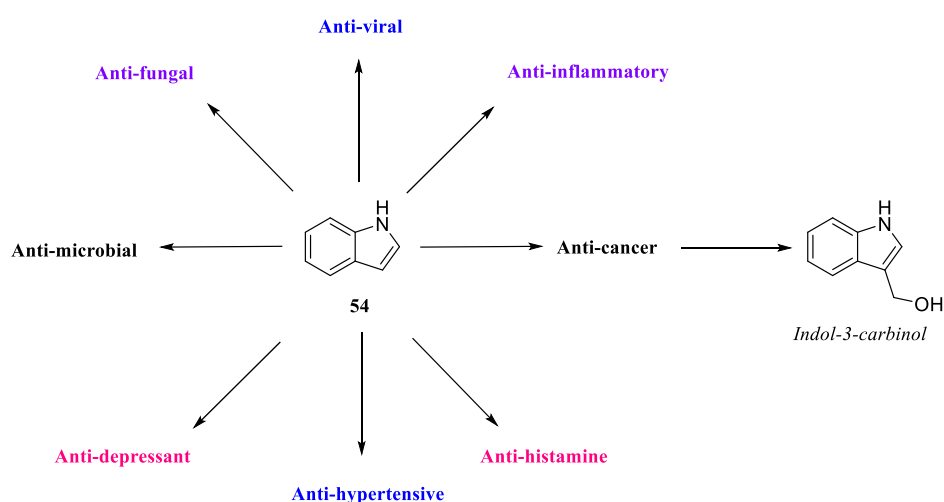


Figure 49: Use of indole core in drug therapies²⁸²

Indoles have several different pharmacological and physiochemical features which makes them ideal for the incorporation into medicinal chemistry scaffolds. These features include:

- pKa of NH is 16.7 – can affect the ability of a drug candidate to cross the cellular membrane
- Enhanced nucleophilic substitutions of benzylic carbons – allows for structure activity relationships (SAR) to be conducted which could allow the identification of a more potent drug candidate
- Less prone to oxidation in the presence of electron withdrawing group (EWG) on the indole core – enhanced metabolic stability

- Very electron rich, therefore easily oxidisable – *in the absence of EWG which allows for the extensive synthesis of analogues*
- Bioisosteric replacement for phenols– *NH moiety can aid in the retention of aromaticity through resonance*

The indole core has also been integrated into synthetic small-molecule compounds which exhibit anti-cancer activity, including VEGFR₂ inhibitors, as discussed in the next section.

3.1.1. Indoles as VEGFR₂ inhibitors

Currently, there are limited examples of small-molecule synthetic indoles incorporated into the core scaffold of VEGFR₂ inhibitors (Figure 50), apart from the closely related indol-2-one core found in Sunitinib. However, there is a large precedence in the literature for the use of indoles as a part of a natural product scaffold, such as alkaloids. Tripathy *et al.* demonstrated the ability of indole **55** to inhibit HUVEC proliferation *in vitro* (IC₅₀ 6 nM).²⁸³ 6''-Debromohamacanthin A **58** is a bis-indole alkaloid from *Spongosorites* sp., a marine sponge, which has anti-tumour, anti-viral, anti-microbial and anti-inflammatory properties.²⁸⁴ Bis-indole alkaloid **58** exhibited modest activity for VEGF stimulated proliferation of HUVEC in a dose dependant manner.²⁸⁴ Again, brucine **56** is a natural plant alkaloid from *Strychnos nux-vomica* L. with similar properties as **10**. Brucine **56** showed modest VEGFR₂ inhibition of 21 μM and was found to inhibit the phosphorylation of VEGFR₂ in a dose dependant manner.²⁸⁵

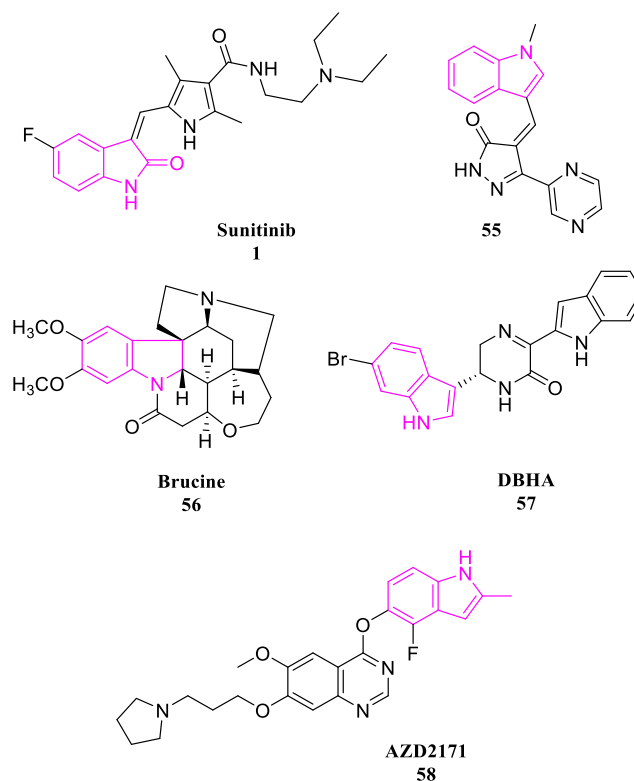


Figure 50: Structure of various indoles (pink) and indol-2-ones²⁸³⁻²⁸⁶

Figure 50 highlights **58** (AZD2171) which contains the indole core initially developed by AstraZeneca and is a sub-nanomolar inhibitor of VEGFR₂ (<1 nM), which exhibits no selectivity over VEGFR₁ or VEGFR₃ (5 nM and < 3 nM respectively).²⁸⁶ However, **58** exhibits little selectivity over closely related kinases (c-kit and PDGFR β) and excellent selectivity over non-related kinases.²⁸⁶ Importantly, **58** is also able to inhibit VEGF_A stimulated phosphorylation of VEGFR₂ in HUVECs, in a dose dependant manner.²⁸⁶ The binding mode of **58** is shown in Figure 49, binding is mediated through the quinazoline and a further interaction is formed between the indole NH and Asp1046, this places the indole within the hydrophobic back pocket. The binding mode for the closely related AG-028262, is similar to **58**, with the interaction from Asp1046 formed from an amide group of the benzothiophene. Consequently, this demonstrates the ability of small-molecules which have incorporated the indole core to target the VEGFR₂ binding pocket demonstrating potential to be developed into a PET imaging probe specific for VEGFR₂.

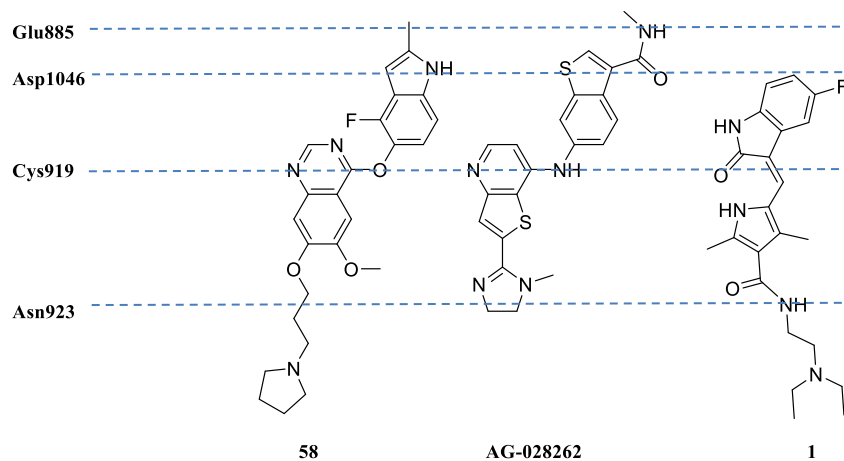


Figure 51: Binding modes of AZD2171 **58**, AG-028262 and **1** with VEGFR₂ (adapted from²⁶⁴)

3.1.2. Indoles as PET imaging agents

There are several examples in the literature of experimental radiotracers, radiolabelled with fluorine-18, containing the indole scaffold (Figure 52). Indole **59** has been developed to image β -amyloid plaques in Alzheimer's disease.²⁸⁷ Serotonin (5-HT) receptors PET imaging with [¹⁸F]-**60** exhibited favourable biological characteristics, whilst being capable of crossing the blood-brain barrier.²⁸⁸ GE-180 has been radiolabelled with fluorine-18 ([¹⁸F]-**61**) and was developed to target translocator protein 18 kDa (TSPO), used in imaging inflammation.^{289, 290} Indole **62** targets COX-2, used as a biomarker for evaluating its expression in a variety of diseases including inflammation and cancer.

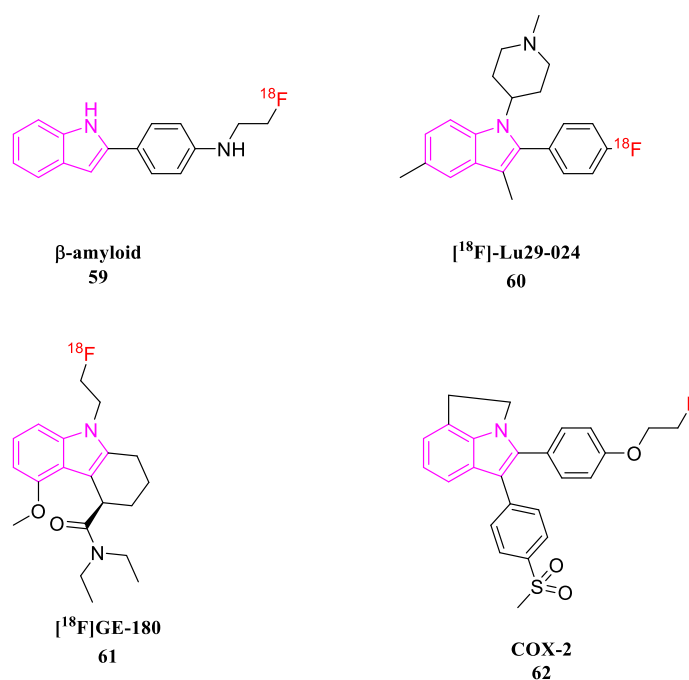


Figure 52: Structures of some experimental PET candidates containing fluorine, the indole fragment is highlighted in pink and the positioning of fluorine-18 in red^{287-289, 291}

The indole containing PET candidates highlighted above, all display favourable characteristics in biological assays. These characteristics include metabolic stability, ease of radiolabelling and favourable biodistribution. More importantly the indole core displayed sufficient stability during radiolabelling.

3.2 Rationale

The indole heterocycle is ubiquitous in nature and has been incorporated into small-molecules that target VEGFR₂, as discussed in the previous section (3.1.1). Further analysis of the patent by Connolly *et al.* (WO2007/109783) revealed the same oxime-pyrimidine core as the library which incorporated the urea moiety (Chapter Two). However the urea was replaced with an indole.²⁹² The new scaffold identifies an indole-pyrimidine ether bridged core, as shown in Figure 53. This lead scaffold **63** offers superior VEGFR₂ enzyme activity and moderate cellular penetration, whilst retaining high affinity for VEGFR₂, compared to the urea library as highlighted by Huang *et al.*^{266, 292}

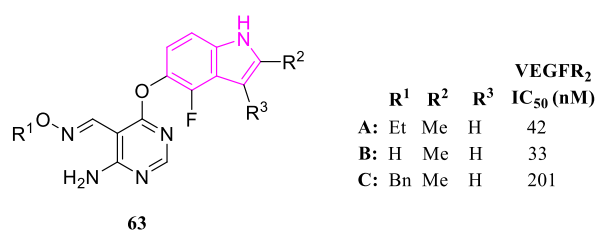


Figure 53: New molecular architecture, with the indole fragment highlighted in pink and the previous pyrimidine highlighted in black, with some VEGFR₂ affinity data from the literature²⁹²

The binding mode of the urea focused library to VEGFR₂ was discussed Chapter Two (2.2.1) and it was expected the binding mode of these two scaffolds would be identical. However docking studies revealed **63** binds in the opposite manner to the scaffold discussed in Chapter Two, as shown in Figure 54, and also opposite to the binding described for the indoles and closely related benzothiophenes (3.1.1). Notably, the pyrimidine forms a hydrogen bond with Glu885 not Cys919 as expected.²⁹³ Therefore this limits the functional groups, pendant from the oxime moiety, to smaller aliphatic groups for fluorine-18 radiolabelling.

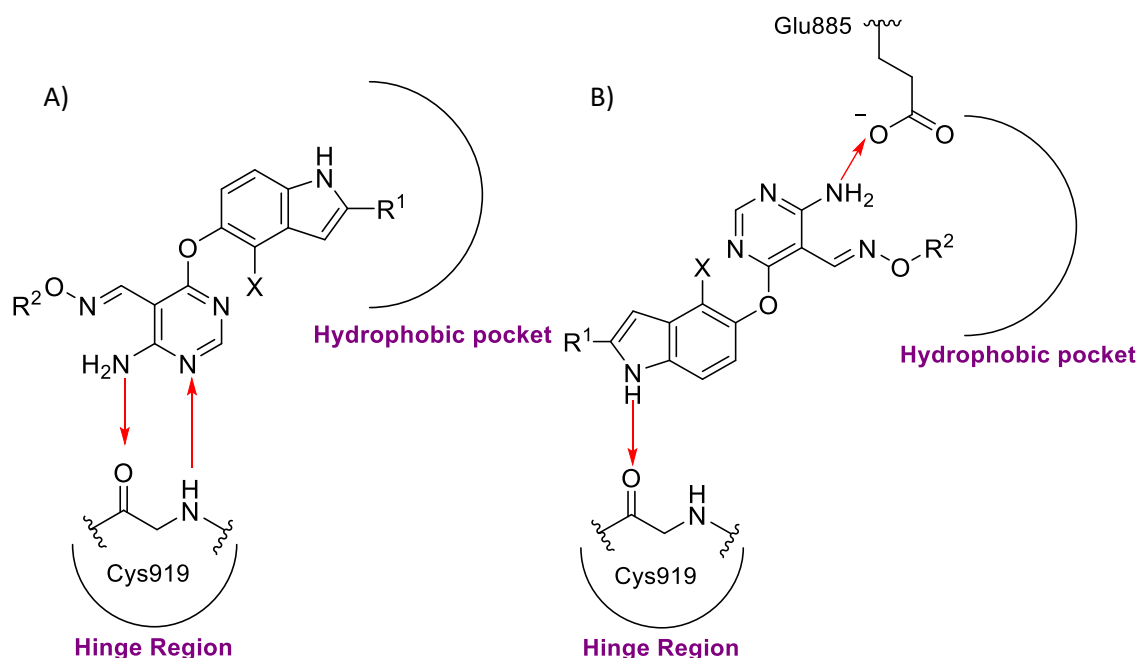
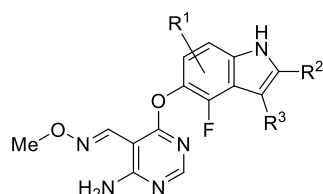


Figure 54: A) expected binding mode, based on the predicted binding mode of the urea focused compounds B) Predicted binding mode provided by *in silico* docking using Schrödinger Gold (2014-2) and visualised on Chemical Computing Group MOE (2013-8802). (PDB: 2OH4)

3.2.1. Design of an indole focused library

Lipophilicity is an important factor when developing a successful candidate for PET imaging, avoiding high non-specific binding, as discussed in Chapter One (1.3.3.4). The optimal cLogP for PET imaging should ideally be around 1-4.¹⁴⁹ In medicinal chemistry there are different strategies deployed to lower the cLogP of a scaffold. An extensive literature search conducted to find strategies in medicinal chemistry to lower cLogP highlights the use of electron withdrawing groups. These strategies include the use of nitrile, nitro and methoxy groups are also used to lower cLogP.^{294, 295} This strategy to lower cLogP was used to identify a compound easily radiolabelled with fluorine-18, whilst retaining the original selectivity for VEGFR₂. The choice of functional group positioned around the indole has a marked effect on lipophilicity, as highlighted by cLogP in Table 13.

Table 13: Impact of the position of the functional group on cLogP¹

R ¹	R ²	R ³	cLog P
H	H	H	3.89 ± 0.74
Me	H	H	4.73 ± 0.76
7-OMe			3.11 ± 1.07
6-OMe			2.54 ± 0.76
7-CF ₃			4.78 ± 1.21
6-CF₃			4.01 ± 1.21
7-CN			3.69 ± 1.08
6-CN			4.43 ± 0.76
	CN		3.45 ± 1.08
	CF ₃		4.88 ± 1.13
	OMe		4.11 ± 1.08
		CN	3.07 ± 1.11
		CF ₃	4.48 ± 1.32
		OMe	3.81 ± 1.08

¹clogP values calculated using ACD Chem Sketch V12.01

As shown in Table 13, the optimal position for the incorporation of the OMe group is at the 6 position and the CN group at either the R₂ or R₃ position and thus the proposed new molecular architecture is shown in Figure 55, also shows the proposed new position of the PET radiolabel on **63**. Although not lowering the lipophilicity, the incorporation of a CF₃ group at the 2nd position of the indole, allows for ¹⁸F incorporation, as identified by Huiban *et al.* and Carroll *et al.*^{242, 296} It is envisaged that the PET tag will be incorporated off the oxime functionality through a simple alkylation, with a prosthetic group.

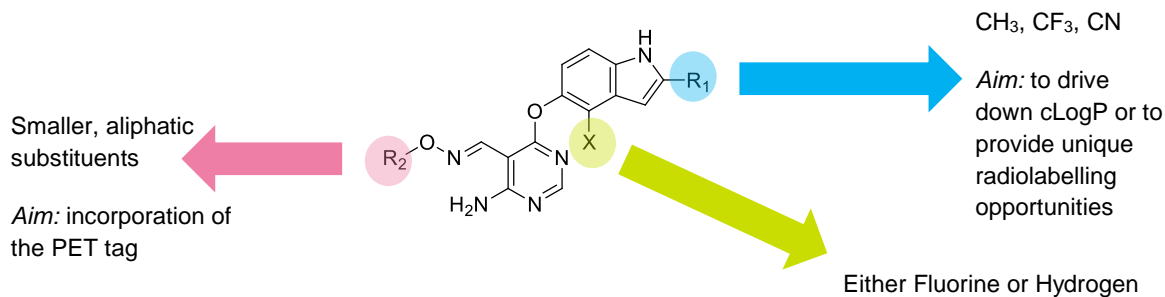


Figure 55: Structure of the molecular architecture showing the positions in which the library can be diversified from the original structure described by Connolly *et al.*²⁹²

3.2.2. Considerations of the indole focused library for developing a successful PET candidate

There are several criteria to be considered when developing this indole scaffold into a successful candidate:

- Selectivity and affinity for the target – As previously described Huang *et al.* have demonstrated the indoles meet this requirement, through achieving a affinity of 42 nM for ethyl substitution at the R₂ position (Figure 51) with a 100 fold selectivity over other kinases
- Ease of radiolabelling – As shown in Figure 55, there are several places in which fluorine-18 can be incorporated into the scaffold. Thus making the radiofluorination the last step, lowering the reaction time increasing the possibility of enhanced radiochemical yields
- Lipophilicity – As previously discussed lipophilicity is important as this can determine the percentage of radiotracer bound in the plasma which can confound PET imaging. The synthesis of different indoles, with different cLogP values, attempting to alleviate any potential problems

All the aforementioned criteria highlight the indole scaffold satisfies the requirements to be developed into a successful PET candidate and is, therefore, the focus of this Chapter.

3.3 Synthesis of Indoles

The useful nature of the indole scaffold has led to many methods being identified for their synthesis. These methods provide a multitude of substitution patterns, ranging from the unsubstituted to the highly substituted. The conventional numbering system and a selection of the most well-known methods are shown below in Figure 56.

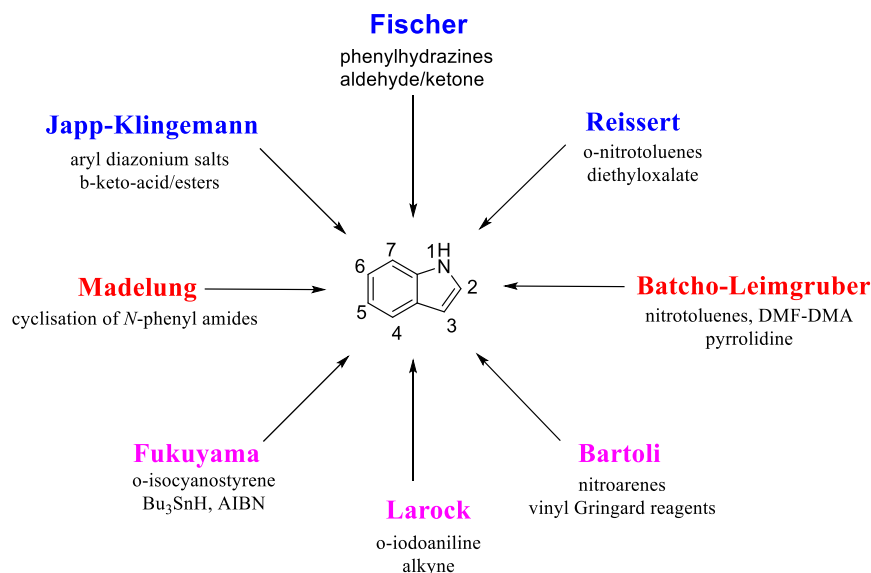


Figure 56: Common methods utilised to synthesise indole **54**, also highlighting the conventional numbering system of indoles.

3.3.1. Fischer indole synthesis

The Fischer indole synthesis can be considered one of the most practiced methods in the preparation of indoles. First identified by Fischer in 1883, this method involves the conversion of arylhydrazones into indoles, in the presence of an acid, typically ZnCl₂.²⁹⁷ The aryl hydrazones are synthesised through the treatment of aryl hydrazines with an aldehyde or a ketone, the mechanism is shown in Figure 57.²⁹⁷

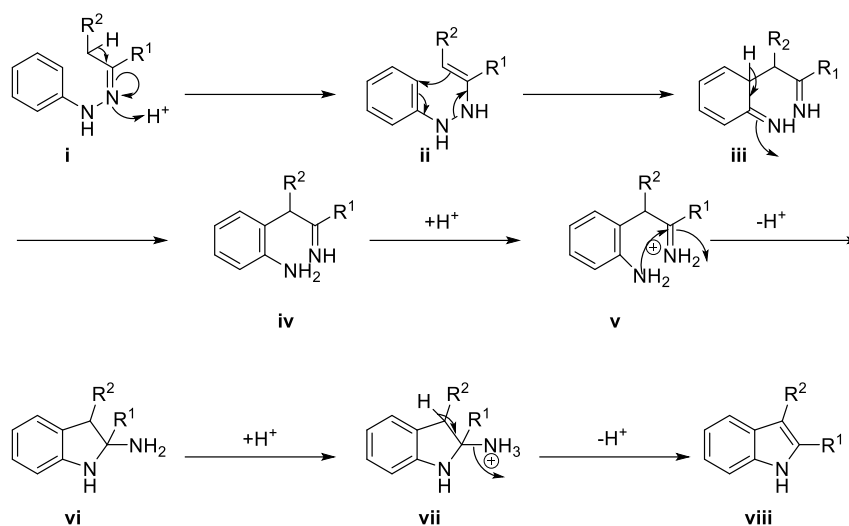


Figure 57: Mechanism of Fischer indole synthesis

The Fischer indole synthesis is initiated through tautomerisation of the hydrazone **i-ii**, which is followed by a [3,3]-sigmatropic rearrangement. The final step in this mechanism is the re-aromatization of the system, with the evolution of ammonia. This indole synthesis can lead to a wide range of derivatives at the 2 and 3 position. The simplistic nature of Fischer indole synthesis often leads to mono-functionalised indoles. Also, relatively few aryl hydrazines are commercially available, due to their general toxicity, thus limiting the scope of the Fischer indole synthesis.²⁹⁸ Due to this there has been an explosion in the methodology for synthesising indoles.

3.4 Results and discussion

3.4.1. Chemistry of the indole series

As discussed in the rationale three different indole scaffolds were planned (3.2.1 – Figure 53). As shown in Figure 58, **65** and **66** do not contain the fluorine at the 4th position of the indole, due the inability to synthesise appropriate precursors, as judged by retrosynthetic analysis. Therefore, **65** contains a radiolabelling opportunity of the 2nd position, whereas in **66** the radiolabelling opportunity will be pendant of the oxime. The synthesis of each of these compounds and their incorporation into the main scaffold, will be discussed in this chapter.

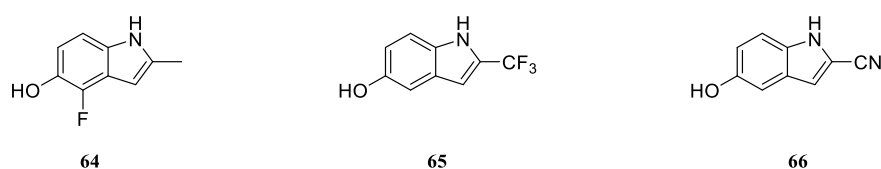
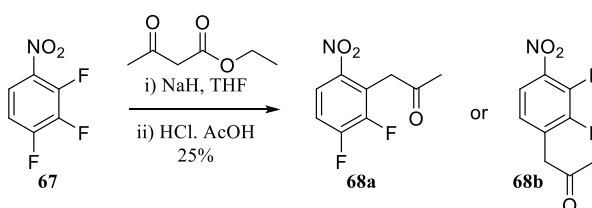


Figure 58: Structures of the indoles required **64-66**

3.4.1.1. Synthesis of 4-fluoro-2-methyl-1H-indol-5-ol **64**

The synthesis of 4-fluoro-2-methyl-1H-indol-5-ol **64** began with the nucleophilic substitution of **67** with ethyl acetoacetate. Tight temperature control (0-5 °C) was required for this reaction, otherwise poor yields were observed from over substitution (Scheme 20). Allowing ethyl acetoacetate to react, in the presence of sodium hydride, at low temperatures allowed the complete, irreversible formation of the enolate required for the nucleophilic substitution of **67**. Subsequent acid deprotection and decarboxylation of the intermediate, revealed **68a** in poor yields, also two regio-isomers, **68a** (ortho) and **68b** (para) to the nitro substituent were generated. This isomer generation can be rationalised through the resonance stabilising nature of the nitro group, which can only be achieved through nucleophilic attack on either the para or ortho fluorine.



Scheme 20: Synthesis of **68a** and **68b**

Generation of the ethyl acetoacetate enolate required stirring at $-10\text{ }^{\circ}\text{C}$ for 25 minutes before the careful addition of **67**. This reaction generated two regio-isomers, as previously discussed, which could be separated by column chromatography and identified through NOESY interactions on NMR, identifying those protons which are close in space. Upon examination of the ^1H NMR there was no preference between sites of attack, with both yielding a 1-to-1 ratio. Figure 59 shows only the para isomer is likely to cause a signal on a NOESY NMR (protons responsible highlighted in red). Whereas for the ortho isomer no interaction should be seen as the corresponding protons are not located closely in space, the protons responsible are highlighted in blue. Despite this being an interesting finding the para isomer could not be taken forward for further chemical transformations due to the inability to synthesise the required indole **64**.

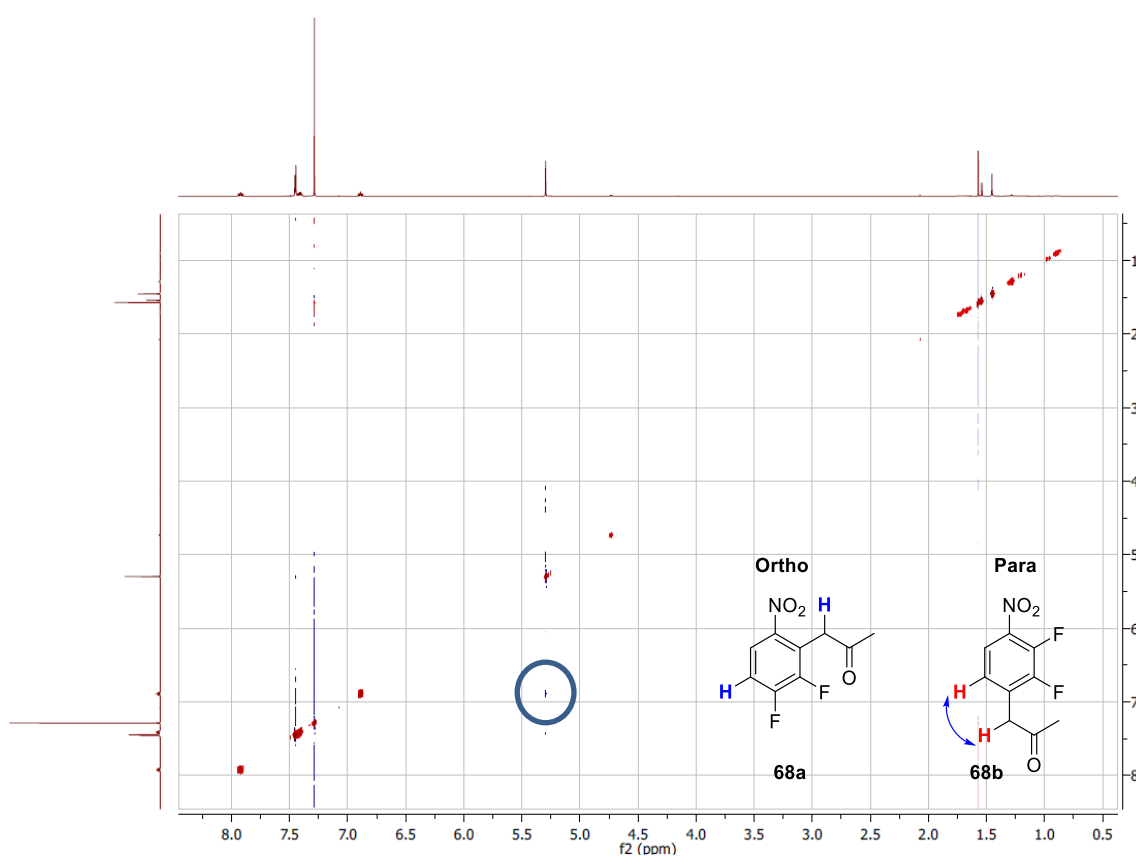
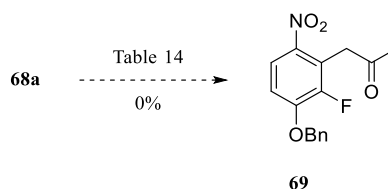


Figure 59: Identification of the protons likely to cause a signal on NOESY NMR evaluation of the isomers of **68b**, a signal is seen in the area circled

Literature conditions for the introduction of the hydroxyl at the para-nitro position were not successful (Scheme 21). The literature precedence involving the use of benzyl alcohol and

lithium hydroxide was unsuccessful, with the synthesis of unidentifiable compounds, producing a gum-like material. LCMS did not elucidate the products from this reaction further, as these nitro compounds did not ionise under ESI conditions. Comparison of the UV trace obtained revealed the complete disappearance of starting material. It can be postulated that some form of attack took place on the ketone.



Scheme 21: Attempted introduction of the benzyl moiety to **69**

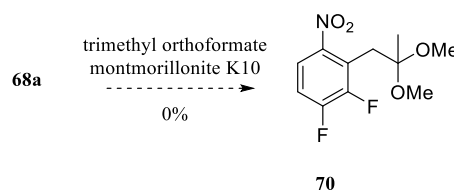
Further literature analysis revealed the benzyl group might be introduced through irreversible benzyl alkoxide formation with sodium hydride. However this method was not successful, presumably the benzyl alkoxide reacted at the ketone position undergoing a nucleophilic addition reaction. Further attempts to attach the benzyloxy group are shown in Table 14.

Table 14: Attempts at the introduction of the benzyloxy moiety to **69**

Entry	Base	Solvent	Outcome
a	LiOH	neat	unknown product
b	NaH	DMF	probable attack on the ketone moiety - ¹ H NMR highlighted several products
c	NaH	DMA	as above
d	K ₂ CO ₃	DMF	no reaction

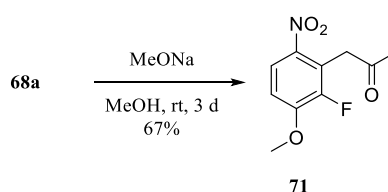
Alternative strategies were explored to introduce the benzyloxy moiety of **69** and a literature precedence for the protection of the ketone was revealed. This ketone protection strategy avoids any attack on the ketone moiety (Scheme 22). Attempted protection with trimethyl orthoformate in the presence of Montmorillonite K10 (a catalytic clay) under anhydrous

conditions did not yield **70**, even after several days, TLC analysis revealed starting material only. Disappointingly *p*-toluenesulfonic acid catalysed protection of the ketone was also unsuccessful.



Scheme 22: Attempts at protecting the ketone functionality

Examination of indole **64** revealed the need for an unprotected hydroxyl, consequently other protecting groups which introduced the hydroxyl into the scaffold were sought. A clear literature precedence highlighted the use of sodium and methanol, to generate fresh sodium methoxide. However, using commercially available sodium methoxide the methoxy group was successfully introduced to **71**, without the need to use the moisture and air sensitive sodium metal (Scheme 23). Despite the modest yields, the reaction occurred over an extended 72 hour period, which could be followed by NMR analysis of the reaction mixture. Pleasingly, **68a** could be recovered and recycled back into the reaction.



Scheme 23: Attachment of the methoxy group to form **71**

The introduction of the methoxy moiety could be monitored by ^1H NMR, by monitoring the change in the shifts of protons in **68a**. As shown in Figure 60, the pure ^1H NMR for **71** is at the bottom of the stacked image, the reaction appears to proceed slowly at 18 hours. The reaction seems to slow between 48 and 70 hours. After 70 hours the reaction was deemed finished as the ratios of **68a** to **71** remained unchanged. Also shown in Figure 58 are the intermediates generated during the course of the reaction, these were not isolated and not present in the crude NMR after work up, also shown in Figure 58.

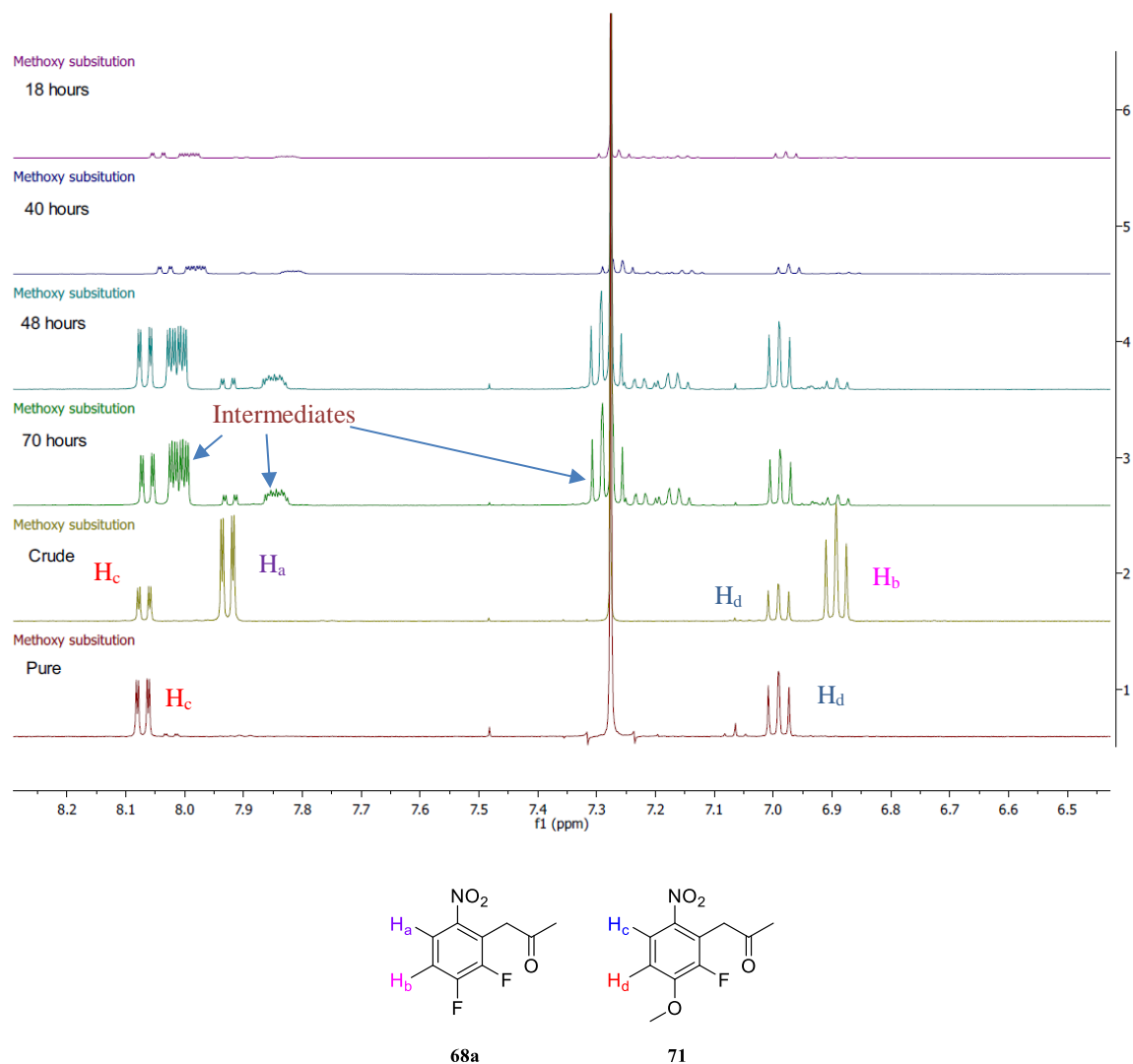
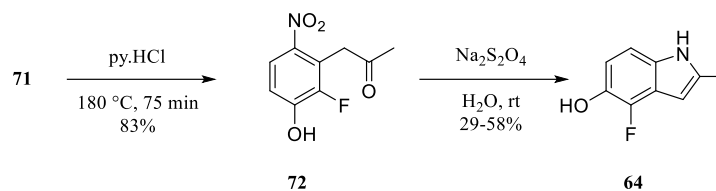


Figure 60: The transformation of **68a** into **71** over a 72 hour time period; Pure ^1H NMR of **71** (bottom) indicates a pure sample after column chromatography. The aromatic region (6.5ppm – 8.2 ppm) is represented as these highlight the marked differences in the aromatic regions and the transformations can be followed

The remaining steps in the synthesis of 4-fluoro-2-methyl-1*H*-indol-5-ol **64** are shown in Scheme 24. The removal of the methyl group, to reveal the hydroxyl, proceeded smoothly under neat conditions using four equivalents of pyridine hydrochloride, giving **72** in a 50% yield. Unfortunately **71** could not be recovered and unwanted, unidentifiable by-products were observed due to the harsh conditions required.



Scheme 24: Remaining steps towards the synthesis of 2-methyl-1*H*-indol-5-ol **64**

The reduction of **72** using sodium dithionite afforded the cyclised product **64** and monitoring by LCMS indicated this reductive cyclisation was typically complete in 90 minutes. None of the aniline was observed indicating once the aniline is formed a reductive cyclisation occurs. The yield was relatively disappointing (29-58%) for a simple intramolecular cyclisation, with the starting material **72** unrecoverable.

The mechanism for the reductive cyclisation is shown below in Figure 61. The cyclisation occurs immediately, with aniline **i** not observable by LCMS. The mechanism is similar to the Riessert indole synthesis, which also comprises of a reductive cyclisation and is capable of synthesising highly diverse indoles.²⁹⁹

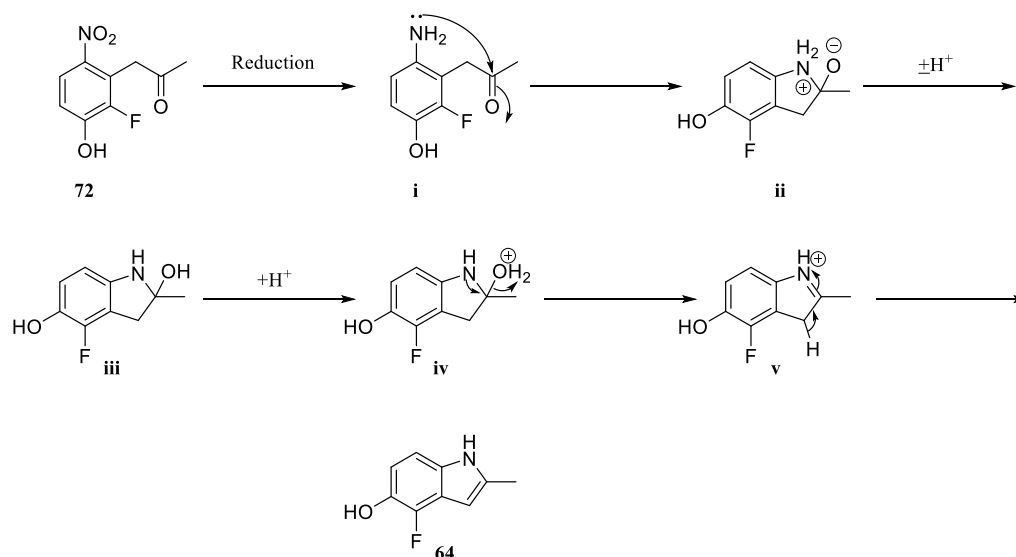
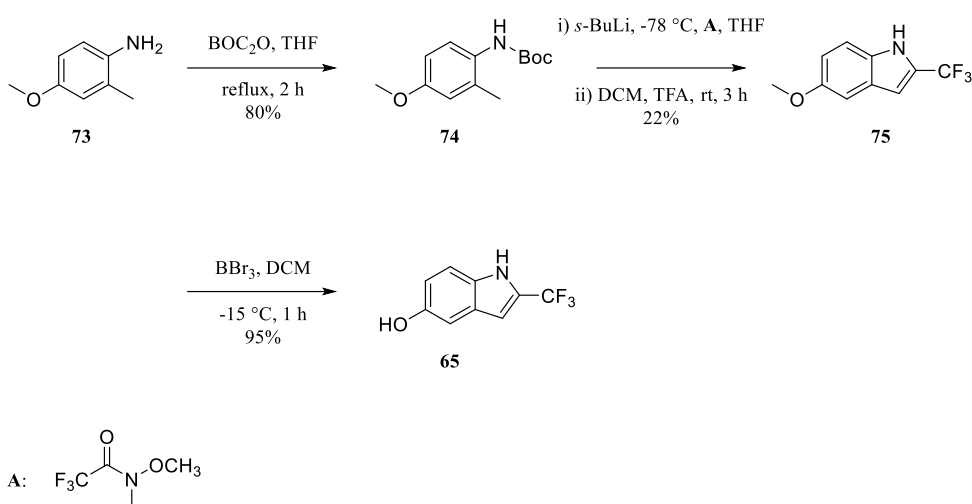


Figure 61: Mechanism for the conversion of **72** to **64**

3.4.1.2. Synthesis of 2-trifluoromethyl-1*H*-indol-5-ol **65**

The synthesis of 2-trifluoromethyl-1*H*-indol-5-ol **65** began with the BOC protection of aniline **73**, allowed the single deprotonation of the aniline whilst directing the deprotonation to occur at the methyl group. Column chromatography purification of **74** was unachievable, therefore recrystallisation from hexane was utilised, as per the literature. Pre-stirring **74** with *sec*-BuLi allowed full deprotonation of the methyl group. Addition of Weinreb amide **A** resulted in the BOC protected indole, TFA deprotection afforded **75** in a 22% yield over the two steps, after column chromatography purification (Scheme 25). Deprotection of **75** using BBr₃ to reveal indole **65** proceeded in a 95% yield, after column chromatography.



Scheme 25: Full synthesis of target indole **65**

Although the mechanism to form **75** is similar to the Smith modified Madelung synthesis, the mechanism does not involve a heteroatom Peterson olefination step. However the cyclisation step still involves a 5-*exo-trig* ring closure (Figure 62). The first step is the deprotonation of the methylene group of **74** using *s*-BuLi. The Weinreb amide **A** undergoes nucleophilic attack from the deprotonated methylene group, resulting in the expulsion of *N*, *O*-dimethylhydroxylamine. Nucleophilic attack on the ketone occurs from the BOC protected amine forming **65**, after TFA mediated BOC deprotection. BOC deprotection did not occur during the synthesis of the indole, as evidenced by a crude ¹H NMR and LCMS, but through deprotection using TFA.

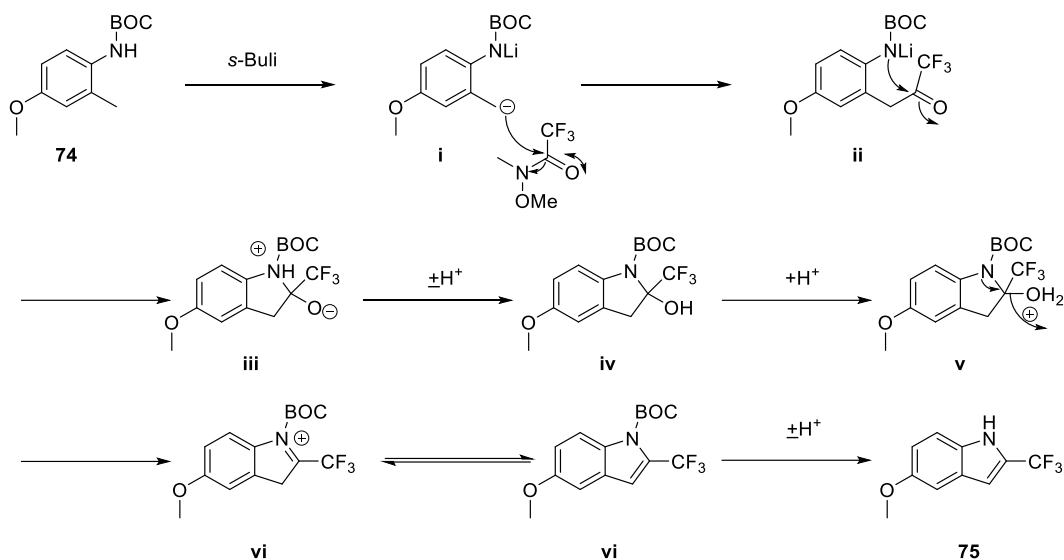
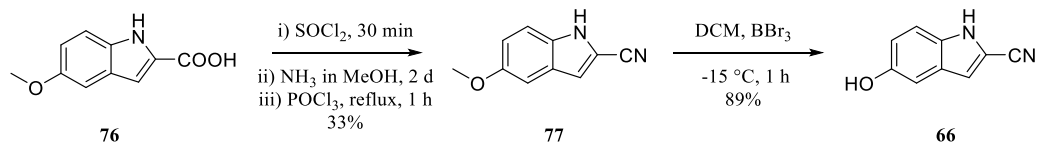


Figure 62: Mechanism for the conversion of **74** to **75**

3.4.1.3. Synthesis of 5-hydroxy-1*H*-indole-2-carbonitrile **66**

The synthesis of indole **66** began with the conversion of the indole-2-carboxylic acid **76** to the corresponding acid chloride. Once synthesis of indole-2-acyl chloride was complete, evidenced by TLC, the reactants were removed under reduced pressure. The amide was afforded using 7*N* ammonia, in MeOH (Scheme 26).



Scheme 26: Synthesis target indole **66**

Subsequent dehydration using neat, refluxing POCl₃ afforded the nitrile **77** in 33% yield (over the three steps) after column chromatography purification. A plausible mechanism for the dehydration is shown below by Figure 63.

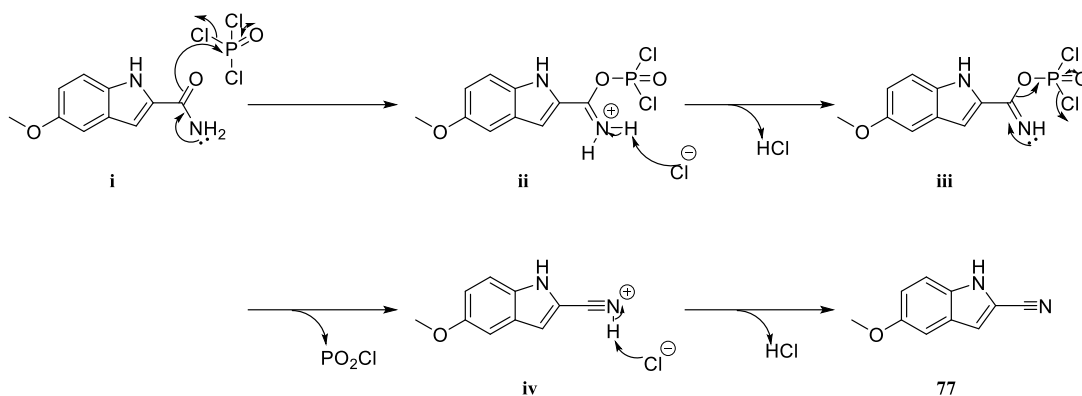
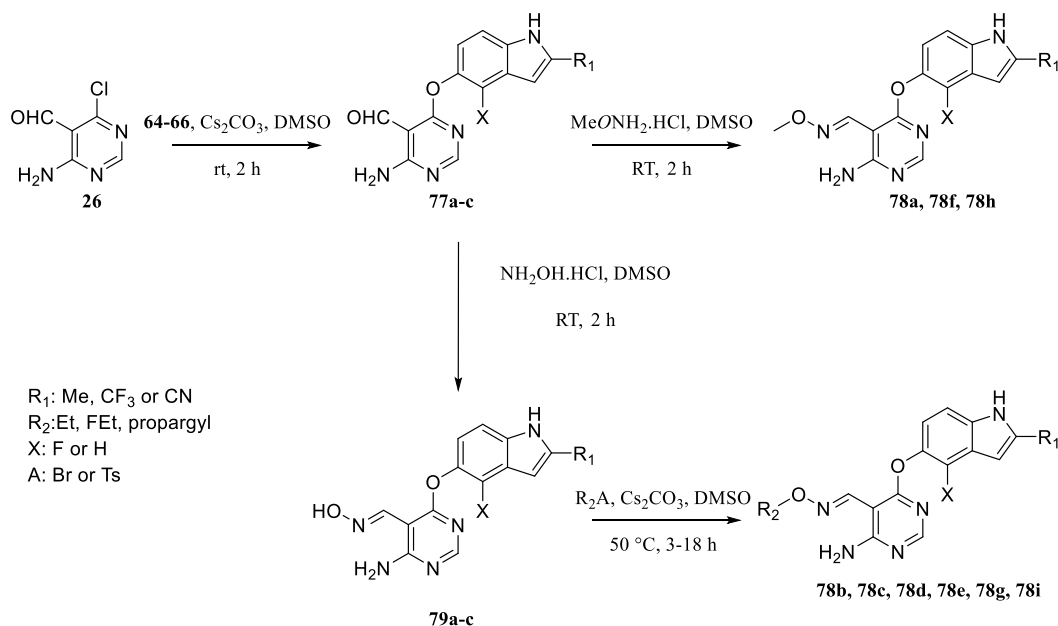


Figure 63: POCl₃ mediated dehydration of 5-methoxy-1*H*-indole-2-carboxamide to **77**

The final step in the synthesis of indole **66** was the deprotection of **77** using BBr₃ in DCM, affording **66** in an 86% yield after column chromatography purification, as shown in Scheme 26.

3.4.1.4. Synthesis of the indole core scaffold

A convergent approach was utilised for the synthesis of the final compounds of the indole focused library. The synthesis is shown in Scheme 27 and began with the nucleophilic substitution of **26** with the indoles **64-66**.



Scheme 27: Synthesis of the final compounds **78a-i**

After the alkylation of the indoles with the core scaffold, the synthetic pathway diverged. For the commercially available *O*-alkylated oximes the final products were formed directly (**78a**, **78f** and **78h**). The mechanism is shown in Figure 64 below and is a simple condensation between the *O*-hydroxylamine hydrochloride and the aldehyde.

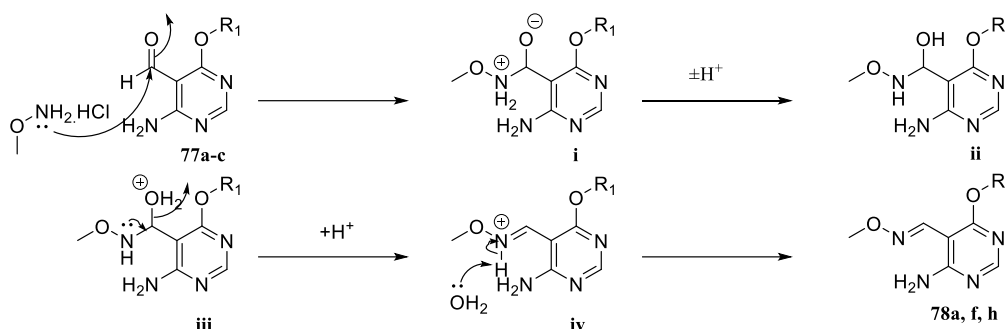
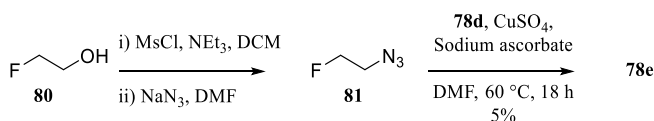


Figure 64: Mechanism for the condensation of the carbaldehyde and *O*-methylhydroxylamine hydrochloride

For the compounds where the corresponding hydroxylamines were not easily available, or for the easy incorporation of a fluorine-18 motif, the condensation of hydroxylamine was utilised. Alkylation of the hydroxylamine (**79a-c**) with the various alkyl groups proceeded in 3-18 hours to yield **78b**, **c**, **d**, **g**, **i**.



Scheme 28: Click synthesis of **78e** from alkyne **78d**

Although not the result of a direct alkylation of **79a**, **78e** was synthesised via a copper-catalysed azide-alkyne cycloaddition (CuAAC) of **78d** with **81**, as shown in Scheme 28. Although the formation of **78e** proceeded overnight, this was a very poor yielding reaction (3%). A plausible rationale for this is the co-ordination the copper in the pyrimidine complex. Copper is important for this reaction due to its catalytic nature, as shown in Figure 65. Presence of the copper made purification of **78e** difficult, thus decreasing the yield of the reaction.

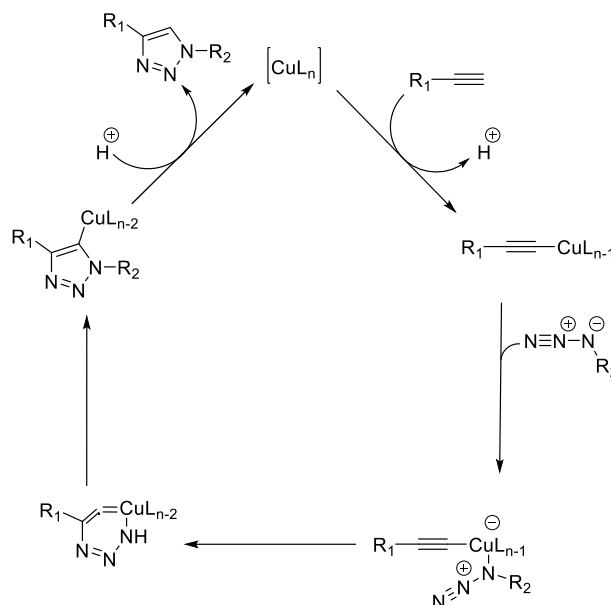
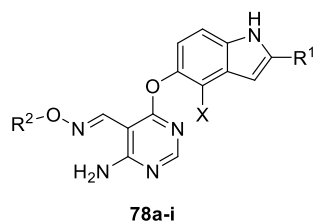


Figure 65: Catalytic cycle of Copper catalysed Azide Alkyne Cycloaddition

A total of nine compounds were synthesised for initial biological evaluation, as shown in Table 15.

Table 15: Structures of the final compounds synthesised for this indole focused library (**78a-i**)



Compound	X	R ¹	R ²	Yield (%)
78a	F	CH ₃	CH ₃	98
78b	F	CH ₃	CH ₂ CH ₃	77
78c	F	CH ₃	CH ₂ CH ₂ F	39
78d	F	CH ₃	CH ₂ CCH	30
78e	F	CH ₃		3
78f	H	CF ₃	CH ₃	98
78g	H	CF ₃	CH ₂ CH ₂ F	23
78h	H	CN	CH ₃	62
78i	H	C N	CH ₂ CH ₂ F	18

3.4.2. *Biology of the indole series*

As discussed previously in Chapter One (1.3.3.3), selectivity is a major requirement when developing a novel PET candidate. A selectivity assay was developed using VEGFR2 non-expressing cell lines HCT116 (human colorectal carcinoma cell line), A549 (human lung adenocarcinoma cell line), treated with high concentrations of probe.³⁰⁰⁻³⁰⁵ If the library is specific, they will not affect cell lines which do not express VEGFR₂. However if they are unspecific they are likely to target more than one kinase or signalling pathway. It is known that VEGFR₂ inhibitors do affect proliferation at higher concentrations only, therefore if effects on proliferation are observed at lower concentrations this can be attributed to off-target effects. Consequently, assessing cell lines for their VEGFR₂ expression is important before examining the libraries effects on proliferation. As Figure 66 shows whilst HUVECs demonstrated strong VEGFR₂ expression as expected, both the HCT116 and A549 did not. It is known that VEGFR₂ expression can be upregulated under hypoxic conditions, therefore this variable was also investigated.³⁰⁶ Although bands were detected with the harsh lysis buffers, this could not be characterised as VEGFR₂ but non-specific binding of the antibody. This also confirmed that VEGFR₂ is not expressed in either the HCT116 or A549 cell lines, which is consistent with the data Smith *et al.* report for VEGFR₂ expression in cell lines.⁵⁶

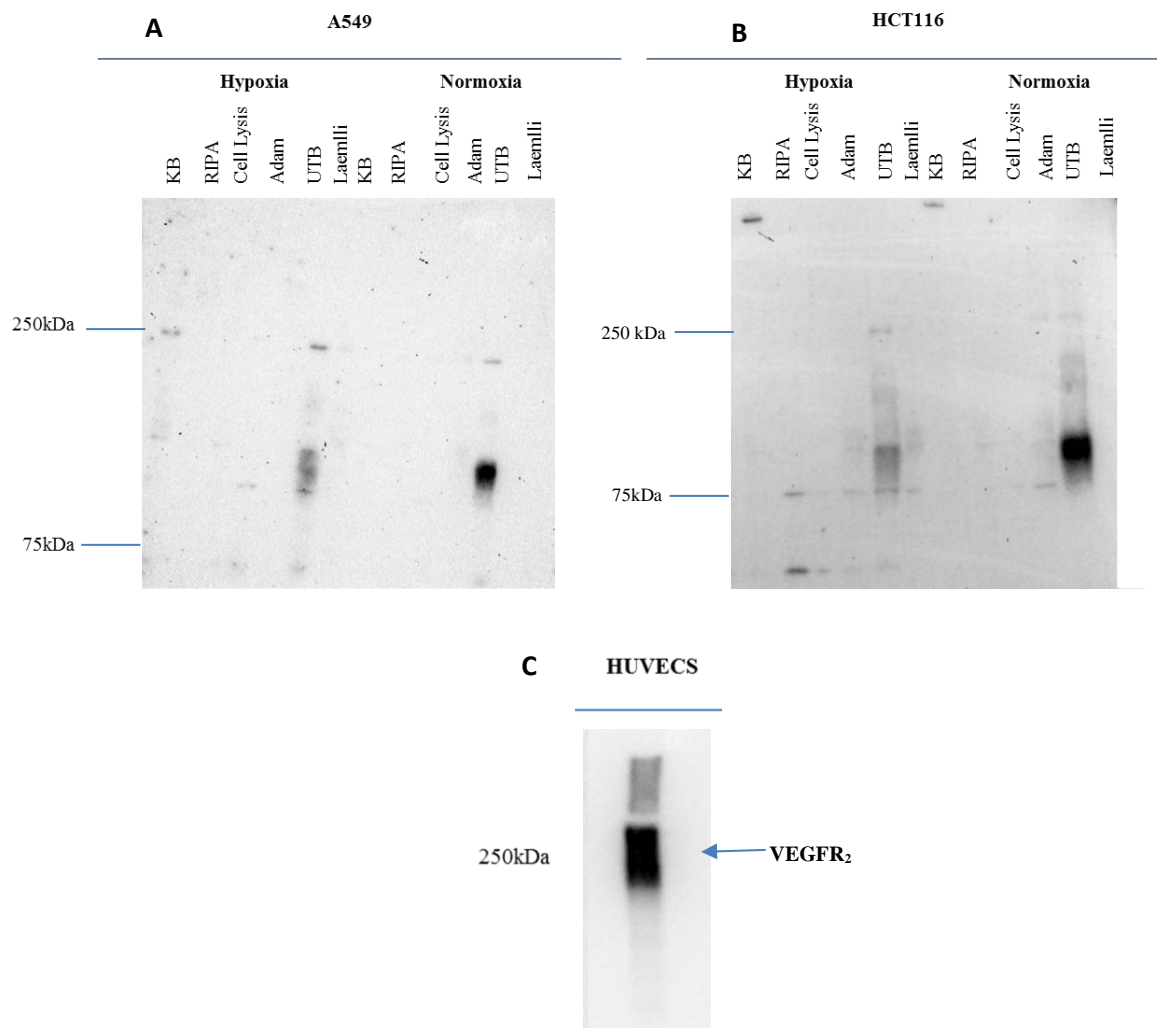


Figure 66: Effects of different lysis buffers on VEGFR₂ pull-down in either normoxic or hypoxic conditions. A) A549 B) HCT116 C) HUVEC. Cells were harvested by scraping and lysed in the different buffers. 50 μ g of lysate was loaded onto the 6% acrylamide gel and separated by SDS-PAGE.

3.4.2.1. Cellular proliferation assay

Establishing the non-VEGFR₂ expression status of the A549 and HCT116 cell lines allows for the initial assessment of non-specific effects. As discussed previously (3.4.2) there should be no effect on proliferation at lower doses, as there is no VEGFR₂ expression. Therefore, to assess this an MTS assay was selected to examine this. The MTS assay works on the basis of reducing the tetrazolium salt **84** to the formazan. However the tetrazolium salt is not able to penetrate the cellular membrane. To overcome this, MTS is used in combination with electron acceptor agents which are cell penetrable. The electron acceptor agent used is phenazine ethyl sulfate (PES – **82**). The electron acceptor **82** is reduced in the mitochondria to **83**, crosses the cell membrane back into the culture medium where tetrazolium **84** is converted into the formazan **85** (Figure 67).³⁰⁷ Data obtained from this assay can be used to

determine half maximal inhibitory (IC_{50}) data, the concentration required to cause 50% inhibition *in vitro*.

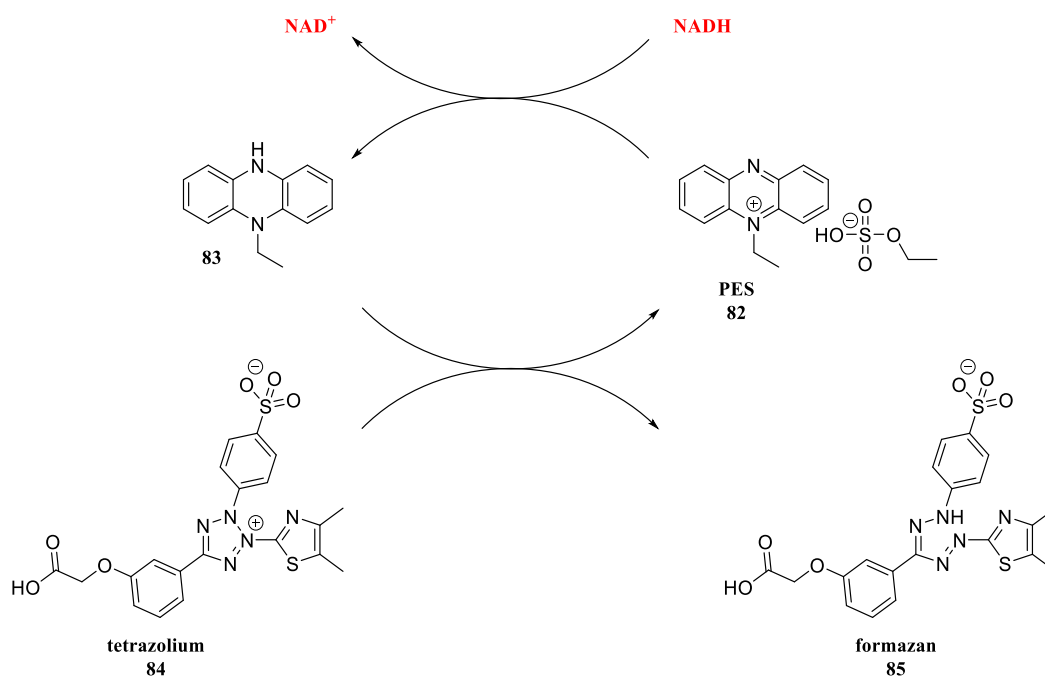
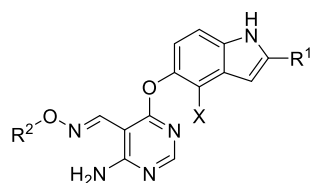


Figure 67: Reduction of tetrazolium salt **84** to the formazan product **85** by the mitochondria - the main principle of an MTS assay

As this cellular proliferation assay is based around the metabolic activity of the mitochondria, any effects observed in cell lines that lack $VEGFR_2$ expression can be attributed to off-target/non-selective interactions. $VEGFR_2$ inhibition has a direct impact in proliferation, via various downstream pathways.

Table 16: IC₅₀ data for the indole library (DMSO final concentration 0.0002%)

Compound	X	R ¹	R ²	IC ₅₀ (μM)	
				HCT116	A549
78a	F	CH ₃	CH ₃	0.452	0.416
78b*	F	CH ₃	CH ₂ CH ₃	0.093	0.021
78c	F	CH ₃	CH ₂ CH ₂ F	0.066	0.048
78d*	F	CH ₃	CH ₂ CCH	0.073	0.139
78e	F	CH ₃		>2	>2
78f	H	CF ₃	CH ₃	>2	0.122
78g	H	CF ₃	CH ₂ CH ₂ F	0.833	>2
78h	H	CN	CH ₃	>2	>2
78i	H	CN	CH ₂ CH ₂ F	0.289	>2

*Synthesised from the Connolly *et al.* patent²⁹² the remaining compounds are novel. IC₅₀ graphs are located in Appendix Two 7.2.2

Table 16 highlights the IC₅₀ data obtained from this assay. **78c** appears to have the greatest effect on both HCT116 and A549 cell lines (66 nM and 48 nM respectively). The data obtained for **78b** and **78d**, synthesised to allow direct comparison with the literature, show slightly higher potencies than those published by Huang *et al.* for the HCT116 cell line (93 nM and 73 nM versus 36 nM and 28 nM respectively), although no studies were performed to highlight any potential off-target effects.²⁶⁶ However this could be due to the different proliferation assay utilised. Despite **78e** and **78h** not exhibiting the same toxicities at low concentrations as the other seven compounds, these were not taken forward for further in-depth biological characterisation. The yield for the CuAAC for synthesis of **78e** was not high yielding and difficult purification did not allow for further in-depth biological validation. Whereas **78h** does not contain a fluorine which could be radiolabelled for PET imaging. Although published VEGFR₂ inhibitors affect proliferation, the effect on proliferation is only observed at much higher concentrations (Figure 68). Xia *et al.* obtained efficacy data for HCT116 against YLT192 **86**, in which a potency of 7.4 μM was observed.³⁰⁰ This effect on proliferation of a non-VEGFR₂ expressing cell line is much higher and more in line with an inhibitor which is specific for VEGFR₂. Solubility of this library was poor and led to a great variation in results. However it can be discerned, despite the poor solubility, this library was very toxic at very low concentrations. During treatment with the indole library, a ‘cell

death' like phenotype consisting of rounding and cellular detachment from the plate. Nuclear staining was then carried out for further characterisation.

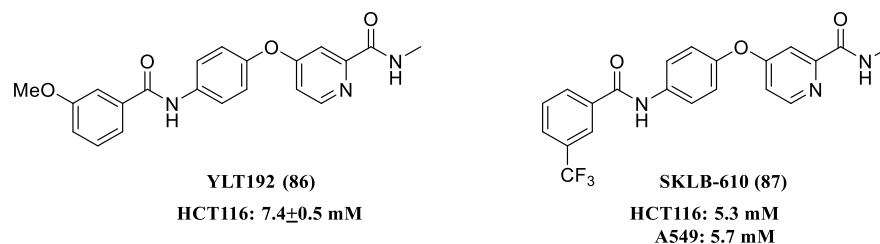


Figure 68: IC₅₀ data for two developed VEGFR₂ inhibitors

3.4.2.2. Evidence of non-specific toxicities

Nuclear staining

Nuclear staining techniques, such as DAPI (4'-5-diaminophenylindole), can be used to visualise structures within a cell. DAPI forms complexes with DNA, through interactions with the minor groove of adenine-thymine rich regions.³⁰⁸ Visualisation of DNA is extremely important to assess whether the cells are undergoing an apoptosis-like death, in light of the cellular proliferation assay data. Cells die by apoptosis (also known as programmed cell death) or by necrosis, both of which can be visualised by DAPI staining. Apoptosis is characterised by pyknosis, chromatin condensation followed by plasma membrane blebbing and karyorrhexis, with pyknosis the most characteristic feature of apoptosis.³⁰⁹ Figure 69 highlights data obtained from the nuclear staining, demonstrating pyknosis is not present but multinucleation can be observed. This could be indicative of mitotic catastrophe, although would require definite data to prove this which is beyond the scope of this project. As observed by the figure below, there is a decrease in cell number for both cell lines and some cells appear out of focus due to rounding.

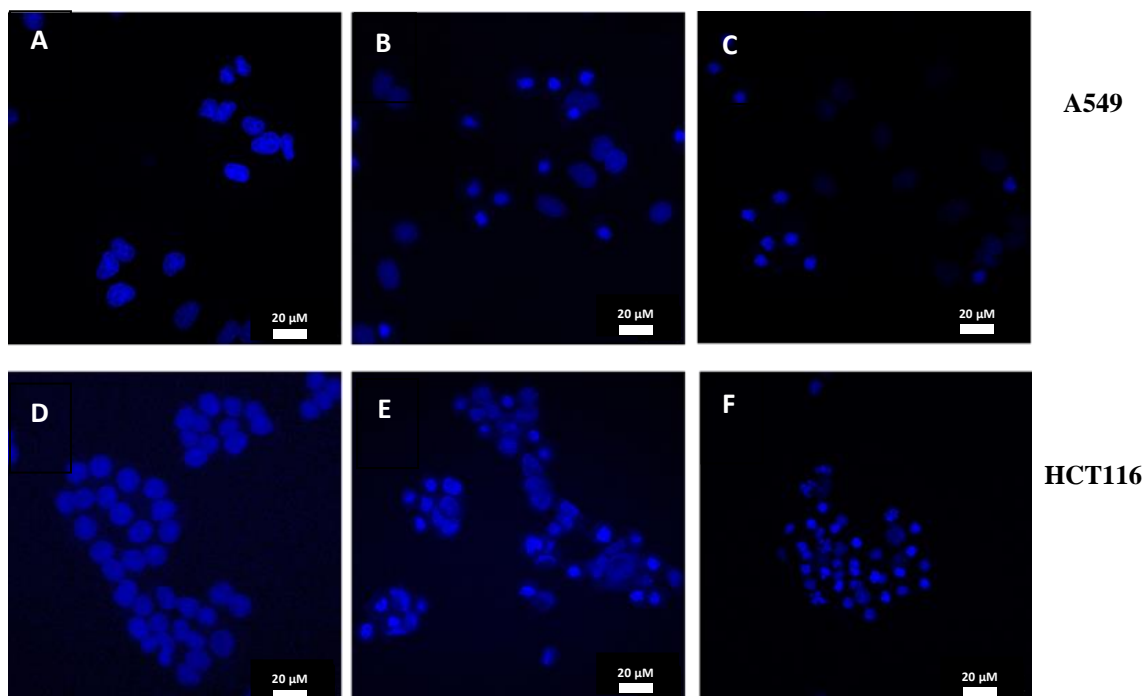


Figure 69: DAPI staining of A549 (A-C) and HCT116 (D-F). Cells were treated for 16 hours, on coverslips, before being fixed for staining. DMSO concentration 0.2%. A and D) Vehicle (DMSO) treated B and E) Treatment with **78a** at 452 nM C and F) Treatment with **78c** at 66 nM. Blue channel only

Effects observed on β -tubulin levels

The assays utilised thus far indicate that this library exhibits off-target toxic effects at low concentrations. Nuclear staining assays indicating the cell lines were not undergoing apoptotic cell death, but exhibit a mitotic arrest-type phenotypic. This was further supported by an apparent dose dependant decrease in β -tubulin levels, presented below in Figure 70. The dose was selected around the IC_{50} calculated from the cellular proliferation assay described previously. Importantly, levels of GAPDH are not affected by treatment with **78a** or **78c** in any of the cell lines tested. This could indicate a specific effect on β -tubulin, although more extensive investigations are required to conclusively prove this.

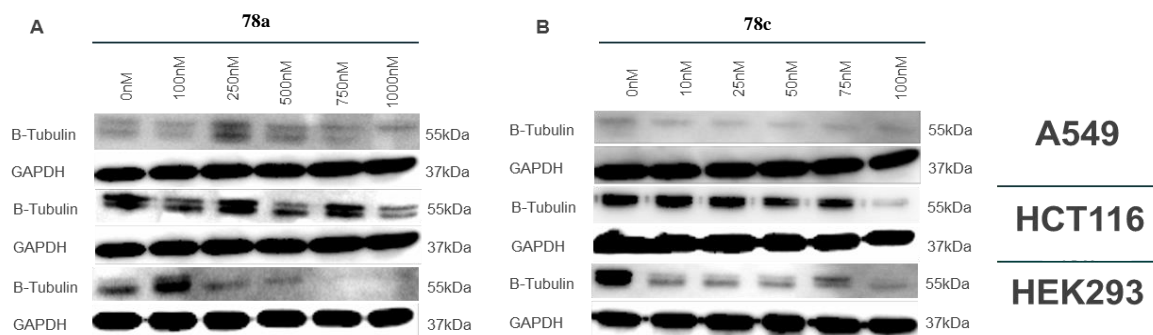


Figure 70: Treatment of A549, HCT116 and HEK293 cells causes a dose dependent decrease in beta tubulin protein expression. A549, HCT116 and HEK293 cells were cultured in DMEM + 10% FCS until 60% confluent. Media was then removed and replaced with fresh media containing 0-1000 nM of indole compound **78a** (panel a) or **78c** (panel b) for 24 h.

β -tubulin plays a pivotal role in cellular polarity and motility, intracellular traffic and mitosis.^{310, 311} β -tubulin forms heterodimers, smaller subunits of microtubules and upon transition from interphase to mitosis, the microtubule rearranges forming the mitotic spindle needed for chromosome segregation.^{311, 312} The turnover of the mitotic spindles is rapid, 60-90 seconds, which can be associated with an increased catastrophe rate.³¹³ If levels are depleted through unknown mechanisms, then the amount of β -tubulin available for mitosis is decreased. This could force the cell to die through a mitotic catastrophe type mechanism. There is a class of compounds which are known to cause the tubulin to be degraded within the proteasome. The cinnamaldehydes which contained a α,β -unsaturated carbonyl unit forms interactions with tubulin, resulting in the aggregation of tubulin within the insoluble fraction.³¹⁴ Importantly, the cinnamaldehyde based inhibitors were not characterised as a microtubule-targeting agent due to the lack of tubulin degradation. The imbalance between the soluble and insoluble tubulin prevents microtubule polymerisation dynamics, preventing cells from entering the M phase ultimately causing G₂ arrest.³¹⁴ However, it cannot be definitively prove if the indole focused library behaves in this manner.

3.4.2.3. Evidence of the indole as mitotic inhibitors

There is literature precedence which highlights the dual VEGFR₂/ β -tubulin inhibitor properties of some inhibitors, three examples of which are given in Figure 71. These inhibitors were purposely developed for this dual inhibitor status. All three examples comprise of the key features of either a VEGFR₂ or a tubulin inhibitor, into one scaffold and assessed for its efficacy against both targets. There is structural similarity between **88** and **89**, but both were developed by independent groups. On examination of these three

structures, there is no similarity to the indole focused library described in this chapter. Moreover, more compelling evidence comes from the cellular proliferation assay where an IC_{50} obtained on **90** of approximately $1 \mu M$ for both HCT116 and A549 cell lines.³¹⁵

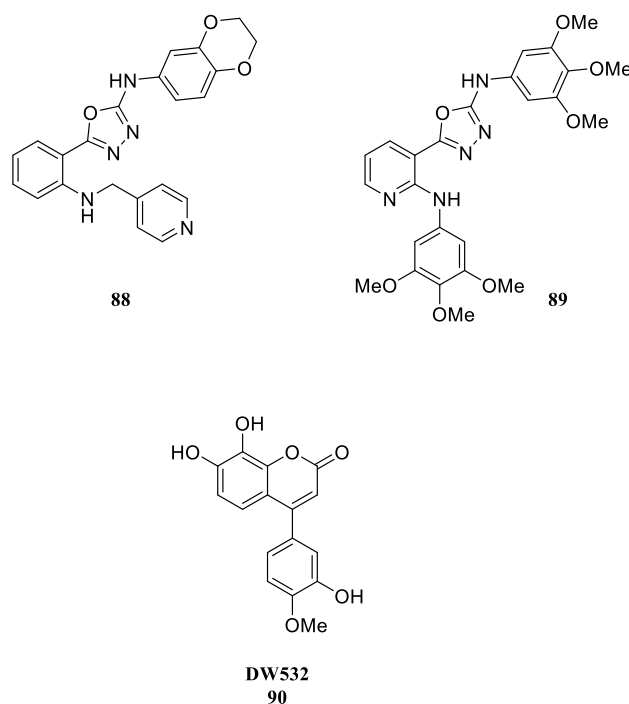
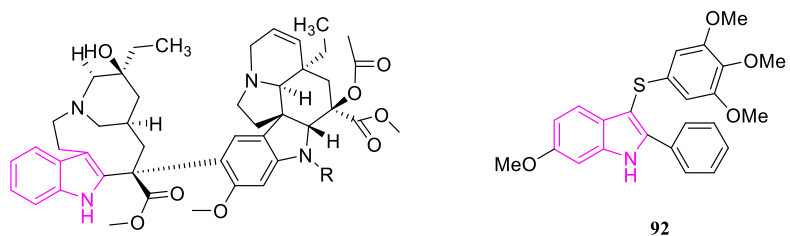


Figure 71: Structures of three dual VEGFR₂, tubulin inhibitors³¹⁶

There is a large literature precedence where indoles have been incorporated into the scaffold of mitotic inhibitors, an excellent review can be found here.³¹⁷ The earliest known indole based tubulin inhibitors are **91a** and **91b** (vinblastine and vincristine respectively - Figure 72).³¹⁸ From proliferation assays, **91a** has an IC_{50} of 900 nM, whilst **91b** has an IC_{50} of 23 nM in the leukemia cell line HL-60.³¹⁹ Both **91a** and **91b** are known to cause cell arrest during the M phase, through the direct binding to microtubules which disrupts the microtubule dynamics.^{320, 321} Recently developed as mitotic/tubulin inhibitors are **92** and **93**, each having an IC_{50} of 2 nM (MCF-7) and 190 nM (A549) respectively, these values were obtained from cellular proliferation assays.^{322, 323} More informative assays are required to determine the true mechanism of action of this indole focused library, however the evidence presented above precludes its use as a PET candidate.



R
Vinblastine (91a): CH₃
Vincristine (91b): CHO

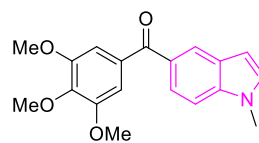


Figure 72: Structures of mitotic/tubulin inhibitors^{318, 322, 323}

3.5 Summary

Patent WO2007/109783 highlighted a series of indole-pyrimidine ether bridged compounds which exhibited high affinity for VEGFR₂, whilst maintaining cellular activity. *In silico* docking highlighted a potential reverse binding mode unlike the previous urea scaffold (Chapter Two) which limits the size of substituents, pendant to the oxime, to smaller aliphatic substituents. The focus of this indole library was to lower cLogP to increase cellular penetration and allow more efficient PET imaging, to allow for easier image interpretation through decreased non-specific binding. The indole scaffold identified to do this was the 5-hydroxy-1*H*-indole-2-carbonitrile **66**, through the withdrawal of electron density of the indole system. Although not lowering cLogP, 2-trifluoromethyl-1*H*-indole **65** was chosen in order to exploit the radiochemistry associated with trifluoromethylation identified by the Gouverneur and Sanford groups.

Synthesis of the indole scaffolds was often difficult and required optimisation. Despite this, once the indole nuclei were synthesised, the main scaffolds were relatively simple to access, requiring little optimisation. The click reaction was disappointing with little conversion to the click compound, presumably through the co-ordination of the copper with the nitrogen contained in the scaffold. Overall nine compounds (**78a-i**), with seven entirely novel (**78a**, **78c**, **78e-i**), were put forward for biological evaluation.

A selectivity screen was first performed on this indole focused library, as selectivity is of major importance in the development of a PET candidate. A cellular proliferation assay carried out in cells lacking VEGFR₂ expression was used to identify off-target binding. Results from this assay highlighted high affinity non-selective binding as evidenced by the low IC₅₀ values obtained for entirely novel candidate **78c** (IC₅₀ of 42 nM against A549). This precludes the indole focused library's use as a PET imaging agent. Further nuclear staining assays further confirmed a mitotic arrest type phenotype, although this requires further studies to confirm this.

β -tubulin plays an important role during mitosis, through forming the mitotic spindles required for successful mitosis. Therefore, if levels of β -tubulin levels are depleted then this could also cause the results observed from the nuclear staining studies on the HCT116 and A549 cell lines. Although there are examples of dual VEGFR₂/ β -tubulin inhibitors, there is no structural similarity between the examples and the indole focused library. It is important to note the extremely low values obtained from cellular proliferation assays are similar to literature published for known mitotic inhibitors.

Despite the lack of data for the VEGFR₂ targeting nature of this indole focused library, off-target bindings were observed from the proliferation, nuclear staining and western blot assays. Non VEGFR₂ expressing cell lines A549 and HCT116 were selected for the assays which all confirmed off-target binding was observed for this library. Therefore, this library of indole focused pyrimidine compounds lack the necessary specificity required for successful PET imaging. Widespread off-target binding is observed with this library and, therefore, cannot be taken forward for further biological characterisation, the manner of off-target binding was not characterised. Chapter Four will discuss a new library of compounds synthesised and biologically evaluated, using a new, more informative biological assay.

Chapter Four

Quinazoline focused library

4. Quinazoline focused library

4.1 Quinazolines in medicinal chemistry

Quinazoline **94** and 4(3*H*)-quinazolinone **95** (Figure 73) are fused heterocycles of immense interest in the pharmaceutical industry owing to their diverse use in anti-cancer, anti-inflammatory, anti-convulsant and anti-hypertensive agents.³²⁴ The quinazoline scaffold can be considered an amalgam of both the pteridine and purine nuclei, therefore it is not a surprise that the vast majority of these compounds are ATP competitive type I kinase inhibitors which bind to the active conformation, discussed in detail in Chapter One (1.2.3).³²⁵ However to determine whether an inhibitor is a type I or a type II, the inhibitor needs to crystallise into the ATP of the kinase of interest and X-ray studies performed. As previously covered in Chapter One (1.2.3), type II inhibitors do not directly compete with ATP and bind to a hydrophobic pocket of the inactive kinase.³²⁶ Typically one to three hydrogen bonds are formed between the hinge region (around Cys919 of VEGFR₂) and the inhibitor. It is well-known that kinases catalyse the attachment of phosphorous groups to the tyrosine residues, resulting in the conversion of ATP to ADP. In tyrosine kinases this occurs via the tyrosine residues, in serine-threonine kinases this occurs on the serine residues. Therefore if the inhibitor is bound within the nucleotide binding domain, the kinase cannot catalyse the attachment of phosphorous groups to the tyrosine residue of VEGFR₂, which prevents downstream activation of the signalling pathway.

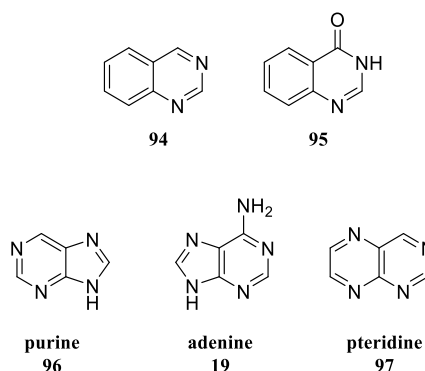


Figure 73: Structure of quinazoline **94**, 4(3*H*)-quinazolinone **95**, adenine **19**, purine **96** and pteridine bases **97**

Quinazolines are distributed widely in the scaffolds of anti-cancer agents and, in particular, kinase inhibitors. Figure 74 highlights the quinazoline core in the use of inhibitors targeting specific kinase signalling pathways.

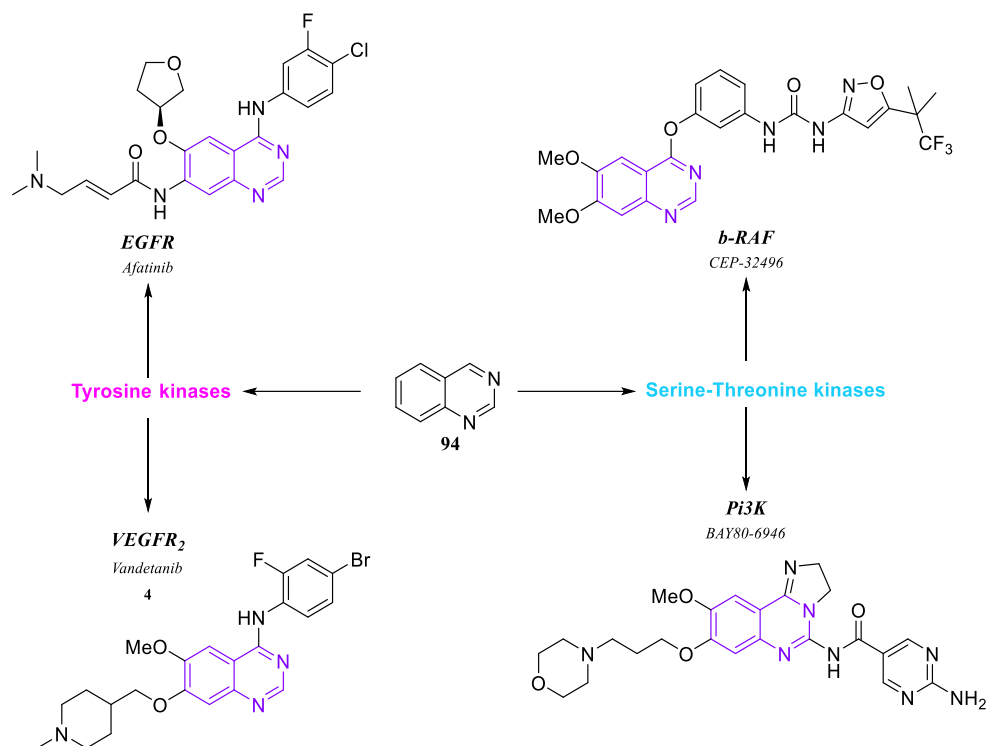


Figure 74: Common quinazoline based kinase inhibitors³²⁷⁻³³⁰

4.1.1. Quinazoline as VEGFR₂ inhibitors

Examples of drugs that have gone to market or reached clinical trials containing the quinazoline core are presented in Figure 75. AZD2171 **58** demonstrates excellent selectivity over non-related kinases but poor selectivity over the VEGFR family, as previously discussed in detail in Chapter Three (3.1.1). However, as discussed in Chapter Three (3.1.1), the key binding residues of **58** are through the quinazoline to hinge region around Cys919, identical to that of the other quinazolines. Vandetanib, **4**, exhibits high affinity for VEGFR₂ but also targets EGFR and RET. Therefore, most examples of quinazoline based inhibitors could potentially lack the necessary specificity required for PET imaging, although this should be considered on a case by case basis. This is due to the conserved nature of the ATP binding pocket of kinases in the active conformation, therefore a lack of selectivity and specificity is observed between the kinases. The typical binding modes of these quinazolines in VEGFR₂ is shown in Figure 73.

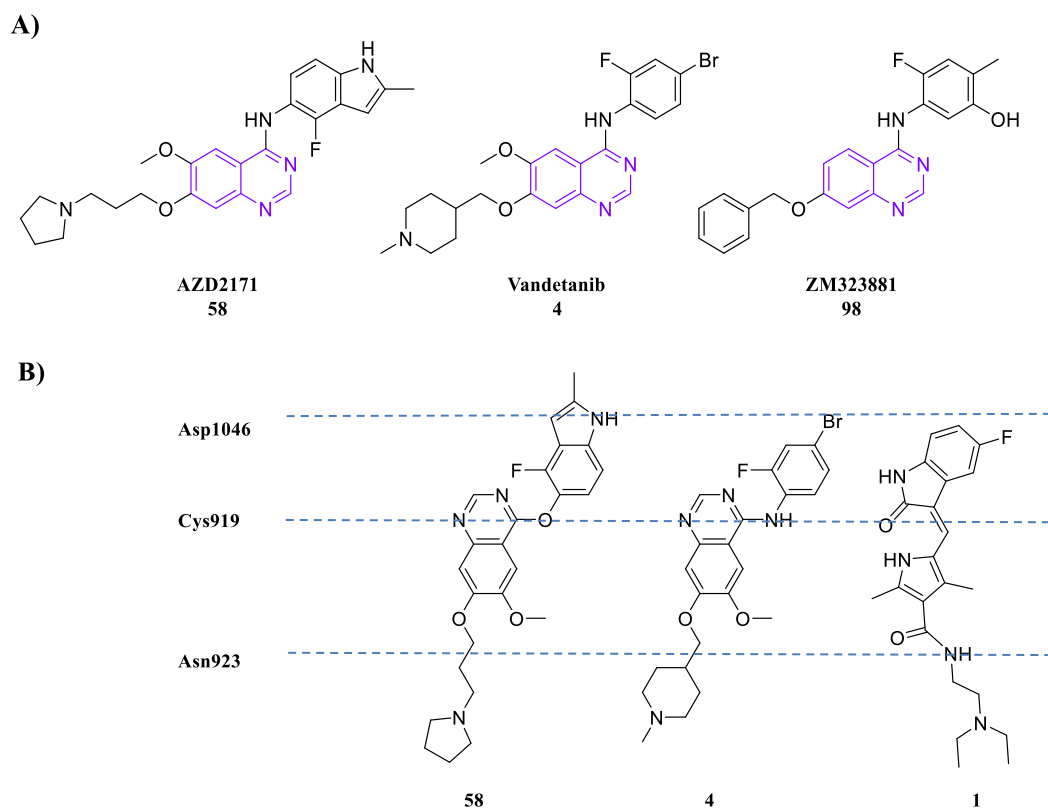


Figure 75: Common VEGFR₂ inhibitors A) Structures of three relevant quinazoline (highlighted in purple) TKIs B) The typical binding mode of these VEGFR₂ inhibitors with **1** as a comparison (adapted from²⁶⁴)

ZM323881 **98** (Figure 75) is the only reported selective inhibitor of VEGFR₂, the selectivity profile is summarised in Table 17. This reported selective inhibitor is known to inhibit VEGFR₂ phosphorylation, after stimulation with VEGF_A, in an *ex vivo* assay with frog lung tissue, an organ known to express high levels of VEGFR₂.³³¹ There is established literature precedence confirming **98** as a selective VEGFR₂ inhibitor.³³¹⁻³³⁴

Table 17: The known selectivity profile for **98**³³¹

Entry	Kinase	IC ₅₀ (μM)
a	VEGFR ₁	>50
b	VEGFR ₂	0.002
c	PDGFRβ	>50
d	FGFR1	>50
e	EGFR	>50
f	HER2	>50

4.2 Rationale

4.2.1. Selection of the target compounds

As identified in the previous section **98** has well established biological data revealing this as the only VEGFR₂ selective inhibitor. Therefore, this chapter is concerned with developing a PET candidate based on **98**. Examining the docking pose of **98** with VEGFR₂ reveals an unexpected binding configuration. Unlike the quinazoline based inhibitors discussed previously in Chapter Four (4.1.1.), the quinazoline core points towards the back hydrophobic pocket. This contrasts with the other quinazoline based structures, in which the quinazolines forms a hydrogen bond with the critical Cys919, via a bridging water (Figure 77). Importantly, hydrophobic interactions are formed with Glu885 as well as Leu1035, which are all located in the ATP binding pocket, confirming this scaffold could potentially demonstrate affinity for VEGFR₂. This unusual binding mode may be responsible for the selectivity profile observed for **98**.

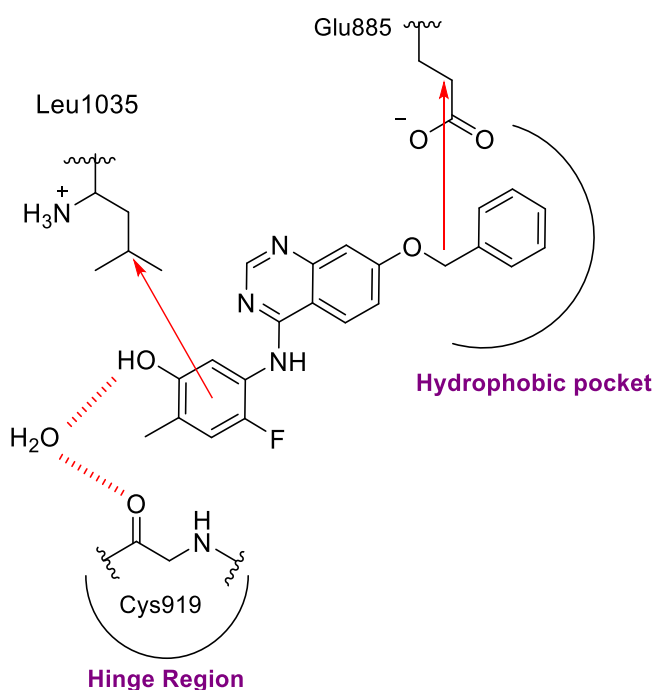


Figure 77: Docking pose of **98** in VEGFR₂. Docking was performed using Schrödinger Gold (2014-2) and visualised on Chemical Computing Group MOE (2013-8802). PDB code: 3VHE

4.2.2. Design of an quinazoline focused library

Examining the structure of **98**, three potential fluorination sites can be identified (Figure 78). The first potential site involves radiolabelling of the fluorine currently present on the aniline fragment of **98**. This scaffold based around **98** is ideal as there is already biological evaluation indicating it is the only known selective inhibitor of VEGFR₂. Modifications of the benzyl ring, smaller fluorine substitutions are ideal as its atomic size is similar with hydrogen and is thought to enhance metabolic activity either by electron withdrawing on the whole ring or blocking the site of metabolism.³³⁹

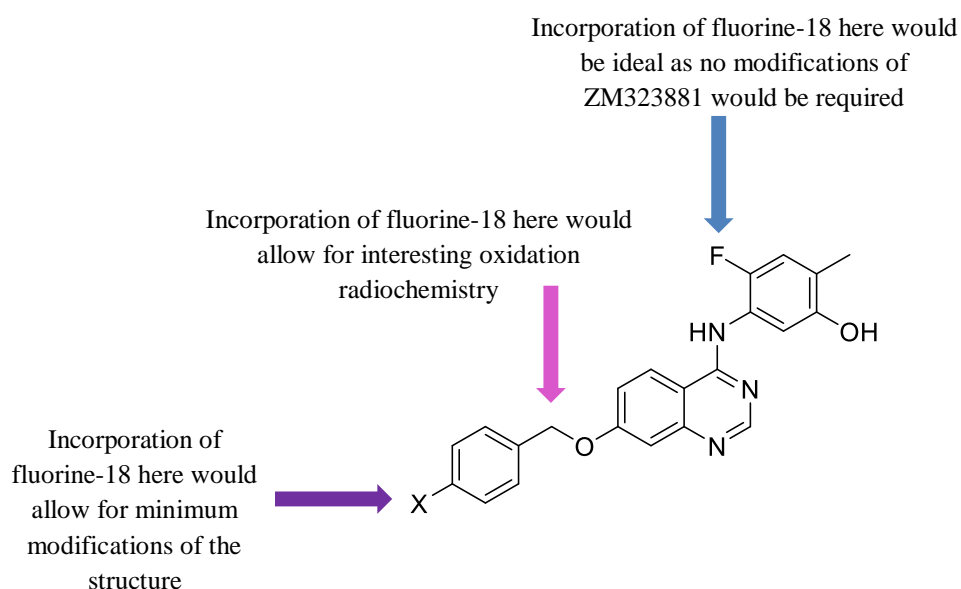


Figure 78: Identification of possible fluorine-18 positions on the scaffold of **98**

4.2.3. Considerations of the quinazoline focused library for developing a successful PET candidate

There are several criteria to be considered when developing this quinazoline scaffold into a successful candidate:

- Selectivity and affinity for the target – As previously discussed in this Chapter (4.2.1), ZM323881 is the only known selective VEGFR₂ inhibitor
- Lipophilicity – As previously discussed lipophilicity is important as this can determine the percentage of radiotracer bound in the plasma which can confound PET imaging however this is not the most important consideration. Although cLogP is higher than ideal, several radiotracers have been successfully developed and these were not precluded from further studies. Important to note the cLogP of this library

is within the same range as the newly developed quinazoline-based PET probes (Figure 77)

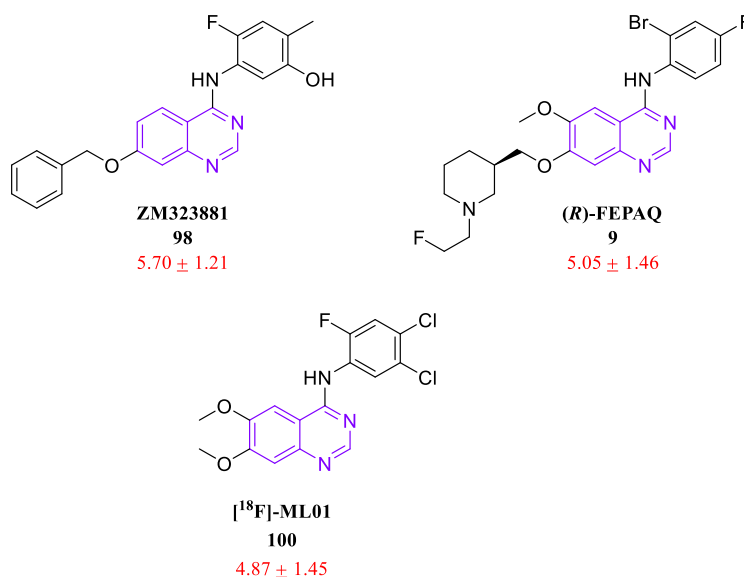


Figure 79: cLogP* values (highlighted in red) for some quinazoline based PET candidates (* calculated using ACD Chem Sketch V12.01)

- Ease of radiolabelling – As shown in Figure 78, there are several places in which fluorine-18 can be incorporated into the scaffold. Many of these sites are amenable to late-stage radiolabelling which is highly desired from the standpoint of ease of radiolabelling and should also allow for higher radiochemical yields
- Metabolism – Incorporation of the fluorine has the potential to block metabolism at the benzyl position or the para phenyl position, leading to less radiolabelled metabolites which can confound image interpretation, discussed in Chapter One (1.3.3.5)

4.3 Results and discussion

4.3.1. Chemistry of the Quinazoline series

The target compounds for synthesis are shown in Figure 80.

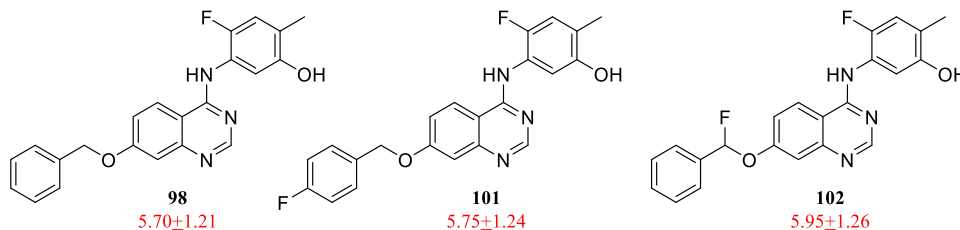


Figure 80: Structures of three proposed compounds and cLogP based around **98** (* calculated using ACD Chem Sketch V12.01)

4.3.1.1. Synthesis via Quinazolinone

Literature precedence for the synthesis of quinazolines revealed a synthetic route via the quinazolinone. The first step in the synthesis was the formation of the quinazoline scaffold (Scheme 29), via the Niementowski synthesis which is the most widely utilised approach for the synthesis of quinazolinones (Figure 81). Condensation of anthranilic acid derivatives with amides, proceed via an *o*-amidobenzamide, as shown in Figure 79.³⁴⁰ The scope of yields for this condensation is variable, ranging from poor to quantitative, with a typical reaction time of six hours. Recently publications have highlighted the use of microwave assisted Niementowski reactions.³⁴¹⁻³⁴³ The Niementowski quinazoline synthesis of **104** proceeded without any problems, giving a 97% yield, without the requirement for aqueous work-up or purification.

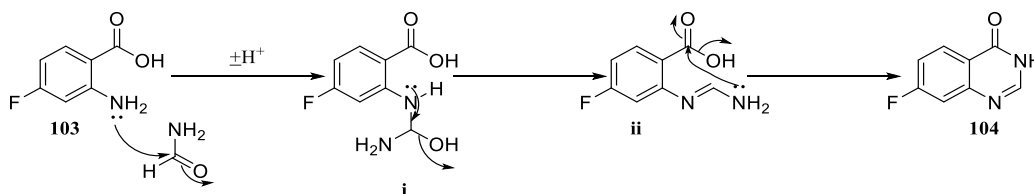
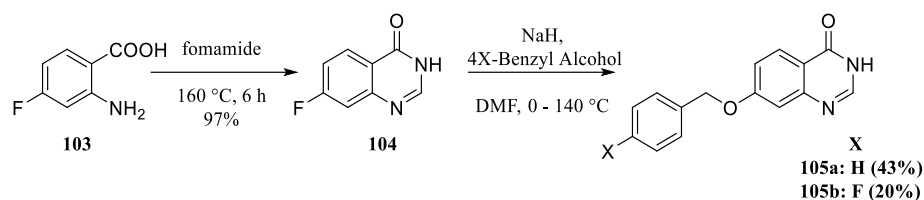
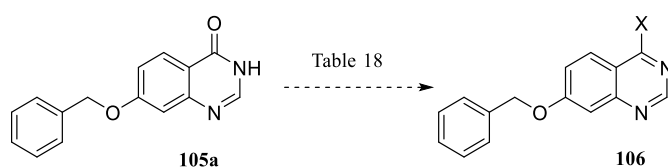


Figure 81: Niementowski mechanism for the synthesis of **104**



Scheme 29: Synthesis of quinazolinone intermediate **105a** and **105b**

The next step in the synthesis towards the target quinazolines **98**, **101** and **102** was the nucleophilic substitution of **104** with either benzyl alcohol or 4-fluorobenzyl alcohol. Rigorous temperature control (0-5 °C) for the generation of the irreversible benzyl alkoxide was required to avoid over deprotonation of the benzyl alcohol. Despite allowing the reaction mixture to warm to room temperature and subsequent stirring for 18 hours, no reaction occurred. Pleasingly, heating to 140 °C afforded the alkylated quinazolinones **105a** and **105b**, with yields comparable to the literature. The penultimate step in the synthesis of these target quinazolines was the introduction of a suitable leaving group and re-aromatisation of the ring (Scheme 30).



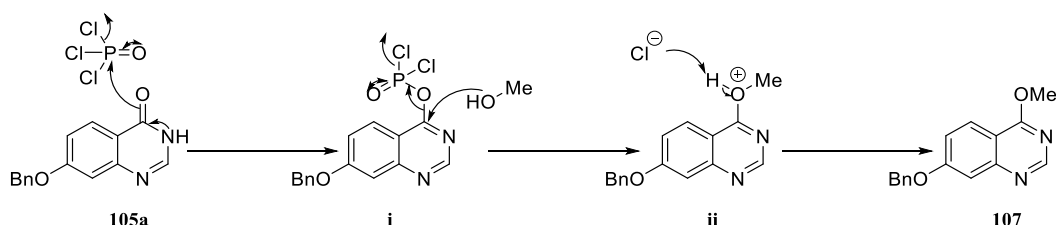
Scheme 30: Rearomatisation of **106**, for the introduction of a suitable leaving group

Despite a literature precedence for the introduction of a leaving group at the 4 position of **106**, this was not achieved. Table 18 summarises the different strategies to achieve the rearomatisation, suitable leaving groups attempted were Cl, Br and OTf.

Table 18: Attempts at the introduction of a suitable leaving group (X) on **106**

Entry	X	Conditions	Outcome
a	Cl	SOCl ₂ , DMF (cat), reflux 1 h	unidentifiable products
b	Cl	SOCl ₂ , DMF (cat), reflux 30 minute	polymerisation of 105a
c	Cl	SOCl ₂ , DMF (cat), 50 °C, 1 h	unidentifiable products
d	Cl	POCl ₃ , 50 °C, 30 minutes	unidentifiable products
e	Cl	POCl ₃ , 50 °C, monitored	reaction stuck at intermediate i
f	Br	POBr ₃ , 70 °C, monitored	no reaction
g	OTf	Tf ₂ O, 2,6-lutidine, 0 °C, 2 h	no reaction

Interestingly, as entry **e** highlights, the reaction did not proceed beyond the intermediate. **i** These reactions were monitored by LCMS, after quenching with methanol to remove excess POCl₃. Product **107** was the only species identified, apart from a small presence of **105a**. Figure 82 highlights the mechanism in which the methoxy adduct is formed. Addition of excess POCl₃ did not yield the expected product.

**Figure 82:** Structure and mechanism of product **107** - identified by LCMS

In light of the evidence presented above, a literature survey was conducted to identify alternative synthetic methods. The next section will discuss the new procedure for the synthesis of the quinazoline scaffold.

4.3.1.2. Synthesis via PyBOP coupling

The literature survey highlighted the potential for synthesising the quinazoline scaffold utilising coupling reagents. For example, Wan *et al.* published a study in which quinazolines were synthesised from their respective quinazolinones in a one pot manner.³⁴⁴ This publication provided a wide scope of nucleophiles (nitrogen, oxygen and sulfur) using

benzotriazol-1-yl-oxy-tris(dimethylamino) phosphonium hexafluorophosphate (BOP - Figure 83).

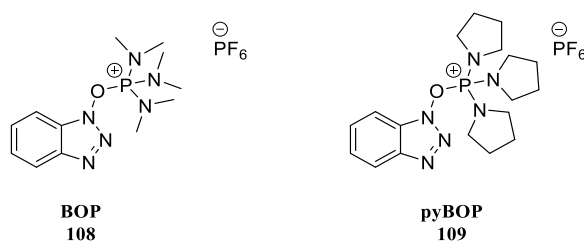
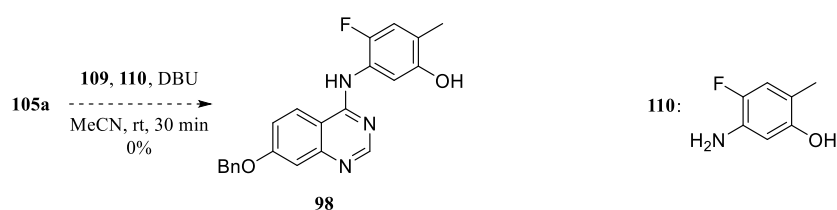


Figure 83: Structures of coupling reagents BOP **108** and PyBOP **109**

Due to the well-known difficulty in working with hexamethylphosphoramide, Wan *et al.* modified the synthetic method to involve the use of **109** (Figure 83). The use of **109** was investigated as an alternative to **108** and found longer reaction times were needed, however this is tolerated due to not needing to remove hexamethylphosphoramide from the reaction mixture.³⁴⁴ Scheme 31 highlights the revised synthetic procedure for the synthesis of the quinazoline scaffold.



Scheme 31: PyBOP mediated synthesis of target compound **98**

Following the reaction by LCMS indicated the reaction was complete in 30 minutes. Leaving the reaction for longer resulted in the formation of unidentified by-products. Upon column chromatography purification and subsequent NMR, this reaction was not successful in synthesising **98** and **111** was the identified product (Figure 84). This was confirmed by ¹H NMR, through the identification of the aniline peak (two protons at 5.13 ppm).

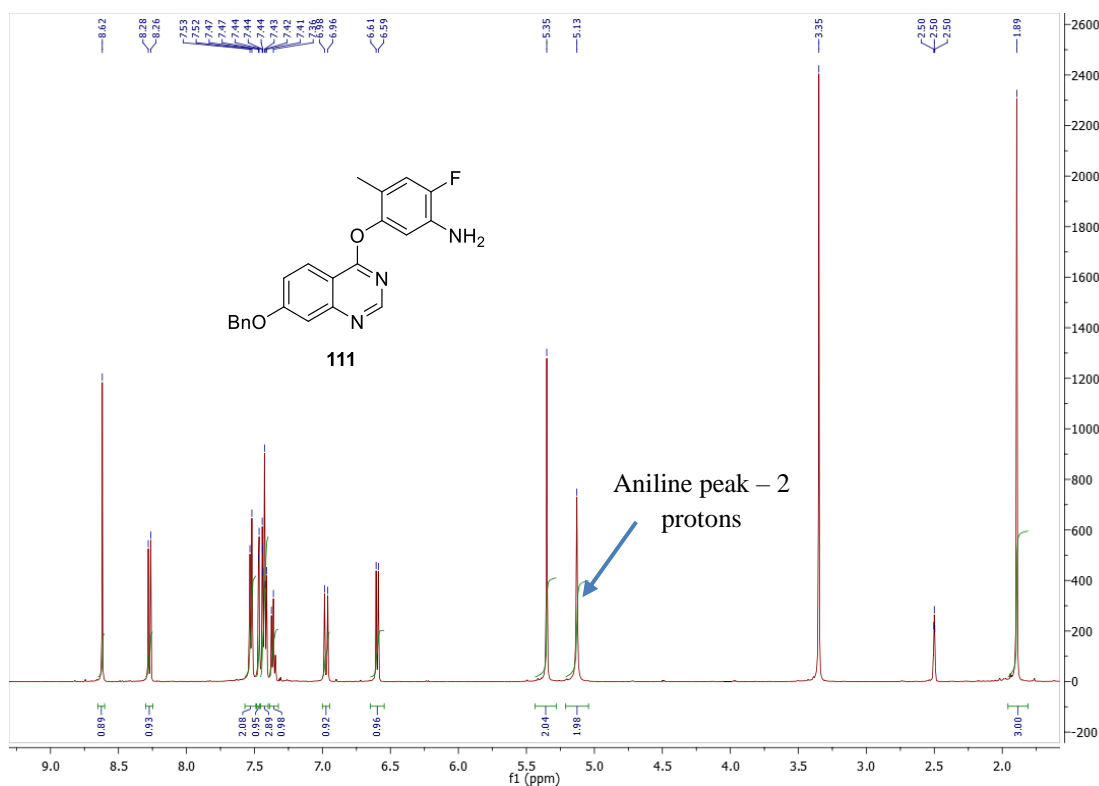


Figure 84: Structure of **111**, the product of the PyBOP **109** mediated synthesis and ^1H NMR identifying the aniline protons

No trace of **98** was observed in either ^1H or ^{13}C NMR. The mechanism of the PyBOP mediated coupling is shown in Figure 85. Wan *et al.* postulated two possible mechanisms for this PyBOP mediated coupling. Initial tautomerisation of **105a**, followed by the nucleophilic attack of anion **ii** on phosphonium **109** formed exclusively **112**.

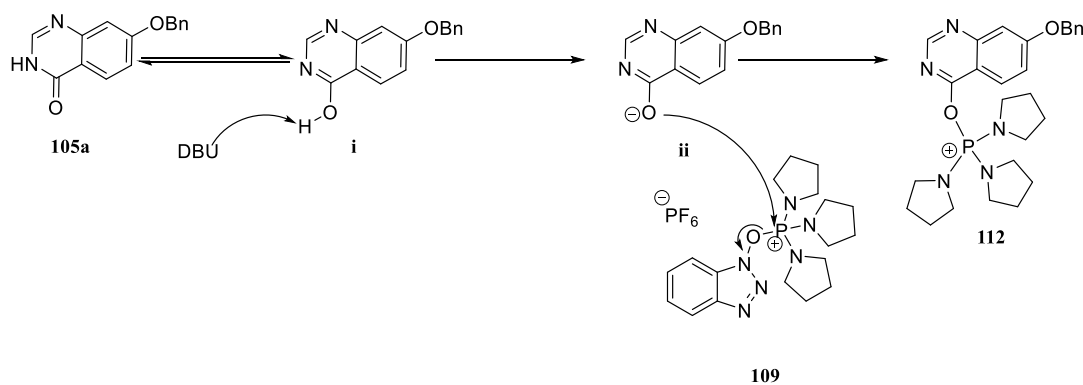


Figure 85: Initial attack of PyBOP on **105a**

The second half of this mechanism is shown in Figure 86. The mechanism is divergent here for the two different nucleophiles present in **110**. Although aniline is not considered a weak nucleophile, the phenol moiety of **110** will deprotonate first, thus making the phenol the stronger nucleophile. Therefore two different mechanisms can be proposed, for a weak nucleophile and a strong nucleophile. Firstly, for the strong nucleophile the mechanism is depicted by the red arrows. The deprotected phenol is strong enough to directly react with **112**, displacing **113** from the complex. For the weak nucleophile, deprotected hydroxyl benzotriazole reacts with **11** forming intermediate **i**. Aniline **110** is then able to displace the deprotected hydroxyl benzotriazole adduct forming **98**. Through monitoring the reaction, no traces of **98** were observed or the intermediate **i**, thus explaining the preferential synthesis of **111**.

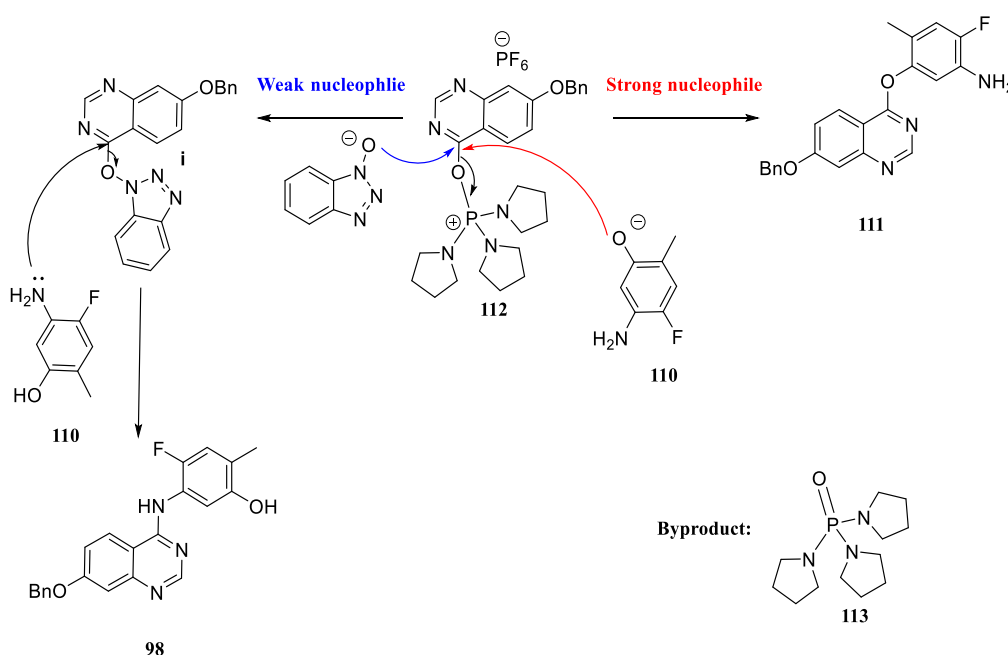
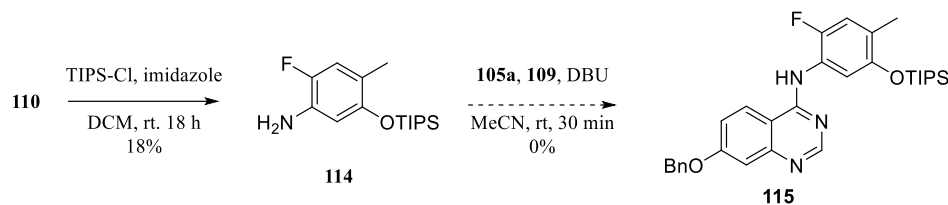


Figure 86: Second half of the PyBOP mediated synthesis of **98** and **111**

In order to circumvent this unwanted side reaction, phenol **110** was TIPS protected in an 18% yield (Scheme 32). Unfortunately, during the course of the reaction **114** became deprotected and **111** was formed, not the expected **115**.



Scheme 32: TIPS protection of **110** and subsequent PyBOP mediated coupling with **105a**

With the synthesis of the quinazoline scaffold inaccessible via the quinazolinone, a literature survey was performed to identify an alternative method not involving the quinazolinone intermediate.

4.3.1.3. Synthesis via the Dimroth rearrangement

A literature survey highlighted the synthesis of two kinase inhibitors, **99** and **116** via the Dimroth rearrangement (Figure 87).^{345, 346} The Dimroth rearrangement offered fewer reaction steps with accelerated reaction times.

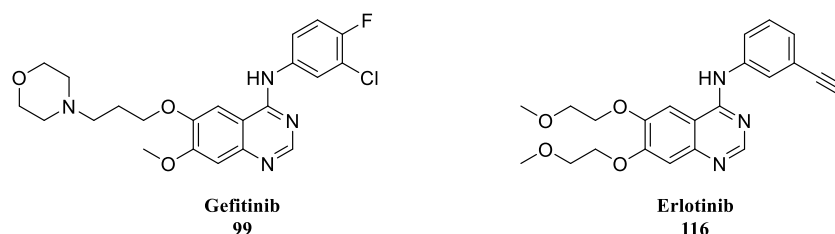
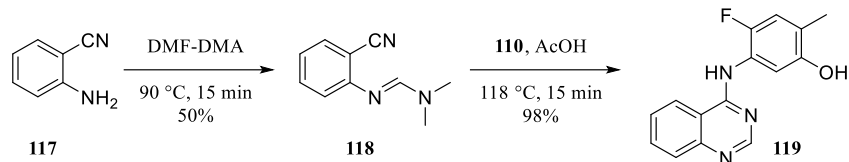


Figure 87: Structures of Gefitinib **99** and Erlotinib **116** synthesised via the Dimroth rearrangement

A proof of concept reaction was undertaken to assess the suitability of the Dimroth rearrangement for the synthesis of the target quinazolines (Scheme 33). Pleasingly, the reaction of DMF-DMA with **117** resulted in formamididine **118** in a 50% yield. Although no side products were observed by LCMS, column chromatography was required to remove excess DMF-DMA, due to its high boiling point. Dimroth rearrangement of **118** with **110** resulted in quinazoline **119**, in a 98% yield.



Scheme 33: Synthesis of **119**, a trial Dimroth rearrangement

Precipitation of quinazoline **119** was afforded by addition of diethyl ether, without the need for further chromatographic purification, as judged by LCMS and ^1H NMR. As clearly seen in Figure 88, both the NH and OH peaks can be identified. Due to the success of this trial reaction, the Dimroth rearrangement was taken forward to synthesise the target quinazolines.

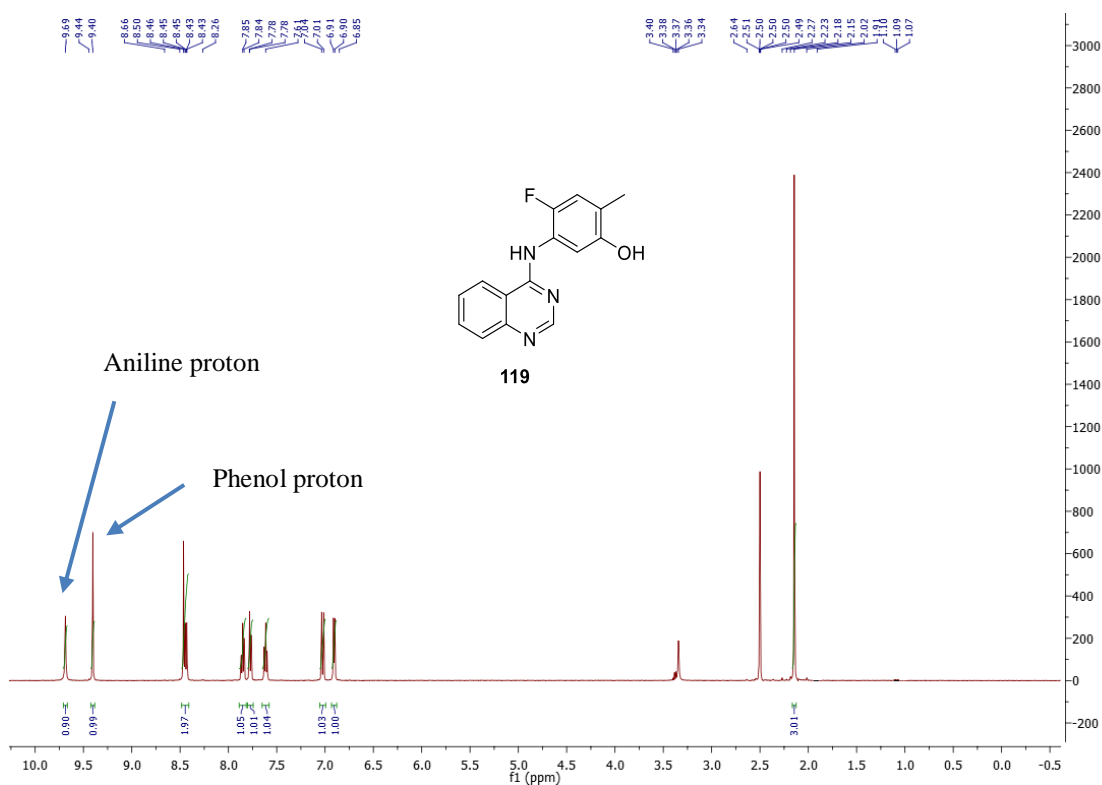


Figure 88: ^1H NMR for **119**, highlighting the NH and OH proton

The mechanism for the Dimroth rearrangement is shown in Figure 89. Attack of the aniline on the formamidine results in the expulsion of dimethylamine. Cyclisation of the scaffold follows, with aniline **110** forming part of the endocyclic nitrogen ring. Attack by water results

in the ring opening of the system, tautomerisation of **iii** allows for the aromatisation of **iv** to form quinazoline **119**.

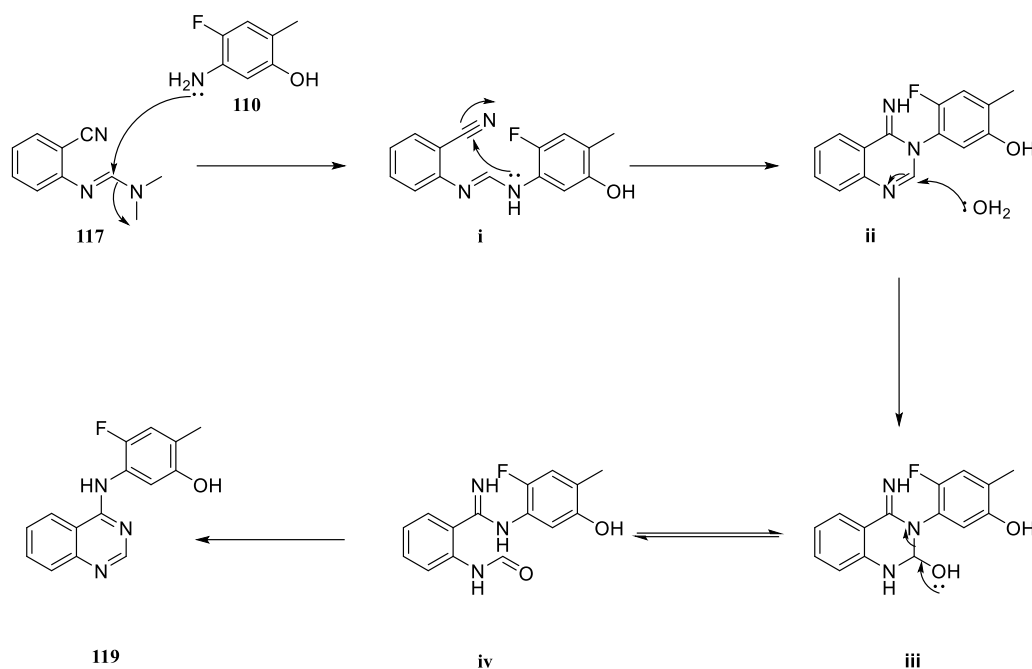
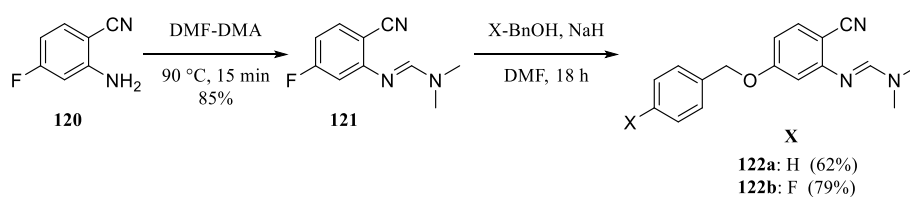


Figure 89: Mechanism of the Dimroth rearrangement, as highlighted by Asgari *et al.*³⁴⁶

Retrosynthetic analysis revealed the need for the fluorine at the para position to the nitrile. This allowed the introduction of the benzyl moiety required in the scaffold. Formation of the formamidine **121** was extremely successful with no side products identified in an 85% yield. Introduction of the benzyl moiety of **122a** proved to be more successful than on the quinazolinone. Formation of the irreversible alkoxide at 0-5 °C, warming to room temperature and subsequent stirring for 18 hours afforded **122a** and **122b** in a 62 and 79% yield respectively. **122a** did not require chromatographic purification, however **122b** required purification from 4-fluorobenzyl alcohol (Scheme 34).



Scheme 34: Synthesis of formamidines **122a** and **122b**

The final step in the synthesis of these quinazolines was the Dimroth rearrangement. A hybrid compound **123** of **98** and **4** was included in the library as a quick probe into the origin of the selectivity for VEGFR₂ arises from. The differences between **98** and **4** are shown in Figure 90. The differences are highlighted in pink at the 6 position of the quinazoline ring, further differences include the methoxy side chain at position 7 (highlighted in grey) and the substitution of the aniline ring (highlighted in blue). Docking studies revealed the benzyl groups points back into the hydrophobic pocket, limiting substitution here. The question posed is does the selectivity come from this unusual binding pose, or through interactions with Cys919 and the phenol moiety via a water molecule. Therefore, by substituting the aniline ring of **98** with the aniline ring of **4**, this could provide some limited evidence for the selectivity demonstrated by **98**.

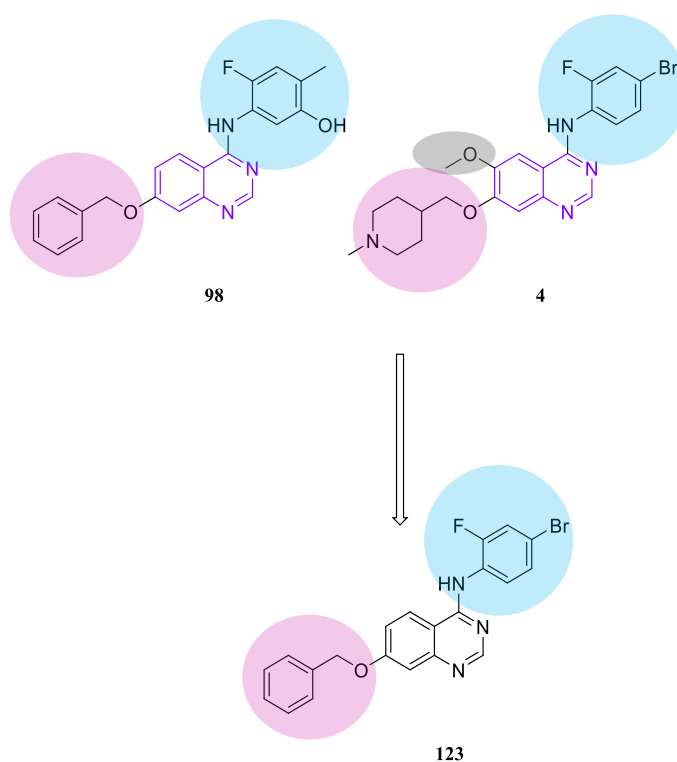
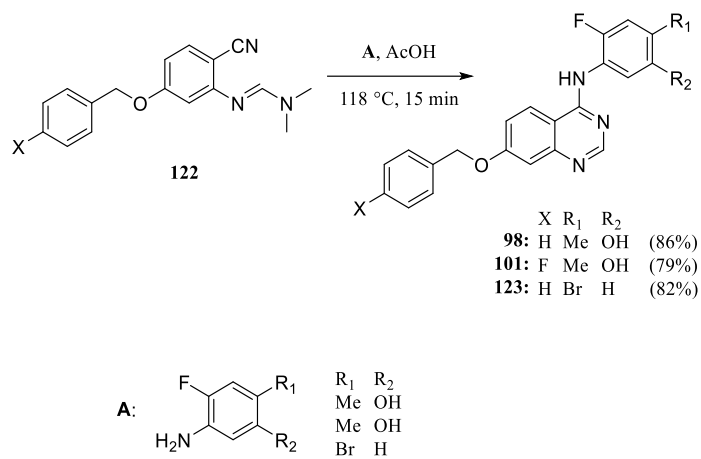


Figure 90: Structural similarities of **98** and **4**, leading to the hybrid compound **123**

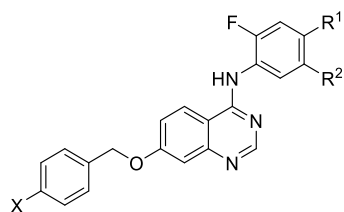
As highlighted through the synthesis of **119**, the reaction is complete within 15 minutes. Purification of quinazolines **98**, **101** and **123** was achieved through precipitation with diethyl ether followed by column chromatography (Scheme 35). The analysis (¹H NMR) of **98** was identical to those published in the literature.³³¹



Scheme 35: Synthesis of final compounds **98**, **101** and **123**

Compounds for further biological evaluation are shown in Table 19.

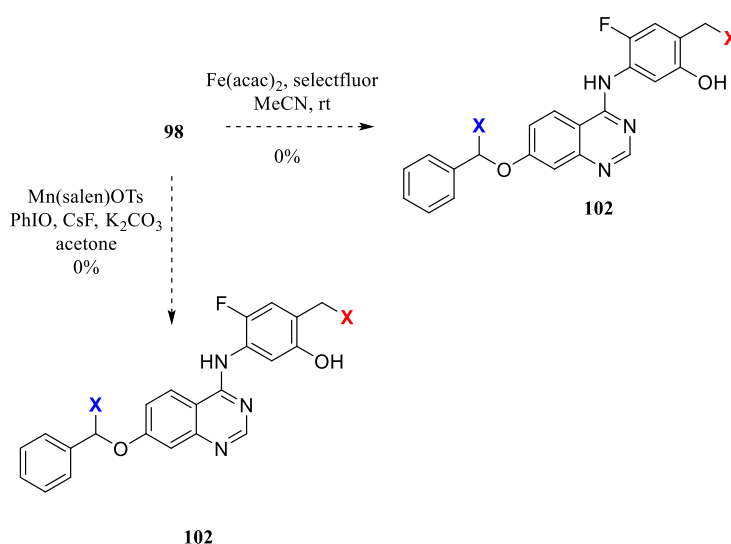
Table 19: Quinazoline library for biological evaluation



Compound	X	R ¹	R ²	Yield (%)
98	H	Me	OH	86
101	F	Me	OH	79
123	H	Br	H	82

4.3.1.4. Benzylic fluorination

As previously discussed, the introduction of a fluorine at the benzylic position of **98** would be interesting both for the radiochemical synthesis and to investigate if enhanced metabolic stability is observed. Bloom *et al.* developed a method using iron to catalyse benzylic fluorinations, shown in Scheme 36. Although this method did result in the introduction of fluorine on the scaffold (evidenced by LCMS), the desired product could not be isolated and adequately identified. Examination of **98** revealed two potential positions in which the reaction could occur, highlighted in red and blue. Liu *et al.* also published a manganese salen based benzylic fluorination.^{347, 348} However, this was also not successful in achieving the synthesis of **102**.



Scheme 36: Attempts to fluorinate the benzylic position of **102** from **98**

4.3.2. Screening of the quinazoline focused library

Although the biological evaluation used to evaluate the indole focused library (Chapter Three) was screening for non-specific toxicities, this library was based around the only known selective VEGFR₂ inhibitor **98** (ZM323881). Therefore, the basic non-specific toxicity studies were not required, consequently this section will describe assays which highlight a radiochemical based biological evaluation and a kinase screen used to evaluate this library of compounds.

4.3.2.2. Kinase based screening

A kinase-based screen allows for data to be obtained for specific kinases, allowing for a probe into affinity and selectivity of this quinazoline library. The kinases tested were selected on the following premise:

- Structurally related to VEGFR₂ – *all members of the VEGFR₂ family, all members of the PDGFR family*
- Known inhibitors (mainly clinical) targeting kinases were selected for testing of this quinazoline focused library.³⁴⁹

There are several methods available for the evaluation of a potential VEGFR₂ inhibitor library. Several companies offer a wide range of targets for profiling, typically 100-400 kinases, in parallel using different assays.³⁵⁰ The most common kinase profiling assay is a radioactive filter binding assay which is used by approximately half the commercial kinases profiling labs, due to its reliability.³⁵¹ The radioactive filter binding assay gives a readout of direct kinase activity with the sensitivity required.³⁵⁰ Non-radioactive methods of kinase inhibitor profiling include fluorescence based assays, Caliper format or a competitive binding assay of kinases expressed on bacteriophages.³⁵⁰ Regardless of the assay format, the kinase inhibitor profiling falls into three distinct categories:

- Dose-response binding – *This assay gives a K_d readout for each target, in the absence of ATP*³⁵⁰
- Dose-response activity assay – *This assay determines an IC_{50} for each target, in the presence of ATP. As this assay is ATP dependent, the ATP concentration used is at K_{M-ATP}* ³⁵⁰

- A single concentration measurement – *This assay offers the potential for a quick assessment of kinases selectivity, however is liable to increased variation in results*³⁵⁰

A Z-LYTE assay was selected to evaluate this quinazoline focused library. The Z-LYTE assay works on fluorescence resonance energy transfer (FRET). The FRET assay does not require expensive radioactive substrates or antibodies. The Z-LYTE assays works on the premise that the peptide substrate tagged with coumarin (donor fluorophore) and fluorescein (acceptor fluorophore), making the FRET pair (Figure 91) which is used in the assay.

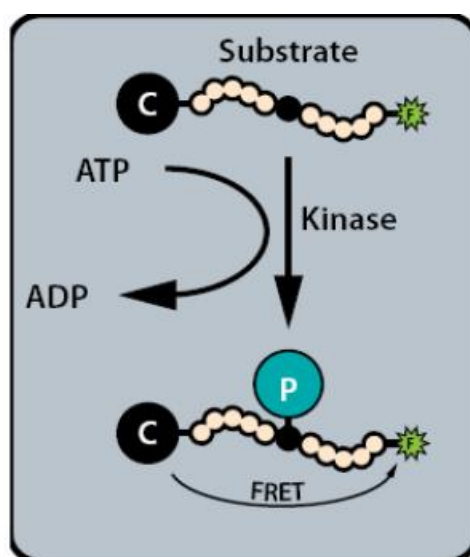


Figure 91: Z-LYTE kinase assay - The principles. The investigated kinase transfers the γ -phosphate to the tyrosine/serine/threonine residue on the FRET peptide³⁵²

The results of the Z-LYTE assay, performed by InvitrogenTM, are presented below in Table 20. The results from the Z-Lyte assay highlight **98** is not selective, showing a lack of selectivity between the VEGFR family and the closely related PDGFR α and the non-related RET, EGFR. Unfortunately, the close analogue **101** also demonstrated this lack of selectivity against the same kinases. Unfortunately, **123** highlighted a profile which only demonstrates weak binding to the tested kinases.

Table 20: Heat map for the data obtained from the Z-LYTE assay (% inhibition against a panel of kinases at 1 μ M. ATP concentration is K_{mapp} . *ATP 100 μ M)

	98	101	123
ABL	50	52	6
Aurora A	5	-1	1
Aurora B	-14	3	-15
bRAF*	12	1	3
CSF1R	22	7	12
EGFR	78	63	53
HER₂	-4	5	-2
FGFR₁	13	13	9
VEGFR₁	80	79	-7
FLT₃	4	-3	5
VEGFR₃	99	100	12
VEGFR₂	100	103	40
cKIT	25	35	7
MEK1	11	8	3
cMET	7	5	6
PDGFRα	67	69	12
PDGFRβ	7	-4	8
RET	98	99	32

Due to the selectivity profile described above affinity data was obtained for VEGFR₂. As shown in Table 21 the selectivity profile for **123** highlighted a weak binding profile and did not inhibit VEGFR₂ activity, whereas, **98** demonstrates similar activity as that highlighted by previous literature. Pleasingly, the substitution for the fluorine on the benzyl ring, does not perturb activity too much (with a K_i of 3.75 versus 2.375 for **101** and **98** respectively).

Table 21: Activity against VEGFR₂ for **98**, **101** and **123** (ATP concentration is at K_{mapp})

Compound	VEGFR₂ IC₅₀ (nM)	K_i
98	4.75	2.375
101	7.5	3.75
123	>1000	n/a

Due to **101** also exhibiting strong inhibition of both RET and VEGFR₃ at the tested concentration (1 μ M), a full dose response curve was obtained for these kinases. As shown in Table 22, the K_i for VEGFR₃ and RET are 8.35 and 16.25 respectively. Full dose response curves are located in Appendix Three (7.2.3).

Table 22: Activity against VEGFR₃ and RET for **101** (ATP concentration is at K_{mapp})

Kinase	IC ₅₀ (nM)	K _i
VEGFR ₃	16.7	8.35
RET	32.5	16.25

The differences in activity against VEGFR₂ for these three different quinazolines can only be explained by the substitution of the aniline. As previously explained in this Chapter (4.2.2), **98** had an unusual binding mode for VEGFR₂, with the aniline moiety forming interactions with the hinge region of VEGFR₂, and the phenol forming the critical hydrogen bond Cys919. In comparison, whilst **123** binds in the pocket in the same mode as **98** and **123**, there is no hydrogen bond formed with Cys919 which could explain the weak binding profile observed.

As described in Chapter One (1.4.3.3), selectivity and affinity are essential in the development of a VEGFR₂ specific PET imaging probe. As demonstrated by the biological data presented in this section, both **98** and **101** fulfil the affinity requirement, however this kinase screening needs to be expanded further. Despite **98** not showing the selectivity described in the literature,³³¹ further *in vitro* studies are required to determine the expression levels of VEGFR₃ and RET in VEGFR₂ positive cell lines. This would determine whether the activity against either VEGFR₃ or RET would cause difficult data interpretation due to similar expression levels and K_i to VEGFR₂.

4.3.2.1. Development of tools for evaluation of radiolabelled compounds

Owing to the success Li *et al.* demonstrated with the specificity achieved with [⁶⁴Cu]-DOTA-ZDG2,²⁰⁶ this was developed for this project. Through modification the macrocycle which allows the incorporation of other radioisotopes such as gallium-68 and [¹⁸F]-AIF, the development of **125** (NOTA-ZD-G2 - Figure 92) was attempted. Unfortunately, despite following the method reported in the paper, the **125** complex was not successfully synthesised, Chapter Five will discuss the synthesis of this precursor. After establishing the specific nature of **125**, this could have the potential to be used in a competition assay against **98**, **101** and **123**.

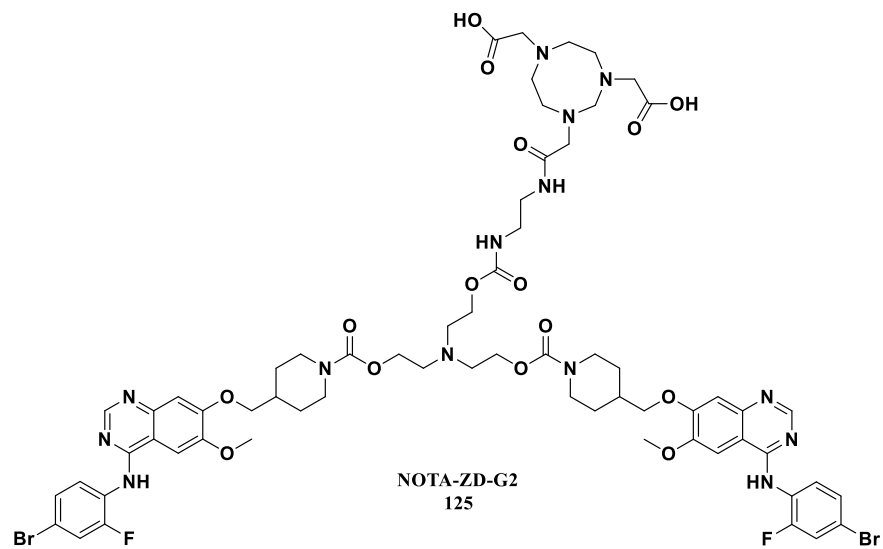


Figure 92: Structure of target 125

4.4 Conclusions

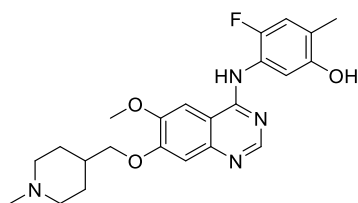
Several reports identified **98** (ZM323881) as a selective inhibitor of VEGFR₂,^{331, 353} therefore it was used as the ‘molecular architecture’ for this chapter. This inhibitor consists of a quinazoline core and synthesis was attempted via the quinazolinone **104**. However, the rearomatisation of **104** with SOCl₂ and POCl₃ were not successful. Alternative methods involving the use of coupling reagents were sought. Duspara *et al.* highlight the use of **108** in the coupling of quinazolinones with various aromatic and aliphatic anilines.²⁷¹ Due to the associated toxicities of by-product hexamethylphosphoramide from using coupling reagent **108**, **109** was selected for this coupling. Despite best efforts **98** was not formed during this reaction, rather **111** was the exclusive product. This can be explained through the pKa of both the aniline and phenol moieties of **110** (Figure 83).

Literature precedence was highlighted for the synthesis of commercial, clinically relevant inhibitors **99** and **116**, which did not include the quinazolinone intermediate. The Dimroth rearrangement was applied to a trial reaction and successfully synthesised quinazoline **119**. For the synthesis of this quinazoline focused library, the synthetic procedure offered a route which is one step shorter than the published procedure with easier purifications, less toxic reagents and easier purifications. Synthesis of the key intermediate formamidine **121** was achieved in 15 minutes with quick chromatography purification. Nucleophilic substitution of the fluoro substituent was achieved overnight in excellent yields often not requiring chromatography purification. The Dimroth rearrangement was complete in 15 minutes with **98** requiring precipitation with diethyl ether as its form of purification. Conversely, whilst also complete in 15 minutes **101** and **123** required simple chromatography purification. Unfortunately the proposed compound **102** could not be achieved through either Fe(acac)₂ or manganese salen benzylic fluorination conditions.

Kinase based screening, using the Z-LYTE assay platform, was used to assess the selectivity of the quinazoline focused library. Firstly, this library was screened against a panel of closely related kinases and non-related kinases known to be targeted by clinically relevant VEGFR₂ inhibitors. This selectivity screen highlighted **98** and **101** not to be clearly selective, when tested at a 1 μM concentration. The other members of the VEGFR family (1 and 3) were targeted by **98** (81 and 101% inhibition respectively) and **101** (79 and 100% inhibition respectively). Other kinases targeted by **98** include ABL1 (50% inhibition), EGFR (78% inhibition), PDGFR α (73% inhibition) and RET (98% inhibition).

Fortunately, both **98** and **101** exhibited activity against VEGFR₂ (with a K_i of 2.375 and 3.75 respectively). The activity exhibited by **98** was similar to that described in the literature (2

nM). Unfortunately, **123** did not inhibit VEGFR₂ in the range of concentrations tested (IC₅₀ > 1 μM) and therefore can be concluded that **123** only weakly binds to this panel of kinases. However to completely preclude this quinazoline focused library from the development of a VEGFR₂ specific PET probe, the expression levels of RET and VEGFR₃ needs to be determined in VEGFR₂ positive cell lines. Also, the synthesis of another hybrid compound should be developed is presented in Figure 93, to probe whether the selectivity comes from the piperidine moiety.



Proposed compound for further testing

Figure 93: Proposed compound which should be synthesised to determine where the selectivity for VEGFR₂ arises from

In vitro selectivity assays were devised around dimer **124**, published by Li *et al.*²⁰⁶ This assay presented an ideal opportunity to obtain on-target data for VEGFR₂ inhibition. However, as will be discussed in Chapter Five (5.2.1.4), the synthesis of target **125** could not be achieved.

Chapter Five

Radiochemistry

5. Radiochemistry

5.1 Selection of the library for radiochemical evaluation

Based on the results of Chapter Four, the quinazoline focused library was selected for evaluation of route for radiolabelling precursors. This chapter will describe the incorporation of fluorine-18 into the quinazoline focused library.

5.2 Results and discussion

5.2.1. Chemistry

5.2.1.1. Synthesis of a precursor for **98**

Figure 94 highlights potential strategies for the synthesis of a suitable precursor for radiolabelling.

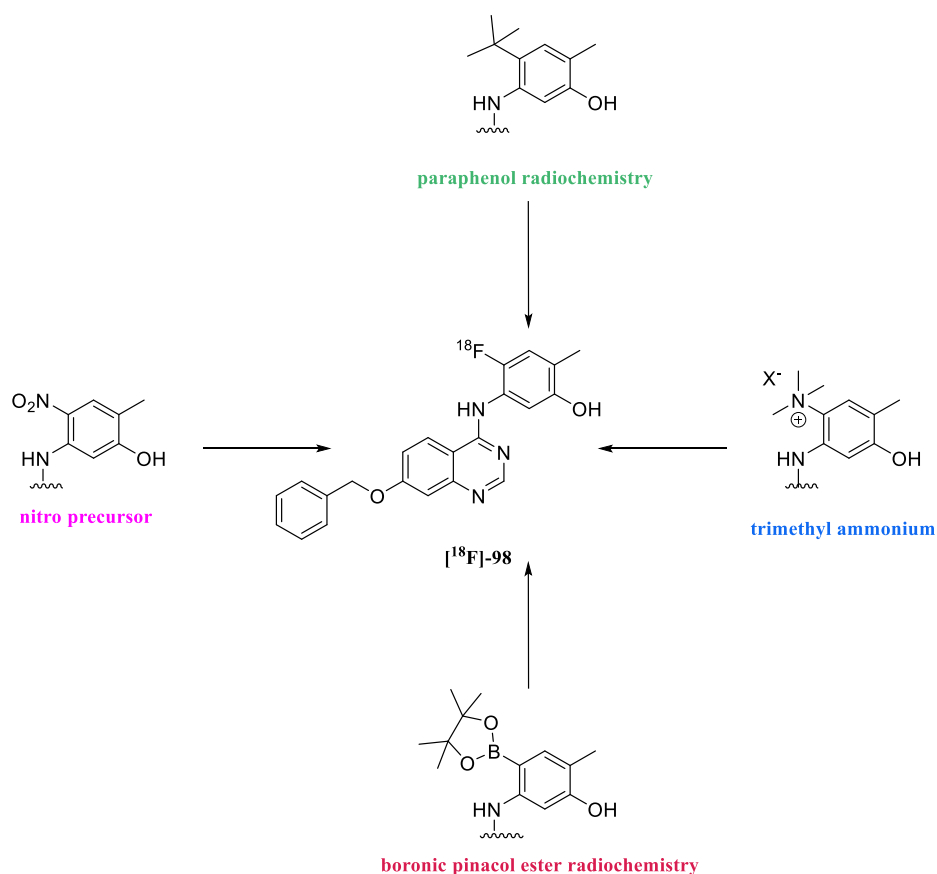


Figure 94: Envisaged strategies for the radiochemical synthesis of $[^{18}\text{F}]\text{-98}$

Despite having more established radiochemistry, both the nitro and trimethyl ammonium are not easily accessible through conventional chemistry. A survey of the literature highlighted a precedence for the radiolabelling of para-phenol groups and copper catalysed fluorination of boronic pinacol esters, as identified by both the Sanford and the Gouverneur groups, both discussed in Chapter One (1.3.1.1).^{249, 250} On further examination of **98**, both these techniques could be utilised for the synthesis of a suitable precursor for radiolabelling. Figure 95 proposes the precursors required for adapting the procedures developed by the Gouverneur group.²⁴⁹

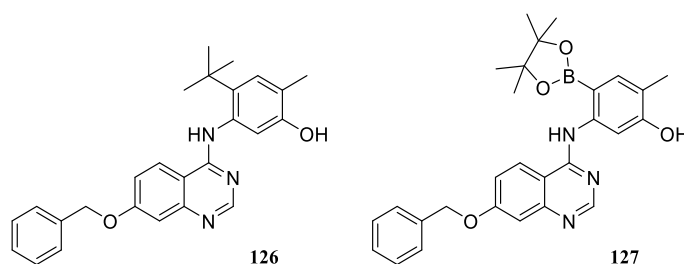
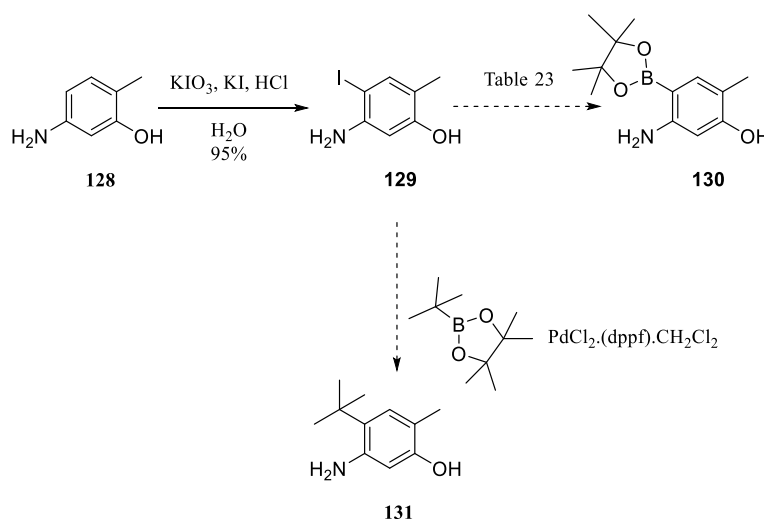


Figure 95: Proposed structures of the precursors **126** and **127** for **98**

By examining the structures of **126** and **127** a convergent approach could be used for the synthesis of both these precursors. Scheme 37 highlights the approach used. Compound **129** was synthesised by iodination of cresol **128** in a 95% yield. The synthesis of **129** allows further diversification by Suzuki and Miyaura borylation reactions, synthesising fragments required for the Dimroth cyclisation to **126** and **127**.



Scheme 37: Synthesis of **129** for further diversification for an appropriate precursor

The synthesis of **130** was attempted using different conditions to borylate **129**, as shown in Table 23. However, as the borylation of **129** was not achieved, attention was focused on the introduction of the *tert*-butyl moiety of **131**. Examining the structure of **129**, this was not surprising as the phenol moiety is unprotected and pushes electrons into the ring which deactivates the system from performing the oxidative addition to the palladium.

Table 23: Summary of the attempts to introduce the boronic pinacol ester on **129**

Entry	Catalyst (% loading)	Base	Time	Solvent	Boron source	Outcome
a	Pd (5%)	NEt ₃	18 h	1,4-dioxane	BH(pin)	no reaction
b	PdCl ₂ (PPh ₃) ₄ (5%)	KOAc	2.5 h (mw)	1,4-dioxane	B ₂ (pin) ₂	no reaction
c	PdCl ₂ (PPh ₃) ₄ (5%)	KOAc	2.5 h (mw)	DMF	B ₂ (pin) ₂	no reaction
d	PdCl ₂ (PPh ₃) ₄ (7.5%)	KOAc	1.5 h (mw)	DMF	B ₂ (pin) ₂	no reaction

The reaction could have failed due to the electron donating nature of both the phenol and aniline moiety, deactivating **129** from undergoing oxidative addition to the palladium complex. Due to the failure to introduce the boronic ester moiety to **129**, Scheme 37 also highlights the Suzuki reaction of cresol **129**. As the synthesis of **131** was not successful, under standard conditions, priority was given to the synthesis of the other precursors for [¹⁸F]-**101** and [¹⁸F]-**123**.

5.2.1.2. Synthesis of a precursor for **101**

An ideal precursor for **101** is a nitro, trimethyl ammonium or a boronic pinacol ester in that preceding order due to the complexity of the radiolabelling procedures (Figure 96). The nitro and trimethyl ammonium groups can be radiolabelled using conventional radiolabelling strategies. The boronic ester radiochemistry could be achieved using those methods highlighted by the Gouverneur group.²⁴⁹ In the interest of time and for easy radiolabelling, attention was focused solely on the synthesis of a nitro or trimethylammonium precursor. As discussed in Chapter One (1.3.3.7), one of the criterion of a PET tracer should be ease of radiolabelling. Both the nitro and trimethyl ammonium both satisfy this criteria as the radiolabelling step will be conducted in the last step. By examining the structure of **101**, the synthesis of a nitro or trimethyl ammonium precursor requires less elaborate chemistry, due to ease of availability of all reagents.

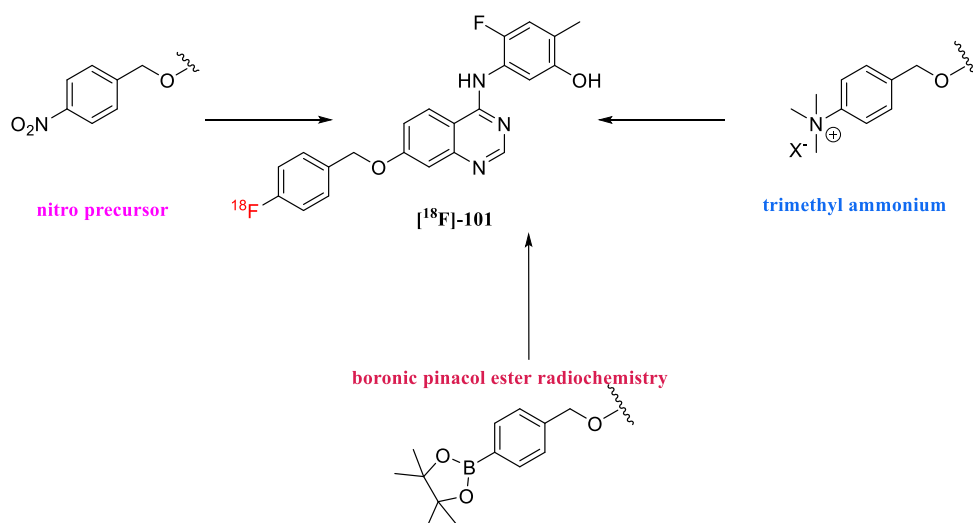
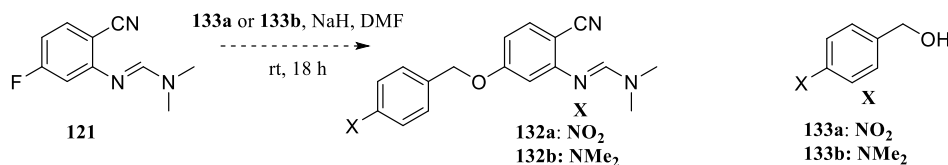


Figure 96: Proposed radiochemical strategies for the synthesis of [¹⁸F]-**101**

Scheme 38 describes the synthesis of **132a** which was initially attempted using the same methods as those highlighted in Chapter Four (4.3.1.3). The nucleophilic of **121** with 4-nitrobenzyl alcohol **133a** did not yield **132a** over the course of 24 hours. Additional heating also only yielded a disappointing conversion to **132a** as confirmed by LCMS which was not isolated (Scheme 38).



Scheme 38: Attempted synthesis of **132a** and **132b**

Disappointingly, the reaction of **121** with **133b** was not successful under any conditions. A plausible explanation could be when product **132b** is formed it is debenzylated forming an aminoquinone type structure (Figure 97). Although the aminoquinone was not observed by LCMS, **134** was the only fragment isolated by the mass spec.

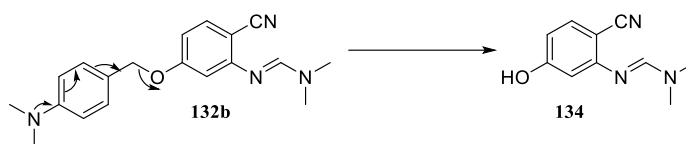
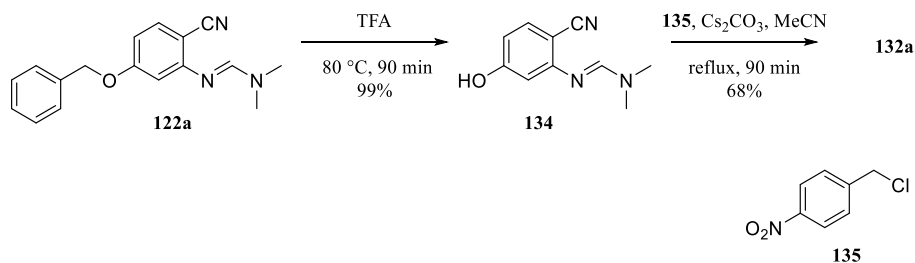


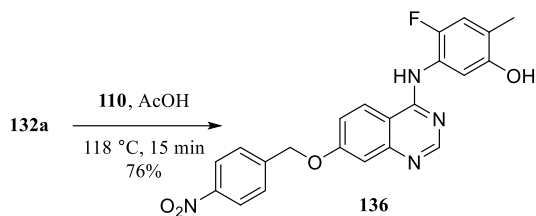
Figure 97: Plausible side reaction - resulting in the synthesis of **146**

Revision of the synthetic strategy allowed the microwave assisted deprotection of the benzyl group of **122a**, revealing the hydroxyl moiety of **134** in an 89% yield (Scheme 39). Alkylation of **134** with 1.5 equivalents of **135** afforded **132a** in a 71% yield, after column chromatography purification.



Scheme 39: Alternative strategy to synthesise **132a**

The Dimroth rearrangement of **132a** proceeded in a smooth manner, affording **136** in an 84% yield (Scheme 40).



Scheme 40: Synthesis of the precursor **136**

5.2.1.3. Synthesis of the radiochemical precursor to **123**

Two distinct strategies were envisaged for the synthesis of a precursor for **123**. The first strategy involved direct fluorination on the quinazoline scaffold, whilst the second strategy involved fluorination of the aniline fragment (Figure 98).

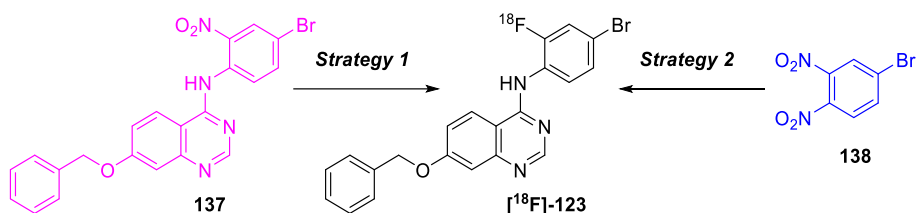
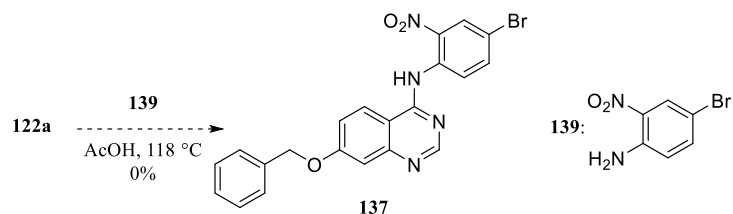


Figure 98: Approaches utilised for the synthesis of a precursor to **123**

The first strategy envisaged the direct fluorination of the scaffold, via a nitro precursor. The Dimroth rearrangement with the nitroaniline **139** and **122a**, only reached a 10% conversion via LCMS over a 90 minute period (Scheme 41). This contrasts with the synthesis time of the cold standards, in which reaction times were 15 minutes and **137** could not be separated from **139**, by TLC. Due to the half-life of fluorine-18 this strategy was attractive due to the fluorination occurring in the last step of the synthesis. Conversely, the scaffold is largely deactivated and not susceptible towards fluorination, therefore this precursor was dropped in favour of the more attractive strategy two which will be discussed further in this Chapter (5.2.2.2).



Scheme 41: Attempted synthesis of precursor **137**

5.2.1.4. Synthesis of NOTA-ZD-G2 **125**

As discussed in Chapter Four, **125** was selected for use as a potential screening tool. Therefore, this section will discuss the synthesis of **125** only (Figure 99).

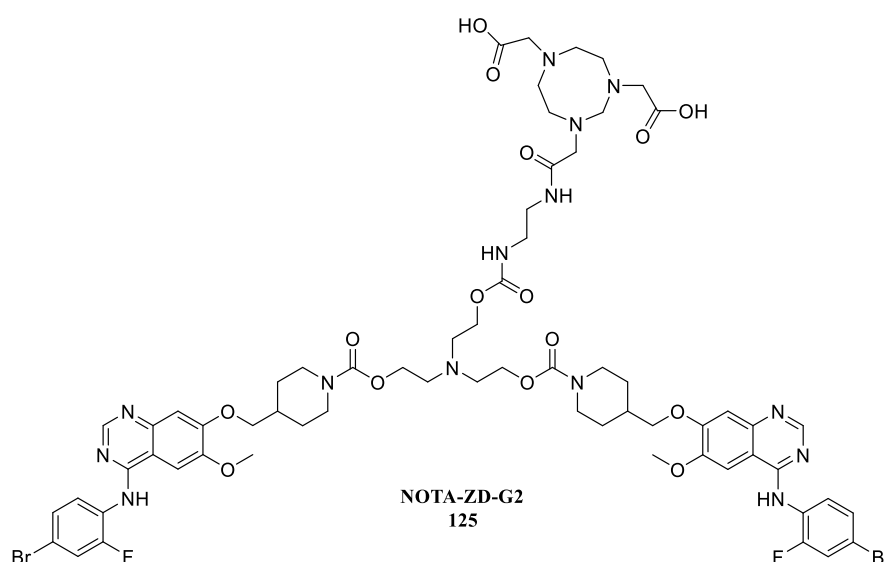
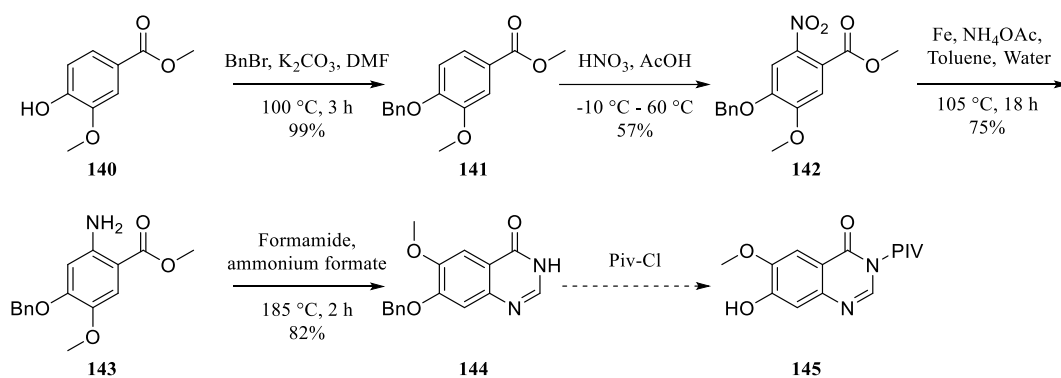


Figure 99: Structure of target **NOTA-ZD-G2 125**

The published method of synthesising quinazoline **4** fragment of **125** involves many protection and deprotection methods.²⁰³ Initially the synthesis of **4** was simple and the synthetic procedure is shown in Scheme 42. The first step was the benzylation of methyl vanillinate **140** in a 99% yield. According to literature precedence, nitration of **141** should have proceeded to completion at room temperature. After optimisation, it was found that cooling to 0 °C for a period of 20 minutes was enough for complete generation of the nitronium ion and avoiding exotherm, followed by gentle heating to 60 °C was sufficient to cause nitration of **141**, but in varying yields of 19-57%. A literature survey highlighted two distinct methods for the reduction of **142**. These methods included using either iron powder and ammonium acetate or sodium borohydride and nickel dichloride. Utilising the sodium borohydride, nickel dichloride reaction a gum-like product was obtained which could not be

successfully purified. Switching to the other literature method for reduction, iron powder and ammonium acetate, the reduction was successful but often resulted in variable yields (36-75%). This could be due to the iron powder and ammonium acetate aggregating in the reaction flask. The work-up procedure stated the sample is stirred in ethyl acetate, to extract any aniline from the aggregated reduction products. Insufficient extraction from the iron aggregates could be responsible for the observed varying yields. Reduction using conventional hydrogenation was not utilised due to sensitivity of the benzyl group towards cleavage.



Scheme 42: Initial attempted synthesis of **4**, via quinazoline **144**

The Niementowski cyclisation of **143**,²⁰³ proceeded smoothly with a yield of 82%. Pivalate protection and debenzoylation to afford **145**, was very disappointing and the product was not successfully purified from the reaction mixture, leading to a review of the remaining steps of the synthetic pathway.

Further analysis of the proposed synthetic pathway revealed several more protection and deprotection steps. Analysis of the literature revealed an 11 step synthesis to **146** (Figure 100) prior the steps required for the conjugation of the NOTA macrocycle.

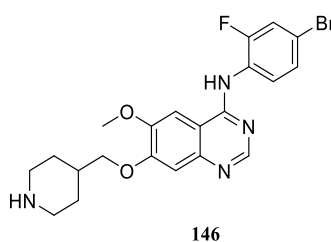
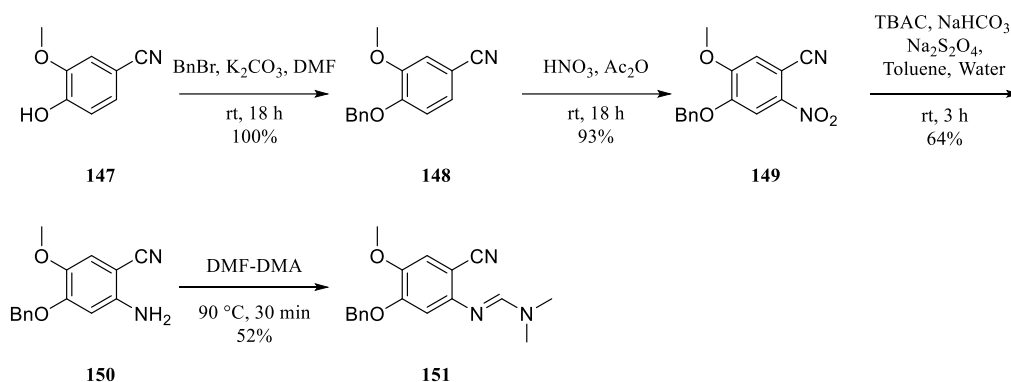


Figure 100: Structure of key intermediate **146**

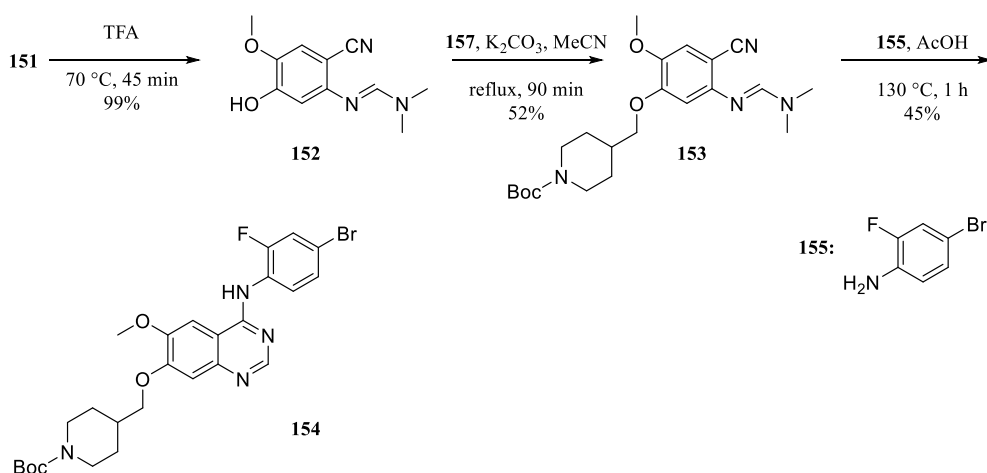
Due to the success of the Dimroth rearrangement towards the synthesis of the quinazolines described in Chapter Four (4.4.1.3), this method was utilised for the synthesis of **146**. The modified synthetic pathway is depicted by Scheme 43. First step in the synthesis was benzyl protection of **147**, which resulted in a quantitative yield of **148** and did not require any aqueous work up procedure as precipitation with brine allowed for the collection of **148** without any DMF impurity (as seen by ^1H NMR). Again, the nitration of **148** proceeded more smoothly overnight and the addition of water afforded **149** as a precipitate in a 92% yield. Thus far this procedure is simpler and higher yielding than the synthesis via quinazolinone **144**, due to the minimal synthetic steps required and the lack of numerous protection and deprotection steps with the use of less toxic reagents.



Scheme 43: Synthesis of *N,N*-dimethylformamidine **151** – the key intermediate for the Dimroth mediated synthesis

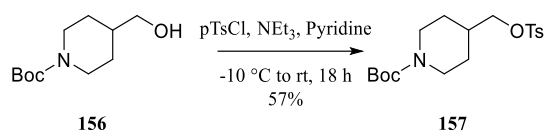
Reduction of **149** required little optimisation, however it was determined that tetrabutylammonium chloride (TBAC) was essential, as switching this phase transfer catalyst to another ammonium chloride was detrimental to the reaction. Work up of **150** required optimisation as **149** and **150** could not be separated on a TLC plate, due to very similar R_f values. Reducing the volume of the organic phase and addition of diethyl ether, cooling to 0 °C followed by the addition of HCl in dioxane, resulted in the hydrochloride salt of **150**. Collection of the hydrochloride salt and subsequent desalting in methanol and adjusting the pH to 8 affords **150** without any impurity, as judged by ^1H NMR and LCMS. Formation of *N,N*-dimethylformamidine **151** required a large excess of DMF-DMA due to solubility issues in toluene and smaller volumes of DMF-DMA. Attempts to aid solubility failed as **151** was insoluble in solvents required for the formation of formamidine. Therefore, column chromatography removed any excess DMF-DMA to afford **150** in an 85% yield.

Introduction of piperidine moiety was achieved through TFA deprotection of the benzyl group, as hydrogenation cannot be applied due to the sensitivity of the *N,N*-dimethylformamidine group (Scheme 44). This TFA debenzylation was quantitative in yield and was alkylated with tosylate **157**, which after column chromatography afforded **153** in a 58% yield. The Dimroth rearrangement step was found to require one hour at 130 °C to achieve the cyclisation to **154** in a 45% yield. Unfortunately, **153** underwent some decyanation (<5%) which is observed to some degree in all Dimroth rearrangements, also some **152** remained regardless of any extra heating.



Scheme 44: Synthesis of **154** via the Dimroth rearrangement

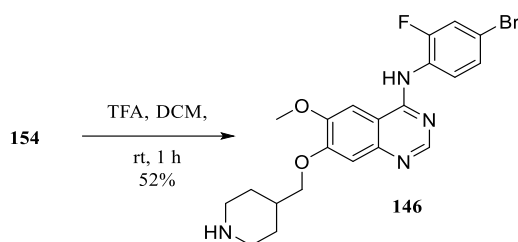
A literature precedence for the synthesis of tosylate **157**, began with the simple alkylation of the hydroxyl **156** with tosyl chloride to achieve **157** in a 57% yield after column chromatography purification (Scheme 45).



Scheme 45: Synthesis of tosylate **156**

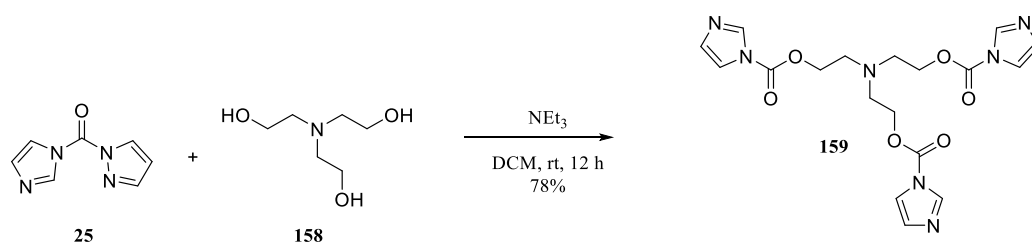
Now the synthesis of quinazoline **154** had been achieved, deprotection of the BOC protecting group revealed piperidine **146**. In contrast, the literature method utilises the standard TFA in DCM deprotection and an aqueous work up resulted in loss of product (Scheme 46).

However, performing direct chromatography (0-20% MeOH: DCM) afforded **146** in a 52% yield, without loss of product.



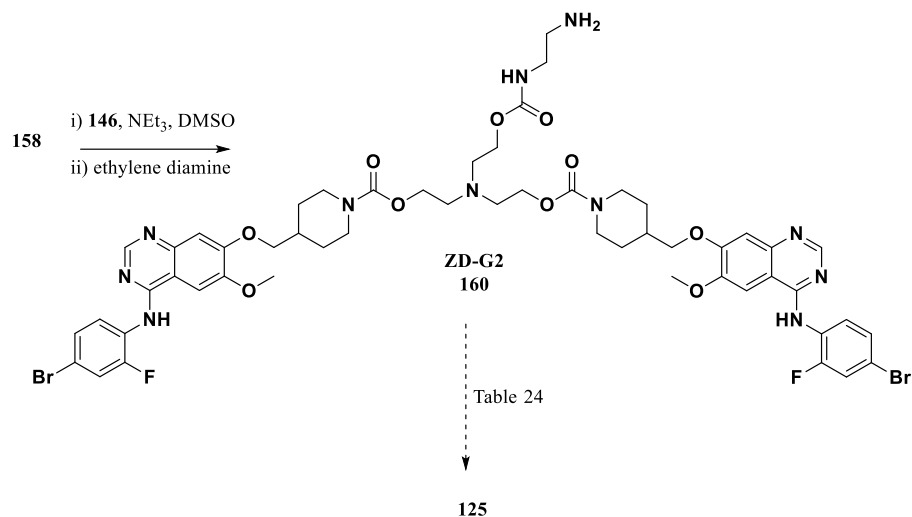
Scheme 46: TFA deprotection of the piperidine to reveal **146**

In order to form the linker required to synthesise **159**, triethanolamine **158** was reacted with **25** (CDI) in the presence of triethylamine which yielded **159** (Scheme 47).



Scheme 47: Synthesis of linker **158**

The linker **159** was combined with two equivalents of **146** and one equivalent of ethylene diamine to form **160**, which was then purified by semi-prep HPLC in yields between 9-15% (Scheme 48).



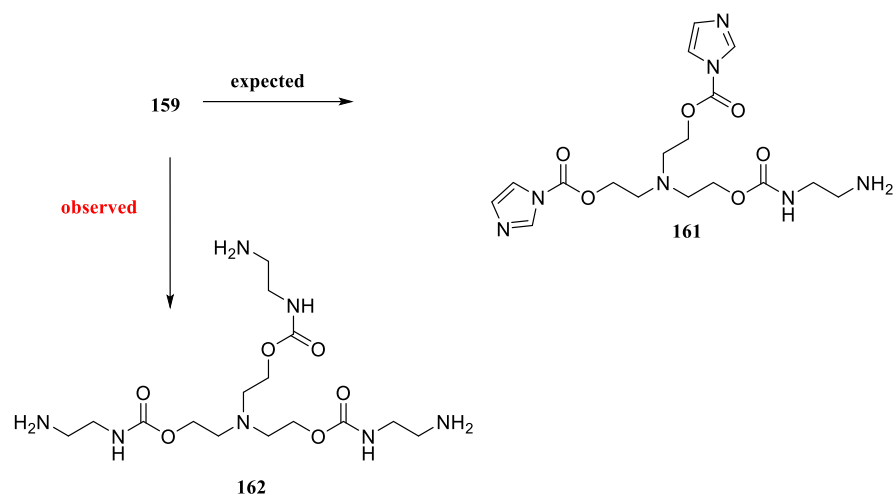
Scheme 48: Synthesis of **125**

Attempts to conjugate the NOTA onto the scaffold of **160** consistently proved unsuccessful. Table 24 summarises attempts to perform this conjugation.

Table 24: Attempts at the conjugation of NOTA-NHS with **160**

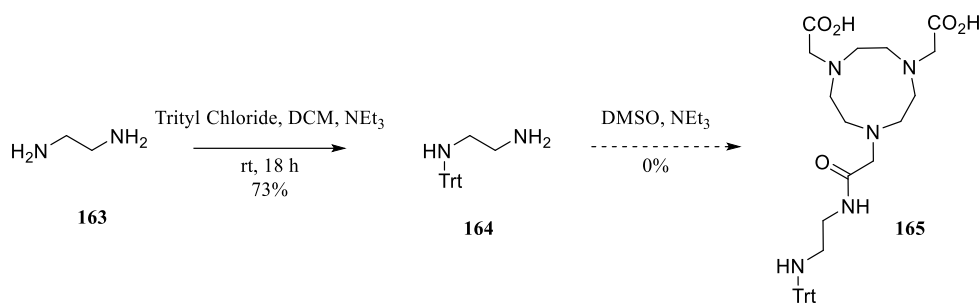
Time	NOTA-NHS equivalents	NEt ₃ equivalents	Outcome
18 h	1	1	No reaction
48 h	1 followed by 10 after 18 h	1	No reaction
48 h	1 followed by 10 after 18 h	1 followed by a further 1 after 18 h	No reaction

Alternative strategies to aid the NOTA-NHS conjugation with **146** were explored (Scheme 49). Initial attempts to couple **159** with one equivalent of ethylene diamine resulted in the unexpected formation of **162**. This occurred through displacement of all three imidazoles with ethylene diamine, which did not result in the synthesis of **161**.



Scheme 49: Alternative strategies for NOTA-NHS conjugation

Despite published procedures for the conjugation of the NOTA, no conjugation was observed. Alternative strategies using HPLC as an evaluation tool, led to the conjugation of **163** with trityl chloride, incorporating protecting group into **164** with a chromophore for easy detection (Scheme 50). Initial attempts to conjugate the NHS-NOTA ester proved successful, although subsequent attempts at the conjugation failed.



Scheme 50: Attempts at the NOTA conjugation with a chromophore

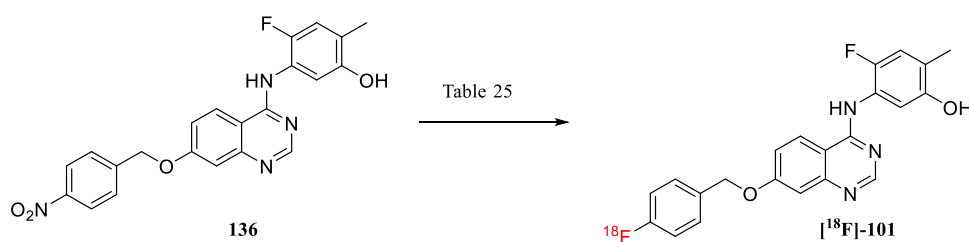
However, due to time constraints an alternative strategy for biological evaluation was utilised as discussed in Chapter Four.

5.2.2. Radiochemistry

Attempts to radiolabel via an S_NAr reaction using no carrier added fluorine are outlined in this next section. Solubility of the quinazolines was a major issue, with the quinazoline compounds only being soluble in DMSO, DMF and DMA.

5.2.2.1. Synthesis of [^{18}F]-101

Initial attempts to fluorinate **136** failed due to inactivated nature of the benzyl group towards nucleophilic substitution with the fluoride (Scheme 51). During the optimisation of the radiochemistry, a major side product was identified. The side product was identified as the debenzylated product **166**. Unfortunately the precursor was base sensitive. The optimisation for this radiolabelling is shown in Table 25.



Scheme 51: Radiosynthesis of [^{18}F]-101

Table 25: Summary of the conditions utilised for the attempted fluorination of **136**, using 2 mg of precursor with a 300 μ L reaction volume.

Entry	K ₂₂₂ (mg)	Base (mg)	Solvent	Temperature (°C)	Time (minutes)	Conventional or microwave	Outcome
a	3	K ₂ CO ₃ (2)	DMSO	100	20	conventional	no product, 166
b	2	200 μ L of 1M K ₂ CO ₃	DMSO	100	20	conventional	no product, 166
c	2	K ₂ CO ₃ (0.7)	DMF	150	10	conventional	no product, 166
d	2	K ₂ CO ₃ (1.4)	DMF	150	10	conventional	some radiolabelling, 166
e	2 (18- C-6)	K ₂ CO ₃ (0.7)	DMF	150	10	conventional	no product, 166
f	-	Cs ₂ CO ₃ (2)	DMF	150	10	conventional	no product, 166
g	2	KHCO ₃ (2)	DMF	150	10	conventional	no product, 166
h	2	K ₂ CO ₃ (0.7)	DMSO	150	5	conventional	some radiolabelling, 166
i	2	K ₂ CO ₃ (0.7)	DMA	150	10	conventional	no product, 166 with lots of fluorinated by-products some
j	2	K ₂ CO ₃ (0.7)	DMF	150	5	mw	radiolabelling, 166
k	2	K ₂ CO ₃ (0.7)	DMF	150	10	mw	complete degradation of 136 and 166
l	2	K ₂ CO ₃ (0.7)	DMSO	150	5	mw	no radiolabelling, 166

Entries **d** and **j** in the above table are the only two conditions which successfully produced some fluorinated product. The microwave provided more consistent results than the conventional heating block. However, due to unknown reasons, the reaction could not

always be replicated. As shown in Figure 101b there is the presence of a large amount of by-product with a retention time of four minutes.

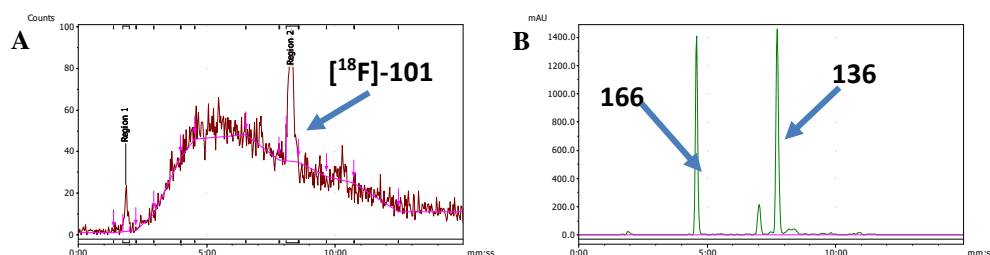


Figure 101: A) Radiochromatogram for entry J of Table 25, showing excess fluoride streaking the column with the peak at approximately eight minutes. B) HPLC chromatogram demonstrating by-product **166** at approximately four minutes, with UV detection.

Figure 101b shows the development of the by-product **166**, allowing the reaction mixture to decay, until no radioactivity was detected, mass spectrometry analysis was performed to identify the by-product. Mass spectrometry analysis highlighted the presence of the debenzylated product **166** (Figure 102), which occurred during the reaction. This by-product was further confirmed through the synthesis of a cold standard of **166** and comparison of HPLC retention times.

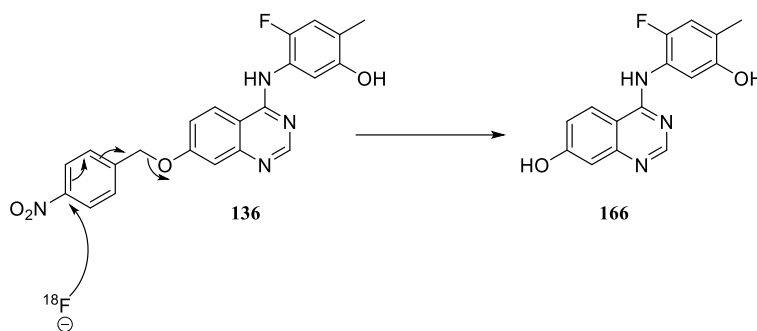
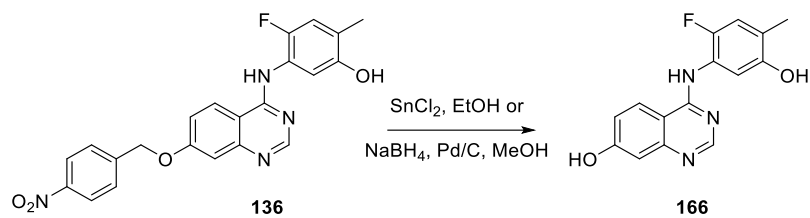


Figure 102: Structure of the identified by-product **166** by mass spectrometry.

A method for the HPLC purification of **166** from **101** was not achieved due to overlapping peaks with narrow retention times. In order to investigate any purification methods and examining the structure of the compound, the only way to force separation was reduction of the nitro to the aniline. It is important to note that upon reduction of the nitro precursor, debenzylation was also observed. This could be suggestive that **136** is not suitable for radiolabelling via a $\text{S}_{\text{N}}\text{Ar}$ approach.



Scheme 52: Reduction conditions utilised in order to purify the reaction, producing by-product **166**

Owing to the lack of success thus far, the fluorination of **136** was attempted on a TRASIS automated synthesis module which removes any manual errors from the fluoride drying step, a possible source of variability or error in the radiolabelling procedure. A fluoride drying programme is well established in-house on this system (Figure 103).

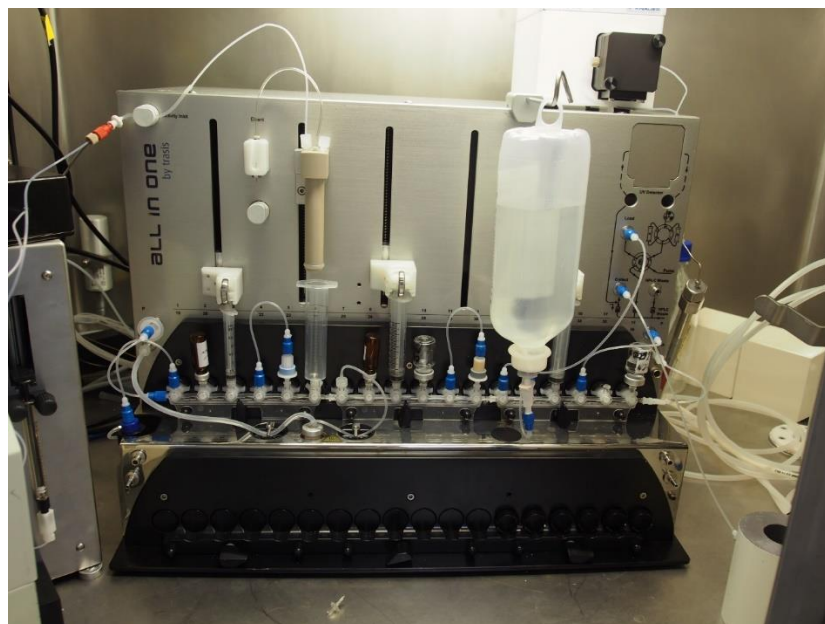
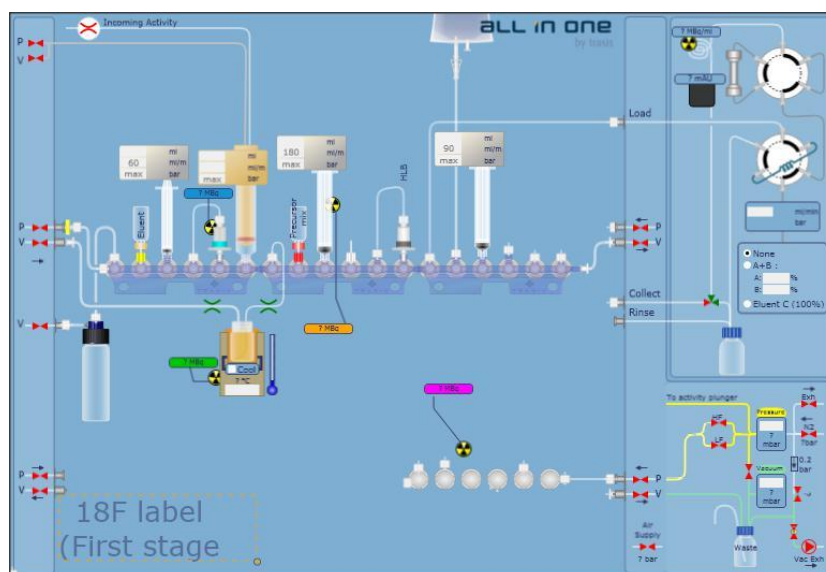


Figure 103: A) Programme used for the attempted fluorination B) Picture of the TRASIS Allinone synthesiser used

However, attempting the fluorination using identical conditions to those identified manually, except with a larger volume limiting any loss in the transfer to the reactor vessel, also proved unsuccessful. Table 26 shows the two conditions attempted on the TRASIS module.

Table 26: Attempts at the synthesis of [^{18}F]-**101** from **136** using the TRASIS allinone synthesiser

Entry	DMF (μL)	MeCN (μL)	outcome*
a	400	0	0.03% radiolabelling not purified
b	400	600	0.03% radiolabelling not purified

*This is the % of activity remaining in the reaction vial (decay corrected) after measuring activity in waste and QMA cartridge

The radiochemical peak was confirmed through spiking the sample with the cold standard, a delay of ten seconds is typical, as shown in Figure 104.

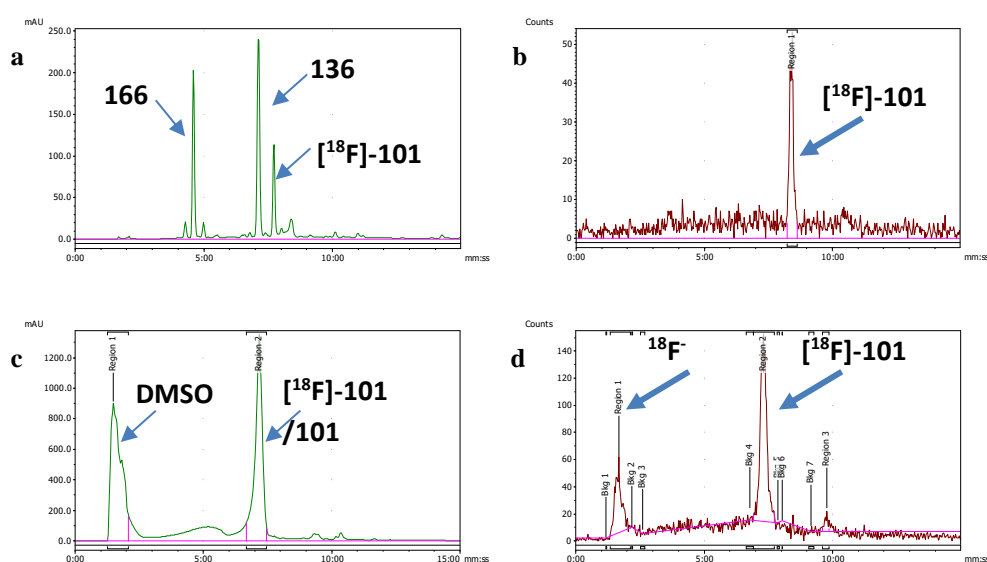


Figure 104: A) UV trace for the crude reaction mixture from TRASIS labelling B) Fluorine-18 trace for the radioactivity for the crude reaction C) Spike sample for synthesis confirmation using the same crude reaction mixture D) Fluorine-18 trace for the spike sample (approximately 10 second delay from UV detection to radio-detection)

Figure 104 shows the representative HPLC traces obtained from the TRASIS labelling method. Figure 104a and 104b are representative of the crude reaction mixture, however when the crude reaction mixture was spiked with an authentic sample of **101**, a shift in the radioactivity peak was observed over a 20 minute period (Figure 104d). This demonstrates radiotracer instability highlighting its degradation and more studies are required to allow further biological evaluation, due to its lack of reproducibility. This lack of reproducibility stems from the production of by-product **166**, occurring in every reaction to differing degrees.

To circumvent this, non-S_NAr based fluorinations could be utilised for radiolabelling purposes. These strategies, as previously discussed in this section, are the copper mediated fluorinations of boron groups as identified by the Gouverneur and Sanford groups. The mechanism proposed by Sanford is shown in Figure 105. It would be interesting to note whether the instability observed during the TRASIS automated radiolabelling would also be a feature of the Sanford or the Gouverneur techniques. However as the unlabelled cold standard **101** is stable, this could be a feature of the matrix the radiolabelling occurs in, which causes the observed instability and changing the type of radiolabelling could circumvent this, such as switching from nucleophilic radiolabelling to the boron radiolabelling.

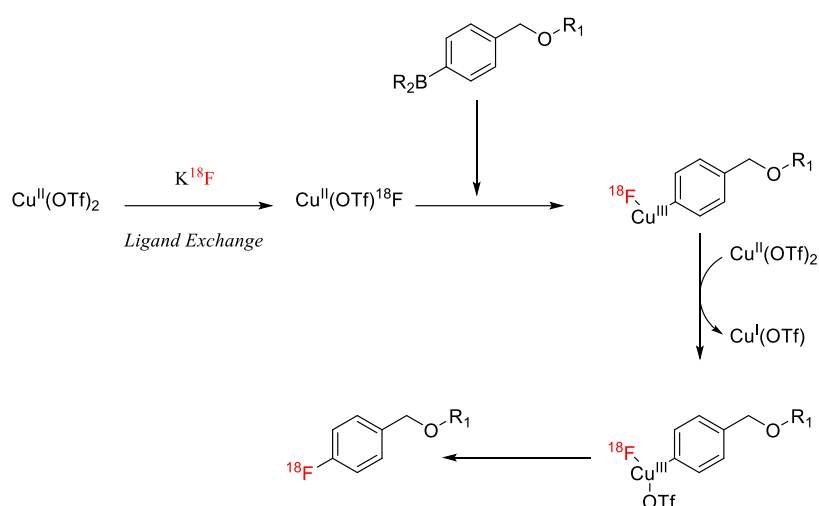
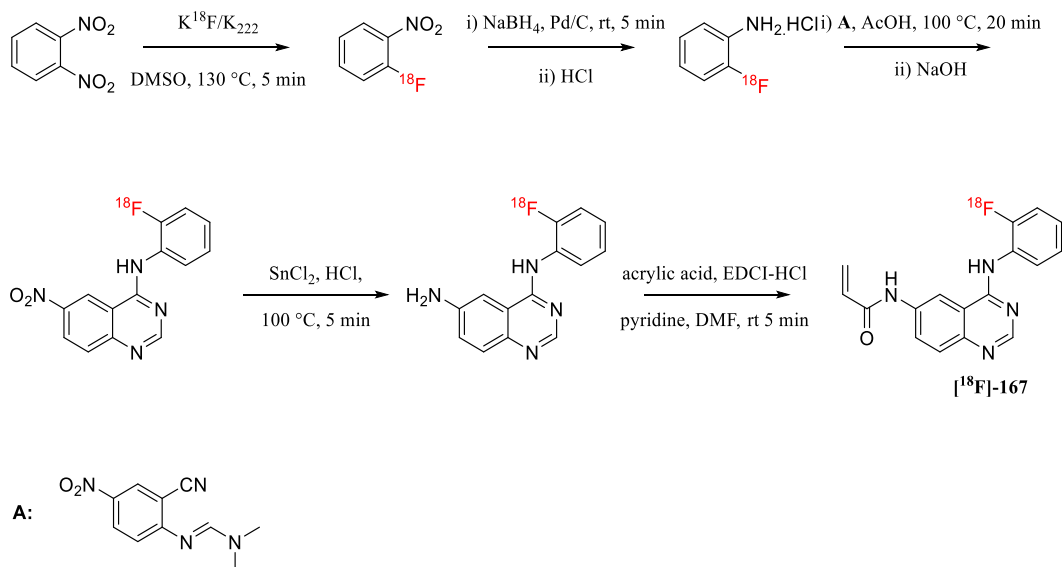


Figure 105: Proposed mechanism for the fluorination of boronic species, postulated by Sanford's group²⁴⁸

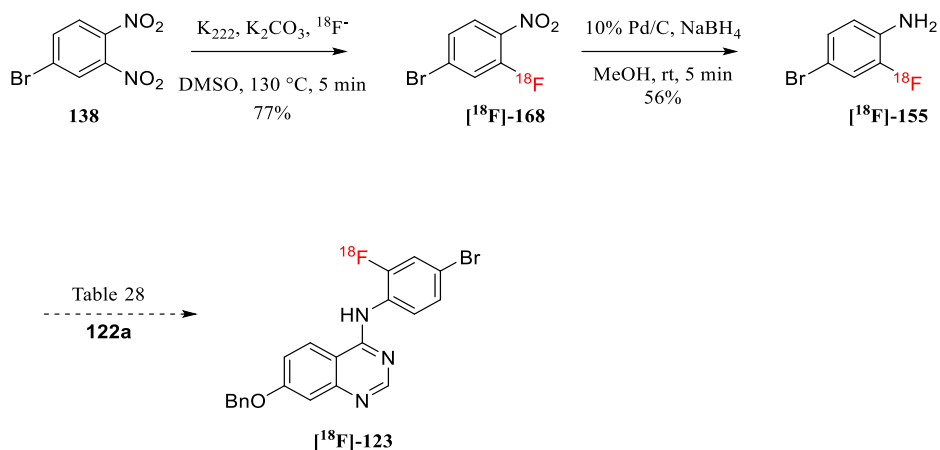
5.2.2.2. Synthesis of [^{18}F]-**123**

As previously explained in this Chapter (5.2.1.3) the synthesis of **137**, for the direct fluorination on the quinazoline scaffold, was not successful. A review of the literature highlighted the synthesis of [^{18}F]-**167** by Vasdev *et al.* which was synthesised via the Dimroth rearrangement (Scheme 53).³⁵⁴



Scheme 53: Synthesis and structure of [^{18}F]-**167**, synthesised via the Dimroth rearrangement

Based on earlier work in Chapter Four (4.1.3.4), and due to the precedence established by Vasdev *et al.*, the radiochemical synthesis of the quinazoline via the Dimroth rearrangement was attempted.³⁵⁴ The synthesis of the aniline fragment is shown in Scheme 54. A literature precedence for the synthesis of [^{18}F]-fluoroanilines is well established, thus providing an excellent reference point for reaction optimisation.³⁵⁵ Scheme 54 highlights the synthetic procedure established for this reaction, whilst Table 27 describes the optimisation for the initial fluorination, when using 5 mg of **138**.



Scheme 54: Radiosynthesis of the aniline fragment required for the Dimroth rearrangement, yields are reported as decay corrected

As shown in Table 27, increasing the amount of potassium carbonate in the reaction was detrimental for successful fluorination of **138**. Interestingly, the fluorination only occurs at the position shown in Scheme 54, due to the mesomeric effect of the bromine. This was further confirmed by HPLC comparison of the standards.

Table 27: Investigation of the amount of base used in the initial fluorination attempts, using 5 mg of **138**

Entry	K ₂₂₂ (mg)	K ₂ CO ₃ (mg)	% Purity	Major Product
a	5	0.5	98	Yes
b	5	1	52	No

Figure 106a shows the crude HPLC chromatogram obtained for the initial fluorination, which highlights there is no competition for the fluorination position. Solvent exchange using a C18 cartridge allows the use of methanol directly into the scintillation vial. Reduction of [¹⁸F]-**168** to proceed smoothly, at room temperature using Pd/C in methanol. A crude sample (20 μL of a 2 mL reaction volume) injected onto the HPLC indicated [¹⁸F]-**168** was not present after a five minute reaction time. Figure 106b indicates impurities (regions 1-3)

which are present in the initial step. These impurities can be detected when the baseline is expanded in Figure 106a.

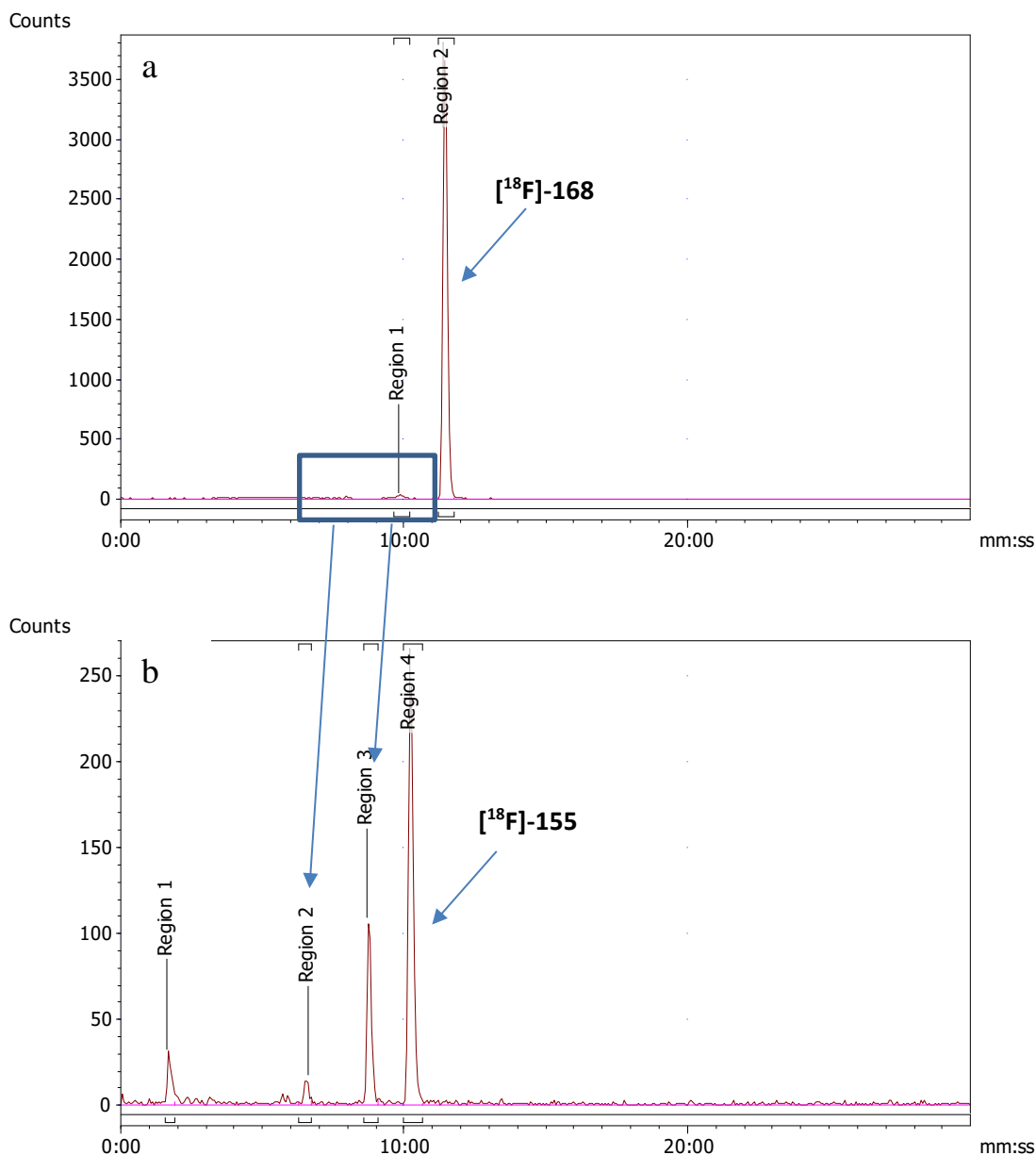


Figure 106: A) HPLC radiochromatogram for the radiosynthesis of $[^{18}\text{F}]\text{-168}$, showing a minimum radiochemical purity of 95%. B) Reduction of $[^{18}\text{F}]\text{-168}$ to $[^{18}\text{F}]\text{-155}$ (region 4). Regions 1-3 can be seen upon expansion of the top chromatogram

The third step in the radiosynthesis of $[^{18}\text{F}]\text{-123}$ was the Dimroth rearrangement. Removal of methanol was necessary as the rearrangement required acetic acid for the rearrangement. Direct removal of the methanol under a nitrogen flow and heating, resulted in the loss of $[^{18}\text{F}]\text{-155}$, owing to its volatility. An alternative removal of the methanol was required. Following filtration of the reaction mixture through a particle filter in order to remove

palladium-carbon catalyst, the reaction mixture was trapped by the utilisation of a HLB cartridge (Figure 107). This also allowed the facilitation of solvent exchange, from methanol to acetic acid.

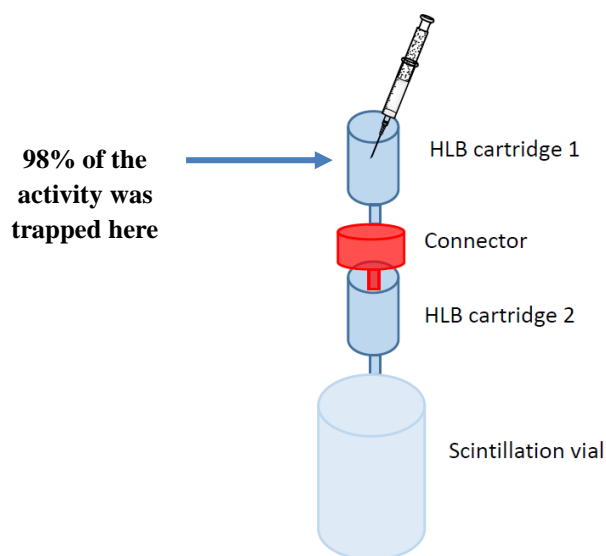
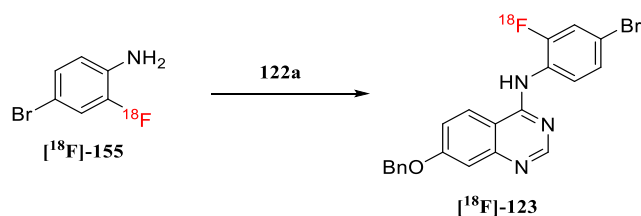


Figure 107: Schematic showing the position of the cartridges to identify where the activity would be trapped. The blue arrow indicates where the radioactivity was trapped

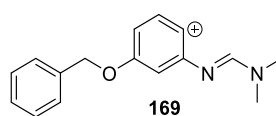
Ensuring the radioactivity is trapped on the HLB cartridges, Figure 107 shows the initial positioning of the cartridges, each cartridge and vial is counted to locate the activity. Pleasingly the activity trapped on the first HLB cartridge, resulting in only one cartridge required in further experiments. A smaller 30 mg cartridge was utilised in order to ensure the smallest volume of acetic acid necessary to remove the activity from the cartridge for the final reaction step. The Dimroth rearrangement required optimisation as shown in Table 28.

Table 28: Summary of the Dimroth rearrangement conditions used to synthesise [¹⁸F]-**123**

Entry*	Heating	Time (minute)	Temperature (°C)	Outcome	Solvent
a	conventional	10	100	decyanation	AcOH
b	conventional	15	120	decyanation	AcOH
c	conventional	20	120	decyanation	AcOH
d	conventional	20	130	decyanation	AcOH
e	microwave	10	118	decyanation	AcOH
f	microwave	10	118	decyanation	<i>t</i> -BuOH then AcOH
g	microwave	20	118	decyanation	AcOH
h	microwave	15	118	and probable product	AcOH

*10 mg of **122a** used in this optimisation

As indicated in Table 28, a major by-product was seen on the UV-HPLC trace. Allowing the sample to decay until no radioactivity remained, mass spectrometry revealed the starting material, using 10 mg, was probably decyanating (Figure 108). Interestingly, the main product obtained during the radiolabelling is **169**, which is also observed in the synthesis of the reference standard to a lesser degree (<1%). A rational explanation for the decyanation is elusive; the reaction mixture has been purified by this stage to remove bulk free fluoride, potassium carbonate and kryptofix. Thermal instability is unlikely to cause the decyanation, as the reaction is conducted at the same temperature as the reference standard.

**Figure 108:** Possible by-product obtained during the Dimroth rearrangement as indicated by LCMS

Pleasingly the mass spectrometry analysis highlighted that the benzyl group on this scaffold is stable towards the fluorination conditions. Thus strengthening the theory, during the synthesis of [¹⁸F]-**101**, the product is debenzylating during the radiolabelling.

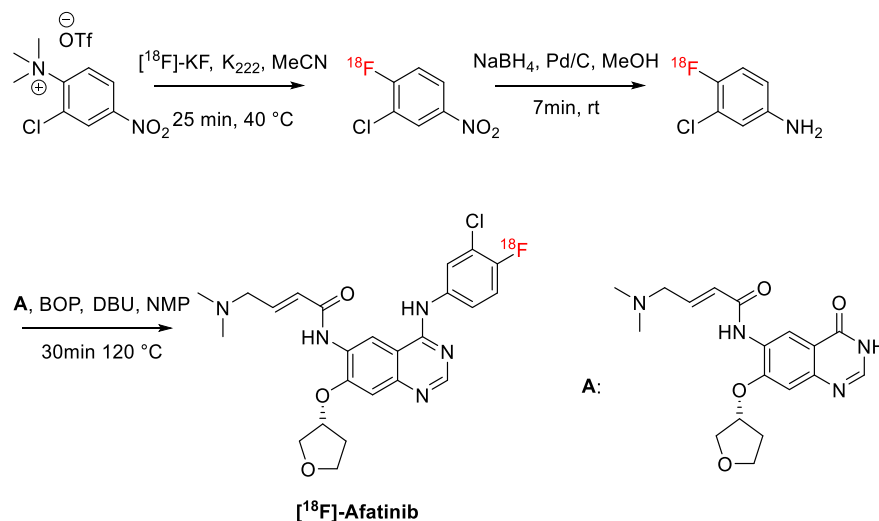
5.3 Conclusions

This chapter describes the synthesis of precursors and their subsequent investigation under suitable radiolabelling conditions. Despite the biological validation described in Chapter Four (4.3.2.2), no suitable precursor could be synthesised for radiolabelling with fluorine-18 for **98** (ZM323881). However, a precursor for the closely related analogue **101** was synthesised and fluorination of the nitro prosthetic group was attempted.

Initial fluorination of **136** highlighted the scaffold underwent debenylation which is postulated to be either base associated or as a by-product of the incorporation of the fluorine-18 itself. Changes in the amount of base present, the solvent of choice, the reaction temperature and mode of heating had no influence on the debenylation. The debenylation product was identified by mass spectrometry and confirmed via HPLC to be **166**, through the synthesis of a standard. All the optimisation were performed manually, therefore the reaction was conducted on a TRASIS allinone, which removes any manual error in drying of the fluoride, a by using well-established in-house drying programme. On one occasion the fluorination appeared successful, however the reaction showed decomposition. No examples of fluorination of a benzyloxy group are present in the literature and could, therefore, be interesting to develop on alternative scaffolds. However, alternative non-S_NAr may allow the scaffold to be radiolabelled, utilising this otherwise inaccessible PET candidate.

Two alternative strategies were planned for the radiosynthesis of [¹⁸F]-**123**; however only one strategy was utilised. Whilst fluorination of **138** was highly successful and reproducible, the Dimroth rearrangement required to complete the synthesis was not successful. Major by-products were formed in this reaction, namely the production of **169** which did occur during the synthesis of the cold standards. It is interesting to note that the production of **169** only commenced after the addition of acetic acid. Despite literature conditions for the Dimroth rearrangement in the synthesis of [¹⁸F]-**166**, under the conditions outlined in this thesis, the Dimroth rearrangement was not successful.

Interesting alternatives would be to attempt the coupling of the corresponding quinazolinone using [¹⁸F]-**155** under the coupling conditions (pyBOP) described in Chapter Four (section 4.4.1.2). This methodology has recently been utilised in the synthesis of [¹⁸F]-Afatinib, which has activity against EGFR, HER2 and HER4.³⁵⁶ Although the PyBOP coupling was not ideal for aniline **110**, this method could be utilised for aniline **155**. This is due to **155** not possessing the phenol which complicated the synthesis of the quinazolines via this coupling method. Another alternative would be to attempt resynthesis the 4-chloroquinazoline and proceed with the radiochemistry this route.



Scheme 55: Incorporation of fluorine-18 to afford [¹⁸F]-Afatinib, via BOP coupling

This chapter also describes the attempted synthesis of **125**, a dimer which has been described as having high affinity for VEGFR₂ and has applications in the screening of potential VEGFR₂ binding candidates. The initial synthesis, according to published literature, was slow and laborious with several protection and deprotection steps and the use of expensive reagents. The synthesis of key intermediate **146** was accessed via the Dimroth rearrangement previously described in Chapter Four. The synthesis of **146** was achieved in fewer steps with the use of more environmentally friendly reagents. Although dimer **160** was synthesised, the NOTA macrocycle could not be linked to successfully synthesise **125**. Alternative chromophore based strategies were utilised, however the coupling of the NOTA macrocycle was not successful. Chapter Four has already described the biological evaluation of the quinazoline focused library, via a kinase assay.

Upon successful radiosynthesis of either [¹⁸F]-**101** or [¹⁸F]-**123**, cellular uptake, metabolism assays and serum stability is the next logical step. If favourable characteristics were observed from this biological characterisation, the next step is to evaluate the biodistribution in healthy mice. If favourable biodistribution is seen, the next step is to evaluate the tracer in VEGFR₂ positive and VEGFR₂ negative xenografts, using U87-MG as the positive control.

Chapter Six

Summary

6.0 Summary

6.1 Summary

Angiogenesis is the development of vasculature from pre-existing vessels, and is tightly controlled in the physiological state. However in pathological settings, such as cancer, angiogenesis is widely dysregulated and this was first recognised by Judah Folkman (Chapter One - 1.1.2). Consequently, angiogenesis is widely recognised as a hallmark of cancer and is required for both tumour growth and metastatic spread. The angiogenic signalling process is highly complex, although the VEGF-VEGFR₂ signalling system is thought to be the key mediator of angiogenic signalling. Therefore, considerable effort has focused on developing new therapeutic agents based on either mAB or TKI against this target. However despite the efforts to develop new therapeutic agents targeting the VEGF-VEGFR₂ signalling system, response to anti-angiogenic therapy exhibits significant inter-patient variability. Therefore the identification of a biomarker capable of either determining those patients most likely to benefit from anti-angiogenic therapy or monitoring therapeutic response from anti-angiogenic therapy is required. Despite efforts to identify a circulating or tissue biomarker, no single suitable biomarker has been identified. Molecular imaging based biomarkers could be beneficial for patients as there is no requirement for repeated biopsies, however using US or MRI no biomarker has been identified.

This project sought to develop a PET radioligand with the requirements outlined in Chapter One (1.3.3). The majority of clinically relevant TKI are promiscuous inhibitors, due to the highly conserved nature of the active kinase ATP binding site. This presents a challenge when developing a PET radioligand which is capable of selectively targeting the ATP binding site of VEGFR₂. Another major challenging when developing a VEGFR₂ specific probe is lipophilicity, as the majority of TKIs are bicyclic this can mean a higher than ideal cLogP for PET imaging. Therefore this project focused on reducing the lipophilicity of the proposed PET imaging candidates, while retaining the selectivity and affinity required for binding with VEGFR₂ and also incorporating fluorine-18 at an easily accessible (for radiochemistry) position.

Connolly et al. highlighted the use of a pyrimidine in the place of the traditional bicyclic structures, which is capable of mimicking the bicyclic structures through intra-molecular hydrogen bonding; this further utilised a urea scaffold attached to a phenyl and then ether linked to the pyrimidine. The urea allowed a handle to access the back hydrophobic pocket present in the active conformation of VEGFR₂, which would be beneficial in forming ideal supramolecular interactions which could lead to increased affinity and selectivity. Synthesis

of the ureas via isocyanates, chloroformates and coupling agent CDI was not successful. Therefore an alternative library was identified where the phenyl urea was replaced with an indole, whilst retaining the pyrimidine-oxime. A library of nine compounds were synthesised with the intention of radiolabelling pendant to the oxime, via an alkylation reaction. Initial biological validation of this library in a proliferation assay, using non-VEGFR₂ expressing cell lines, highlighted that this library was toxic at very low concentrations. Although **78e** and **78h** did not affect proliferation to the same degree, comparison with literature data of known VEGFR₂ inhibitors revealed the effect on proliferation was still more pronounced than expected (Chapter Three – 3.4.2.1). Nuclear staining studies with DAPI, confirmed the cells were dying although could not identify the mechanism of cell death which was observed during the proliferation assay. Due to factors discussed this library was not taken forward for further development as a VEGFR₂ specific PET radioligand.

The only known VEGFR₂ selective TKI is ZM323881, therefore a focused library derived from this structure to allow for facile radiochemistry was investigated. Synthesis of the ZM323881 analogues via the traditional quinazolinone was not successful (Chapter Four – 4.3.1.1). The literature highlighted a precedence of using coupling agents BOP and PyBOP for the coupling of quinazolinones and anilines. Despite this precedence, attachment was via the phenol not the aniline as expected. Further literature highlighted the synthesis of quinazolines avoiding the quinazolinone, utilising the Dimroth rearrangement. Synthesis via the Dimroth rearrangement required little chromatography purification. A Z-Lyte assay, provided by Invitrogen, highlighted ZM323881 (**98**) not to be as selective as published in the literature. Pleasingly, analogue **101** did display moderate selectivity only targeting RET and VEGFR₃ and based on this data, this library was selected for radiolabelling. The synthesis of a precursor for **98** was not achieved as there was no easily accessible precursor. Radiolabelling of **101** was attempted via the nitro prosthetic group; however the precursor demonstrated general instability regardless of the radiochemistry procedure employed. In future work, radiolabelling via a non-SNAr route is suggested, exploiting the work of Gouverneur and Sanford.

Further future work for this project would be to assess the expression of RET and VEGFR₃ in cell lines. In addition the quinazoline library requires a metabolism study to assess for any radioactive metabolites that may confound in vivo imaging. The next step would be to perform biodistribution studies in healthy mice, then assess whether the PET radioligand accumulates within VEGFR₂ positive xenografts (U87).

This project highlights the common problems often seen when developing a PET radioligand, such as a lack of selectivity, unknown non-specific toxicities, inadequate

lipophilicity and the optimisation of radiolabelling procedures. This project identified a promising candidate with potential to be a successful VEGFR₂ specific PET radioligand after further studies described above. The development of a VEGFR₂ PET radioligand would still be highly beneficial to clinicians when deciding on treatment course, or monitoring these therapeutic agents to improve patient outcomes.

Chapter Seven

Experimental

7. Experimental

7.1 Chemistry

7.1.1. General Comments

Unless otherwise stated, reagents and solvents were purchased from commercial suppliers (Sigma Aldrich, Apollo Scientific, Fisher, Acros Organic and Alfa Aesar) and used without further purification. Chromatography solvents were HPLC grade and also used without further purification.

TLC, Melting points and IR

Thin-layer chromatography was conducted on standard commercial aluminium pre-coated plates with a 0.2 mm layer of silica gel (Merck 60-254) with UV₂₅₄ detection. Chromatography was performed using silica gel 40 (Fluka 40-63 μm) or using a Biotage Isolera purification system, quoting solvents v/v. All melting points were determined on a Leica Galen III melting point apparatus and are uncorrected.

Infrared spectra were recorded on a Bruker alpha-p FT-IR.

NMR

¹H NMR spectra were recorded on a Bruker Advance 500 MHz spectrometer using an internal deuterium lock or a JEOL-ECP 400 MHz FT-NMR. Chemical shifts (δ) are measured in parts per million (ppm) were referenced to the following residual solvent peaks: CHCl₃ (δ 7.26), DMSO (δ 2.5) or MeOH (δ 3.35). Compound assignments were aided by 2D NMR techniques; COSY, HSQC, DEPT and NOSEY. Data is presented in the following format: chemical shift (multiplicity, integration, coupling constant (J in Hz)). Multiplicities are quoted as following: s (singlet), brs (broad singlet), d (doublet), t (triplet), q (quartet), quin (quintet), dd (doublet of doublets), dt (doublet of triplets), ddd (doublet of doublet of doublet) and m (multiplet). All aromatic doublets are assumed to be true doublets.

¹³C NMR spectra were recorded on a Bruker Advance 500 MHz spectrometer using an internal deuterium lock or a JEOL-ECP 400 MHz FT-NMR. Chemical shifts (δ) are measured in parts per million (ppm) relative to tetramethylsilane (TMS) and were referenced to the following residual solvent peaks: CHCl₃ (δ 77.23) or DMSO (δ 39.51). Data is

presented in the following format: chemical shift (assignment). Where it is the case splitting is caused by fluorine, Data is presented in the following format: chemical shift (multiplicity, coupling constant (J in Hz)).

^{19}F NMR spectra were recorded on a Bruker Advance 500 MHz spectrometer and were referenced to an external standard of CFCl_3 (neat) set to $\delta=0$ ppm.

HRMS and Purity

High resolution mass spectrometry (HRMS) was performed on an Agilent 1200 series HPLC system, with diode array detector operating at 254 nm, fitted with a Merck Chromolith SpeedROD RP-18e 50×4.6 nm column at a temperature of 22 °C, connected to a Agilent 6520 Quadrupole Time Of Flight (QToF) mass spectrometer (simultaneous ESI and APCI). The following solvent system, at a flow rate of 2 mL min^{-1} was used: solvent A: Methanol: solvent B: 0.1% formic acid in water. Gradient elution was as follows: 1: (A: B) to 9:1 (A: B) for 1 minute, then reversion back to 1:9 (A:B) over 0.3 minutes, 1:9 (A:B) for 0.2 minutes (Method A).

Purity of compounds (at a concentration of $1 \mu\text{M}$) are indicated by HPLC purity as described above (Method A) or on an Agilent 1200 series (Phenomenex Luna® $5 \mu\text{m}$ C18(2) 100 \AA , LC Column 150×4.6 mm) utilising the following gradient system at 1 mL min^{-1} (2). Solvent A: Water and 10 mM NaH_2PO_4 Solvent B: Acetonitrile and 0.1% H_3PO_4 . Gradient elution was as follows: 80:20 (A:B) to 55:45 (A:B) for 5 minutes, then to 5:95 (A:B) in 10 minutes and held for a further 5 minutes, followed by reversion back to 80:20 (A:B) over 1 minute and held for a further 9 minutes (Method B).

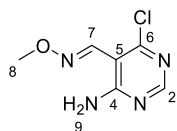
All purities are expressed as a percentage (%).

Semi-Prep HPLC purification

Standard injections of $500 \mu\text{L}$ of the sample (with needle wash) were made onto an ACE 5 C18-PFP column (5μ , 250×10 mm Advanced Chromatography Technologies, Aberdeen, UK). Chromatographic separation at ambient temperature was carried out using a 1200 Series Preparative HPLC (Agilent, Santa Clara, USA) over a 15 minute gradient elution from 60:40 to 0:100 water: methanol (both modified with 0.1% formic acid) at a flow rate of 5 mL min^{-1} . UV-Vis spectra were acquired at 254 nm on a 1200 Series Prep Scale diode

array detector (Agilent, Santa Clara, USA). Post-UV & pre-MS splitting was achieved using an Active Split (Agilent, Santa Clara, USA) before being infused into a 6120 Series Quad mass spectrometer fitted with an ESI/APCI Multimode ionisation source (Agilent, Santa Clara, USA). LC eluent and nebulising gas was introduced into the grounded nebuliser with spray direction orthogonal to the capillary axis. 2kV was applied to the charging electrode to generate a charged aerosol. The aerosol was dried by infrared emitters (200 °C) and heated drying gas (12 L min⁻¹ of nitrogen at 350 °C, 4.13 MPa), producing ions by ESI. Aerosol and ions were transferred by nebulising gas to the APCI zone where infrared emitters vaporized solvent and analyte. A corona discharge was produced between the corona needle and APCI counter electrode by applying a current of 4 µA, ionizing the solvent to transfer charge to analyte molecules, producing ions by APCI. ESI and APCI ions simultaneously entered the transfer capillary along which a potential difference of 4 kV was applied. The fragmentor voltage was set at 175 V and skimmer at 65 V. Signal was optimised by AutoTune.m. Profile mass spectrometry data was acquired in positive ionisation mode over a scan range of m/z 60-1000 (scan rate 1.0). Collection was triggered by UV signal and collected on a 1200 Series Fraction Collector (Agilent, Santa Clara, USA).

Microwave reactions were performed on a Biotage Initiator. Buchi Rotavapor 210 equipped with a diaphragm vacuum pump was used to remove bulk solvent; trace solvent was removed using a Schlenk line with an oil pump.

(E)-4-amino-6-chloropyrimidine-5-carbaldehyde O-methyloxime²⁹² (27)

4-Amino-6-chloropyrimidine-5-carbaldehyde (1.0 g, 6.35 mmol), *O*-methylhydroxylamine (0.94 g, 11.25 mmol) was dissolved in acetic acid (25 mL) and water (4 mL). The solution was stirred overnight at ambient temperature and concentrated under reduced pressure. The residue was dissolved in water (50 mL) and washed with EtOAc (3 × 70 mL). The combined organic phases were dried over MgSO₄ and concentrated under reduced pressure to afford the title compound as a yellow solid (0.95 g, 91%).

R_f: 0.59 (7:3 EtOAc: hexane)

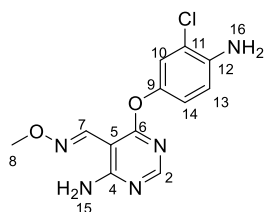
¹H NMR (400 MHz, *d*₆-DMSO) δ: 4.00 (s, 3H⁸, CNOCH₃), 7.56 (s, 1H⁷, CHN), 7.82 (brs, 2H⁹, ArNH₂), 8.53 (s, 1H², ArH)

¹³C NMR (100 MHz, *d*₆-DMSO) δ: 62.40 (s, C-8), 103.96 (s, C-5), 145.32 (s, C-7), 157.28 (s, C-4), 158.93 (s, C-2), 160.85 (s, C-6)

MS (ESI): 187.04 [M+H]⁺; 209.02 [M+Na]⁺

Data consistent with literature.

4-Amino-6-(4-amino-3-chlorophenoxy)pyrimidine-5-carbaldehyde *O*-methyl oxime²⁹²
(28b)



(*E*)-4-Amino-6-chloropyrimidine-5-carbaldehyde *O*-methyloxime (200 mg, 1 mmol), 4-amino-3-chlorophenol (190 mg, 1.03 mmol) and caesium carbonate (300 mg, 343 mmol) were dissolved in DMSO (25 mL) and stirred at ambient temperature for two hours. The reaction mixture was poured onto water (25 mL) and washed with EtOAc (3 × 20 mL). The combined organic layers were dried over MgSO₄ and concentrated under reduced pressure. The crude compound was purified by column chromatography (1:1 EtOAc: hexane) to afford the title compound as a red solid (161 mg, 51%).

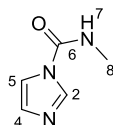
R_f: 0.61 (1:1 EtOAc: hexane)

¹H NMR (400 MHz, *d*₆-DMSO) δ: 3.97 (s, 3H⁸, OCH₃), 6.56 (d, 1H¹⁴, ArH, *J* = 7.9 Hz), 6.67 (d, 1H¹³, ArH, *J* = 7.9 Hz), 7.79 (s, 1H¹⁰, ArH), 8.24 (s, 1H², ArH), 8.48 (s, 1H⁷, ArH)

¹³C NMR (100 MHz, *d*₆-DMSO) δ: 62.39 (s, C-8), 102.63 (s, C-13), 118.35 (s, C-14), 118.68 (s, C-5), 123.21 (s, C-10), 126.54 (s, C-11), 140.25 (s, C-12), 145.32 (s, C-7), 146.98 (s, C-9), 153.59 (s, C-4), 157.26 (s, C-2), 168.54 (s, C-6)

LCMS (ESI): 294.2 [M+H]⁺

Data consistent with literature.

***N*-methyl-1*H*-imidazole-1-carboxamide²⁷¹ (33a)**

1,1'-Carbonyldiimidazole (3.56 g, 22 mmol) was added to a flask charged with methylammonium chloride (1.35 g, 20 mmol). Anhydrous acetonitrile (6 mL) and DMF (2 mL) under nitrogen was added resulting in an off white solution, the mixture is stirred at ambient temperature for three hours, and then placed in a freeze dryer overnight. The resulting off white solid was purified by column chromatography (1:25 MeOH: DCM) to afford the title compound as a white solid. (2.14 g, 86%).

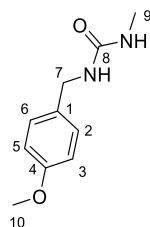
R_f : 0.25 (1:25 MeOH: DCM)

Mp: 110-112 °C

^1H NMR (400 MHz, CDCl_3) δ : 3.04 (d, 3H⁸, CH_3 , $J = 4.5$ Hz), 6.89 (brs, 1H⁷, NH), 7.07 (brs, 1H⁴, ArH), 7.43 (s, 1H⁵, ArH), 8.18 (brs, 1H², ArH)

^{13}C NMR (100 MHz, CDCl_3) δ : 27.45 (s, C-8), 116.17 (s, C-5), 130.15 (s, C-4), 136.2 (s, C-2), 149.58 (s, C-6)

Data consistent with literature.

1-(4-Methoxybenzyl)-3-methylurea³⁵⁷ (35)

A small flask was charged with *N*-methyl carbanoyldiimidazole (33 mg, 0.1 mmol) and 4-methoxybenzylamine (27 mg, 0.1 mmol) with NEt_3 (15 μl , 0.1 mmol) with anhydrous DCM (1 mL). The resultant red solution was stirred at ambient temperature for 18 hours. The solution was monitored using TLC (1:1 EtOAc: hexane). The solution was concentrated under reduced pressure and purified using column chromatography (1:25 MeOH: DCM followed by 6:4 EtOAc: hexane) to afford the title compound as a yellow solid (22 mg, 56%).

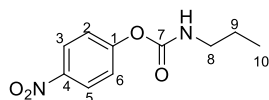
R_f : 0.32 (6:4 EtOAc: hexane)

^1H NMR (400 MHz, CDCl_3) δ : 2.72 (s, 3H⁹, NCH_3), 3.73 (s, 3H¹⁰, OCH_3), 4.25 (d, 2H⁷, NCH_2 , $J = 6.3$ Hz), 6.81 (d, 2H^{3,5}, ArH , $J = 8.7$ Hz), 7.17 (m, 2H^{2,6}, ArH)

^{13}C NMR (100 MHz, CDCl_3) δ : 26.95 (s, C-9), 44.20 (s, C-7), 55.30 (s, C-10), 114.04 (s, C-3 and C-5), 128.85 (s, C-2 and C-6), 130.61 (s, C-1)

NB: C-8 not observed

Data consistent with literature.

4-Nitrophenyl propylcarbamate³⁵⁸ (37a)

To a round bottomed flask propylamine (80 μ L, 1 mmol), pyridine (0.2 mL, 1 mmol) were dissolved in anhydrous DCM (10 mL). 4-Nitrophenyl chloroformate (202 mg, 1 mmol) was added and the resultant yellow solution was refluxed for a period of six hours. The resulting orange solution was quenched using DCM (5 mL) and washed with 1M NaHCO₃ (5 mL), water (5 mL) and brine (10 mL). The organic phase was dried over Na₂SO₄ and concentrated under reduced pressure and purified using column chromatography (6:4 EtOAc: hexane) to afford the title compound as a yellow solid (96 mg, 43%).

R_f: 0.51 (6:4 EtOAc: hexane)

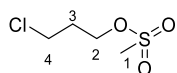
Mp: 99-101 °C

¹H NMR (400 MHz, CDCl₃) δ : 0.92 (t, 3H¹⁰, CH₃, J = 7.4 Hz), 1.55-1.59 (m, 2H⁹, CH₂), 3.19-3.23 (m, 2H⁸, CH₂), 5.21 (brs, 1H¹¹, NH) 7.24 (d, 2H^{2,6}, ArH, J = 9.0 Hz), 8.17 (d, 2H^{3,5}, ArH, J = 9.0 Hz)

¹³C NMR (100 MHz, CDCl₃) δ : 11.28 (s, C-10), 22.92 (s, C-9), 44.01 (s, C-8), 121.9 (s, C-2 and C-6), 125.1 (s, C-3 and C-5), 144.9 (s, C-4), 153.8 (s, C-7), 156.3 (s, C-1)

LCMS: 247.1 [M+Na]⁺

Data consistent with literature.

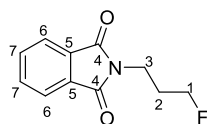
3-Chloropropyl methanesulfonate³⁵⁹ (43)

3-Chloropropan-1-ol (17.75 g, 187.5 mmol) and pyridine (19.75 g, 250 mmol) was cooled to 0 °C. Methanesulfonyl chloride (21.5 g, 187.5 mmol) was added slowly over a period of 90 minutes and stirred for a further three hours. The solution was diluted with water (100 mL) and acidified with 6M HCl and washed with diethyl ether (3 × 150 mL). The combined organic extracts were washed with water (100 mL) and Na₂CO₃ (100 mL), dried over Na₂SO₄ and concentrated under reduced pressure. Column chromatography purification (100% EtOAc) on a neutral alumina column afforded the title compound as a pale yellow oil (10.28 g, 32%).

¹H NMR (400 MHz, CDCl₃) δ: 2.15 (quintet, 2H³, CH₂, *J* = 6.1 Hz), 2.98 (s, 3H¹, CH₃), 3.61 (t, 2H⁴, CH₂, *J* = 6.1 Hz), 4.33 (t, 2H², CH₂, *J* = 6.0 Hz)

¹³C (100 MHz, CDCl₃) δ: 28.98 (s, C-3), 37.19 (s, C-1), 41.89 (s, C-4), 66.44 (s, C-2)

Data consistent with literature.

2-(3-Fluoropropyl)isoindoline-1,3-dione³⁶⁰ (45)

A solution of 3-fluoropropyl methane sulfonate (0.5 g, 3.2 mmol) in anhydrous DMF (5 mL) was treated with potassium phthalimide (0.65 g, 3.58 mmol) at ambient temperature. The white emulsion was heated to 70 °C for two hours, before the addition of water (10 mL). The yellow solution was stirred at ambient temperature for 10 minutes, before cooling to 0 °C for one hour, where upon cooling a yellow solid crashed out. The yellow solid was filtered and washed with water (3 × 10 mL), yielding the title compound as a fine white powder (0.35 g, 53%).

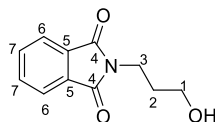
¹H NMR (400 MHz, CDCl₃) δ: 2.11 (dquin, 2H², CH₂, *J* = 6.9, 24.9 Hz), 3.83 (t, 2H³, CH₂, *J* = 6.9 Hz), 4.55 (dt, 2H¹, CH₂, *J* = 6.7, 46.8 Hz), 7.75 (m, 4H^{6,7}, ArH).

¹³C NMR (100 MHz, CDCl₃) δ: 25.74 (d, C-2, *J* = 18.6 Hz), 30.75 (d, C-3, *J* = 5.5 Hz), 77.00, 79.85 (d, C-1, *J* = 171.2 Hz), 119.79 (s, C-6), 130.16 (s, C-7), 130.51 (s, C-5), 165.40 (s, C-4)

¹⁹F NMR (376 MHz, CDCl₃) δ: -219.01

EI: 207.3 [M-1]

Data consistent with literature.

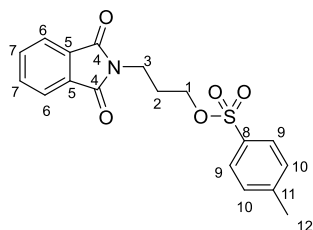
2-(3-Hydroxypropyl)isoindoline-1,3-dione³⁶¹ (48)

Potassium phthalimide (1.5 g, 8.1 mmol) and 3-chloropropan-1-ol (0.69 g, 7.3 mmol) was dissolved in anhydrous DMF (20 mL) and the mixture was heated to 60 °C for four hours, in which time the rest of the potassium phthalimide dissolved. The reaction flask was allowed to cool to ambient temperature and filtered to remove any resultant KCl. The filtrate was concentrated under reduced pressure and diethyl ether (40 mL) added and washed with plenty of water (3 × 20 mL), 0.5M NaHCO₃ (20 mL) and brine (20 mL). The combined organic extracts were dried over Na₂SO₄, concentrated under reduced pressure to gain a white precipitate and allow to crash out overnight in a desiccator over P₂O₅, affording the title compound as a white crystalline solid (201 mg, 13%).

¹H NMR (400 MHz, CDCl₃) δ: 2.02 (quintet, 2H², CH₂, *J* = 6.5 Hz), 3.68 (t, 2H¹, CH₂, *J* = 6.35 Hz), 3.87 (t, 2H³, CH₂, *J* = 6.5 Hz), 7.79 (m, 2H⁶, ArH), 7.86 (m, 2H⁷, ArH).

¹³C NMR (100 MHz, CDCl₃) δ: 34.85 (s, C-2), 41.71 (s, C-3), 59.50 (s, C-1), 123.60 (s, C-6), 130.68 (s, C-5), 134.33 (s, C-7), 159.86 (s, C-4)

Data consistent with literature.

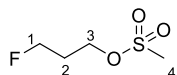
***N*-(3-tosyloxypropyl)-phthalimide³⁶² (49)**

To a round bottomed flask charged with *N*-(3-hydroxypropyl)-phthalimide (0.2 g, 0.97 mmol) in DCM (15 mL) with NEt₃ (0.24 g, 1.455 mmol) was stirred at 0 °C for 10 minutes. *p*-Toluene sulfonylchloride was added carefully, over a 20 minute period, to avoid excessive bubbling and the reaction was stirred at ambient temperature overnight. The reaction was quenched through the addition of water (30 mL), observing an exotherm, and washed with DCM (3 × 30 mL). The combined organic extracts were washed with brine (50 mL) and dried over Na₂SO₄. Concentration under reduced pressure afforded the title compound as a slightly oily yellow solid (0.20 g, 70%).

¹H NMR (400 MHz, CDCl₃) δ: 1.34 (t, 2H², CH₂, *J* = 6.0 Hz), 2.29 (s, 3H¹², CH₃), 3.07 (m, 4H^{1,3}, CH₂), 7.12 (d, 2H⁹, ArH, *J* = 8.1 Hz), 7.35 (d, 2H¹⁰, ArH, *J* = 8.1 Hz), 7.74 (m, 2H⁷, ArH), 7.78 (m, 2H⁶, ArH).

¹³C NMR (100 MHz, CDCl₃) δ: 21.2 (s, C-12), 35.8 (s, C-2), 45.92 (s, C-3), 69.6 (s, C-3), 125.90 (s, C-9), 127.03 (s, C-10), 128.75 (s, C-6), 130.23 (s, C-7), 132.3 (s, C-5), 139.5 (s, C-8), 142.3 (s, C-11), 160.1 (s, C-4)

Data consistent with literature.

3-Fluoropropyl methanesulfonate³⁶³ (50)

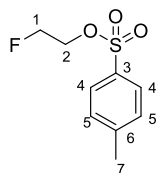
3-Fluoropropan-1-ol (0.781 g, 10 mmol) was dissolved in DCM (10 mL) and NEt_3 (1.68 mL, 12 mmol) was added. Methane sulfonylchloride (0.86 mL, 11 mmol) in DCM (5 mL) was added dropwise to the ice-cold reaction mixture. The reaction mixture was stirred at 0-5 °C for two hours. The reaction mixture was then washed with water (15 mL), saturated NaHCO_3 (15 mL), water (20 mL) and brine (20 mL). The combined organic layers were dried over MgSO_4 , filtered and concentrated under reduced pressure to afford the title compound as a colourless oil (0.681 g, 45%).

^1H NMR (400 MHz, CDCl_3) δ : 2.08 (quint, 2H^2 , $\text{FCH}_2\text{CH}_2\text{CH}_2$, $J = 5.7, 23.5$ Hz), 2.97 (s, 3H^4 , CH_3), 4.30 (t, 2H^3 , $\text{FCH}_2\text{CH}_2\text{CH}_2$, $J = 5.7$ Hz), 4.51 (dt, 2H^1 , $\text{FCH}_2\text{CH}_2\text{CH}_2$, $J = 5.7, 39.2$ Hz)

^{13}C NMR (100 MHz, CDCl_3) δ : 26.85 (s, C-2, $J = 20.60$ Hz), 33.94 (s, C-4), 62.37 (s, C-3, $J = 4.60$ Hz), 76.17 (s, C-1, $J = 165$ Hz)

^{19}F NMR (376 MHz, CDCl_3) δ : -178.85

Data consistent with literature.

2-Fluoroethyl tosylate³⁶⁴ (51)

p-Toluenesulfonyl chloride (270 mg, 1.41 mmol) was added to a solution of 2-fluoroethanol (60 mg, 0.94 mmol) in anhydrous DCM (2 mL). NEt₃ (200 mL, 1.41 mmol) and a catalytic amount of DMAP (13 mg, 0.11 mmol) was also added. The reaction mixture was stirred for two hours at ambient temperature. The reaction mixture was partitioned between 1M HCl (10 mL) and DCM (20 mL). The organic layer was washed with K₂CO₃ solution, dried over MgSO₄ and the solvent removed under reduced pressure to afford fluoroethyl tosylate as a colourless soil (201 mg, 98%).

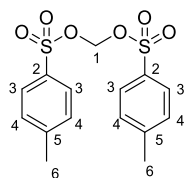
R_f: 0.3 (8:2 hexane: EtOAc)

¹H NMR (500 MHz, CDCl₃) δ: 2.42 (s, 3H⁷, ArCH₃), 4.23 (ddd, 2H², CH₂, *J* = 3.0, 5.0, 27.5 Hz), 4.54 (ddd, 2H¹, CH₂, *J* = 3.1, 5.0, 47.2 Hz), 7.34 (d, 2H⁵, ArH, *J* = 8.1 Hz), 7.77 (d, 2H⁴, ArH, *J* = 8.1 Hz)

¹³C (125 MHz, CDCl₃) δ: 21.57 (s, C-7), 68.73 (d, C-2, *J* = 20.6 Hz), 80.61 (d, C-1, *J* = 173.1 Hz), 127.89 (s, C-4), 129.99 (s, C-5), 132.49 (s, C-6), 145.27 (s, C-3)

¹⁹F (471 MHz, CDCl₃) δ: -223.27

Data consistent with literature.

Methylene ditosylate³⁶⁵ (**51**)

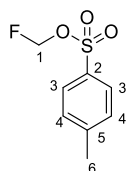
Diiodomethane (0.9 g, 7.46 mmol) was combined with silver tosylate (4.64 g, 16.6 mmol) in anhydrous acetonitrile and the mixture was heated at reflux for 20 hours. The mixture was cooled and the solvent removed under reduced pressure, the resultant residue was slurried with DCM and filtered through celite. The filtrate was evaporated yielding methylene ditosylate as a white solid (2.09 g, 35%).

¹H NMR (500 MHz, CDCl₃) δ: 2.47 (s, 6H⁶, ArCH₃), 5.83 (s, 2H¹, CH₂), 7.23-7.29 (m, 4H⁴, ArH), 7.58-7.64 (m, 4H³, ArH)

¹³C NMR (125 MHz, CDCl₃) δ: 21.73 (s, C-6), 87.97 (s, C-1), 127.97 (s, C-3), 129.76 (s, C-4), 133.24 (s, C-5), 145.39 (s, C-2)

HRMS (ESI, m/z): calc'd for C₁₅H₁₆O₆S₂Na 379.0281; obs 379.0274 [M+Na]

Data consistent with literature.

Fluoromethyl tosylate³⁶⁶ (52)

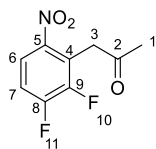
Methylene ditosylate (500 mg, 1.4 mmol) and caesium fluoride (1.065 g, 7.01 mmol) were dissolved in *tert*-amyl alcohol (3 mL) and irradiated in a microwave for 15 minutes at 90 °C. The reaction was allowed to cool and all *tert*-amyl alcohol was removed under reduced pressure, ice-cold diethyl ether was added, the suspension filtered and washed with plenty of ice-cold diethyl ether. The filtrate was concentrated under reduced pressure to yield the title compound as a colourless oil (272 mg, 65%).

¹H NMR (500 MHz, CDCl₃) δ: 2.43 (s, 3H⁶, ArCH₃), 5.72 (d, 2H¹, CH₂, *J* = 51.0 Hz), 7.35 (d, 2H⁴, ArH, *J* = 8.0 Hz), 7.81 (d, 2H³, ArH, *J* = 8.0 Hz)

¹³C (125 MHz, CDCl₃) δ: 21.67 (s, C-6), 98.16 (d, C-1, *J* = 221 Hz), 127.87 (s, C-3), 129.96 (s, C-4), 133.77 (s, C-5), 145.63 (s, C-2)

¹⁹F (471 MHz, CDCl₃) δ: -153.24 (t, *J* = 50.7 Hz)

Data consistent with literature.

1-(2,3-Difluoro-6-nitrophenyl)propan-2-one³⁶⁷ (68a)

Sodium hydride, 60% w/w in mineral oil, (450 mg, 18 mmol) was dissolved in anhydrous THF (5 mL), under a nitrogen blanket, and cooled to 10 °C. Ethyl acetoacetate (2.27 mL, 18 mmol) was added whilst keeping the temperature below 15 °C. The mixture was stirred for 15 minutes on ice, then 1,2,3-fluoro-4-nitrobenzene (1.03 mL, 9 mmol) was added. The mixture was stirred for a further 15 minutes on ice, before being allowed to slowly warm to ambient temperature and stirred for 24 hours. The mixture was concentrated under reduced pressure and the residue partitioned between EtOAc (50 mL) and 2M HCl (25 mL), the organics were washed with water (3 × 25 mL), brine (25 mL) and dried over MgSO₄ before being concentrated under reduced pressure. The residue was dissolved in concentrated HCl (15mL) and acetic acid (10mL) and allowed to reflux for 15 hours. After 15 hours the mixture was allowed to cool to ambient temperature, concentrated under reduced pressure and partitioned between 5% NaHCO₃ (25 mL) and EtOAc (3 × 25 mL), the combined organic layers were washed with saturated NaHCO₃ (25 mL), water (25 mL) and brine (25 mL). The combined organic layers were then dried over MgSO₄ and concentrated under reduced pressure. Purification by column chromatography (4:3 EtOAc: hexane) yielded 1-(2,3-difluoro-6-nitrophenyl)propan-2-one as a yellow oil (505 mg, 25%).

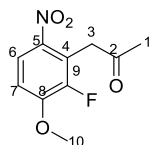
R_f: 0.65 (3:1 EtOAc: hexane)

¹H NMR (500 MHz, CDCl₃) δ: 2.33 (s, 3H¹, CH₃), 4.25 (d, 2H³, CH₂, *J* = 1.6 Hz), 7.11 (ddd, 1H⁷, ArH, *J* = 2.1, 6.5, 8.6 Hz), 7.86 (ddd, 1H⁶, ArH, *J* = 2.1, 6.6, 8.7 Hz)

¹³C NMR (125 MHz, CDCl₃) δ: 29.9 (s, C-1), 43.4 (s, C-3), 120.2 (t, C-6, *J* = 3.9 Hz), 125.5 (t, C-7, *J* = 4.4 Hz), 130.4 (d, C-4, *J* = 13.6 Hz), 137.3 (s, C-5), 146.2 (dd, C-9, *J* = 16.4, 16.2 Hz), 149.8 (dd, C-8, *J* = 12.3, 252.0 Hz), 201.8 (s, C-2)

¹⁹F NMR (471 MHz, CDCl₃) δ: -125.93 (s, 1F¹¹), -135.76 (s, 1F¹⁰)

Data consistent with literature.

1-(2-Fluoro-3-methoxy-6-nitrophenyl)propan-2-one^{367, 368} (71)

1-(2,3-Difluoro-6-nitrophenyl)propan-2-one (5 g, 23 mmol) and sodium methoxide (6.9 g, 127 mmol) was dissolved in anhydrous methanol (10 mL) and stirred for 72 hours at ambient temperature. The solution was concentrated under reduced pressure and the residue extracted with EtOAc (100 mL) and 1M HCl (10 mL). The organic layer was washed with brine (2 × 50 mL) and dried over MgSO₄. Column chromatography purification (1:3 EtOAc: hexane) yielded the title compound as a white solid (2.89 g, 67%).

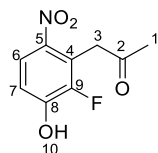
R_f: 0.37 (1:3 EtOAc: hexane)

¹H NMR (500 MHz, CDCl₃) δ: 2.37 (s, 3H¹, CH₃), 3.98 (s, 3H¹⁰, OCH₃), 4.23 (d, 2H³, CH₂, *J* = 4.0 Hz), 7.02 – 6.92 (m, 1H⁷, ArH), 7.99-8.04 (m, 1H⁶, ArH)

¹³C NMR (125 MHz, CDCl₃) δ: 30.18 (s, C-1), 40.53 (s, C-3), 56.57 (s, C-10), 110.13 (s, C-7), 120.38 (s, C-4), 122.30 (s, C-6), 141.04 (d, C-9, *J* = 189.2 Hz), 151.22 (s, C-5), 152.39 (s, C-8), 202.64 (C-2)

¹⁹F NMR (471 MHz, CDCl₃) δ: -134.37

Data consistent with literature.

1-(2-Fluoro-3-hydroxy-6-nitrophenyl)propan-2-one^{368, 369} (**72**)

1-(2-Fluoro-3-methoxy-6-nitrophenyl)propan-2-one (50 mg, 0.23 mmol) was added to a flask charged with pyridinium chloride (9 mg, 0.78 mmol) and heated to 180 °C for 75 minutes. The mixture was quenched with EtOAc (5 mL) and 2M HCl (2 mL) and filtered. The organic layer was washed with brine (2 × 10 mL) and dried over MgSO₄ and concentrated under reduced pressure. The crude reaction mixture was purified by column chromatography (1:1 EtOAc: hexane) to yield the title compound as a yellow oil (39 mg, 83%).

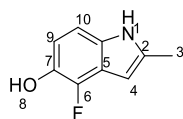
R_f: 0.48 (50% EtOAc: hexane)

¹H NMR (500 MHz, CDCl₃) δ: 2.39 (s, 3H¹, CH₃), 4.23 (s, 2H³, CH₂), 6.11 (brs, 1H¹⁰, OH), 7.08 (dd, 1H⁷, ArH, *J* = 1.8, 9.0 Hz), 8.04 (dd, 1H⁶, ArH, *J* = 1.8, 9.0 Hz)

¹³C NMR (125 MHz, CDCl₃) δ: 30.10 (s, C-1), 39.87 (s, C-3), 115.71 (s, C-7), 119.67 (s, C-4), 122.68 (s, C-6), 148.09 (s, C-5), 148.81 (d, C-9, *J* = 16.5 Hz), 149.98 (s, C-8), 203.16 (C-2)

¹⁹F NMR (471 MHz, CDCl₃): -140.36

Data consistent with literature.

4-Fluoro-2-methyl-1*H*-indol-5-ol³⁶⁷ (**64**)

1-(2-Fluoro-3-hydroxy-6-nitrophenyl)propan-2-one (38.8 mg, 0.18 mmol) was dissolved in water (1 mL) and sodium dithionite (174.4 mg, 1 mmol) was added and the reaction monitored using LCMS. The mixture was extracted with EtOAc (3 × 15 mL) and the organic layer washed with brine (10 mL) and dried over MgSO₄. The organic layer was concentrated under reduced pressure and purified using column chromatography (3:7 EtOAc: hexane) to afford the title compound as an off-white solid (11 mg, 29%).

R_f: 0.42 (3:7 EtOAc: hexane)

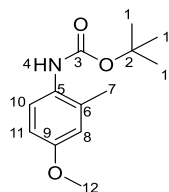
¹H NMR (500 MHz, CDCl₃) δ: 2.44 (s, 3H³, CH₃), 4.21 (s, 1H⁸, OH), 6.24 (m, 1H⁴, ArH), 6.81 (t, 1H⁹, ArH, *J* = 8.4 Hz), 6.94 (dt, 1H¹⁰, ArH, *J* = 0.9, 8.4 Hz), 7.83 (brs, 1H¹, NH)

¹³C NMR (125 MHz, CDCl₃) δ: 13.74 (s, C-3), 95.94 (s, C-4), 105.95 (s, C-10), 111.39 (s, C-9), 132.61 (s, C-11), 135.87 (s, C-2), 136.14 (s, C-7), 141.94 (s, C-6)

¹⁹F (471 MHz, CDCl₃) δ: -151.73

HRMS (ESI, *m/z*): calc'd for C₉H₁₀NOF 166.0663 found: 166.0674 [M+H]⁺

Data consistent with literature.

***N*-(*tert*-butoxycarbonyl)-4-methoxy-2-methylaniline³⁷⁰ (74)**

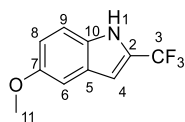
A solution of 4-methoxy-2-methylaniline (5 g, 36 mmol) and BOC₂O (9.14 g, 41.9 mmol) was dissolved in THF (45 mL) and was slowly heated to reflux. Reflux was maintained for two hours before the solution was cooled and the mixture was concentrated under reduced pressure. The residue was dissolved in EtOAc (100 mL) and washed with 1M citric acid (100 mL), the organic layer was dried with MgSO₄ and concentrated under reduced pressure. The crude product was recrystallised using hexane to yield the title compound as a purple solid (7.24 g, 80%).

¹H NMR (500 MHz, *d*₆-DMSO) δ: 1.44 (s, 9H¹, CCH₃), 2.15 (s, 3H⁷, ArCH₃), 3.70 (s, 3H¹², OCH₃), 6.69 (dd, 1H⁸, ArH, *J*= 3.0 Hz, 8.6 Hz), 6.75 (d, 1H¹¹, ArH, *J*= 2.9 Hz), 7.11 (d, 1H¹⁰, ArH, *J*= 8.6 Hz), 8.34 (brs, 1H⁴, NH)

¹³C NMR (125 MHz, *d*₆-DMSO) δ: 18.46 (s, C-7), 28.64 (s, C-1), 55.55 (s, C-12), 78.72 (s, C-2), 110.85 (s, C-10), 111.56 (s, C-11), 127.97 (s, C-8), 134.61 (s, C-5), 146.66 (s, C-6), 154.41 (s, C-3), 156.92 (s, C-9)

HRMS (ESI): C₁₃H₁₉NO₃ calc'd: 238.1438 found: 238.1445 [M+H]⁺

Data consistent with literature.

5-Methoxy-2-trifluoromethylindole³⁷¹ (75)

N-(*tert*-butoxycarbonyl)-4-methoxy-2-methylaniline (1 g, 4.21 mmol) was dissolved in anhydrous THF (12.5 mL), cooled to -40 °C and *sec*-butyllithium (7.5 mL, 9.75 mmol) was added. The mixture was stirred at -40 °C for 15 minutes before the addition of *N*-methyl-*N*-methoxytrifluoroacetamide (0.66 g, 4.21 mmol) in anhydrous THF (10 mL) was added. The mixture was stirred for a further one hour before being allowed to warm to ambient temperature. The mixture was poured onto diethyl ether: 1M HCl (1:1-50mL), the organic layer was separated and washed with water (50 mL), brine (50 mL) and dried over MgSO₄ and concentrated under reduced pressure. The crude product (0.7 g) was dissolved in DCM (4 mL) and TFA (0.75 mL) was added, the mixture was stirred at ambient temperature for three hours. The crude reaction mixture was concentrated under reduced pressure and partitioned between DCM (20 mL) and water (20 mL). The organic layer was washed with water (20 mL), brine (20 mL), dried over MgSO₄ and concentrated under reduced pressure. Column chromatography purification (1:20 EtOAc: hexane) yielded the title compound as a brown solid (200 mg, 22%).

R_f: 0.45 (1:20 EtOAc: hexane)

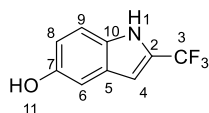
¹H NMR (500 MHz, CDCl₃) δ: 3.88 (s, 3H¹¹, OCH₃), 6.87 (dp, 1H⁴, ArH, *J*= 1.1, 2.3 Hz), 7.02 (dd, 1H⁸, ArH, *J*= 2.4, 8.9 Hz), 7.12 (d, 1H⁶, ArH, *J*= 2.4 Hz), 7.34 (dt, 1H⁹, ArH, *J*= 0.8, 8.9 Hz), 8.33 (brs, 1H¹, NH)

¹³C NMR (125 MHz, CDCl₃) δ: 55.76 (s, C-11), 102.74 (s, C-4), 103.92 (s, C-6), 112.56 (s, C-8), 115.84 (s, C-9), 120.13 (s, C-5), 122.26 (s, C-3), 127.10 (s, C-10), 131.25 (s, C-2), 154.93 (s, C-7)

¹⁹F NMR (471 MHz, CDCl₃) δ: -60.51

HRMS (ESI): calc'd for C₁₀H₈F₃NO: 216.0631 found: 216.0631 [M+H]⁺

Data consistent with literature.

2-(Trifluoromethyl)-1*H*-indol-5-ol³⁷¹ (65)

A solution of 5-methoxy-2-trifluoromethylindole (200 mg, 0.93 mmol) in DCM (1.5 mL) was cooled to -15 °C where a solution of 1M boron tribromide in DCM (1.86 mL, 1.85 mmol) was added slowly over five minutes. The reaction was warmed to ambient temperature and stirred for 45 minutes. The mixture was cooled to 0 °C and saturated NaHCO₃ (10 mL) was added and the mixture washed with EtOAc (3 × 10mL). The combined organic layer was dried over MgSO₄ and concentrated under reduced pressure to yield the title compound as a pale yellow solid (177 mg, 95%).

R_f: 0.79 (1:1 EtOAc: hexane)

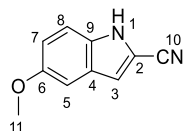
¹H NMR (500 MHz, CDCl₃) δ: 4.60 (s, 1H¹¹, OH), 6.83 (dp, 1H⁴, ArH, *J* = 1.2, 2.4 Hz), 6.94 (dd, 1H⁶, ArH, *J* = 2.5, 8.8 Hz), 7.08 (d, 1H⁸, ArH, *J* = 8.6 Hz), 7.32 (dt, 1H⁹, ArH, *J* = 8.7, 0.8 Hz), 8.28 (brs, 1H¹, NH)

¹³C NMR (125 MHz, CDCl₃) δ: 103.59 (C-4), 105.91 (C-6), 112.55 (C-9), 115.11 (C-8), 123.45 (C-3), 127.37 (C-5), 127.92 (C-10) 139.70 (C-2), 152.38 (C-7)

¹⁹F NMR (471 MHz, CDCl₃) δ: -60.06

HRMS (ESI): calc'd for C₉H₆F₃NO: 202.0474 found: 202.0477 [M+H]⁺

Data consistent with literature.

5-Methoxy-1*H*-indole-2-carbonitrile^{372, 373} (**77**)

Indole-2-carboxylic acid (2.0 g, 12.4 mmol) was dissolved in anhydrous diethyl ether (15 mL) and thionyl chloride (1.9 mL, 26 mmol) was added. The solution was stirred at ambient temperature for one hour before being concentrated under reduced pressure. The residue was suspended in 7M NH₃ (in MeOH, 25 mL) and stirred for 72 hours. The solvent was removed under reduced pressure and then suspended in POCl₃ (15 mL) and refluxed for one hour. The reaction was cooled to ambient temperature and poured onto ice-water, basified with aq ammonium hydroxide to pH 9 and washed with DCM (3 × 50 mL). The combined organic layers were dried over MgSO₄ and concentrated under reduced pressure. Column chromatography afforded the title compound as a brown solid (586 mg, 33%).

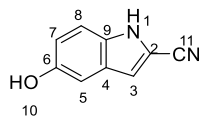
R_f: 0.77 (1:1 EtOAc: hexane)

Mp: 129-133 °C

¹H NMR (500 MHz, CDCl₃) δ: 3.87 (s, 3H¹¹, OCH₃), 7.05-7.09 (m, 2H^{3, 7}, ArH), 7.13 (dd, 1H⁵, ArH, *J* = 1.0, 2.1 Hz), 7.30 -7.35 (m, 1H⁸, ArH), 8.44 (brs, 1H¹, NH)

¹³C NMR (125 MHz, CDCl₃) δ: 55.68 (s, C-11), 101.95 (s, C-3), 112.54 (s, C-10), 113.92 (s, C-5), 117.63 (s, C-8), 118.00 (s, C-7), 124.32 (s, C-2), 126.74 (s, C-9), 132.05 (s, C-4), 155.41 (s, C-6)

Data consistent with literature.

5-Hydroxy-1*H*-indole-2-carbonitrile (66)

A solution of 5-methoxy-1*H*-indole-2-carbonitrile (200 mg, 1.16 mmol) in anhydrous DCM (1.5 mL) was cooled to -15 °C where a solution of 1M boron tribromide in DCM (0.5 mL) was added slowly over five minutes. The reaction was warmed to ambient temperature and stirred for 45 minutes. The mixture was cooled to 0 °C and saturated NaHCO₃ (2 mL) was added and the mixture washed with EtOAc (3 × 5 mL). The combined organic layers were dried over MgSO₄ and concentrated under reduced pressure to yield the title compound as a dark brown solid (163 mg, 89%).

R_f : 0.58 (1:1 EtOAc: hexane)

Mp: 207-209 °C

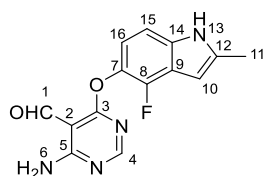
¹H NMR (500 MHz, CDCl₃) δ: 6.99-7.02 (m, 2H^{3,5}, *ArH*), 7.17 (dd, 1H⁵, *J* = 1.6, 2.3 Hz, *ArH*), 7.28 -7.31 (m, 1H⁵, *ArH*), 8.38 (brs, 1H¹, *NH*)

¹³C NMR (125 MHz, CDCl₃) δ: 103.08 (s, C-3), 110.23 (s, C-10), 114.99 (s, C-8), 115.42 (s, C-5), 118.00 (s, C-7), 124.32 (s, C-2), 126.74 (s, C-9), 132.05 (s, C-4), 155.41 (s, C-6)

General procedure for the alkylation of 4-amino-6-chloropyrimidine-5-carbaldehyde with the appropriate indole (77a-c)

The appropriate indole (1 eq) was added to a flask charged with 4-amino-6-chloropyrimidine-5-carbaldehyde (1.12 eq) and caesium carbonate (2 eq) in DMSO (0.5 mL). The mixture was stirred at ambient temperature for two hours before being poured onto water (5 mL) and extracted with EtOAc (3 × 5 mL). The combined organic layers were washed with brine (10 mL) and dried over MgSO₄, concentrated under reduced pressure and purified by column chromatography to yield the title compound.

4-Amino-6-((4-fluoro-2-methyl-1*H*-indol-5-yl)oxy)pyrimidine-5-carbaldehyde²⁹² (77a)



White solid (128 mg, 37%)

R_f: 0.56 (9.5:0.5 DCM: MeOH)

Mp: 213 °C (decomp)

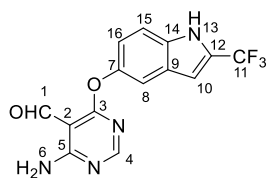
¹H NMR (500 MHz, *d*₆-DMSO) δ: 2.4 (s, 3H¹¹, CH₃), 6.22 (dt, 1H¹⁰, ArH, *J* = 0.9, 2.1 Hz), 6.93 (dd, 1H¹⁶, ArH, *J* = 7.4, 8.5 Hz), 7.11 (dd, 1H¹⁵, ArH, *J* = 0.9, 8.5 Hz), 8.15 (s, 1H⁴, ArH), 8.50 (brs, 2H⁶, NH₂), 10.42 (s, 1H¹, CHO), 11.32 (s, 1H¹³, NH)

¹³C NMR (125 MHz, *d*₆-DMSO) δ: 13.80 (s, C-11), 95.56 (s, C-10), 97.19 (s, C-2), 107.08 (s, C-15), 115.95 (s, C-9), 118.09 (s, C-14), 118.24 (s, C-16), 136.68 (s, C-7), 138.06 (s, C-12), 147.11 (s, C-8), 162.08 (s, C-5), 163.37 (s, C-4), 171.14 (s, C-3), 189.24 (s, C-1)

¹⁹F (471 MHz, *d*₆-DMSO) δ: -139.95

HRMS (ESI, *m/z*) = calc'd for C₁₄H₁₁N₄O₂F 287.0939 found: 287.0934 [M+H]⁺

Data consistent with literature.

4-Amino-6-((2-trifluoromethyl)-1H-indo-5-yl)oxy)pyrimidine-5-carbaldehyde (77b)

Yellow solid (156 mg, 52%)

R_f : 0.72 (9.5:0.5 DCM: MeOH)

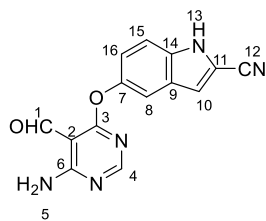
Mp: 203 °C

^1H NMR (500 MHz, d_6 -DMSO) δ : 7.03 (dt, 1H^{10} , ArH, $J = 1.2, 2.1$ Hz), 7.18 (dd, 1H^{16} , ArH, $J = 2.4, 8.8$ Hz), 7.48-7.54 (m, $2\text{H}^{8, 15}$, ArH), 8.14 (s, 1H^4 , ArH), 8.40 (brs, 1H^6 , NH_2), 8.50 (brs, 1H^6 , NH_2), 10.40 (s, 1H^1 , CHO), 12.40 (s, 1H^{13} , NH)

^{13}C NMR (125 MHz, d_6 -DMSO) δ : 97.61 (s, C-10), 103.77 (s, C-2), 113.42 (s, C-15), 114.45 (s, C-16), 119.49 (s, C-8), 120.07 (s, C-11), 126.53 (s, C-9), 134.91 (s, C-14), 146.56 (s, C-12), 149.58 (s, C-4), 161.99 (s, C-5), 163.99 (s, C-7), 171.67 (s, C-3), 189.50 (s, C-1)

^{19}F (471 MHz, d_6 -DMSO) δ : -58.97

HRMS (ESI, m/z) = calc'd for $\text{C}_{14}\text{H}_9\text{N}_4\text{O}_2\text{F}_3$ 323.075 found: 323.0759 $[\text{M}+\text{H}]^+$

5-((6-Amino-5-formylpyrimidine-4-yl)oxy)-1H-indole-2-carbonitrile (77c)

Brown solid (58 mg, 39%)

R_f : 0.65 (9.5:0.5 DCM: MeOH)

Mp: 199-201 °C

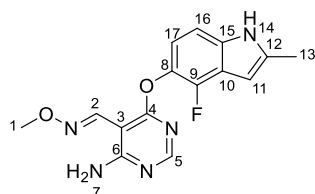
^1H NMR (500 MHz, d_6 -DMSO) δ : 7.23 (dd, 1H^{16} , ArH, $J = 2.3, 8.9$ Hz), 7.37 (dd, 1H^{10} , ArH, $J = 0.9, 2.1$ Hz), 7.51 (dt, 1H^8 , ArH, $J = 0.9, 8.9$ Hz), 7.53 (d, 1H^{15} , ArH, $J = 8.9$ Hz), 8.16 (s, 1H^4 , ArH), 8.45 (brs, 2H^6 , NH_2), 10.39 (s, 1H^{13} , NH), 12.52 (s, 1H^1 , CHO)

^{13}C NMR (125 MHz, d_6 -DMSO) δ : 97.60 (s, C-2), 107.40 (s, C-12), 113.40 (s, C-10), 113.61 (s, C-8), 114.26 (s, C-15), 121.47 (s, C-16), 124.56 (s, C-11), 126.23 (s, C-9), 146.98 (s, C-14), 161.98 (s, C-4), 163.39 (s, C-5), 171.59 (s, C-7), 181.94 (s, C-3), 189.46 (s, C-1)

HRMS (ESI, m/z) = calc'd for $\text{C}_{14}\text{H}_9\text{N}_5\text{O}_2$ 280.0829 found: 280.0826 $[\text{M}+\text{H}]^+$

General procedure for the synthesis of methyl oxime derivatives (78a, 78f and 78h)

To a solution of the appropriate aldehyde (1 eq) in DMSO (2 mL), *O*-methylhydroxylamine hydrochloride (4.7 eq) was added and stirred at ambient temperature for two hours. The mixture was then poured onto water (10 mL) and partitioned with EtOAc (3 × 10 mL), dried with MgSO₄ and concentrated under reduced pressure. Column chromatography purification yielded the title compound.

(*E*)-4-Amino-6-((4-fluoro-2-methyl-1*H*-indol-3yl)oxy)pyrimidine-5-carbaldehyde *O*-methyl oxime (78a)

White solid (31 mg, 98%)

R_f : 0.25 (1:1 EtOAc: hexane)

R_t : 3.00 minutes, 98.3% (Method A)

Mp: 160-162 °C

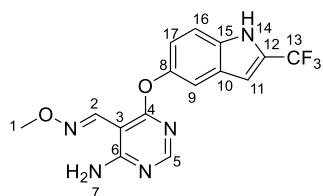
¹H NMR (500 MHz, *d*₆-DMSO) δ : 2.40 (s, 3H¹³, CH₃), 3.97 (s, 3H¹, CH₃), 6.21 (s, 1H¹¹, ArH), 6.88 (t, 1H¹⁷, ArH, *J* = 7.3 Hz), 7.08 (d, 1H¹⁶, ArH, *J* = 7.3 Hz), 8.02 (s, 1H⁵, ArH), 8.60 (s, 1H², ArH), 11.25 (s, 1H¹⁴, NH).

¹³C NMR (125 MHz, *d*₆-DMSO) δ : 13.78 (C-13), 65.52 (C-1), 91.01 (s, C-3), 95.50 (s, C-11), 106.95 (s, C-10), 106.99 (s, C-16), 116.13 (s, C-17), 131.22 (s, C-15), 137.91 (s, C-8), 138.52 (s, C-12), 143.96 (s, C-9), 153.62 (s, C-2), 157.95 (s, C-6), 161.79 (s, C-5), 167.16 (C-4)

¹⁹F (471 MHz, *d*₆-DMSO) δ : -140.20

HRMS (ESI, *m/z*) = calc'd for C₁₅H₁₄N₅O₂F 316.1204 found: 316.1201 [M+H]⁺

(E)-4-Amino-6-((2-trifluoromethyl)-1H-indo-5-yl)oxy)pyrimidine-5-carbaldehyde O-methyl oxime (78f)



Yellow solid (68mg, 98%)

R_f : 0.46 (10% EtOAc: hexane)

R_t : 2.991 minutes, 97.2% (Method A)

Mp: 168 °C (decomp)

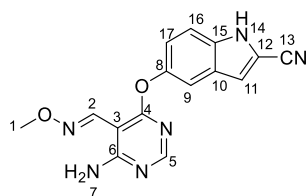
^1H NMR (500 MHz, d_6 -DMSO) δ : 3.95 (s, 3H¹, OCH₃), 7.01 (dt, 1H¹¹, ArH, J = 1.1, 2.3 Hz), 7.10 (dd, 1H¹⁷, ArH, J = 3.3, 8.9 Hz), 7.45 (d, 1H⁹, ArH, J = 2.3 Hz), 7.48 (d, 1H¹⁶, ArH, J = 8.9 Hz), 7.58 (brs, 1H⁷, NH₂), 8.02 (s, 1H⁵, CHN), 8.12 (brs, 1H⁷, NH₂), 8.59 (s, 1H², ArH), 12.36 (s, 1H, NH)

^{13}C NMR (125 MHz, d_6 -DMSO) δ : 62.49 (C-1), 91.53 (s, C-3), 103.71 (s, C-11), 113.33 (s, C-9), 114.24 (s, C-16), 120.08 (s, C-17), 126.54 (s, C-13), 131.05 (s, C-10), 134.75 (s, C-15), 136.31 (s, C-8), 144.21 (s, C-2), 147.02 (s, C-12), 157.91 (s, C-6), 161.81 (s, C-5), 167.64 (s, C-4)

^{19}F (471 MHz, d_6 -DMSO) δ : -58.95

HRMS (ESI, m/z) = calc'd for C₁₅H₁₃N₅O₂F₃ 352.1016 found: 352.1038 [M+H]⁺

(E)-5-((6-Amino-5-((methoxyimino)methyl)pyrimidin-4-yl)oxy)-1H-indole-2-carbonitrile (78h)



White solid (15 mg, 62%)

R_f : 0.33 (50% EtOAc: hexane)

R_t : 2.852 minutes, 96.2% (Method A)

Mp: 155 °C (decomp)

^1H NMR (500 MHz, d_6 -DMSO) δ : 3.95 (s, 3H¹, OCH₃), 7.16 (dd, 1H¹⁷, ArH, $J = 2.3, 8.9$ Hz), 7.34 (s, 1H¹¹, ArH), 7.46 (d, 1H⁹, ArH, $J = 2.3$ Hz), 7.48 (d, 1H¹⁶, ArH, $J = 8.9$ Hz), 7.58 (brs, 2H⁷, NH), 8.03 (s, 1H⁵, ArH), 8.58 (s, 1H², CHN), 12.48 (s, 1H¹⁴, NH)

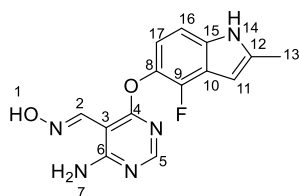
^{13}C NMR (125 MHz, d_6 -DMSO) δ : 63.27 (s, C-1), 91.96 (s, C-3), 109.53 (s, C-9), 113.01 (s, C-13) 116.36 (s, C-11), 118.69 (s, C-16), 120.21 (s, C-17), 123.29 (s, C-12) 127.98 (s, C-10), 134.19 (s, C-15), 136.21 (s, C-8), 142.98 (s, C-2), 155.99 (s, C-6), 162.02 (s, C-5), 166.65 (s, C-4)

HRMS (ESI, m/z) = calc'd for C₁₅H₁₂N₆O₂ 309.1095 found: 309.1088 [M+H]⁺

General procedure for the synthesis of hydroxyl oxime

To a solution of the appropriate aldehyde (1 eq) in DMSO (2 mL), hydroxylamine hydrochloride (4.7 eq) was added and stirred at ambient temperature for two hours. The mixture was then poured onto water (10 mL) and partitioned with EtOAc (3 × 10 mL), dried with MgSO₄ and concentrated under reduced pressure. Column chromatography purification yielded the title compound.

(*E*)-4-Amino-6-((4-fluoro-2-methyl-1*H*-indol-5-yl)oxy)pyrimidine-5-carbaldehyde oxime²⁹² (79a)



White solid (50 mg, 60%)

R_f: 0.33 (7:3 EtOAc: hexane)

Mp: 152 °C (decomp)

¹H NMR (500 MHz, *d*₆-DMSO) δ: 2.39 (s, 3H¹³, CH₃), 6.20 (dt, 1H¹¹, ArH, *J* = 1.0, 2.1 Hz), 6.87 (dd, 1H¹⁷, ArH, *J* = 2.8, 8.6 Hz), 7.08 (dd, 1H¹⁶, ArH, *J* = 1.0, 8.6 Hz), 7.69 (brs, 1H⁷, NH), 7.98 (s, 1H², CHN), 8.00 (brs, 1H⁷, NH), 8.54 (s, 1H⁵, ArH), 11.27 (s, 1H¹⁴, NH), 11.46 (s, 1H¹, OH)

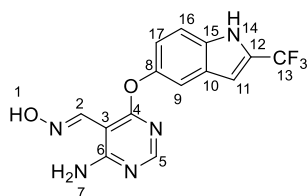
¹³C NMR (125 MHz, *d*₆-DMSO) δ: 13.79 (s, C-13), 95.50 (s, C-3), 106.96 (s, C-11), 116.20 (s, C-16), 118.14 (s, C-17), 118.28 (s, C-10), 131.30 (s, C-15), 136.59 (s, C-8), 137.89 (s, C-12), 143.64 (s, C-2), 147.35 (s, C-9), 157.38 (s, C-6), 161.87 (s, C-5), 166.68 (s, C-4)

¹⁹F (471 MHz, *d*₆-DMSO) δ: -140.26

HRMS (ESI, *m/z*) = calc'd for C₁₄H₁₂N₅O₂F 302.1048 found: 302.1036 [M+H]⁺

Data consistent with literature.

(E)-4-Amino-6-((2-trifluoromethyl)-1H-indo-5-yl)oxy)pyrimidine-5-carbaldehyde oxime (79b)



Yellow solid (58 mg, 52%)

R_f : 0.18 (7:3 EtOAc: hexane)

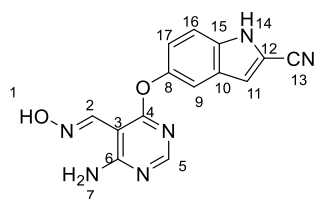
^1H NMR (500 MHz, d_6 -DMSO) δ : 6.56 (s, 1H^9 , ArH), 6.90 (dd, 1H^{17} , ArH, $J = 2.3, 8.9$ Hz), 7.44 (d, 1H, ArH, $J = 2.3$ Hz), 7.13 (dt, 1H^{16} , ArH, $J = 0.8, 8.9$ Hz), 7.89 (d, 1H^{11} , ArH, $J = 2.8$ Hz), 8.00 (s, 2H^7 , NH), 8.44 (s, 1H^2 , ArH), 8.53 (s, 1H^5 , ArH), 11.09 (s, 1H^1 , OH) 11.86 (s, 1H^{14} , NH).

^{13}C NMR (125 MHz, d_6 -DMSO) δ : 94.06 (s, C-3), 102.99 (s, C-11), 113.20 (s, C-9), 115.81 (s, C-16), 122.32 (s, C-17), 126.10 (s, C-13), 130.99 (s, C-10), 134.01 (s, C-15), 136.92 (s, C-8), 143.28 (s, C-2), 147.98 (s, C-12), 159.99 (s, C-5), 161.02 (s, C-6), 167.52 (s, C-4)

^{19}F (471 MHz, d_6 -DMSO) δ : -58.94

HRMS (ESI, m/z) = calc'd for $\text{C}_{14}\text{H}_{10}\text{N}_5\text{O}_2\text{F}_3$ 338.0859 found: 338.0849 $[\text{M}+\text{H}]^+$

(E)-5-Amino-((6-amino-5-((hydroxyimino)methyl)pyrimidine-4-yl)oxy)-1H-indole-2-carbonitrile (79c)



Off-white solid (68mg, 63%)

R_f : 0.45 (7:3 EtOAc: hexane)

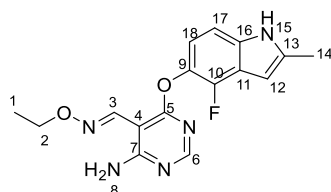
^1H NMR (500 MHz, d_6 -DMSO) δ : 7.16 (dd, 1H^{17} , ArH , $J = 2.1, 8.9$ Hz), 7.34 (dd, 1H^{11} , ArH , $J = 0.9, 2.1$ Hz), 7.45 (d, 1H^9 , ArH , $J = 2.3$ Hz), 7.47 (dt, 1H^{16} , ArH , $J = 0.8, 8.9$ Hz), 7.61-7.77 (brs, 2H^7 , NH_2), 8.00 (s, 1H^5 , ArH), 8.52 (s, 1H^2 , CHN), 11.43 (s, 1H^{14} , NH), 12.48 (s, 1H^1 , CN-OH)

^{13}C NMR (125 MHz, d_6 -DMSO) δ : 92.56 (s, C-3), 107.24 (s, C-13), 113.32 (s, C-9), 113.54 (s, C-11), 113.96 (s, C-16), 114.89 (s, C-12), 121.51 (s, C-17), 126.51 (s, C-10), 135.06 (s, C-15), 143.81 (s, C-2), 147.55 (s, C-8), 157.32 (s, C-5) 161.90 (s, C-6), 167.04 (s, C-4)

HRMS (ESI, m/z) = calc'd for $\text{C}_{14}\text{H}_{10}\text{N}_6\text{O}_2$ 295.0865 found: 295.0859 $[\text{M}+\text{H}]^+$

General procedure for the alkylation of the appropriate oxime

The appropriate oxime (1 eq) was added to flask charged with caesium carbonate (1 eq) and the alkylating agent (1.1 eq) in DMF (1 mL/mmol). The mixture was heated to 50 °C until TLC indicated the reaction was finished (typically 3-18 hours). The reaction mixture was diluted with water (10 mL) and washed with EtOAc (3 × 10mL). The combined organic layers were washed with water (30 mL) and purified via column chromatography.

(E)-4-Amino-6-((4-fluoro-2-methyl-1*H*-indol-3yl)oxy)pyrimidine-5-carbaldehyde *O*-ethyl oxime²⁹² (78b)

Synthesised from ethyl bromide

White solid (17 mg, 77%)

R_f : 0.69 (100% EtOAc) R_t : 2.879 minutes, 96.26% (Method A)

Mp: 185 °C (decomp)

^1H NMR (500 MHz, MeOD) δ : 1.22-1.38 (m, 3H¹, CH₂CH₃), 2.44 (d, 3H¹⁴, CH₃, J = 1.0 Hz), 4.27 (q, 2H², CH₂, J = 7.1 Hz), 6.22 (p, 1H¹², ArH, J = 0.9 Hz), 6.85 (dd, 1H¹⁷, ArH, J = 7.3, 8.6 Hz), 7.09 (dt, 1H¹⁸, ArH, J = 0.6, 8.5 Hz), 7.95 (s, 1H⁶, ArH), 8.67 (s, 1H¹⁵, CHN)

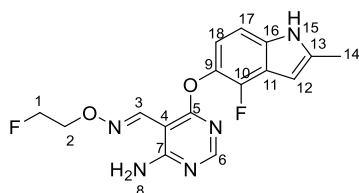
^{13}C NMR (125 MHz, MeOD) δ : 11.99 (s, C-1), 13.35 (s, C-14), 69.73 (s, C-2), 91.81 (s, C-4), 95.00 (s, C-12), 105.90 (s, C-18), 111.01 (s, C-17), 115.10 (s, C-11), 131.02 (s, C-16), 135.62 (s, C-13), 137.11 (s, C-9), 143.02 (s, C-3), 147.31 (s, C-10), 156.75 (s, C-6), 161.53 (s, C-7), 167.10 (s, C-5)

^{19}F (471 MHz, MeOD) δ : -142.34 (d, J = 7.1 Hz)

HRMS (ESI, m/z) = calc'd for C₁₆H₁₆N₅O₂F 330.1361 found: 330.1358 [M+H]⁺

Data consistent with literature.

(E)-4-Amino-6-((4-fluoro-2-methyl-1H-indol-3yl)oxy)pyrimidine-5-carbaldehyde O-(2-fluoroethyl) oxime (78c)



Synthesised from fluoroethyl tosylate

Off-white solid (41 mg, 39%)

R_f : 0.58 (100% EtOAc)

R_t : 2.884 minutes, 99.1% (Method A)

Mp: 215 °C (decomp)

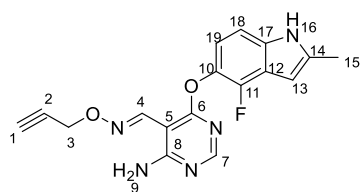
^1H NMR (500 MHz, d_6 -DMSO) δ : 2.39 (d, 3H¹⁴, CH₃, J = 1.1 Hz), 4.43 (ddd, 2H², CH₂, J = 3.3, 4.5, 30.4 Hz), 4.71 (ddd, 2H¹, CH₂, J = 3.3, 4.5, 48.0 Hz), 6.20 (dt, 1H¹², ArH, J = 1.0, 2.0 Hz), 6.88 (dd, 1H¹⁸, ArH, J = 7.4, 8.6 Hz), 7.09 (dd, 1H¹⁷, ArH, J = 0.9, 8.7 Hz), 7.57 (brs, 1H⁸, NH), 8.02 (s, 1H⁶, ArH), 8.14 (brs, 1H⁸, NH) 8.65 (s, 1H³, CHN) 11.28 (brs, 1H¹⁵, NH)

^{13}C NMR (125 MHz, d_6 -DMSO) δ : 13.79 (s, C-14), 73.69 (d, C-2, J = 18.4 Hz), 82.10 (d, C-1, J = 166.0 Hz), 90.98 (s, C-4), 95.50 (s, C-12), 106.98 (s, C-17), 116.14 (s, C-18), 118.11 (s, C-11), 125.65 (s, C-16), 130.32 (s, C-13), 136.62 (s, C-9), 137.81 (s, C-10), 144.54 (s, C-3), 158.07 (s, C-6), 161.77 (s, C-7), 167.25 (s, C-5)

^{19}F (471 MHz, d_6 -DMSO) δ : -140.21 (s), -180.87 (s)

HRMS (ESI, m/z) = calc'd for C₁₆H₁₅N₅O₂F₂ 348.1267 found: 348.1282 [M+H]⁺

(*E*)-4-Amino-6-((4-fluoro-2-methyl-1*H*-indol-3yl)oxy)pyrimidine-5-carbaldehyde *O*-prop-2-yn-1-yl oxime²⁹² (78d)



Synthesised from propargyl bromide

White solid (10 mg, 30%)

R_f : 0.70 (100% EtOAc)

R_t : 2.771 minute, 97.3% (Method A)

Mp: 219 °C (decomp)

^1H NMR (500 MHz, d_6 -DMSO) δ : 2.39 (s, 3H¹⁵, CH₃), 3.57 (t, 1H¹, CCH, $J = 2.4$ Hz), 4.87 (d, 2H³, CH₂, $J = 2.4$ Hz), 6.20 (dt, 1H¹³, ArH, $J = 1.0, 2.1$ Hz), 6.88 (dd, 1H¹⁹, ArH, $J = 7.4, 8.6$ Hz), 7.09 (dd, 1H¹⁸, ArH, $J = 0.9, 8.5$ Hz), 7.59 (brs, 1H⁹, NH), 8.03 (s, 1H, ArH), 8.23 (s, 1H⁷, ArH), 8.23 (brs, 1H⁹, NH), 8.64 (s, 1H⁴, ArH), 11.28 (s, 1H¹⁶, NH)

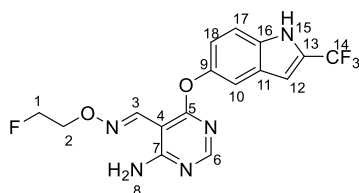
^{13}C NMR (125 MHz, d_6 -DMSO) δ : 13.79 (s, C-15), 62.11 (s, C-3), 78.29 (s, C-1), 80.42 (s, C-2), 90.84 (s, C-5), 95.51 (s, C-13), 106.89 (s, C-18), 114.23 (s, C-10), 116.36 (s, C-19), 128.54 (s, C-12), 132.65 (s, C-14), 136.75 (s, C-11), 137.92 (s, C-17), 145.23 (s, C-4), 157.23 (s, C-8), 158.87 (s, C-7), 161.82 (s, C-6)

^{19}F (471 MHz, d_6 -DMSO) δ : -140.18 (dd, $J = 2.7, 7.5$ Hz)

HRMS (ESI, m/z) = calc'd for C₁₇H₁₄N₅O₂F 340.1204 found: 340.1189 [M+H]⁺

Data consistent with literature.

(*E*)-4-Amino-6-((2-trifluoromethyl)-1*H*-indo-5-yl)oxy)pyrimidine-5-carbaldehyde *O*-2-fluoroethyl oxime (78g)



Synthesised from fluoroethyl tosylate

Light yellow solid (11 mg, 23%)

R_f : 0.30 (1:1 EtOAc: hexane)

R_t : 2.975 minutes, 96.7% (Method A)

Mp: 183 °C (decomp)

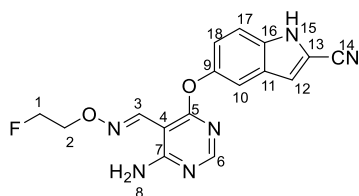
^1H NMR (500 MHz, d_6 -DMSO) δ : 4.43 (dt, 2H², CH₂, J = 4.0, 30.4 Hz), 4.63-4.79 (m, 2H¹, CH₂F), 7.05 (dt, 1H¹¹, ArH, J = 1.3, 2.0 Hz), 7.11 (dd, 1H¹⁸, ArH, J = 2.1, 8.3 Hz), 7.48 (d, 1H¹⁰, ArH, J = 2.3 Hz), 7.51 (d, 1H¹⁷, ArH, J = 8.3 Hz), 7.57 (brs, 1H⁸, NH), 8.03 (s, 1H, ArH), 8.13 (brs, 1H⁸, NH), 8.64 (s, 1H³, CHN), 11.89 (brs, 1H¹⁵, NH)

^{13}C NMR (125 MHz, d_6 -DMSO) δ : 74.32 (s, C-2, J = 19.1 Hz), 81.65 (d, C-1, J = 164.8 Hz), 90.99 (s, C-4), 113.98 (s, C-10), 116.04 (s, C-17), 121.32 (s, C-18), 127.05 (s, C-14), 131.11 (s, C-16), 135.62 (s, C-9), 104.23 (s, C-12), 145.96 (s, C-13), 149.32 (s, C-3), 154.56 (s, C-6), 162.01 (s, C-7), 166.9 (s, C-5)

^{19}F (471 MHz, d_6 -DMSO) δ : -181.23 (s, 1F), -57.34 (d, 3F, J = 4.9 Hz)

HRMS (ESI, m/z) = calc'd for C₁₆H₁₃N₅O₂F₄ 384.1078 found: 384.1073 [M+H]⁺

(E)-5-((6-Amino-5-(((2-fluoroethoxy)imino)methyl)pyrimidin-4-yl)oxy)-1H-indole-2-carbonitrile (78i)



Synthesised from fluoroethyl tosylate

Light brown solid (9 mg, 18%)

R_f : 0.68 (100% EtOAc)

R_t : 2.74 minutes, 95.6% (Method A)

Mp: 179 °C (decomp)

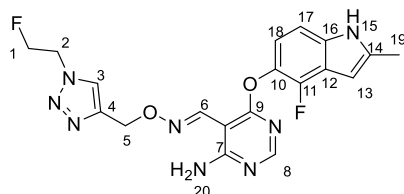
$^1\text{H NMR}$ (500 MHz, d_6 -DMSO) δ : 4.43 (ddd, 2H^2 , CH_2 , $J = 3.1, 5.8, 30.5$ Hz), 4.71 (dt, 2H^1 , CH_2F , $J = 3.1, 5.8, 30.5$ Hz), 7.18 (dd, 1H^{18} , ArH , $J = 7.4$ Hz), 7.35 (m, 1H^{12} , ArH), 7.46 (dd, 1H^{17} , ArH , $J = 0.9, 7.4$ Hz), 7.51 (dd, 1H^{10} , ArH , $J = 2.3, 4.4$ Hz), 8.02 (s, 1H^6 , ArH), 8.67 (s, 1H^3 , CHN), 11.43 (brs, 1H^{15} , NH)

^{19}F (471 MHz, d_6 -DMSO) δ : -180.98

NB: Amine 8 not observed, not enough material for carbon (too dilute sample)

HRMS (ESI, m/z) = calc'd for $\text{C}_{16}\text{H}_{13}\text{N}_6\text{O}_2\text{F}$ 341.1164 found: 341.1161 $[\text{M}+\text{H}]^+$

(E)-4-amino-6-((4-fluoro-2-methyl-1*H*-indol-5-yl)oxy)pyrimidine-5-carbaldehyde O-((1-(2-fluoroethyl)-1*H*-1,2,3-triazol-4-yl)methyl) oxime (78e)



2-Fluoroethyl tosylate (436 mg, 2 mmol) and sodium azide (390 mg, 6 mmol) in dry DMF (10 mL) were allowed to stir at ambient temperature for two days under a blanket of nitrogen. Product was not isolated due to the volatility of fluoroethyl azide and assumed to have reacted to 100% completion, giving a fluoroethylazide reagent (0.2 M). Copper (II) sulphate (4.6 mg, 0.02 mmol), ascorbic acid (6 mg, 0.035 mmol) was added to a flask under nitrogen, followed by (E)-4-amino-6-((4-fluoro-2-methyl-1*H*-indol-3-yl)oxy)pyrimidine-5-carbaldehyde O-prop-2-yn-1-yl oxime (156 mg, 0.46 mmol) in anhydrous DMF (5 mL) was added, followed by the addition of fluoroethylazide solution (10 mL). The reaction was heated to 90 °C and stirred for two hours. The solution was allowed to cool down and poured into 10% aq NH₄Cl, extracted with DCM and the organic phase dried over Na₂SO₄. Bulk solvent was removed *in vacuo* and pure product was isolated by column chromatography (100% EtOAc) to give a pale brown solid (5 mg, 3%)

R_f: 0.78 (100% EtOAc)

R_t: 2.621 minutes, 97.1% (Method A)

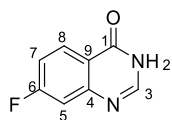
Mp: 179 °C (decomp)

¹H NMR (500 MHz, *d*₆-DMSO) δ: 2.38 (s, 3H¹⁹, CH₃), 4.76-4.80 (m, 2H², CH₂), 4.71-4.89 (ddd, 2H¹, CH₂, *J* = 4.7, 18.6, 33.2 Hz), 5.30 (s, 2H⁵, CH₂), 6.19 (s, 1H¹³, ArH), 6.87 (dd, 1H¹⁸, ArH, *J* = 6.9, 8.6 Hz), 7.09 (dd, 1H¹⁷, ArH, *J* = 1.3, 8.6 Hz), 8.00 (s, 1H⁸, ArH), 8.16 (brs, 2H²⁰, NH), 8.31 (s, 1H³, ArH), 8.59 (s, 1H⁶, CHN), 11.27 (brs, 1H¹⁵, NH)

¹⁹F (471 MHz, *d*₆-DMSO) δ: -140.20, -179.09 (CH₂CH₂F)

NB: not enough material for ¹³C NMR characterisation

HRMS (ESI, *m/z*) = calc'd for C₁₉H₁₈N₈O₂F₂ 429.1594 found: 429.1589 [M+H]⁺

7-Fluoroquinazolin-4-(3H)-one³⁷⁴ (104)

2-Amino-4-fluorobenzoic acid (3 g, 19.3 mmol) was stirred in formamide (30 mL) at 150 °C for six hours. The reaction mixture was allowed to cool and then poured onto ice water (100 mL) and the resultant precipitate collected as a pale yellow solid (3.07 g, 97%).

Mp: 239-241 °C

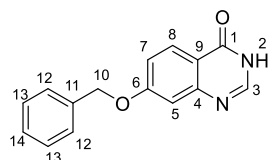
¹H NMR (500 MHz, *d*₆-DMSO) δ: 7.39 (td, 1H⁷, *ArH*, *J* = 6.3 Hz, 8.8 Hz), 7.45 (dd, 1H⁸, *ArH*, *J* = 2.6 Hz, 8.7 Hz), 8.13 (s, 1H⁵, *ArH*), 8.18 (dd, 1H³, *ArH*, *J* = 6.3 Hz, 8.8 Hz), 12.33 (brs, 1H¹, *NH*)

¹³C NMR (125 MHz, *d*₆-DMSO) δ: 110.6-117.3 (C-5 and C-7) 120.10 (C-9), 129.41(C-8), 147.33 (C-3), 151.33 (C-4), 165.02 (C-1), 167.01 (C-6)

¹⁹F NMR (471 MHz, *d*₆-DMSO) δ: -104.53 (td, *J* = 6.3, 9.4 Hz)

HRMS (ESI, *m/z*): calc'd for C₈H₆FN₂O 165.0459 [M+H]⁺; found 165.0463 [M+H]⁺

Data consistent with literature.

7-(Benzyloxy)fluoroquinazolin-4-(3*H*)-one³⁷⁴ (105a)

Sodium hydride, 60% dispersed in mineral oil, (300 mg, 7.24 mmol) was cooled to 0°C in anhydrous DMF (8 mL), benzyl alcohol (0.76 mL, 7.24 mmol) was added slowly and the solution stirred at 0 °C for a further 15 minutes. 7-Fluoroquinazolin-4-(3*H*)-one (300 mg, 1.81 mmol) in anhydrous DMF (5 mL) was added slowly to avoid an exothermic reaction. The reaction mixture was then heated to 140 °C for 90 minutes and then cooled to ambient temperature. The mixture was acidified to pH 3, filtered and washed with water (20 mL) and diethyl ether (20 mL) to yield 7-(benzyloxy)fluoroquinazolin-4-(3*H*)-one as a grey solid (198 mg, 43%).

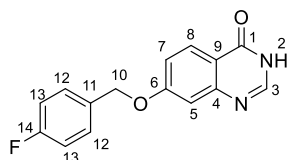
Mp: 210-212 °C

¹H NMR (500 MHz, *d*₆-DMSO) δ: 5.26 (s, 2H¹⁰, ArCH₂), 7.14-7.21 (m, 2H^{5,7}, ArH), 7.33-7.38 (m, 1H¹³, ArH), 7.39-7.44 (m, 2H¹², ArH), 7.46-7.51 (m, 2H¹¹, ArH), 7.99-8.07 (m, 2H^{3,8}, ArH), 12.10 (brs, 1H², NH)

¹³C NMR (125 MHz, *d*₆-DMSO) δ: 70.13 (s, C-10), 109.93 (s, C-5), 116.63(s, C-7), 117.17 (s, C-9), 127.96(s, C-8), 128.27(s, C-12), 128.52 (s, C-14), 128.99 (s, C-13), 136.87 (s, C-11), 146.46(s, C-3), 151.39 (s, C-4), 160.69 (s, C-1), 163.38 (s, C-6)

HRMS (ESI, m/z): calc'd for C₁₅H₁₂FN₂O₂ 253.0972 [M+H]⁺; found 253.0972 [M+H]⁺

Data consistent with literature.

7-((4-Fluorobenzyl)oxy)fluoroquinazolin-4-(3H)-one³⁷⁵ (105b)

Sodium hydride (1 g, 24.3 mmol) was cooled to 0 °C in DMF (8 mL), 4-fluorobenzyl alcohol (2.65 mL, 24.3 mmol) was added slowly and the solution stirred at 0 °C for a further 15 minutes. 7-Fluoroquinazolin-4-(3H)-one (1 g, 6.09 mmol) in DMF (5 mL) was added slowly to avoid an exothermic reaction. The reaction mixture was then heated to 140 °C for 90 minutes and then cooled to ambient temperature. The mixture was acidified to pH 3, filtered and washed with water (20 mL) and diethyl ether (20 mL) to yield 7-((4-fluorobenzyl)oxy)fluoroquinazolin-4-(3H)-one as a cream solid (321 mg, 20%).

Mp: 191-193 °C

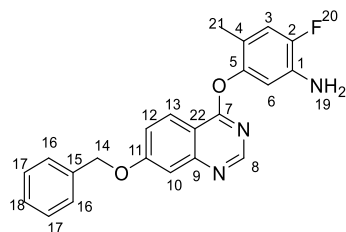
¹H NMR (500 MHz, *d*₆-DMSO) δ: 5.24 (s, 2H¹⁰, ArCH₂), 7.14-7.27 (m, 6H^{5, 7, 12, 13}, ArH), 7.52-7.58 (m, 2H^{3,8}, ArH), 7.98-8.09 (m, 2H^{3,8}, ArH), 12.11 (brs, 1H², NH)

¹³C NMR (125 MHz, *d*₆-DMSO) δ: 69.41 (s, C-10), 109.87 (s, C-5), 115.80 (d, *J* = 21.5 Hz), 117.15 (s, C-13), 127.97 (s, C-8), 130.61 (d, C-14, *J* = 8.2 Hz), 133.10 (s, C-4), 146.51 (s, C-3), 149.89 (s, C-4), 161.37 (s, C-1), 163.27 (s, C-6)

¹⁹F NMR (471 MHz, *d*₆-DMSO) δ: -114.14 (tt, 1F¹⁴, *J* = 5.6, 9.0 Hz)

HRMS (ESI, *m/z*): calc'd for C₁₅H₁₂FN₂O₂ 271.0877 [M+H]⁺; found 271.0874 [M+H]⁺

Data consistent with literature.

5-((7-(Benzyloxy) quinazolin-4-yl)oxy)-2-fluoro-4-methylaniline (111)

7-(Benzyloxy)fluoroquinazolin-4-(3*H*)-one (100 mg, 0.396 mmol), pyBOP (268 mg, 0.515 mmol) was dissolved in MeCN (5.9 mL) and stir for one minute. DBU (91 mg, 0.595 mmol) and 2-fluoro-5-hydroxy-4-methylaniline (168 mg, 1.19 mmol) was added and mixture stirred at ambient temperature for 30 minutes. The reaction mixture was concentrated under reduced pressure and columned (1:1 to 8:2 EtOAc: hexane), yielding 5-((7-benzyloxy) quinazolin-4-yl)oxy)-2-fluoro-4-methylaniline as an off-white solid (67 mg, 45%).

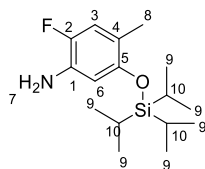
R_f: 0.33 (1:1 EtOAc: hexane)

¹H NMR (500 MHz, *d*₆-DMSO) δ: 1.89 (s, 3H²¹, ArCH₃), 5.13 (s, 2H¹⁹ NH₂), 5.35 (s, 2H¹⁴, ArCH₂), 6.60 (d, 1H⁶, ArH, *J* = 8.1 Hz), 6.97 (d, 1H³, ArH, *J* = 11.8 Hz) 7.34-7.39 (m, 1H¹⁸, ArH), 7.40-7.46 (m, 3H^{17, 12}, ArH), 7.47 (d, 1H¹⁰, *J* = 2.5 Hz), 7.51-7.56 (m, 2H¹⁶, ArH), 8.27 (d, 1H¹³, ArH, *J* = 9.0 Hz), 8.62 (s, 1H⁸, ArH)

¹³C NMR (125 MHz, *d*₆-DMSO) δ: 15.30 (s, C-21), 70.33 (s, C-14), 108.24 (s, C-10), 110.05-110.40 (m, C-6), 116.78 (s, C-2) 117.10-117.31 (m, C-3), 120.74 (s, C-12) 125.37 (s, C-13), 128.32 (s, C-16), 128.56 (s, C-18), 129.01 (s, C-17), 135.59 (d, C-1, *J* = 14.8Hz), 136.70 (s, C-15), 147.06 (s, C-5), 148.67 (d, C-2, *J* = 234.8Hz) 153.98 (s, C-9), 155.24 (s, C-8), 163.36 (s, C-11), 165.98 (s, C-5)

¹⁹F NMR (471 MHz, *d*₆-DMSO) δ: -138.50 (dd, 1F²⁰, *J* = 8.1, 11.9 Hz)

HRMS (ESI, *m/z*): calc'd for C₂₂H₁₈N₃O₂F 376.1456 [M+H]⁺; found 376.1442 [M+H]⁺

2-Fluoro-4-methyl-5-(triisopropylsilyloxy)aniline (114)

Triisopropylsilyl chloride (227 μL , 1.06 mmol) was added to a stirred solution of 2-fluoro-5-hydroxy-4-methylaniline (100 mg, 0.708 mmol), imidazole (72 mg, 1.06 mmol) in anhydrous DCM (2 mL). The resultant mixture was stirred at ambient temperature overnight before the addition of water (5 mL). The reaction mixture was separated and the organic phase was dried over MgSO_4 and concentrated under reduced pressure. Column chromatography purification (4:6 to 8:2 EtOAc: Hexane) afforded the title compound (30mg, 18%).

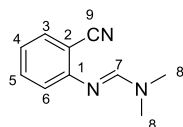
R_f : 0.82 (3:7 EtOAc: hexane)

^1H NMR (500 MHz, CDCl_3) δ : 1.12 (d, 18H^9 , CHCH_3), 1.23-1.32 (m, 3H^{10} , CH), 2.13 (s, 2H^8 , CH_3), 3.50 (brs, 2H^7 , NH_2), 6.26 (dd, 1H^6 , ArH , $J = 7.9$ Hz), 6.75 (ddd, 1H^3 , ArH , $J = 0.8, 11.4$ Hz)

^{13}C NMR (125 MHz, CDCl_3) δ : 13.00 (s, C-8), 16.21 (s, C-9), 18.04 (s, C-10), 107.12 (d, C-6, $J = 3.4$ Hz), 116.82 (d, C-3, $J = 19.6$ Hz), 118.49 (d, C-4, $J = 6.3$ Hz), 138.82 (d, C-1, $J = 14.4$ Hz), 146.22 (d, C-2, $J = 231$ Hz), 150.20 (d, C-5, $J = 2.2$ Hz),

^{19}F NMR (471 MHz, $d\text{-CDCl}_3$) δ : -145.11 (dd, $J = 7.8, 11.4$ Hz)

HRMS (ESI, m/z): calc'd for $\text{C}_{16}\text{H}_{28}\text{FNOSi}$ 298.1997 $[\text{M}+\text{H}]^+$; found 298.1994 $[\text{M}+\text{H}]^+$

(E)-N'-(2-cyanophenyl)-N,N-dimethylformimidamide³⁷⁶ (118)

Anthranilonitrile (500 mg, 4.2 mmol) was suspended in DMF-DMA (1.25 mL, 10.5 mmol) and subjected to microwave irradiation for 15 minutes at 90 °C. The solution was cooled to ambient temperature and purified by column chromatography (2:8 EtOAc: DCM) to afford the title compound as an oil which crystallised on standing (368 mg, 50%).

R_f: 0.67 (2:8 EtOAc: DCM)

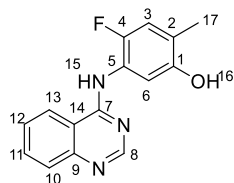
Mp: 30-33 °C

¹H NMR (500 MHz, *d*₆-DMSO) δ: 2.93 (s, 3H⁸, NCH₃), 3.06 (s, 3H⁸, NCH₃), 7.00 (td, 1H⁴, ArH, *J* = 1.1, 7.7 Hz), 7.10-7.16 (m, 1H⁶, ArH), 7.48 (ddd, 1H⁵, ArH, *J* = 1.6, 7.7, 8.2 Hz), 7.58 (dd, 1H³, ArH, *J* = 1.5, 7.8 Hz), 7.92 (s, 1H⁷, NCHN)

¹³C NMR (125 MHz, *d*₆-DMSO) δ: 34.45 (s, C-8), 40.01 (s, C-8), 106.33 (s, C-2), 119.10 (s, C-6), 119.43 (s, C-9), 122.01 (s, C4), 133.40 (s, C-3), 134.15 (s C-5), 155.31 (s, C-1), 155.50 (s, C-7)

HRMS (ESI, *m/z*): calc'd for C₁₀H₁₁N₃ 174.1026 found: 174.1033 [M+H]⁺

Data consistent with literature.

4-Fluoro-2-methyl-5-(quinazolin-4-ylamino)phenol (119)

(*E*)-*N*'-(2-cyanophenyl)-*N*, *N*-dimethylformimidamide (150 mg, 0.866 mmol) was combined with 5-amino-4-fluoro-2-methylphenol (120 mg, 0.85 mmol) in acetic acid (1 mL) and subjected to microwave irradiation for 15 minutes at 118 °C. Diethyl ether (2 mL) was added to the reaction mixture and the resultant precipitate was collected to afford the title compound as a white solid (228 mg, 98%).

*R*_f: 0.19 (1:1 EtOAc: hexane)

*R*_t: 1.793 minutes, 99.5% (Method A)

*M*_p: 206-208 °C

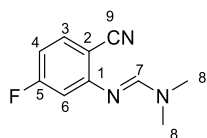
¹H NMR (500 MHz, *d*₆-DMSO) δ: 2.15 (s, 3H¹⁷, ArCH₃), 6.91 (d, 1H⁶, ArH, *J* = 10.7 Hz), 7.02 (d, 1H³, ArH, *J* = 10.7 Hz), 7.61 (ddd, 1H¹², ArH, *J* = 1.4, 6.8, 8.1 Hz), 7.74-7.80 (m, 1H¹¹, ArH), 7.85 (ddd, 1H¹³, ArH, *J* = 1.4, 6.9, 8.2 Hz), 8.41-8.48 (m, 2H^{8,10}, ArH), 9.40 (s, 1H¹⁶, OH), 9.69 (brs, 1H¹⁵, NH)

¹³C NMR (125 MHz, *d*₆-DMSO) δ: 16.11 (s, C-17), 114.16 (s, C-6), 115.23 (s, C-2), 117.42 (s, C-3), 117.98 (s, C-14), 123.50 (s, C-12), 126.70 (s, C-13), 128.09 (s, C-10), 133.50 (s, C-11), 149.5 (s, C-16), 149.93 (s, C-9), 150.45 (d, C-4, *J* = 237.0 Hz), 151.60 (s, C-1), 155.20 (s, C-8), 159.17 (s, C-7)

¹⁹F (471 MHz, *d*₆-DMSO) δ: -132.12 (dd, *J* = 6.8, 10.9 Hz)

IR (cm⁻¹): 1023, 1208, 1469, 1549, 1636, 2903, 3447

HRMS (ESI, *m/z*): calc'd for C₁₅H₁₂FN₃O 270.1037 found: 270.1038 [M+H]⁺

(E)-N'-(2-cyano-5-fluorophenyl)-N, N-dimethylformimidamide (121)

2-Amino-4-fluorobenzonitrile (250 mg, 1.8 mmol) was suspended in DMF-DMA (0.61 mL, 4.59 mmol) and subjected to microwave irradiation for 15 minutes at 90 °C. The solution was cooled to ambient temperature and purified by column chromatography (2:8 EtOAc: DCM) to afford the title compound as an oil which crystallised on standing as colourless needles (298 mg, 85%).

R_f: 0.72 (2:8 EtOAc: DCM)

Mp: 50-53 °C

¹H NMR (500 MHz, *d*₆-DMSO) δ: 3.00 (s, 3H⁸, NCH₃), 3.08 (s, 3H⁸, NCH₃), 6.83 (td, 1H⁴, ArH, *J* = 2.5, 11.5 Hz), 7.07 (dd, 1H⁶, ArH, *J* = 2.5, 11.5 Hz), 7.65 (dd, 1H³, ArH, *J* = 6.5, 8.6 Hz), 8.03 (s, 1H⁷, NCHN)

¹³C NMR (125 MHz, *d*₆-DMSO) δ: 34.52 (s, C-8), 40.48 (s, C-8), 103.05 (d, C-2, *J* = 2.3 Hz), 105.76 (d, C-6, *J* = 22.4 Hz), 109.34 (d, C-4, *J* = 23.6 Hz), 118.46 (s, C-9), 135.62 (d, C-3, *J* = 11.3 Hz), 156.24 (s, C-7), 158.19 (d, C-1, *J* = 9.9 Hz), 165.77 (d, C-5, *J* = 251.7 Hz)

¹⁹F (471 MHz, *d*₆-DMSO) δ: -104.09- -104.18 (m, 1F)

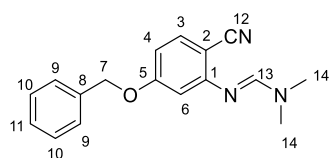
IR (cm⁻¹): 971.93, 1754, 2976

HRMS (ESI, *m/z*): calc'd for C₁₀H₁₀FN₃ 192.0932 found: 192.0931 [M+H]⁺

General procedure for the nucleophilic substitution of (*E*)-*N'*-(2-cyano-5-fluorophenyl)-*N,N*-dimethylformimidamide

To a solution of sodium hydride (4 eq) in DMF (2 mL), substituted benzyl alcohol (4 eq) and stirred at ambient temperature. After 30 minutes (*E*)-*N'*-(2-cyano-5-fluorophenyl)-*N,N*-dimethylformimidamide (1 eq) in DMF (1 mL) was added and the solution stirred overnight at ambient temperature. The reaction was quenched through the addition of water (10 mL) and washed with EtOAc (3 × 10mL). The combined organic phases were and dried over MgSO₄ and concentrated under reduced pressure to afford the title compound.

(*E*)-*N'*-(5-benzyloxy-2-cyanophenyl)-*N,N*-dimethylformimidamide (122a)



Colourless crystalline solid (136 mg, 62%)

R_f: 0.40 (1:1EtOAc: hexane)

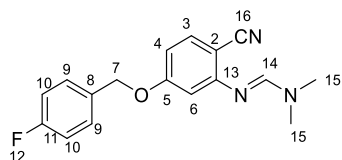
R_t: 2.055 minute, 99.1% (Method A)

Mp: 123-125 °C

¹H NMR (500 MHz, *d*₆-DMSO) δ: 2.98 (s, 3H¹⁴, NCH₃), 3.07 (s, 3H¹⁴, NCH₃), 5.15 (s, 2H⁷, ArCH₂C), 6.66 (dd, 1H⁴, ArH, *J* = 2.4, 8.6 Hz), 6.79 (d, 1H⁶, ArH, *J* = 2.4 Hz), 7.32-7.38 (m, 1H¹¹, ArH), 7.38-7.43 (m, 2H¹⁰, ArH), 7.43-7.47 (m, 2H⁹, ArH) 7.50 (d, 1H³, ArH, *J* = 8.6 Hz), 7.96 (s, 1H¹³, NCHN)

¹³C NMR (125 MHz, *d*₆-DMSO) δ: 34.47 (s, C-14), 40.18 (s, C-14), 69.98 (s, C-7), 98.91 (s, C-2), 104.97 (s, C-6), 109.66 (s, C-4), 119.39 (s, C-12), 128.33 (s, C-10), 128.50 (s, C-11), 128.95 (s, C-9), 134.65 (s, C-3), 136.93 (s, C-8), 155.49 (s, C-13), 157.45 (s, C-1), 162.92 (s, C-5)

HRMS (ESI, *m/z*): calc'd for C₁₇H₁₇N₃ONa 302.1264 found: 302.1261 [M+H]⁺

(E)-N¹-(2-cyano-5-((4-fluorobenzyl)oxy)phenyl)-N,N-dimethylformimidamide (122b)

colourless oil (236 mg, 79%)

R_f: 0.35 (1:1 EtOAc: hexane)

¹H NMR (500 MHz, *d*₆-DMSO) δ: 2.98 (s, 3H¹⁵, NCH₃), 3.07 (s, 3H¹⁵, NCH₃), 5.13 (s, 2H⁷, ArCH₂), 6.66 (dd, 1H⁴, ArH, *J* = 2.4, 8.6 Hz), 6.79 (d, 1H⁶, ArH, *J* = 2.4 Hz), 7.11-7.17 (m, 2H⁹, ArH), 7.31-7.36 (m, 3H^{3,10}, ArH), 7.96 (s, 1H¹⁴, CHN)

¹³C NMR (125 MHz, *d*₆-DMSO) δ: 35.62 (s, C-15), 42.01 (s, C-15), 69.98 (s, C-7), 97.65 (s, C-2), 105.51 (s, C-6), 107.99 (s, C-4), 117.39 (s, C-10), 127.87 (s, C-9), 128.50 (s, C-11), 132.13 (s, C-8), 135.31 (s, C-3), 148.32 (s, C-11), 153.99 (s, C-14), 157.45 (s, C-1), 162.92 (s, C-5)

¹⁹F NMR (471 MHz, *d*₆-DMSO) δ: -116.52 (tt, *J* = 5.6, 9.8 Hz).

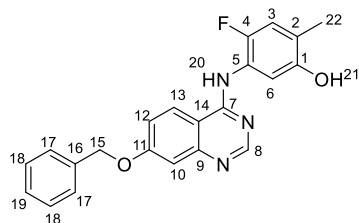
IR (cm⁻¹): 819, 977.08, 1095, 1173, 2213

HRMS (ESI, *m/z*): calc'd for C₁₇H₁₆FN₃O 298.135 found: 298.1352 [M+H]⁺

General procedure for the Dimroth mediated rearrangement

The appropriate *N,N*-dimethylformimidamide (1 eq) was combined with 5-amino-4-fluoro-2-methylphenol (1 eq) in acetic acid (0.6 mL) and subjected to microwave irradiation for 15 minutes at 118 °C. Either diethyl ether (3 mL) was added to the reaction mixture and the resultant precipitate collected or the reaction mixture was loaded on a column and purified by column chromatography to afford the respective quinazolines.

5-((7-Benzyloxyquinazolin-4-yl)amino)-4-fluoro-2-methylphenol (98)



Off-white solid (115 mg, 86%)

R_f : 0.23 (1:1 EtOAc: hexane)

R_t : 7.42 minutes, 98.92% (Method B)

Mp: 201 °C (decomp)

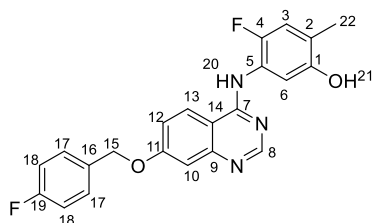
^1H NMR (500 MHz, d_6 -DMSO) δ : 2.14 (s, 3H²², ArCH₃), 5.29 (s, 2H¹⁵, ArCH₂C), 6.90 (d, 1H⁶, ArH, J = 6.8 Hz), 7.00 (d, 1H³, ArH, J = 10.7 Hz), 7.25 (d, 1H¹⁰, ArH, J = 2.6 Hz), 7.29 (dd, 1H¹², ArH, J = 2.6, 9.1 Hz), 7.33-7.38 (m, 1H¹⁹, ArH), 7.40-7.45 (m, 2H¹⁸, ArH), 7.48-7.54 (m, 2H¹⁷, ArH), 8.35 (d, 1H¹³, ArH, J = 9.1 Hz), 8.38 (s, 1H⁸, ArH), 9.36 (s, 1H²¹, OH), 9.50 (brs, 1H²⁰, NH)

^{13}C NMR (125 MHz, d_6 -DMSO) δ : 16.08 (s, C-22), 70.04 (s, C-15), 108.52 (s, C-10), 109.63 (s, C-14), 114.17 (s, C-6), 117.43 (d, C-3, J = 21.3 Hz) 118.39 (s, C-12), 123.17-123.94 (m, C-4), 125.15 (s, C-13), 128.30 (s, C-18), 128.47 (s, C-17), 128.97 (s, C-19), 136.95 (s, C-16), 149.48 (s, C-5), 151.36 (s, C-9), 151.54 (s, C-7), 152.35 (s, C-1), 155.77 (s, C-8), 158.77 (s, C-11), 162.11 (s, C-7)

^{19}F (471 MHz, d_6 -DMSO) δ : -132.37 (dd, 1F, J = 6.9, 10.8 Hz)

IR (cm⁻¹): 1056, 1193, 1334, 1414, 1509, 1582, 1618, 2917, 3129, 3444

HRMS (ESI, m/z): calc'd for C₂₂H₁₈FN₃O₂ 376.1037 found: 376.1444 [M+H]⁺

4-Fluoro-5-((7-(4-fluorobenzyl)oxy))quinazoline-4-yl)amino)-2-methylphenol (101)

White solid (98 mg, 79%)

R_f: 0.35 (1:1 EtOAc: hexane)

R_t: 7.18 minute, 98.42% (Method B)

Mp: 207 °C (decomp)

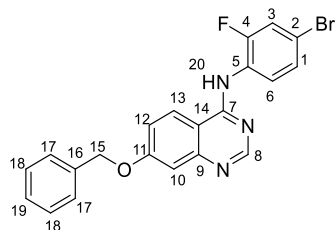
¹H NMR (500 MHz, *d*₆-DMSO) δ: 2.14 (s, 3H²², ArCH₃), 5.27 (s, 2H¹⁵, ArCH₂C), 6.90 (dd, 1H⁶, ArH, *J* = 2.3, 6.8 Hz), 7.00 (d, 1H³, ArH, *J* = 10.7 Hz), 7.21-7.31 (m, 4H^{17, 18}, ArH, *J* = 2.4, 9.7, 12.5 Hz), 7.57 (dd, 2H^{10, 12}, ArH, *J* = 5.5, 8.9 Hz), 8.36 (d, 1H¹³, ArH, *J* = 8.9 Hz), 8.39 (s, 1H⁸, ArH), 9.36 (s, 1H²¹, OH), 9.51 (brs, 1H²⁰, NH)

¹³C NMR (125 MHz, *d*₆-DMSO) δ: 16.08 (s, C-22), 69.32 (s, C-15), 108.51 (s, C-14), 109.66 (s, C-10), 114.16 (s, C-6), 115.72 (s, C-2), 115.89 (s, C-18), 117.53 (s, C-3), 118.37 (s, C-12), 123.91 (s, C-5), 125.91 (s, C-17), 130.61 (s, C-13), 130.63, 130.68 (s, C-16), 149.49 (s, C-9), 151.54 (m, C-4), 155.80 (s, C-1), 156.98 (s, C-11), 158.02 (s, C-7), 158.78 (s, C-8), 162.02 (s, C-19)

¹⁹F (471 MHz, *d*₆-DMSO) δ: -114.17 (td, *J* = 4.8, 8.9 Hz), -132.37 (dd, *J* = 6.9, 11.0 Hz)

IR (cm⁻¹): 1339, 964, 1508, 1607, 1672, 2852

HRMS (ESI, *m/z*): calc'd for C₂₂H₁₇F₂N₃O₂ 394.1362 found: 394.1348 [M+H]⁺

7-(Benzyloxy)-N-(4-bromo—fluorophenyl)quinazolin-4-amine (123)

Cream solid (183 mg, 82%)

R_f : 0.67 (1:1 EtOAc: hexane)

R_t : 8.59 minutes, 98.24% (Method B)

Mp: 186-189 °C

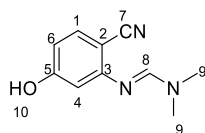
^1H NMR (500 MHz, d_6 -DMSO) δ : 5.30 (s, 2H¹⁵, ArCH₂), 7.29 (d, 1H⁶, ArH, J = 2.6 Hz), 7.30 – 7.42 (m, 4H^{1, 3, 10}, ArH), 7.42 – 7.48 (m, 2H¹⁸, ArH), 7.52 (m, 3H^{17, 19}, ArH), 7.66 (dd, 1H¹², ArH, J = 2.2, 9.9 Hz), 8.37 (d, 1H¹³, ArH, J = 9.1 Hz), 8.42 (s, 1H⁸, ArH), 9.73 (s, 1H²⁰, ArNH).

^{13}C NMR (125 MHz, d_6 -DMSO) δ : 70.10 (s, C-15), 99.99 (s, C-2), 108.46 (s, C-1), 109.63 (s, C-14), 118.75 (s, C-12), 119.70 (s, C-10), 119.89 (s, C-3), 125.20 (s, C-13), 127.96 (s, C-6), 128.32 (s, C-18), 128.50 (s, C-17), 128.97 (s, C-19), 130.13 (s, C-5), 136.88 (s, C-16), 152.31 (s, C-9), 155.51 (s, C-8), 158.43 (s, C-7), 159.73 (m, C-4), 162.31 (s, C-11)

^{19}F (471MHz, d_6 -DMSO) δ : -115.48 (t, J = 8.8 Hz)

IR (cm⁻¹): 1308, 1566, 1619, 2930, 3052, 3446

HRMS (ESI, m/z): calc'd for C₂₁H₁₅FBrN₃O 394.1362 found: 394.1348 [M+H]⁺

(E)-N'-(2-cyano-5-hydroxyphenyl)-N,N-dimethylformimidamide (134)

(E)-N'-(5-benzyloxy-2-cyanophenyl)-N, N-dimethylformimidamide (160 mg, 0.358 mmol) was dissolved in TFA (1.29 mL) and subjected to microwave irradiation for 45 minutes at 70 °C. The reaction mixture was concentrated under reduced pressure and dissolved in DCM (10 mL) and washed with saturated NaHCO₃ (10 mL), dried over MgSO₄ and concentrated under reduced pressure to afford the title compound as a white solid (107 mg, 99%).

R_f: 0.63 (1:1 EtOAc: hexane)

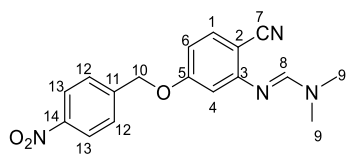
Mp: 173-175 °C

¹H NMR (500 MHz, *d*₆-DMSO) δ: 2.95 (s, 3H⁹, NCH₃), 3.05 (s, 3H⁹, NCH₃), 6.42 (d, 1H⁴, ArH, *J* = 2.2 Hz), 6.50 (dd, 1H⁶, ArH, *J* = 2.3, 8.4 Hz), 7.38 (d, 1H¹, ArH, *J* = 8.4 Hz), 7.82 (s, 1H⁸, ArH), 10.17 (s, 1H¹⁰, OH)

¹³C NMR (125 MHz, *d*₆-DMSO) δ: 34.46 (s, C-9), 39.74 (s, C-9), 97.17 (s, C-2), 105.80 (s, C-4), 110.39 (s, C-7), 113.73 (s, C-6), 155.00 (s, C-3), 157.58 (s, C-8), 162.50 (s, C-5)

IR (cm⁻¹): 1173, 1309, 1672, 2213, 2922

HRMS (ESI, *m/z*): calc'd for C₁₀H₁₁N₃O 190.0985[M+H]⁺; found 190.0981 [M+H]⁺

(E)-N'-(2-cyano-5-((4-nitrobenzyl)oxy)phenyl)-N,N-dimethylformimidamide (132a)

(E)-N'-(2-cyano-5-hydroxyphenyl)-N,N-dimethylformimidamide (160 mg, 0.846 mmol), 4-nitrobenzyl chloride (609 mg, 1.05mmol) and caesium carbonate (550 mg, 1.69mol) was dissolved in MeCN (15 mL) and heated at reflux for two hours. The reaction mixture was concentrated under reduced pressure, then stirred in saturated NaHCO₃ solution (20 mL) and washed with EtOAc (3 × 15 mL). The organic layers were combined and dried over MgSO₄ and concentrated under reduced pressure. Column chromatography purification (1:1 to 100% EtOAc: hexane) afforded the title compound as a colourless oil which solidified on standing (186 mg, 68%).

R_f: 0.63 (7:3 EtOAc: hexane)

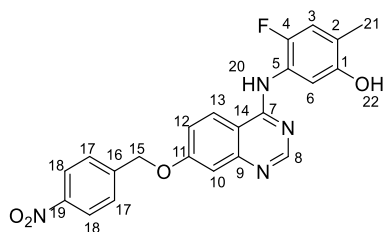
Mp: 122-124 °C

¹H NMR (500 MHz, *d*₆-DMSO) δ: 2.98 (s, 3H⁹, NCH₃), 3.07 (s, 3H⁹, NCH₃), 5.34 (s, 2H¹⁰, ArCH₂), 6.69 (dd, 1H⁴, ArH, *J* = 2.4, 8.6 Hz), 6.81 (d, 1H⁶, ArH, *J* = 2.4 Hz), 7.53 (d, 1H¹, ArH, *J* = 8.6 Hz), 7.69 – 7.77 (m, 2H¹², ArH), 7.96 (s, 1H⁸, ArH), 8.24 – 8.31 (m, 2H¹³, ArH),

¹³C NMR (125 MHz, *d*₆-DMSO) δ: 34.49 (s, C-9), 40.25 (s, C-9), 68.70 (s, C-10), 99.30 (s, C-2), 105.10 (s, C-6), 109.56 (s, C-4), 119.21 (s, C-7), 124.14 (s, C-13), 128.83 (s, C-12), 134.78 (s, C-1), 144.83 (s, C-11), 147.57 (s, C-14), 155.53 (s, C-8), 157.53 (s, C-3), 162.50 (s, C-5)

IR (cm⁻¹): 1235, 1564, 2204, 2960, 3447

HRMS (ESI, *m/z*): calc'd for C₁₇H₁₇N₄O₃ 325.1295 [M+H]⁺; found 325.1294[M+H]⁺

4-Fluoro-2-methyl-5-((7-((4-nitrobenzyl)oxy)quinazolin-4-yl)amino)phenol (136)

(*E*)-*N*'-(2-Cyano-5-((4-nitrobenzyl)oxy)phenyl)-*N,N*-dimethylformimidamide (90 mg, 0.277 mmol) was combined with 5-amino-4-fluoro-2-methylphenol (39 mg, 0.277 mmol) in acetic acid (0.6 mL) and subjected to microwave irradiation for 15 minutes at 118 °C. The reaction mixture was loaded directly onto a column chromatography (1:1 to 100% EtOAc: hexane) which afforded the title compound as an off-white solid (88 mg, 76%).

R_f : 7.22, 97.48% (Method B)

Mp: 122-124 °C

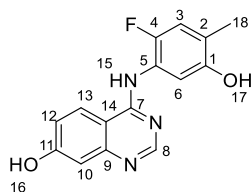
^1H NMR (500 MHz, d_6 -DMSO) δ : 2.14 (s, 3H²¹, ArCH₃), 5.49 (s, 2H¹⁵, ArCH₂), 6.89 (d, 1H⁶, ArH, J = 6.9 Hz), 7.00 (d, 1H³, ArH, J = 10.8 Hz), 7.26 (d, 1H¹⁰, ArH, J = 2.6 Hz), 7.34 (dd, 1H¹², ArH, J = 2.6, 9.1Hz), 7.76 – 7.82 (m, 2H¹⁷, ArH), 8.32 – 8.26 (m, 2H¹⁸, ArH), 8.41 – 8.35 (m, 2H^{8, 13}, ArH), 9.36 (s, 1H²², OH), 9.53 (s, 1H²⁰, NH)

^{13}C NMR (125 MHz, d_6 -DMSO) δ : 16.08 (s, C-21), 68.79 (s, C-15), 108.69 (s, C-10), 109.85 (s, C-14), 114.16 (s, C-6), 117.53 (s, C-3), 118.27 (s, C-12), 123.31 (s, C-5), 124.15 (s, C-18), 125.32 (s, C-13), 128.82 (s, C-17), 138.92 (s, C-16), 144.89 (s, C-9), 147.56 (s, C-19), 149.48 (d, C-4, J = 235.1 Hz), 151.54 (s, C-1), 152.31 (s, C-11), 155.86 (s, C-8), 161.67 (s, C-7)

^{19}F NMR (471 MHz, d_6 -DMSO) δ : -132.35 (dd, J = 7.0, 10.8 Hz)

IR (cm⁻¹): 971.93, 1135, 1410, 1619, 2962, 3431

HRMS (ESI, m/z): calc'd for C₁₇H₁₇N₄O₃ 325.1295 [M+H]⁺; found 325.1294 [M+H]⁺

4-(2-Fluoro-5-hydroxy-4-methylphenyl)amino quinazolin-7-ol (166)

(*E*)-*N*'-(2-cyano-5-((4-nitrobenzyl)oxy)phenyl)-*N,N*-dimethylformimidamide (90 mg, 0.277 mmol) was combined with 5-amino-4-fluoro-2-methylphenol (39 mg, 0.277 mmol) in acetic acid (0.6 mL) and subjected to microwave irradiation for 15 minutes at 118 °C. The reaction mixture was loaded directly onto silica column chromatography (1:1 to 100% EtOAc: hexane) which afforded the title compound as an off-white solid (88 mg, 65%).

*R*_f: 0.32 (100% EtOAc)

*R*_t: 7.22, 97.48% (Method B)

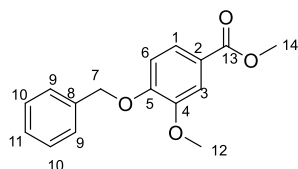
*M*_p: 122-124 °C

¹H NMR (500 MHz, *d*₆-DMSO) δ: 2.13 (s, 3H¹⁷, ArCH₃), 6.90 (d, 1H³, ArH, *J* = 6.9 Hz), 6.96-7.02 (m, 2H^{6,10}, ArH), 7.07 (dd, 1H¹², ArH, *J* = 2.5, 9.0 Hz), 8.27 (d, 1H¹³, ArH, *J* = 9.0 Hz), 8.31 (s, 1H⁸, ArH), 9.33 (s, 1H^{16/17}, OH), 9.38 (s, 1H^{16/17}, OH), 10.43 (s, 1H¹⁵, NH)

¹³C NMR (125 MHz, *d*₆-DMSO) δ: 16.07 (s, C-18), 108.70 (s, C-2), 109.86 (s, C-6), 111.21 (s, C-14), 114.18 (s, C-3), 117.23 (s, C-12), 117.98 (s, C-10), 125.28 (s, C-13), 126.31 (s, C-5), 144.63 (s, C-9), 149.99 (s, C-1), 151.77 (s, C-11), 152.28 (d, C-4, *J* = 230.9 Hz), 155.52 (s, C-8), 161.72 (s, C-7)

¹⁹F NMR (471 MHz, *d*₆-DMSO) δ: -132.50 (dd, *J* = 6.9, 10.7 Hz).

HRMS (ESI, *m/z*): calc'd for C₁₅H₁₂N₃O₂F 286.0986 [M+H]⁺; found 286.0982[M+H]⁺

Methyl-4-(benzyloxy)-3-methoxybenzoate³⁷⁷ (141)

Methyl vanillate (1 g, 5.43 mmol), potassium carbonate (0.835 g, 6.03 mmol) and benzyl bromide (1.40 g, 80.2 mmol) was dissolved in DMF (3.4 mL) under anhydrous conditions and heated to 100 °C for three hours. The reaction mixture was then cooled, poured onto water (25 mL) and washed with ethyl acetate (3 × 25 mL) and with brine (50 mL). The combined organic extracts were dried over MgSO₄ and concentrated under reduced pressure to yield methyl-4-(benzyloxy)-3-methoxybenzoate as a white solid (1.57 g, 99%).

R_f: 0.62 (3:7 EtOAc: hexane)

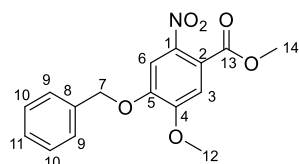
Mp: 84-86 °C

¹H NMR (500 MHz, CDCl₃) δ: 3.90 (s, 3H¹², OCH₃), 3.96 (s, 3H¹⁴, OCH₃), 5.23 (s, 2H⁷, CH₂), 6.91 (d, 1H⁶, ArH, *J* = 8.4 Hz), 7.31-7.36 (m, 1H¹¹, ArH), 7.38-7.41 (m, 2H¹⁰, ArH), 7.44-7.45 (m, 2H⁹, ArH), 7.58 (d, 1H³, ArH, *J* = 2.0 Hz), 7.62 (dd, 1H¹, ArH, *J* = 2.0, 8.4 Hz)

¹³C NMR (125 MHz, CDCl₃) δ: 51.99 (s, C-14), 56.09 (s, C-12), 70.78 (s, C-7), 112.42 (s, C-6), 112.45 (s, C-3), 122.97 (s, C-2), 123.36 (s, C-1), 127.21 (s, C-11), 128.07 (s, C-9), 128.65 (s, C-10), 136.35 (s, C-8), 149.11 (s, C-4), 152.07 (s, C-5), 166.85 (s, C-13)

HRMS (ESI, *m/z*): calc'd for C₁₆H₁₆O₄ 273.1127 [M+H]⁺; found 273.1128 [M+H]⁺

Data consistent with literature.

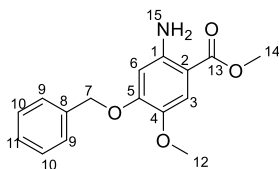
Methyl-4-(benzyloxy)-5-methoxy-2-nitrobenzoate³⁷⁷ (142)

Methyl-4-(benzyloxy)-3-methoxybenzoate (500 mg, 1.84 mmol) in acetic acid (5 mL) was added to a cooled solution of acetic acid (2 mL) and 70% nitric acid (2 mL, 19 equivalents). The reaction mixture was allowed to stir for 20 minutes at -10 °C before being heated to 60 °C for one hour. The reaction mixture was poured onto ice water (100 mL) and the pH adjusted to 7 using 10 M NaOH. The resultant precipitate was collected affording methyl-4-(benzyloxy)-5-methoxy-2-nitrobenzoate as a bright yellow solid (332 mg, 57%).

¹H NMR (500 MHz, CDCl₃) δ: 3.92 (s, 3H¹³, OCH₃), 4.00 (s, 3H¹⁴, OCH₃), 5.23 (s, 2H⁷, CH₂), 7.10 (s, 1H³, ArH), 7.35-7.47 (m, 5H⁹⁻¹¹, ArH), 7.53 (s, 1H⁶, ArH)

¹³C NMR (125 MHz, CDCl₃) δ: 53.28 (s, C-12), 56.65 (s, C-14), 71.44 (s, C-7), 108.90 (s, C-6), 111.02 (s, C-3), 122.00 (s, C-2), 127.53 (s, C-9), 128.59 (s, C-11), 128.85 (s, C-10), 135.09 (s, C-8), 140.17 (s, C-1), 149.36 (s, C-4), 153.07 (s, C-5), 166.30 (s, C-13)

Data consistent with literature.

Methyl-2-amino-4-(benzyloxy)-5-methoxybenzoate³⁷⁸ (**143**)

Methyl-4-(benzyloxy)-5-methoxy-2-nitrobenzoate (300 mg, 0.95 mmol), ammonium acetate (306 mg, 3.97 mmol) and iron powder (211 mg, 3.78 mmol) was dissolved in toluene (5 mL) and water (5 mL). The reaction mixture was heated to 105 °C overnight, before cooling and the addition of ethyl acetate (10 mL). The mixture was stirred at ambient temperature for a further three hours before filtering. The filtrate was washed with water (2 × 15 mL) and brine (15 mL). The organic extracts were dried over MgSO₄ and concentrated under reduced pressure affording methyl-2-amino-4-(benzyloxy)-5-methoxybenzoate as a pale yellow solid (204 mg, 75%).

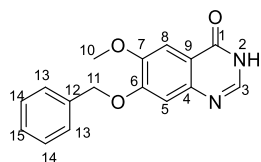
Mp: 119-121 °C

¹H NMR (500 MHz, CDCl₃) δ: 3.85 (s, 3H¹², OCH₃), 3.87 (s, 3H¹⁴, OCH₃), 5.16 (s, 2H⁷, CH₂), 6.22 (s, 1H⁶, ArH), 7.29-7.46 (m, 6H^{3, 9, 10, 11}, ArH)

¹³C NMR (125 MHz, CDCl₃) δ: 51.39 (s, C-12), 56.68 (s, C-14), 70.53 (s, C-7), 101.42 (s, C-6), 102.8 (s, C-2), 113.40 (s, C-3), 127.13 (s, C-9), 128.05 (s, C-11), 128.66 (s, C-10), 136.24 (s, C-8), 141.22 (s, C-1), 146.32 (s, C-4), 154.03 (s, C-5), 158.10 (s, C-13)

HRMS (ESI, m/z): calc'd for C₁₆H₁₆NO₄ 288.1263 [M+H]⁺; found 288.1264 [M+H]⁺

Data consistent with literature.

7-(Benzyloxy)-6-methoxyquinazolin-4-(3*H*)-one³⁷⁹ (144)

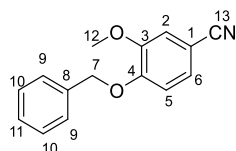
Methyl-2-amino-4-(benzyloxy)-5-methoxybenzoate (200 mg, 0.69 mmol) and ammonium formate (39 mg, 0.626 mmol) was dissolved in formamide (6 mL) and heated to 160 °C for two hours. The reaction mixture was cooled and ice water added and the precipitate filtered. The precipitate was washed with water (3 × 15 mL) affording 7-(benzyloxy)-6-methoxyquinazolin-4-(3*H*)-one as a white solid (153 mg, 82%).

¹H NMR (500 MHz, *d*₆-DMSO) δ: 3.86 (s, 3H¹⁰, OCH₃), 5.24 (s, 2H¹¹, CH₂), 7.22 (s, 1H⁵, Ar*H*), 7.35 (s, 1H⁸, Ar*H*), 7.41 (t, 2H¹⁴, Ar*H*, *J* = 7.5 Hz), 7.44-7.50 (m, 3H^{13, 15}, Ar*H*), 7.96 (s, 1H³, Ar*H*)

¹³C NMR (125 MHz, *d*₆-DMSO) δ: 56.20 (s, C-10), 70.51 (s, C-11), 105.55 (s, C-8), 109.71 (s, C-5), 116.15 (s, C-9), 128.41 (s, C-13), 128.57 (s, C-15), 128.98 (s, C-14), 136.69 (s, C-12), 144.30 (s, C-3), 145.10 (s, C-4), 149.19 (s, C-7), 153.82 (s, C-6), 163.55 (s, C-1)

HRMS (ESI, *m/z*): calc'd for C₁₆H₁₄N₂O₃ 283.1082 [M+H]⁺; found 283.1083 [M+H]⁺

Data consistent with literature.

4-Benzyloxy-3-methoxybenzonitrile³⁸⁰ (148)

4-Hydroxy-3-methoxybenzonitrile (3.4 g, 22.8 mmol) was dissolved in DMF (45 mL), potassium carbonate (4.73 g, 34.2 mmol) was added slowly, followed by benzyl bromide (3.0 mL, 25.1 mmol). The reaction mixture was stirred overnight at ambient temperature then brine (50 mL) solution was added. The precipitate was collected affording the title compound as a white solid (5.45 g, 100%).

R_f: 0.37 (2:8 EtOAc: Hexane)

Mp: 81-83 °C

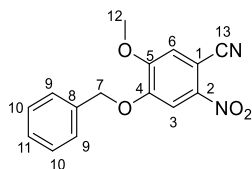
¹H NMR (500 MHz, CDCl₃) δ: 3.91 (s, 3H¹², OCH₃), 5.21 (s, 2H⁷, Ar-CH₂), 6.92 (d, 1H⁵, ArH, *J* = 8.3 Hz), 7.11 (d, 1H², ArH, *J* = 1.9 Hz), 7.22 (dd, 1H⁵, ArH, *J* = 1.9, 8.3 Hz), 7.30-7.46 (m, 5H^{9, 10, 11}, ArH)

¹³C NMR (125 MHz, CDCl₃) δ: 56.19 (s, C-12), 70.89 (s, C-7), 104.17 (s, C-1), 113.31 (s, C-5), 114.39 (s, C-2), 119.21 (s, C-13), 126.25 (s, C-6), 127.24 (s, C-9), 128.31 (s, C-11), 128.76 (s, C-10), 135.80 (s, C-8), 149.66 (s, C-3), 151.99 (s, C-4)

IR (cm⁻¹): 1025, 1134, 1332, 1408, 1509, 1594, 1677, 2220, 3013, 3453

HRMS (ESI, *m/z*): calc'd for C₁₅H₁₃NO₂ 240.1019 found: 240.1017 [M+H]⁺

Data consistent with literature.

4-Benzyloxy-5-methoxy-2-nitrobenzonitrile³⁸¹ (149)

4-Benzyloxy-3-methoxybenzonitrile (3.5 g, 14.62 mmol) was dissolved in acetic anhydride (40 mL), nitric acid (3.6 mL, 65 mmol) was added slowly over a 30 minute period and then stirred overnight. The reaction was poured onto ice-water (25 mL) and the precipitate collected, washed with water affording the title compound as a yellow solid (3.87 g, 93%).

R_f: 0.47 (100% DCM)

Mp: 159-162 °C

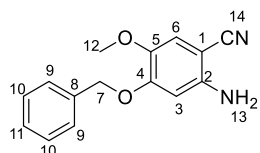
¹H NMR (500 MHz, *d*₆-DMSO) δ: 3.97 (s, 3H¹², OCH₃), 5.33 (s, 2H⁷, ArCH₂), 7.38 (d, 2H⁹, ArH, *J* = 7.2 Hz), 7.42 (ddd, 2H¹⁰, ArH, *J* = 6.8, 8.8 Hz), 7.48 (d, 1H¹¹, ArH, *J* = 6.8 Hz), 7.72 (s, 1H³, ArH), 8.01 (s, 1H⁶, ArH)

¹³C NMR (125 MHz, *d*₆-DMSO) δ: 57.60 (s, C-12), 71.32 (s, C-7), 100.28 (s, C-1), 110.05 (s, C-3), 116.19 (s, C-13), 117.16 (s, C-6), 128.62 (s, C-9), 128.96 (s, C-11), 129.06 (s, C-10), 135.89 (s, C-8), 142.59 (s, C-2), 151.23 (s, C-4), 153.91 (s, C-5)

IR (cm⁻¹): 971.93, 1514, 1571, 2223, 2943

HRMS (ESI, *m/z*): calc'd for C₁₅H₁₂N₂O₄ 285.087 found: 285.0888 [M+H]⁺

Data consistent with literature.

2-Amino-4-benzyloxy-5-methoxybenzonitrile³⁸⁰ (150)

4-Benzyloxy-5-methoxy-2-nitrobenzonitrile (3.46 g, 12.18 mmol), NaHCO₃ (0.22 g, 2.03 mmol) and *tert*-butylammonium chloride (2.25 g, 8.1 mmol) was dissolved in DCM (41 mL) and water (56 ml). The solution was stirred vigorously and sodium dithionite (4.93 g, 28.5 mmol) was added over a two hour period. The solution was stirred for a further hour and extracted. The aqueous phase was extracted twice with DCM (50 mL) and the combined organic layer washed with water (75 mL). The organic layer was dried over MgSO₄ and concentrated to a quarter of the initial volume. HCl in dioxane (0.6 mmol) and ether was added and cooled to 0 °C, the precipitate was collected and washed with diethyl ether. The residue was re-suspended in methanol (45 mL) and basified with saturated NaHCO₃ to pH 8. The solid was collected and to afford the title compound as a yellow solid (1.98 g, 64%).

R_f: 0.76 (1:9 EtOAc: DCM)

Mp: 184-186 °C

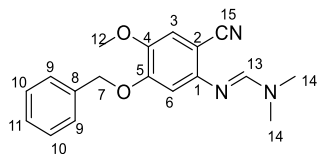
¹H NMR (500 MHz, *d*₆-DMSO) δ: 3.66 (s, 3H¹², OCH₃), 5.05 (s, 2H⁷, ArCH₂), 5.62 (brs, 2H¹³, NH₂), 6.51 (s, 1H³, ArH), 6.91 (s, 1H⁶, ArH), 7.33-7.37 (m 1H¹¹, ArH), 7.40 (ddd, 2H¹⁰, ArH, *J* = 0.9, 6.8, 7.9 Hz), 7.42-7.46 (m, 2H⁹, ArH)

¹³C NMR (125 MHz, *d*₆-DMSO) δ: 56.71 (s, C-12), 70.00 (s, C-7), 84.31 (s, C-1), 100.63 (s, C-3), 114.76 (s, C-6), 119.11 (s, C-14), 128.39 (s, C-9), 128.53 (s, C-11), 128.92 (s, C-10), 136.69 (s, C-4), 140.89 (s, C-5), 148.67 (s, C-2), 153.82 (s, C-8)

IR (cm⁻¹): 971.93, 1381, 1638, 2204, 3241, 3349, 3429

HRMS (ESI, *m/z*): calc'd for C₁₅H₁₄N₂O₂ 255.1128 found: 255.1124 [M+H]⁺

Data consistent with literature.

(E)-N¹-(5-benzyloxy-2-cyano-4-methoxyphenyl)-N,N-dimethylformimidamide³⁸² (151)

2-Amino-4-benzyloxy-5-methoxybenzonitrile (500 mg, 1.97 mmol) was dissolved in DMF-DMA (326 μ L, 2.46 mmol) and irradiated for 15 minutes at 90 °C. The solution was purified by column chromatography (2:8 EtOAc: DCM) to afford the title compound as an orange solid (316 mg, 52%).

R_f: 0.62 (2:8 EtOAc: DCM)

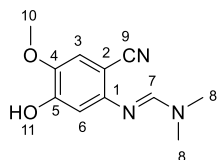
Mp: 130-132 °C

¹H NMR (500 MHz, *d*₆-DMSO) δ : 2.96 (s, 3H¹⁴, NCH₃), 3.06 (s, 3H¹⁴, NCH₃), 3.73 (s, 3H¹², OCH₃), 5.15 (s, 2H⁷, ArCH₂), 6.88 (s, 1H⁶, ArH), 7.12 (s, 1H³, ArH), 7.34-7.38 (m, 1H¹¹, ArH), 7.39-7.44 (m, 2H¹⁰, ArH), 7.44-7.48 (m, 2H⁹, ArH), 7.90 (s, 1H¹³, NCHN)

¹³C NMR (125 MHz, *d*₆-DMSO) δ : 34.41 (s, C-14), 40.37 (s, C-14), 56.49 (s, C-12), 70.40 (s, C-7), 96.61 (s, C-2), 104.40 (s, C-6), 115.00 (s, C-3), 119.51 (s, C-15), 128.51 (s, C-10), 128.56 (s, C-11), 128.97 (s, C-9), 144.60 (s, C-1), 150.93 (s, C-4), 152.88 (s, C-5), 155.01 (s, C-13)

HRMS (ESI, m/z): calc'd for C₁₈H₁₉N₃O₂ 310.155 found: 310.1544 [M+H]⁺

Data consistent with literature.

(E)-N⁷-(2-cyano-5-hydroxy-4-methoxyphenyl)-N,N-dimethylformimidamide³⁸² (152)

(E)-N⁷-(5-benzyloxy-2-cyano-4-methoxyphenyl)-N,N-dimethylformimidamide (100 mg, 0.323 mmol) was dissolved in TFA (1.29 mL) and irradiated for 45 minutes at 70 °C. The reaction mixture was concentrated under reduced pressure and dissolved in DCM (10 mL) and washed with saturated NaHCO₃ (10 mL), dried over MgSO₄ and concentrated under reduced pressure to afford the title compound as a yellow solid (70 mg, 99%).

Mp: 109-111 °C

¹H NMR (500 MHz, *d*₆-DMSO) δ: 2.93 (s, 3H⁸, NCH₃), 3.02 (s, 3H⁸, NCH₃), 3.74 (s, 3H¹⁰, OCH₃), 6.50 (s, 1H⁶, ArH), 7.08 (s, 1H³, ArH), 7.76 (s, 1H⁷, NCHN), 9.84 (s, 1H¹¹, OH)

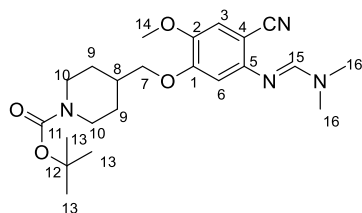
¹³C NMR (125 MHz, *d*₆-DMSO) δ: 34.44 (s, C-8), 40.03 (s, C-8), 56.60 (s, C-10), 95.48 (s, C-2), 106.62 (s, C-6), 115.56 (s, C-3), 119.71 (s, C-9), 143.69 (s, C-5), 148.65 (s, C-1), 152.27 (s, C-4), 154.66 (s, C-7)

IR (cm⁻¹): 1021, 1135, 1251, 1372, 1493, 1509, 1673, 2214, 2852, 2921, 3023

HRMS (ESI, *m/z*): calc'd for C₁₁H₁₃N₃O₂ 220.1081 found: 220.1076 [M+H]⁺

Data consistent with literature.

(*E*)-*tert*-butyl-4-((4-cyano-5-(((dimethylamino)methylene)amino)-2-methoxyphenoxy)methyl)piperidine-1-carboxylate³⁸³ (153)



(*E*)-*N*-(2-cyano-5-hydroxy-4-methoxyphenyl)-*N,N*-dimethylformimidamide (863 mg, 3.94 mmol), tosylate (1.6 g, 4.33 mmol) and caesium carbonate (3.2 g, 9.85 mmol) was dissolved in MeCN (25 mL) and heated at reflux for three hours. The reaction mixture was concentrated under reduced pressure, then stirred in saturated NaHCO₃ solution (30 mL) and extracted with EtOAc (3 × 50 mL). The organic layers were combined and dried over MgSO₄ and concentrated under reduced pressure. Column chromatography purification (1:1 to 100% EtOAc: hexane) afforded the title compound as a colourless oil which solidified on standing (853 mg, 52%).

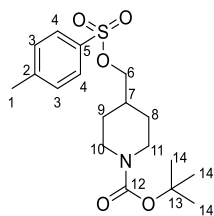
R_f: 0.24 (1:1 EtOAc: hexane)

¹H NMR (500 MHz, *d*₆-DMSO) δ: 1.10-1.18 (m, 2H⁹, CH₂), 1.40 (s, 9H¹³, CCH₃), 1.68 (d, 2H⁹, CH₂, *J* = 10.9 Hz), 2.03 (m, 1H⁸, CCH), 2.92 (m, 2H¹⁰, CH₂), 2.95 (s, 3H¹⁶, NCH₃), 3.05 (s, 3H¹⁶, NCH₃), 3.18 (m, 2H, CH₂), 3.72 (s, 3H¹⁴, OCH₃), 3.89 (d, 2H⁷, OCH₂C, *J* = 6.5 Hz), 6.72 (s, 1H⁶, ArH), 7.08 (s, 1H³, ArH), 7.88 (s, 1H¹⁵, NCHN).

¹³C NMR (125 MHz, *d*₆-DMSO) δ: 26.92 (s, C-9), 28.56 (s, C-13), 34.40 (s, C-16), 35.72 (s, C-8), 39.74 (s, C-16), 42.53 (s, C-10), 56.58 (s, C-14), 72.82 (s, C-7), 78.98 (s, C-12), 96.35 (s, C-4), 103.90 (s, C-6), 115.05 (s, C-3), 119.55 (s, C-17), 141.21 (s, C-5), 144.51 (s, C-2), 153.29 (s, C-1), 154.38 (s, C-15), 154.96 (s, C-11)

HRMS (ESI, *m/z*): calc'd for C₂₂H₃₂N₄O₄ 417.2496 found: 417.2507 [M+H]⁺

Data consistent with literature.

***tert*-Butyl-4-(tosyloxy)methylpiperidine-1-carboxylate³⁸⁴ (157)**

tert-Butyl-4-(hydroxymethyl)piperidine-1-carboxylate (1 g, 4.64 mmol) was stirred in pyridine (3.7 mL) at 0 °C. *p*-Toluene sulfonyl chloride (0.974 mg, 5.11 mmol) was added in one batch under nitrogen and the mixture stirred for 100 minutes at 0 °C. The mixture was allowed to warm to ambient temperature and stirred overnight. The mixture was poured onto water (25 mL) and extracted with ethyl acetate (3 × 15 mL). The organic layer was washed with 1M HCl (15 mL) and brine (15 mL), dried over MgSO₄ and concentrated under reduced pressure. Purification by column chromatography (1:20 to 1:1 EtOAc: hexane) afforded *tert*-butyl-4-(tosyloxy)methylpiperidine-1-carboxylate as a colourless oil which solidified on standing (0.981 g, 57%).

$R_f = 0.58$ (1:1 EtOAc: hexane)

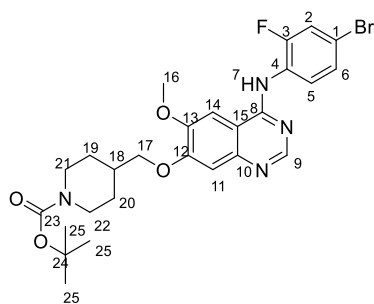
¹H NMR (500 MHz, CDCl₃) δ : 1.11 (dtd, 2H⁸, CH₂, $J = 4.9, 10.0, 13.2$ Hz), 1.42-1.52 (m, 9H¹⁴, CH₃), 1.61-1.69 (m, 2H⁹, CH₂), 1.83 (dddd, 1H⁷, CH, $J = 2.4, 5.0, 10.0, 11.8$ Hz), 2.47 (s, 3H¹, CH₃), 2.61-2.73 (m, 2H¹⁰, CH₂), 3.86 (d, 2H⁶, CH₂, $J = 6.5$ Hz), 7.36 (d, 2H³, ArH, $J = 8.0$ Hz), 7.79 (d, 2H⁴, ArH, $J = 8.0$ Hz)

¹³C NMR (125 MHz, CDCl₃) δ : 14.20 (s, C-1), 21.66 (s, C-8 and C-9), 28.42 (s, C-14), 35.78, (s, C-7) 43.16 (s, C-10 and C-11), 73.98 (s, C-6), 79.54 (s, C-13), 127.87 (s, C-4), 129.88 (s, C-5), 132.90 (s, C-3), 144.85 (s, C-2), 154.66 (s, C-12)

HRMS (ESI): calc'd for C₁₈H₂₇NO₅SNa [M+H]⁺ 392.1502; found [M+H]⁺ 392.1479

Data consistent with literature.

***tert*-Butyl 4-(((4-((4-bromo-2-fluorophenyl)amino)-6-methoxyquinazolin-7-yl)oxy)methyl)piperidine-1-carboxylate^{203, 385} (154)**



(*E*)-*tert*-Butyl-4-((4-cyano-5-(((dimethylamino)methylene)amino)-2-methoxyphenoxy)methyl)piperidine-1-carboxylate (220 mg, 0.528 mmol) was combined with 4-bromo-2-fluoroaniline (101 mg, 0.528 mmol) in acetic acid (1 mL) and subjected to microwave irradiation for one hour at 130 °C. The reaction mixture was loaded directly onto a column (1:1 EtOAc: hexane) to afford the title compound as a white solid (135 mg, 45%).

R_f : 0.50 (9.5:0.5 DCM: MeOH)

Mp: 221-223 °C

¹H NMR (500 MHz, *d*₆-DMSO) δ : 1.14-1.28 (m, 4H¹⁹, CH₂), 1.41 (s, 9H²⁵, CCH₃), 1.79 (d, 2H²⁰, CH₂, $J = 11.3$ Hz), 1.99-2.07 (m, 2H²¹, CH₂), 2.77-2.86 (m, 1H¹⁸, CH₂), 3.32 (s, 2H, CH₂), 3.95-4.07 (m, 5H^{16, 22}, CH₂), 7.19 (s, 1H⁵, ArH), 7.47 (m, 2H^{6, 14}, ArH), 7.53 (t, 1H², ArH, $J = 8.4$ Hz), 7.66 (dd, 1H¹⁴, ArH, $J = 2.2, 10.0$ Hz), 7.79 (s, 1H¹¹, ArH), 8.35 (s, 1H⁹, ArH), 9.53 (s, 1H⁷, NH).

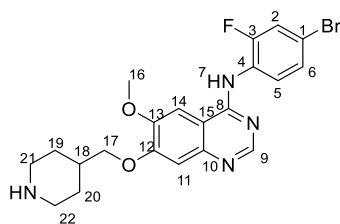
¹³C NMR (125 MHz, *d*₆-DMSO) δ : 27.98 (s, C-25), 28.58 (s, C-19 and C-20), 35.55 (s, C-18), 39.73 (s, C-21 and C-22), 56.63 (s, C-16), 72.88 (s, C-17), 78.98 (s, C-24), 102.43 (s, C-14), 108.18 (s, C-11), 109.05 (s, C-10), 113.96 (s, C-1), 115.32 (s, C-15), 119.88 (s, C-2), 121.65 (s, C-5), 127.94 (s, C-4), 130.01 (s, C-6), 153.38 (s, C-9), 154.16 (s, C-13), 154.37 (s, C-12), 157.32 (s, C-23), 159.23 (s, C-3), 162.53 (s, C-8)

¹⁹F (471 MHz, *d*₆-DMSO) δ : -115.56 (t, $J = 9.0$ Hz)

HRMS (ESI, *m/z*): calc'd for C₂₆H₃₁N₄O₄FBr 561.1507 found: 561.1511 [M+H]⁺

Data consistent with literature.

***N*-(4-Bromo-2-fluorophenyl)-6-methoxy-7-(piperidin-4-ylmethoxy)quinazolin-4-amine^{203, 385} (146)**



(*E*)-*tert*-butyl-4-((4-cyano-5-(((dimethylamino)methylene)amino)-2-methoxyphenoxy)methyl)piperidine-1-carboxylate (600 mg, 1.07 mmol), was dissolved in DCM (1 mL) and TFA (0.3 mL) was added, the solution was stirred at ambient temperature for two hours. The reaction mixture was then concentrated under reduced pressure and loaded directly onto a column (0-1:100-5 MeOH: DCM), affording the title compound as a colourless solid (256 mg, 52%).

*R*_f: 0.27 (9.5:0.5 DCM: MeOH)

Mp: 222-224 °C

¹H NMR (500 MHz, *d*₆-DMSO) δ: 1.30 (ddd, 2H¹⁹, CH₂, *J* = 3.9, 12.6, 24.9 Hz), 1.86 (d, 2H²⁰, CH₂, *J* = 12.5 Hz), 2.08–2.11 (m, 1H¹⁸, CCH), 2.66 (dt, 2H²¹, CH₂, *J* = 2.5, 11.9 Hz), 3.13 (d, 2H²², CH₂, *J* = 12.0 Hz), 3.98 (d, 2H¹⁷, OCH₂, *J* = 6.5 Hz), 4.00 (s, 3H¹⁶, OCH₃), 7.01 (s, 1H⁵, ArH), 7.23 (s, 1H⁶, ArH), 7.33 (s, 1H², ArH), 7.35 (s, 1H¹¹, ArH), 7.36 (s, 1H¹⁴, ArH), 8.46 (s, 1H⁹, ArH), 8.67 (s, 1H⁷, NH)

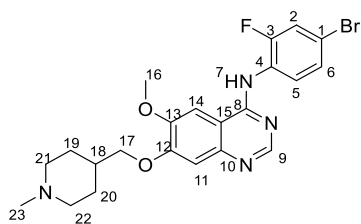
¹³C NMR (125 MHz, *d*₆-DMSO) δ: 27.02 (s, C-19 and C-20), 34.69 (s, C-18), 36.37 (s, C-21 and C-22), 56.68 (s, C-16), 71.99 (s, C-17), 79.01 (s, C-24), 103.32 (s, C-14), 108.86 (s, C-11), 109.51 (s, C-10), 114.07 (s, C-1), 114.99 (s, C-15), 119.58 (s, C-2), 122.69 (s, C-5), 128.32 (s, C-4), 132.61 (s, C-6), 151.99 (s, C-9), 155.09 (s, C-13), 156.32 (s, C-12), 157.98 (s, C-23), 158.99 (s, C-3), 165.35 (s, C-8)

¹⁹F (471 MHz, *d*₆-DMSO) δ: -116.99 (m, 1F)

HRMS (ESI, *m/z*): calc'd for C₂₂H₂₄N₄O₂FBr 463.0018 found: 463.0016 [M+H]⁺

Data consistent with literature.

***N*-(4-bromo-2-fluorophenyl)-6-methoxy-7-((1-methylpiperidin-4-yl)methoxy)quinazolin-4-amine**^{203, 385} (**Vandetanib- 4**)



N-(4-bromo-2-fluorophenyl)-6-methoxy-7-(piperidin-4-ylmethoxy)quinazolin-4-amine (30 mg, 0.065 mmol), sodium triacetoxyborohydride (19 mg, 0.091 mmol) was added to a flask containing formic acid (6 μ L, 0.0845 mmol), acetic acid (5 μ L, 0.078 mmol), DCM (1.6 mL) and methanol (3.2 mL). The flask was stirred for two hours at ambient temperature and then solvent removed under reduced pressure. Saturated NaHCO₃ (3 mL) was added to the residue and the suspension filtered, washed with water (2 mL) and brine (2 mL). The filtrate was extracted with DCM (3 mL) and dried over MgSO₄, solvent removed under reduced pressure, triturated with diethyl ether to afford the title compound as a white solid (6 mg, 20%).

R_f: 0.24 (1:10 MeOH: DCM)

Mp: 228-230 °C

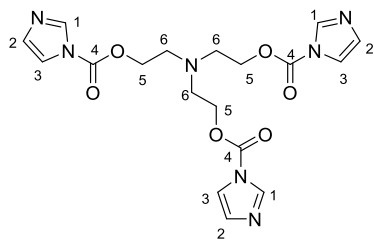
¹H NMR (500 MHz, *d*₆-DMSO) δ : 1.44 (ddd, 2H¹⁹, CH₂, *J* = 3.9, 12.6, 24.8 Hz), 1.85 (d, 2H²⁰, CH₂, *J* = 12.5 Hz), 1.94-1.99 (m, 3H^{17, 21}, CH and CH₂), 2.32 (s, 3H²³, NCH₃), 2.85 (d, 2H²², CH₂, *J* = 11.6 Hz), 3.98 (s, 3H¹⁶, OCH₃), 4.03 (d, 2H¹⁷, OCH₂, *J* = 5.5 Hz), 6.99 (s, 1H⁵, ArH), 7.21 (s, 1H⁶, ArH), 7.26 (s, 1H², ArH), 7.34 (d, 1H¹¹, ArH, *J* = 1.2 Hz), 7.36 (d, 1H¹⁴, ArH, *J* = 1.2 Hz), 8.51 (s, 1H⁹, ArH), 8.68 (brs, 1H⁷, NH)

¹³C NMR (125 MHz, *d*₆-DMSO) δ : 28.68 (s, C-19 and C-20), 34.92 (s, C-18), 46.98 (s, C-23), 49.32 (s, C-21 and C-22), 55.69 (s, C-16), 70.65 (s, C-17), 79.86 (s, C-24), 102.82 (s, C-14), 107.52 (s, C-11), 108.91 (s, C-10), 114.21 (s, C-15), 114.74 (s, C-1), 117.65 (s, C-2), 121.21 (s, C-5), 127.68 (s, C-4), 131.32 (s, C-6), 153.04 (s, C-9), 155.23 (s, C-13), 155.99 (s, C-12), 157.08 (s, C-23), 158.86 (s, C-3), 164.06 (s, C-8)

¹⁹F NMR (471 MHz, *d*₆-DMSO) δ : -115.86 (m, 1F)

HRMS (ESI, *m/z*): calc'd for C₂₁H₂₂N₄O₂FBr 462.1013 found: 462.1003 [M+H]⁺

Data consistent with literature.

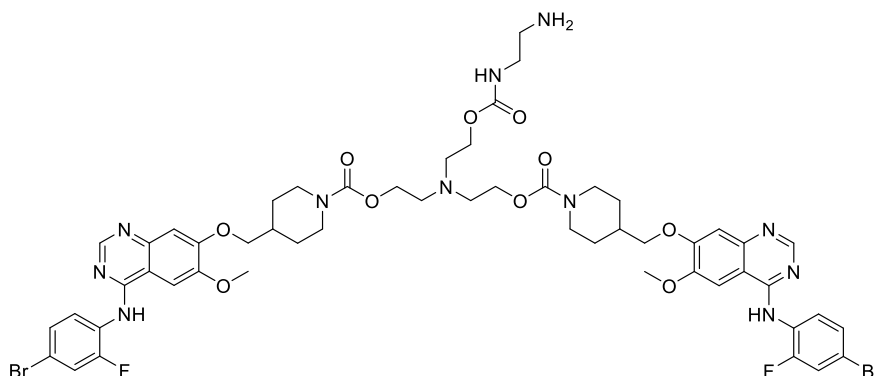
Nitrilotris(ethane-2,1-diyl) tris(1*H*-imidazole-1-carboxylate)³⁸⁶ (159)

Triethylamine (4.0 mL, 28 mmol) was added to a stirred solution of triethanolamine (0.45g, 3mmol) in anhydrous DCM (50 mL). 1,1'-Carbanoyl diimidazole (4.06 g, 24 mmol) was added and the mixture was stirred at ambient temperature for 12 hours. The mixture was cooled to 0 °C, then water (50 mL) was added and stirred for a further 30 minutes. The water was separated and the organic layer was washed with ice-cold water (2 × 50 mL) and brine (50 mL). The organic phase was dried over MgSO₄ and concentrated under reduced pressure to afford the title compound as a colourless oil (1.01 g, 78%).

¹H NMR (500 MHz, CDCl₃): 3.06 (d, 6H⁶, NCH₂, *J* = 5.9 Hz), 4.43 (t, 6H⁵, OCH₂, *J* = 5.9 Hz), 7.08-7.11 (m, 3H², ArH), 7.24 (t, 3H³, ArH, *J* = 1.1Hz), 8.13 (s, 3H¹, ArH)

Data consistent with literature.

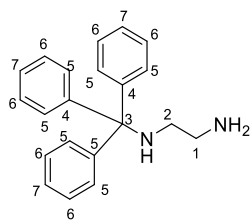
(2-(((2-Aminoethyl)carbamoyloxy)ethyl)azanediy)bis(ethane-2,1-diyl) bis (4-(((4-(4-bromo-2-fluorophenyl)amino)-6-methoxyquinaolin-7-yl)oxy)methyl)piperidine-1-carboxylate³⁸⁶ (**160**)



ZD-G1 (210 mg, 0.42 mmol) was added to a solution of 2,2',2''-nitriлотris(ethane-2,1-diyl)-tris(1H-imidazole-1-carboxylate) (85 mg, 0.22 mmol) in DMSO (2 mL). NEt₃ (400 μL, 2.80 mmol) was added to this solution. The solution was stirred overnight at ambient temperature, ethylene diamine (50 μL) was added and stirred for a further 24 hours. The reaction was quenched by the addition of TFA (20 μL). Purification of the crude ZD-G2 was achieved using the semi-prep method highlighted in the general comments section. The peak containing ZD-G2 was collected, lyophilized and stored in the dark at -20 °C until use.

LCMS: calc'd 1209.92 for C₅₃H₆₁N₁₁O₁₀Br₂F₂ found 1210.5 [M+H]⁺

Data consistent with literature.

***N*¹-tritylethane-1,2-diamine³⁸⁷ (164)**

Anhydrous ethylenediamine (500 mg, 8.32 mmol), potassium carbonate (1.15 g, 8.32 mmol) in DCM (10 mL) were stirred under nitrogen at ambient temperature. Then, triphenylchloro benzene (3.48 g, 12.48 mmol) in DCM (10 mL) was added dropwise to the solution over a period of four hours, and stirring was continued overnight at ambient temperature. The solid material formed and potassium carbonate were filtered off and the filtrate was washed with water (3 × 100 mL). The solution was dried over MgSO₄, concentrated under reduced pressure to afford the title compound as a colourless oil (1.88 g, 73%).

Mp: 81-83 °C.

¹H NMR (500 MHz, MeOD) δ: 2.24 (t, 2H, CH₂, *J* = 6.2 Hz), 2.74 (t, 2H, CH₂, *J* = 6.2 Hz), 7.15-7.21 (m, 3H⁷, *ArH*), 7.24-7.31 (m, 6H⁵, *ArH*), 7.46-7.50 (m, 6H⁶, *ArH*)

¹³C NMR (125 MHz, MeOD) δ: 41.64 (s, C-1), 45.82 (s, C-2), 70.58 (s, C-3), 125.88 (s, C-7), 127.32 (s, C-5), 128.50 (s, C-6), 146.14 (s, C-4)

NB: degradation of product occurred after a period of 7 days when stored under nitrogen at 0 °C

Data consistent with literature.

7.2 Biology

7.2.1. Table of standard solutions

Table 29: General stock solutions

Name	Recipe
10% Sodium dodecyl sulfate	10% (w/v) SDS pH 7.0 in deionised water
5x Laemmli sample buffer	60 mM Tris (pH 6.8), 25% (v/v) glycerol, 2% SDS, 0.1% (w/v) bromophenol blue, 14.4 mM 2-mercaptoethanol, made up to the required volume with deionised water, aliquoted and stored at -20°C.
2x Laemmli sample buffer	5x Laemmli buffer diluted with deionised water to required volume
Kinase buffer	50 mM Tris (pH 7.5), 50 mM NaF, 10 mM β -glycerophosphate, 1 mM EDTA pH 8.0, 1 mM EGTA pH 8.0, 0.2% (v/v) Triton-X-100
10x TBS	500 mM Tris.HCl, pH 7.4
1x TBS-Tween 20	50 mM Tris.HCl, 0.1% Tween 20
Western blot stack (5%)	30% Acrylamide, 0.5M Tris (pH 6.8), 10% SDS, 10% APS, TEMED
Western blot resolve (6%)	Protogel, 1.5 M Tris HCl, 10% SDS, 10%APS, TEMED, dH ₂ O
1x Running buffer	25 mM Tris, 0.2 M glycine, SDS
1x Transfer buffer	50 mM Tris, 0.4 M glycine, MeOH
RIPA buffer	150 mM NaCl, 1% Triton-X, 0.5% sodium deoxycholate, 0.1% SDS 50 mM Tris (pH 8.0)
Coomassie stain	0.2% (w/v) Coomassie brilliant blue R250 (Sigma), 45% (v/v) Methanol, 10% (v/v) ethanoic acid. Made upto volume with deionised water

7.2.3. Culture of cell lines

HCT116, human colon carcinoma, was obtained from the European Collection of Authenticated Cell Cultures (ECACC) and routinely passaged with a ratio of 1:10 biweekly. A549, human caucasian lung carcinoma, was purchased from ECCAC and routinely passaged 1:8 biweekly. HEK293 were kindly donated by Francisco Rivero (Hull-York Medical School) and routinely passaged 1:10 biweekly.

Cell lines were cultured in 10cm dishes (Greiner, UK) containing 10mL of complete medium: Dulbeco`s Modified Eagles Medium (DMEM; Lonza, UK), supplemented with 10% fetal bovine serum (FBS, GIBCO, UK). Cells were maintained in a humidified incubator at 37 °C, in an atmosphere of 5% CO₂.

Upon reaching desired confluence, typically 80-90%, the cell monolayers were passaged in a class II biological safety cabinet (Airstream, ESCO, UK). The medium was removed and the cell monolayer washed with sterile phosphate buffer saline (PBS; Lonza). To dissociate adherent cells, 0.05% trypsin-ethylenediaminetetra acetic acid (Lonza) in PBS was added to the dish (3 mL) for 3-5 minutes at 37 °C and agitated to ensure thorough removal of the monolayer. Complete medium (7 mL) was added to the flask to inhibit the enzymatic action of the trypsin, the cell suspension was recovered and centrifuged at 1000 x g for 5 minutes to pellet the cells. Following removal of the supernatant, the pellet was re-suspended in complete medium, cells were counted and the appropriate number of cells and were placed in a dish with fresh complete medium (10 mL).

Cell counting

The number of cells in suspension were calculated using an improved neubauer haemocytometer. Cell suspension (10 µL) was added to the haemocytometer and the number of viable cells in the 25 squares (volume = 1×10^{-4} cm³) were counted under a light microscope. The average of four counts was taken and the number of cells were calculated.

Cell number = Average cell count x 10^4 (cells/mL)

7.2.3. Cell proliferation assay

Cells (A549, HCT116) were seeded in a 96 well plate, at $1-3.2 \times 10^3$ cells per well, and allowed to adhere for 48 hours, thus allowing externalisation of transmembrane proteins. After the 48 hour period, the media was replaced with fresh media supplemented with 0- μ M of the compounds to be tested and the plates were incubated for a further 24 hours. After the stated 24 hours the compound-containing media was removed and replaced with fresh complete media (100 μ L). 3-(4,5-dimethylthiazol-2-yl)-5-(3-carboxymethoxyphenyl)-2-(4-sulfophenyl)-2H-tetrazolium phenazine ethosulfate (MTS) was added in a 20 μ L volume. The plates were incubated for 4 hours and the absorbance was read using a biotek plate reader. All experiments were completed in triplicate. The IC_{50} values were calculated using Graphpad Prism 6 software.

7.2.4. Nuclear Staining

Cells (A549, HCT116) were seeded into 6 well plates containing glass coverslips at a density of $8.6-19 \times 10^4$ cells per well in 4 mL of complete medium. The cells were incubated for 24 hours before the media was removed and refreshed with complete media containing the IC_{50} dose. The plates were returned to the incubator for 16 hours. After the 16 hour period the medium was removed and the wells washed with warm PBS (1x), ice cold methanol was added and allowed to fix at $-20\text{ }^{\circ}\text{C}$ for five minutes. After the allotted five minutes the wells were washed with PBS (3x) and the coverslips removed from the well and fixed onto a glass slide. The glass slides were stained with 2-(4-Amidinophenyl)-1H-indole-6-carboxamide (DAPI) and the slides were analysed using an Axiovert fluorescence microscope and Zen Blue analysis software (Zeiss).

7.2.5. Protein preparation and Western blot analysis

7.2.5.1. Protein extraction from cells

Cells (A549, HCT116 and HEK293) were harvested from 10 cm dishes using a scraper, to be able to analyse transmembrane receptors, cell suspensions were centrifuged for five minutes at $1000 \times g$. Cell pellets were re-suspended in warm PBS and centrifuged for a second time at $600 \times g$ for 5 minutes. Cell pellets were resuspended in equal volumes of kinase buffer (see general stock solutions Table 29) containing protease inhibitor cocktail (Sigma Aldrich, Gillingham, UK) and $1 \times$ phosphatase inhibitor cocktail (Roche, UK). Cells were lysed on ice for one hour then sonicated on ice in 30s bursts over a five minute period using a bioruptor (Diagenode, Belgium). Any remaining unlysed cells and cellular debris were removed by centrifuging at $20,000 \times g$ for 15 minutes at 4°C . Protein content of the samples was determined as per section 6.2.5.2

7.2.5.2. Determination of protein content

Concentration of protein extracts were determined using the Bradford assay and used as per the manufacturer's instructions. The absorbance at 595 nm was measured using a biotek plate reader. The protein concentration was calculated by comparison with bovine serum albumin standards of known concentration.

7.2.5.3. Sample preparation for SDS polyacrylamide gel electrophoresis

To each protein sample, $5 \times$ Laemmli was added to create a final concentration of $1 \times$ Laemmli solution. Samples were then heated to 65°C for 15 minutes prior to loading or storage at -20°C .

7.2.5.4. SDS polyacrylamide gel electrophoresis

Resolving gels were prepared with either 6% or 10% acrylamide in separating buffer (see Table 29). A 5% acrylamide stacking gel was prepared using stacking buffer (see Table 29). Gels were run in SDS-PAGE running buffer (Table 29) for 135 or 60 minutes, dependant on % acrylamide, at 100 V. All blue markers (Biorad) were used as a size reference marker.

7.2.5.5. Coomassie staining of SDS gels

Although the majority of gels were used for western blotting, in each case a gel was retained for coomassie staining to assess total protein levels and equal loading. To assess total protein

loading, the gels were stained with Brilliant Blue Coomassie (Sigma Aldrich, see Table 29) for a minimum of one hour, before in destaining 5% methanol, 10% acetic acid in dH₂O for a minimum of one hour. The gels were imaged using a Biorad XRS+ ChemiDoc with an exposure time of five minutes.

7.2.5.6. Protein transfer

For immunodetection, the separated proteins were transferred onto a polyvinylidene difluoride (PVDF) membrane (Millipore). The PVDF membrane was pre-soaked in methanol then placed in transfer buffer along with four pieces of filter paper (Whatman) and two Teflon sponges (Biorad) per gel. The components were assembled onto the black side of the transfer cassette in the following order: Teflon sponge, two pieces of filter paper, gel, membrane, two pieces of filter paper, Teflon sponge. After the addition of each layer the assembly was rolled gently to remove air bubbles, at no point was the PVDF membrane touched. The closed cassette was placed into a tank containing cold transfer buffer, with ice packed around the outside of the tank and transferred at 30 V for six hours allowing for sufficient transfer of larger proteins.

7.2.5.7. Immunoblotting

The PVDF membranes were incubated with 5% bovine serum albumin (BSA) in TBS-Tween 20 (Sigma Aldrich) for one hour at ambient temperature with agitation, preventing any non-specific interactions. Primary antibodies were incubated with the membrane under the appropriate conditions (see Table 30). Following incubation with primary antibody, the membranes were washed with TBS-Tween 20, 3 × ten minutes prior to incubation with horseradish peroxidase (HRP) conjugated secondary antibody for one hour at ambient temperature (see Table 30). Following secondary antibody incubation the membrane was washed with TBS-Tween 20 in order to remove any unbound antibody.

7.2.5.8. Enhanced Chemi-Luminescence (ECL) detection of HRP-conjugated secondary antibody binding

The detection of antibody binding was assessed using ECL reagents purchased from Millipore. The working solution was prepared by combining equal amounts of the stable peroxide solution and Luminol/Enhancer solution and used immediately. The washed membrane was incubated with the working solution for five minutes, then placed in a plastic folder. Chemiluminescence was captured on a Chemidoc XRS+ system using exposure times

of 5-15 minutes. To allow size estimation, a white light image of the coloured markers was also collected.

Table 30: Western blotting antibodies and conditions used

Antigen	Antibody type	Species raised in	Species raised against	Dilution factor	Conditions	Supplier information
VEGFR ₂	1°	rabbit	human	1:1000	4 °C overnight, 5% BSA	Cell signalling technology
p-VEGFR ₂ (Y951)	1°	rabbit	human	1:1000	4 °C overnight, 5% BSA	Cell signalling technology
p-VEGFR ₂ (Y996)	1°	rabbit	human	1:1000	4 °C overnight, 5% BSA	Cell signalling technology
p-VEGFR ₂ (Y1054)	1°	rabbit	human	1:1000	4 °C overnight, 5% BSA	Cell signalling technology
p-VEGFR ₂ (Y1175)	1°	rabbit	human	1:1000	4 °C overnight, 5% BSA	Cell signalling technology
β-tubulin	1°	rabbit		1:1000	4 °C overnight, 5% BSA	Cell signalling technology
GAPDH	1°	mouse	rabbit	1:000	4 °C overnight, 5% BSA	Cell signalling technology
cleaved caspase-3	1°	rabbit		1:1000	4 °C overnight, 5% BSA	Cell signalling technology

7.3 Radiochemistry

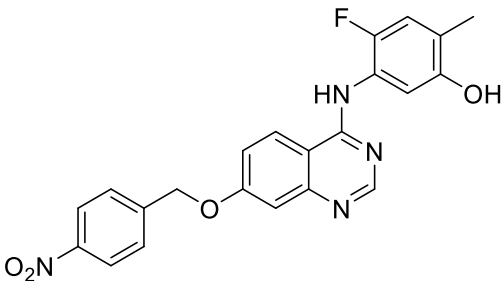
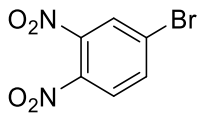
7.3.1. Production

[¹⁸F]-Fluoride was provided by Alliance Medical Radiopharmacy Ltd at the Royal Marsden NHS Foundation Trust (Sutton site). [¹⁸F]-Fluoride was generated from H₂¹⁸O by an accelerated cyclotron proton beam via the ¹⁸O(p, n)¹⁸F reaction on a GE PETrace 16 MeV cyclotron. The beam is directed on a target containing ¹⁸O enriched water, producing no carrier added [¹⁸F]-fluoride which was aliquoted from stock activity for all reactions. Yields quoted for the reactions are expressed as the decay corrected format, for example a reaction began with 200 MBq and 20 MBq were isolated on a cartridge after a 109 minute reaction, decay corrected this would be 40 MBq isolated – a 40% yield.

7.3.2. Manual Radiolabelling

Smaller aliquots were taken from stock activity, typically between 94-500 MBq was collected in a 2 mL V glass vial containing Kryptofix_{2.2.2} and the appropriate base (Table 31). Acetonitrile (300 μL) was added to the flasks and azeotropically dried under a stream of nitrogen at 100-110 °C, followed by a further two additions of acetonitrile (250 μL). Upon dryness, the precursor in the appropriate solvent (DMSO, DMF, DMA) was heated for the given times and temperatures using a heating block or the microwave reactor. Reactions were monitored by taking small aliquots of the reaction mixture and diluted in the starting HPLC phase and using the HPLC programme outlined in the general comments section.

Table 31: Optimised radiolabelling conditions

Entry	Precursor	Base (mg)	K _{2.2.2}
a		K ₂ CO ₃ (0.7 mg)	2 mg
b		K ₂ CO ₃ (0.5 mg)	5 mg

7.2.3. Automated Radiolabelling

No carrier added aqueous [^{18}F]-fluoride (500-600 MBq) in enriched ^{18}O water was aliquoted from stock solution, delivered from the cyclotron, directly to the synthesiser. The activity was trapped on a QMA cartridge. 1 mL of eluent solution (2 mg of $\text{K}_{2.2.2}$, 0.5 mg of K_2CO_3 in water and acetonitrile) was delivered into the reactor vessel. The [^{18}F]-fluoride solution was evaporated to dryness by a combination of a nitrogen stream and vacuum at a temperature of 100 °C for ten minutes, obtaining an [^{18}F]-fluoride/ $\text{K}_{2.2.2}$ /carbonate mixture. Following the evaporation, the nitro precursor (2 mg) in 500 μL of a MeCN: DMF solution was added to the reactor vessel and heated at 150 °C for ten minutes. An aliquot of the reaction mixture was removed for HPLC analysis.

Chapter Eight

References and Appendix

8. References and Appendix

8.1 References

1. D. Ribatti and E. Crivellato, *Dev. Biol.*, 2012, **372**, 157-165.
2. F. Hillen and A. W. Griffioen, *Cancer Metastasis Rev.*, 2007, **26**, 489-502.
3. M. Papetti and I. M. Herman, *Am. J. Physiol. Cell. Physiol.*, 2002, **282**, C947-C970.
4. A. S. Chung, J. Lee and N. Ferrara, *Nat. Rev. Cancer*, 2010, **10**, 505-514.
5. I. M. Olfert and O. Birot, *Microcirculation*, 2011, **18**, 316-330.
6. T. Tonini, F. Rossi and P. P. Claudio, *Oncogene*, 2003, **22**, 6549-6556.
7. G. D. Yancopoulos, S. Davis, N. W. Gale, J. S. Rudge, S. J. Wiegand and J. Holash, *Nature*, 2000, **407**, 242-248.
8. G. Oliver, *Nat. Rev. Immunol.*, 2004, **4**, 35-45.
9. J. Folkman and C. Haudenschild, *Nature*, 1980, **288**, 551-556.
10. N. Ferrara, H.-P. Gerber and J. LeCouter, *Nat. Med.*, 2003, **9**, 669-676.
11. R. K. Jain, *Nat. Med.*, 2003, **9**, 685-693.
12. R. H. Adams and K. Alitalo, *Nat. Rev. Mol. Cell Biol.*, 2007, **8**, 464-478.
13. S. Patan, B. Haenni and P. H. Burri, *Microvasc. Res.*, 1996, **51**, 80-98.
14. A. N. Makanya, R. Hlushchuk and V. G. Djonov, *Angiogenesis*, 2009, **12**, 113-123.
15. S. Rodriguez and U. Huynh-Do, *J. Oncol.*, 2012, **2012**, 141236.
16. S. Neidle, *Cancer drug design and discovery*, Elsevier, 2014.
17. Cell and Signalling, Angiogenesis, <http://www.cellsignal.com/common/content/content.jsp?id=pathways-angiogenesis>, Accessed November, 2015.
18. P. Carmeliet, *Oncology*, 2005, **69 Suppl 3**, 4-10.
19. F. Shalaby, J. Rossant, T. P. Yamaguchi, M. Gertsenstein, X. Wu, M. L. Breitman and A. C. Schuh, *Nature*, 1995, **376**, 62-66.
20. N. Ferrara, K. Carver-Moore, H. Chen, M. Dowd, L. Lu, K. S. O'Shea, L. Powell-Braxton, K. J. Hillan and M. W. Moore, *Nature*, 1996, **380**, 439-442.
21. G. Fong, J. Rossant, M. Gertsenstein and M. L. Breitman, *Nature*, 1995, **376**, 66-70.
22. A. F. Siekmann and N. D. Lawson, *Cell Adh. Migr.*, 2007, **1**, 104-106.
23. W. S. Shim, I. A. Ho and P. E. Wong, *Mol. Cancer Res.*, 2007, **5**, 655-665.
24. J. Folkman, P. Cole and S. Zimmerman, *Ann. Surg.*, 1966, **164**, 491-502.
25. G. H. Algire, H. W. Chalkley, F. Y. Legallais and H. D. Park, *J. Natl. Cancer Inst.*, 1945, **6**, 73-85.

26. M. A. Gimbrone, R. S. Cotran, S. B. Leapman and J. Folkman, *J. Natl. Cancer Inst.*, 1974, **52**, 413-427.
27. M. A. Gimbrone, S. B. Leapman, R. S. Cotran and J. Folkman, *J. Exp. Med.*, 1972, **136**, 261-276.
28. A. Hoeben, B. Landuyt, M. S. Highley, H. Wildiers, A. T. v. Oosterom and E. A. d. Brujin, *Pharmacol. Rev.*, 2004, **56**, 549-580.
29. D. Hanahan and Robert A. Weinberg, *Cell*, 2011, **144**, 646-674.
30. V. Baeriswyl and G. Christofori, *Semin. Cancer Biol.*, 2009, **19**, 329-337.
31. R. M. Bremnes, C. Camps and R. Sirera, *Lung Cancer*, 2006, **51**, 143-158.
32. P. M. Muehlbauer, *Semin. Oncol. Nurs.*, 2003, **19**, 180-192.
33. M. Potente, H. Gerhardt and P. Carmeliet, *Cell*, 2011, **146**, 873-887.
34. R. Roskoski, Jr., *Crit. Rev. Oncol. Hematol.*, 2007, **62**, 179-213.
35. I. S. Moreira, P. A. Fernandes and M. J. Ramos, *Anti-Cancer Agents Med. Chem.*, 2007, **7**, 223-245.
36. B. Dome, M. J. C. Hendrix, S. Paku, J. Tovari and J. Timar, *Am. J. Pathol.*, 2007, **170**, 1-15.
37. J. Welti, S. Loges, S. Dimmeler and P. Carmeliet, *J. Clin. Invest.*, 2013, **123**, 3190-3200.
38. B. Sennino and D. M. McDonald, *Nat. Rev. Cancer*, 2012, **12**, 699-709.
39. B. L. Krock, N. Skuli and M. C. Simon, *Genes Cancer*, 2011, **2**, 1117-1133.
40. S. H. Lee, D. Jeong, Y. S. Han and M. J. Baek, *Ann. Surg. Treat Res.*, 2015, **89**, 1-8.
41. S. Rodriguez and U. Huynh-Do, *J. Oncol.*, 2012, **2012**, 11.
42. N. Ferrara, *Nat. Rev. Cancer*, 2002, **2**, 795-803.
43. A. Veeravagu, A. Hsu, W. Cai, L. Hou, V. Tse and Xiaoyuan, *Recent Pat. Anticancer Drug Discov.*, 2007, **2**, 59-71.
44. M. H. Michalski and X. Chen, *Eur. J. Nucl. Med. Mol. Imaging*, 2001, **38**, 358-377.
45. M. Kowanzetz and N. Ferrara, *Clin. Cancer Res.*, 2006, **12**, 5018-5022.
46. A. Bikfalvi and R. Bicknell, *Trends Pharmacol. Sci.*, 2002, **23**, 576-582.
47. H. M. Pinedo and D. J. Slamon, *The Oncologist*, 2000, **5**, 1-2.
48. T. Tammela, B. Enholm, K. Alitalo and K. Paavonen, *Cardiovasc. Res.*, 2005, **65**, 550-563.
49. J. Tabernero, *Mol. Cancer Res.*, 2007, **5**, 203-220.
50. F. Musumeci, M. Radi, C. Brullo and S. Schenone, *J. Med. Chem.*, 2012, **55**, 10797-10822.
51. K. Holmes, O. L. Roberts, A. M. Thomas and M. J. Cross, *Cell Signal*, 2007, **19**, 2003-2012.

52. D. R. Senger, S. J. Galli, A. M. Dvorak, C. A. Perruzzi, V. S. Harvey and H. F. Dvorak, *Science*, 1983, **219**, 983-985.
53. D. Bisacchi, R. Benelli, C. Vanzetto, N. Ferrari, F. Tosetti and A. Albini, *Cancer Detect. Prev.*, 2003, **27**, 229-238.
54. H. Deshpande, S. Roman, J. Thumar and J. A. Sosa, *Clin. Med. Insights Oncol.*, 2011, **5**, 213-221.
55. H. L. Goel and A. M. Mercurio, *Nat. Rev. Cancer*, 2013, **13**, 871-882.
56. N. R. Smith, D. Baker, N. H. James, K. Ratcliffe, M. Jenkins, S. E. Ashton, G. Sproat, R. Swann, N. Gray, A. Ryan, J. M. Jurgensmeier and C. Womack, *Clin. Cancer Res.*, 2010, **16**, 3548-3561.
57. Z. Wang, C. Dabrosin, X. Yin, M. M. Fuster, A. Arreola, W. K. Rathmell, D. Generali, G. P. Nagaraju, B. El-Rayes, D. Ribatti, Y. C. Chen, K. Honoki, H. Fujii, A. G. Georgakilas, S. Nowsheen, A. Amedei, E. Niccolai, A. Amin, S. S. Ashraf, B. Helferich, X. Yang, G. Guha, D. Bhakta, M. R. Ciriolo, K. Aquilano, S. Chen, D. Halicka, S. I. Mohammed, A. S. Azmi, A. Bilslund, W. N. Keith and L. D. Jensen, *Semin. Cancer Biol.*, 2015, **35**, S224-S243.
58. J. Folkman, *N. Engl. J. Med.*, 1971, **285**, 1182-1186.
59. H. C. Wu and P. C. Li, *J. Cancer. Mol.*, 2008, **4**, 17-22.
60. N. Ferrara, K. J. Hillan and W. Novotny, *Biochem. Biophys. Res. Commun.*, 2005, **333**, 328-335.
61. L. G. Presta, H. Chen, S. J. O'Connor, V. Chisholm, Y. G. Meng, L. Krummen, M. Winkler and N. Ferrara, *Cancer Res.*, 1997, **57**, 4593-4599.
62. Y. S. Lin, C. Nguyen, J. Mendoza, E. Escandon, D. Fei, Y. G. Meng and N. B. Modi, *J. Pharmacol. Exp. Ther.*, 1999, **288**, 371-378.
63. K. Margolin, M. S. Gordon, E. Holmgren, J. Gaudreault, W. Novotny, G. Fyfe, D. Adelman, S. Stalter and J. Breed, *J. Clin. Oncol.*, 2001, **19**, 851-856.
64. M. S. Gordon, K. Margolin, M. Talpaz, G. W. Sledge, E. Holmgren, R. Benjamin, S. Stalter, S. Shak and D. C. Adelman, *J. Clin. Oncol.*, 2001, **19**, 843-850.
65. F. Kabbinavar, H. I. Hurwitz, L. Fehrenbacher, N. J. Meropol, W. F. Novotny, G. Lieberman, S. Griffing and E. Bergsland, *J. Clin. Oncol.*, 2003, **21**, 60-65.
66. M. J. Gil-Gil, C. Mesia, M. Rey and J. Bruna, *Clin. Med. Insights Oncol.*, 2013, **7**, 123-135.
67. A. Barone and J. B. Rubin, *Front. Oncol.*, 2013, **3**, 92.
68. A. A. Tarhini, P. Frankel, K. A. Margolin, S. Christensen, C. Ruel, J. Shipe-Spotloe, D. R. Gandara, A. Chen and J. M. Kirkwood, *Clin. Cancer Res.*, 2011, **17**, 6574-6581.

69. J. Holash, S. Davis, N. Papadopoulos, S. D. Croll, L. Ho, M. Russell, P. Boland, R. Leidich, D. Hylton, E. Burova, E. Ioffe, T. Huang, C. Radziejewski, K. Bailey, J. P. Fandl, T. Daly, S. J. Wiegand, G. D. Yancopoulos and J. S. Rudge, *Proc. Natl. Acad. Sci USA*, 2002, **99**, 11393-11398.
70. W. P. Tew, M. Gordon, J. Murren, J. Dupont, S. Pezzulli, C. Aghajanian, P. Sabbatini, D. Mendelson, L. Schwartz, S. Gettinger, A. Psyrrri, J. M. Cedarbaum and D. R. Spriggs, *Clin. Cancer Res.*, 2010, **16**, 358-366.
71. T. F. Wang and A. C. Lockhart, *Clin. Med. Insights Oncol.*, 2012, **6**, 19-30.
72. E. P. Mitchell, *Clin. Colorectal Cancer*, 2013, **12**, 73-85.
73. C. Huang, *Curr. Opin. Biotech.*, 2009, **20**, 692-699.
74. A. Gaya and V. Tse, *Cancer Treat. Rev.*, 2012, **38**, 484-493.
75. R. Sophie, A. Akhtar, Y. J. Sepah, M. Ibrahim, M. Bittencourt, D. V. Do and Q. D. Nguyen, *Biol. Ther.*, 2012, **2**.
76. P. Saharinen, L. Eklund, K. Pulkki, P. Bono and K. Alitalo, *Trends Mol. Med.*, 2011, **17**, 347-362.
77. S. Wilhelm, C. Carter, M. Lynch, T. Lowinger, J. Dumas, R. A. Smith, B. Schwartz, R. Simantov and S. Kelley, *Nat. Rev. Drug. Discov.*, 2006, **5**, 835-844.
78. G. C. Jayson, R. Kerbel, L. M. Ellis and A. L. Harris, *The Lancet*, 2016, DOI: 10.1016/s0140-6736(15)01088-0.
79. A. S. Reddy and S. Zhang, *Expert Rev. Clin. Pharmacol.*, 2013, **6**, 41-47.
80. P. Giansanti, C. Preisinger, K. V. M. Huber, M. Gridling, G. Superti-Furga, K. L. Bennett and A. J. R. Heck, *ACS Chem. Biol.*, 2014, **9**, 1490-1498.
81. S. L. McGovern, B. T. Helfand, B. Feng and B. K. Shoichet, *J. Med. Chem.*, 2003, **46**, 4265-4272.
82. E. Lee, A. S. Kamlet, D. C. Powers, C. N. Neumann, G. B. Boursalian, T. Furuya, D. C. Choi, J. M. Hooker and T. Ritter, *Science*, 2011, **334**, 639-642.
83. C. Conrad, H. Friedman, D. Reardon, J. Provenzale, E. Jackson, H. Serajuddin, D. Laurent, B. Chen and W. Yung, ASCO Annual Meeting Proceedings, 2004.
84. C. Grávalos, E. Grande and J. M. Gasent, *Crit. Rev. Oncol. Hematol.*, 2010, **76**, 36-43.
85. S. Faivre, G. Demetri, W. Sargent and E. Raymond, *Nat. Rev. Drug Discov.*, 2007, **6**, 734-745.
86. P. T. White and M. S. Cohen, *Expert Opin. Drug Discov.*, 2015, **10**, 427-439.
87. F. A. Schutz, T. K. Choueiri and C. N. Sternberg, *Crit. Rev. Oncol. Hematol.*, 2011, **77**, 163-171.

88. P. W. Miller, N. J. Long, R. Vilar and A. D. Gee, *Angew. Chem. Int. Ed. Engl.*, 2008, **47**, 8998-9033.
89. P. B. Langmuir and A. Yver, *Clin. Pharmacol. Ther.*, 2012, **91**, 71-80.
90. H. G. Zhu, J. Y. Zhao, R. Zhang, L. Liao and J. J. Dong, *Thorac. Cancer*, 2015, **6**, 539-543.
91. L. M. Ellis and D. J. Hicklin, *Clin. Cancer Res.*, 2008, **14**, 6371-6375.
92. G. Bergers and D. Hanahan, *Nat. Rev. Cancer*, 2008, **8**, 592-603.
93. F. Fan, A. Schimming, D. Jaeger and K. Podar, *J. Oncol.*, 2012, **2012**, 281261.
94. M. Singh and N. Ferrara, *Nat. Biotech.*, 2012, **30**, 648-657.
95. F. A. B. Schutz, Y. Je, C. J. Richards and T. K. Choueiri, *J. Clin. Oncol.*, 2012, **30**, 871-877.
96. S. Sivendran, Z. Liu, L. J. Portas, Jr., M. Yu, N. Hahn, G. Sonpavde, W. K. Oh and M. D. Galsky, *Cancer Treat. Rev.*, 2012, **38**, 919-925.
97. C. Sessa, A. Guibal, G. D. Conte and C. Rugg, *Nat. Rev. Clin. Oncol.*, 2008, **5**, 378-391.
98. C. N. Oldenhuis, S. F. Oosting, J. A. Gietema and E. G. de Vries, *Eur. J. Cancer*, 2008, **44**, 946-953.
99. D. G. Duda, *ISRN Cell Biol.*, 2012, **2012**, 587259.
100. M. Wehland, J. Bauer, N. E. Magnusson, M. Infanger and D. Grimm, *Int. J. Mol. Sci.*, 2013, **14**, 9338-9364.
101. R. K. Jain, D. G. Duda, C. G. Willet, D. V. Sahani, A. X. Zhu, J. S. Loeffler, T. T. Batchelor and A. G. Sorensen, *Nat. Rev. Clin. Oncol.*, 2009, **6**, 327-338.
102. A. Ko, E. Dito, B. Schillinger, A. Venook, Z. Xu, E. Bergsland, D. Wong, J. Scott, J. Hwang and M. Tempero, *Invest. New Drugs*, 2008, **26**, 463-471.
103. A. Dowlati, R. Gray, A. B. Sandler, J. H. Schiller and D. H. Johnson, *Clin. Cancer Res.*, 2008, **14**, 1407-1412.
104. J. Dreves, U. Zirriebel, C. I. M. Schmidt-Gersbach, K. Mross, M. Medinger, L. Lee, J. Pinheiro, J. Wood, A. L. Thomas, C. Unger, A. Henry, W. P. Steward, D. Laurent, D. Lebwohl, M. Dugan and D. Marme, *Ann. Oncol.*, 2005, **16**, 558-565.
105. M. Fan, J. Zhang, Z. Wang, B. Wang, Q. Zhang, C. Zheng, T. Li, C. Ni, Z. Wu, Z. Shao and X. Hu, *Breast Cancer Res. Treat.*, 2014, **143**, 141-151.
106. J. Dorndusch, A. Zacharis, M. Meinhardt, K. Erdmann, I. Wolf, M. Froehner, M. P. Worth, S. Zastrow and S. Fuessel, *PLoS ONE*, 2013, **8**, e76386.
107. P. M. Wilson, D. Yang, M. Azuma, M. M. Shi, K. D. Danenberg, D. Lebwohl, A. Sherrod, R. D. Ladner, W. Zhang, P. V. Danenberg, T. Trarbach, G. Folprecht, G. Meinhardt and H. J. Lenz, *Pharmacogenomics J.*, 2013, **13**, 410-416.

108. S. M. Tolaney, D. G. Duda, Y. Boucher, S. Goel, J. Martin, M. Ancukiewicz, H. Potler, J. Incio, J. A. Ligibel and S. J. Isakoff, A phase II study of preoperative (preop) bevacizumab (bev) followed by dose-dense (dd) doxorubicin (A)/cyclophosphamide (C)/paclitaxel (T) in combination with bev in HER2-negative operable breast cancer (BC), 2012.
109. C. G. Willett, D. G. Duda, E. di Tomaso, Y. Boucher, M. Ancukiewicz, D. V. Sahani, J. Lahdenranta, D. C. Chung, A. J. Fischman and G. Y. Lauwers, *J. Clin. Oncol.*, 2009, **27**, 3020-3026.
110. C. G. Willett, Y. Boucher, D. G. Duda, E. di Tomaso, L. L. Munn, R. T. Tong, S. V. Kozin, L. Petit, R. K. Jain and D. C. Chung, *J. Clin. Oncol.*, 2005, **23**, 8136-8139.
111. S. B. Wedam, J. A. Low, S. X. Yang, C. K. Chow, P. Choyke, D. Danforth, S. M. Hewitt, A. Berman, S. M. Steinberg and D. J. Liewehr, *J. Clin. Oncol.*, 2006, **24**, 769-777.
112. R. L. Wahl, H. Jacene, Y. Kasamon and M. A. Lodge, *J. Nucl. Med.*, 2009, **50**, 120S-150S.
113. A. B. Siegel, E. I. Cohen, A. Ocean, D. Lehrer, A. Goldenberg, J. J. Knox, H. Chen, S. Clark-Garvey, A. Weinberg, J. Mandeli, P. Christos, M. Mazumdar, E. Popa, R. S. B. Jr, S. Rafi and J. D. Schwartz, *J. Clin. Oncol.*, 2008, **26**, 2292-2298.
114. A. Stopeck, M. Sheldon, M. Vahedian, G. Cropp, R. Gosalia and A. Hannah, *Clin. Cancer Res.*, 2002, **8**, 2798-2805.
115. H. J. Burstein, A. D. Elias, H. S. Rugo, M. A. Cobleigh, A. C. Wolff, P. D. Eisenberg, M. Lehman, B. J. Adams, C. L. Bello, S. E. DePrimo, C. M. Baum and K. D. Miller, *J. Clin. Oncol.*, 2008, **26**, 1810-1816.
116. D. G. Duda, C. G. Willett, M. Ancukiewicz, E. di Tomaso, M. Shah, B. G. Czito, R. Bentley, M. Poleski, G. Y. Lauwers, M. Carroll, D. Tyler, C. Mantyh, P. Shellito, J. W. Clark and R. K. Jain, *Oncologist*, 2010, **15**, 577-583.
117. G. Fountzilias, H. P. Kourea, M. Bobos, D. Televantou, V. Kotoula, C. Papadimitriou, K. T. Papazisis, E. Timotheadou, I. Efstratiou, A. Koutras, G. Pentheroudakis, C. Christodoulou, G. Aravantinos, D. Miliaras, K. Petraki, C. N. Papandreou, P. Papakostas, D. Bafaloukos, D. Repana, E. Razis, D. Pectasides and A. M. Dimopoulos, *Anticancer Res.*, 2011, **31**, 3007-3018.
118. E. Van Cutsem, S. de Haas, Y. K. Kang, A. Ohtsu, N. C. Tebbutt, J. Ming Xu, W. Peng Yong, B. Langer, P. Delmar, S. J. Scherer and M. A. Shah, *J. Clin. Oncol.*, 2012, **30**, 2119-2127.
119. O. P. Hamnvik, T. K. Choueiri, A. Turchin, R. R. McKay, L. Goyal, M. Davis, M. D. Kaymakcalan and J. S. Williams, *Cancer*, 2015, **121**, 311-319.

120. K. Chen and X. Y. Chen, *Curr. Top. Med. Chem.*, 2010, **10**, 1227-1236.
121. M. de Jong, J. Essers and W. M. van Weerden, *Nat. Rev. Cancer*, 2014, **14**, 481-493.
122. L. Fass, *Mol. Oncol.*, 2008, **2**, 115-152.
123. R. M. Glasspool and T. R. J. Evans, *Eur. J. Cancer*, 2000, **36**, 1661-1670.
124. W. A. Hammond, A. Swaika and K. Mody, *Ther. Adv. Med. Oncol.*, 2016, **8**, 57-84.
125. I. S. Alam, M. A. Arshad, Q. D. Nguyen and E. O. Aboagye, *Eur. J. Nucl. Med. Mol. Imaging*, 2015, **42**, 537-561.
126. I. Edler and K. Lindström, *Ultrasound Med. Biol.*, 2004, **30**, 1565-1644.
127. V. Chan and A. Perlas, *Atlas of Ultrasound-Guided Procedures in Interventional Pain Management*, Springer-Verlag New York, 2011.
128. T. Payen, A. Dizeux, C. Baldini, D. Le Guillou-Buffello, M. Lamuraglia, E. Comperat, O. Lucidarme and S. L. Bridal, *Ultrasound Med. Biol.*, 2015, **41**, 2202-2211.
129. M. Baron Toaldo, V. Salvatore, S. Marinelli, C. Palamà, M. Milazzo, L. Croci, L. Venerandi, M. Cipone, L. Bolondi and F. Piscaglia, *Mol. Imaging Biol.*, 2015, **17**, 29-37.
130. F. A. Gallagher, *Clin. Radiol.*, 2010, **65**, 557-566.
131. J. P. O'Connor, A. Jackson, G. J. Parker and G. C. Jayson, *Br. J. Cancer*, 2007, **96**, 189-195.
132. J. P. B. O'Connor, P. S. Tofts, K. A. Miles, L. M. Parkes, G. Thompson and A. Jackson, *Br. J. Radiol.*, 2011, **84**, S112-S120.
133. N. C. Ton, G. J. M. Parker, A. Jackson, S. Mullamitha, G. A. Buonaccorsi, C. Roberts, Y. Watson, K. Davies, S. Cheung, L. Hope, F. Power, J. Lawrance, J. Valle, M. Saunders, R. Felix, J. A. Soranson, L. Rolfe, K. Zinkewich-Peotti and G. C. Jayson, *Clin. Cancer Res.*, 2007, **13**, 7113-7118.
134. G. C. Jayson, C. Mulatero, M. Ranson, J. Zweit, A. Jackson, L. Broughton, J. Wagstaff, L. Hakansson, G. Groenewegen, J. Lawrance, M. Tang, L. Wauk, D. Levitt, S. Marreaud, F. F. Lehmann, M. Herold and H. Zwierzina, *Eur. J. Cancer*, 2005, **41**, 555-563.
135. B. Overmoyer, P. Silverman, R. Leeming, R. Shenk, J. Lyons, N. Ziats, J. Jesberger, L. Dumadag, S. Remick and H. Chen, Phase II trial of neoadjuvant docetaxel with or without bevacizumab in patients with locally advanced breast cancer, ASCO Annual Meeting Proceedings, 2004.
136. A. Dowlati, K. Robertson, T. Radivoyevitch, J. Waas, N. P. Ziats, P. Hartman, F. W. Abdul-Karim, J. K. Wasman, J. Jesberger, J. Lewin, K. McCrae, P. Ivy and S. C. Remick, *Clin. Cancer Res.*, 2005, **11**, 7938-7944.

137. K. D. Miller, J. M. Trigo, C. Wheeler, A. Barge, J. Rowbottom, G. Sledge and J. Baselga, *Clin. Cancer Res.*, 2005, **11**, 3369-3376.
138. K. T. Flaherty, M. A. Rosen, D. F. Heitjan, M. L. Gallagher, B. Schwartz, M. D. Schnall and P. J. O'Dwyer, *Cancer Biol. Ther.*, 2008, **7**, 496-501.
139. A. O'Donnell, A. Padhani, C. Hayes, A. J. Kakkar, M. Leach, J. M. Trigo, M. Scurr, F. Raynaud, S. Phillips, W. Aherne, A. Hardcastle, P. Workman, A. Hannah and I. Judson, *Br. J. Cancer*, 2005, **93**, 876-883.
140. H. Q. Xiong, R. Herbst, S. C. Faria, C. Scholz, D. Davis, E. F. Jackson, T. Madden, D. McConkey, M. Hicks, K. Hess, C. Charnsangavej and J. L. Abbruzzese, *Invest. New Drugs*, 2004, **22**, 459-466.
141. A. Ellmann and J. Holness, *Continuing Medical Education*, 2013, **31**, 279-283.
142. M. L. James and S. S. Gambhir, *Physiol. Rev.*, 2012, **92**, 897-965.
143. M. W. Groch and W. D. Erwin, *J. Nucl. Med. Technol.*, 2000, **28**, 233-244.
144. I. Dijkgraaf and O. C. Boerman, *Eur. J. Nucl. Med. Mol. Imaging*, 2010, **37**, 104-113.
145. S. Li, M. Peck-Radosavljevic, E. Koller, F. Koller, K. Kaserer, A. Kreil, S. Kapiotis, A. Hamwi, H. A. Weich, P. Valent, P. Angelberger, R. Dudczak and I. Virgolini, *Int. J. Cancer*, 2001, **91**, 789-796.
146. Z. Levashova, M. Backer, C. V. Hamby, J. Pizzonia, J. M. Backer and F. G. Blankenberg, *J. Nucl. Med.*, 2010, **51**, 959-966.
147. N. Savita, S. Maitra and U. Ravishankar, *Apollo Medicine*, 2010, **7**, 190-199.
148. J. A. Blokland, P. Trindev, M. P. Stokkel and E. K. Pauwels, *Eur. J. Radiol.*, 2002, **44**, 70-75.
149. G. Smith, L. Carroll and E. O. Aboagye, *Mol. Imaging Biol.*, 2012, **14**, 653-666.
150. Y. Lee, C. H. Choi, C. J. Kim, H. Kang, T. Kim, J. Lee, J. Lee, D. Bae and B.-G. Kim, *Gynecol. Oncol.*, 2009, **115**, 65-68.
151. S. Vallabhajosula, *Semin. Nucl. Med.*, 2007, **37**, 400-419.
152. W. C. Eckelman, R. C. Reba and G. J. Kelloff, *Drug Discov. Today*, 2008, **13**, 748-759.
153. W. C. Eckelman and D. A. Mankoff, *Nucl. Med. Biol.*, 2015, **42**, 421-425.
154. P. I. Imoukhuede and A. S. Popel, *PLoS ONE*, 2012, **7**, e44791.
155. N. S. Turker, P. Heidari, R. Kucherlapati, M. Kucherlapati and U. Mahmood, *Theranostics*, 2014, **4**, 893-903.
156. Y. Huang, M. Q. Zheng and J. M. Gerdes, *Curr. Top. Med. Chem.*, 2010, **10**.
157. W. C. Eckelman, M. R. Kilbourn and C. A. Mathis, *Nucl. Med. Biol.*, 2006, **33**, 449-451.

158. W. C. Eckelman, C.-Y. Lau and R. D. Neumann, *Nucl. Med. Biol.*, 2014, **41**, 297-298.
159. K. Serdons, A. Verbruggen and G. M. Bormans, *Methods*, 2009, **48**, 104-111.
160. P. I. Imoukhuede and A. S. Popel, *Exp. Cell Res.*, 2011, **317**, 955-965.
161. N. Rahimi, *Front Biosci.*, 2006, **11**, 818-829.
162. V. W. Pike, *Trends Pharmacol. Sci.*, 2009, **30**, 431-440.
163. M. Fumita and R. B. Innis, *Neuropsychopharmacology: The fifth generation of progress*, Lippincott Williams & Wilkins, 2002.
164. G. K. V. Schulthess, *Molecular Anatomic Imaging*, Lippincott Williams and Williams, 2007.
165. K. L. Davis, D. Charney, J. T. Coyle and C. Memeroff, *Nueropsychopharmacology: The fifth generatin of progress*, Lippincott Williams and Wilkins, 2002.
166. R. Sharma and E. Aboagye, *Br. J. Pharmacol.*, 2010, **159**, 1565-1585.
167. G. A. van Dongen, A. J. Poot and D. J. Vugts, *Tumour Biol.*, 2012, **33**, 607-615.
168. A. R. M. v. d. Bilt, A. G. T. T. v. Scheltinga, H. Timmer-Bosscha, C. P. Schröder, L. Pot, J. G. W. Kosterink, A. G. J. v. d. Zee, M. N. L. Hooge, S. d. Jong, E. G. E. d. Vries and A. K. L. Reyners, *Clin. Cancer Res.*, 2012, **18**, 6306-6316.
169. J. E. Bohonowych, U. Gopal and J. S. Isaacs, *J. Oncol.*, 2010, **2010**, 412985.
170. W. B. Nagengast, M. A. de Korte, T. H. Oude Munnink, H. Timmer-Bosscha, W. F. den Dunnen, H. Hollema, J. R. de Jong, M. R. Jensen, C. Quadt, C. Garcia-Echeverria, G. A. van Dongen, M. N. Lub-de Hooge, C. P. Schroder and E. G. de Vries, *J. Nucl. Med.*, 2010, **51**, 761-767.
171. S. B. Gaykema, A. H. Brouwers, M. N. Lub-de Hooge, R. G. Pleijhuis, H. Timmer-Bosscha, L. Pot, G. M. van Dam, S. B. van der Meulen, J. R. de Jong, J. Bart, J. de Vries, L. Jansen, E. G. de Vries and C. P. Schroder, *J. Nucl. Med.*, 2013, **54**, 1014-1018.
172. S. B. Gaykema, C. P. Schroder, J. Vitfell-Rasmussen, S. Chua, T. H. Oude Munnink, A. H. Brouwers, A. H. Bongaerts, M. Akimov, C. Fernandez-Ibarra, M. N. Lub-de Hooge, E. G. de Vries, C. Swanton and U. Banerji, *Clin. Cancer Res.*, 2014, **20**, 3945-3954.
173. S. F. Oosting, A. H. Brouwers, S. C. van Es, W. B. Nagengast, T. H. Oude Munnink, M. N. Lub-de Hooge, H. Hollema, J. R. de Jong, I. J. de Jong, S. de Haas, S. J. Scherer, W. J. Sluiter, R. A. Dierckx, A. H. Bongaerts, J. A. Gietema and E. G. de Vries, *J. Nucl. Med.*, 2015, **56**, 63-69.
174. L. Zhu, G. Niu, X. Fang and X. Chen, *Q. J. Nucl. Med. Mol. Imaging*, 2010, **54**, 291-308.

175. D. R. Collingridge, V. A. Carroll, M. Glaser, E. O. Aboagye, S. Osman, O. C. Hutchinson, H. Barthel, S. K. Luthra, F. Brady, R. Bicknell, P. Price and A. L. Harris, *Cancer Res.*, 2002, **62**, 5912-5919.
176. M. E. V. Dort, P. Navid-Azarbaijani, R. Ranga, A. Rehemtulla, B. D. Ross, A. E. David and M. S. Bhojani, in *Molecular Imaging*, ed. B. Schaller, InTech, 2012, ch. PET and SPECT Imaging of Tumor Angiogenesis, pp. 303-316.
177. K. Hodivala-Dilke, *Curr. Opin. Cell Biol.*, 2008, **20**, 514-519.
178. M. R. Battle, J. L. Goggi, L. Allen, J. Barnett and M. S. Morrison, *J. Nucl. Med.*, 2011, **52**, 424-430.
179. G. Niu and X. Chen, *J. Nucl. Med.*, 2015, DOI: 10.2967/jnumed.115.168278.
180. H. Chen, G. Niu, H. Wu and X. Chen, *Theranostics*, 2016, **6**, 78-92.
181. A. J. Beer, R. Haubner, M. Goebel, S. Luderschmidt, M. E. Spilker, H. Wester, W. A. Weber and M. Schwaiger, *J. Nucl. Med.*, 2005, **46**, 1333-1341.
182. E. S. Mittra, M. L. Goris, A. H. Iagaru, A. Kardan, L. Burton, R. Berganos, E. Chang, S. Liu, B. Shen, F. T. Chin, X. Chen and S. S. Gambhir, *Radiology*, 2011, **260**, 182-191.
183. K. Zheng, N. Liang, J. Zhang, L. Lang, W. Zhang, S. Li, J. Zhao, G. Niu, F. Li, Z. Zhu and X. Chen, *J. Nucl. Med.*, 2015, **56**, 1823-1827.
184. B. J. McParland, M. P. Miller, T. J. Spinks, L. M. Kenny, S. Osman, M. K. Khela, E. Aboagye, R. C. Coombes, A. M. Hui and P. S. Cohen, *J. Nucl. Med.*, 2008, **49**, 1664-1667.
185. R. Haubner, B. Kuhnast, C. Mang, W. A. Weber, H. Kessler, H.-J. Wester and M. Schwaiger, *Bioconjug. Chem.*, 2004, **15**, 61-69.
186. M. Glaser, M. Morrison, M. Solbakken, J. Arukwe, H. Karlsen, U. Wiggen, S. Champion, G. M. Kindberg and A. Cuthbertson, *Bioconjug. Chem.*, 2008, **19**, 951-957.
187. R. Haubner, H. Wester, W. A. Weber, C. Mang, S. I. Ziegler, S. L. Goodman, R. Senekowitsch-Schmidtke, H. Kessler and M. Schwaiger, *Cancer Res.*, 2001, **61**, 1781-1785.
188. R. Haubner, W. A. Weber, A. J. Beer, E. Vabuliene, D. Reim, M. Sarbia, K. Becker, M. Goebel, R. Hein, H. Wester, H. Kessler and M. Schwaiger, *PLoS Med.*, 2005, **2**, e70.
189. Y. Myoken, Y. Kayada, T. Okamoto, M. Kan, G. H. Sato and J. D. Sato, *Proc. Natl. Acad. Sci. USA*, 1991, **88**, 5819-5823.
190. A. J. Beer, S. Lorenzen, S. Metz, K. Herrmann, P. Watzlowik, H. Wester, C. Peschel, F. Lordick and M. Schwaiger, *J. Nucl. Med.*, 2008, **49**, 22-29.

191. F. C. Gaertner, H. Kessler, H. J. Wester, M. Schwaiger and A. J. Beer, *Eur. J. Nucl. Med. Mol. Imaging*, 2012, **39**, 126-138.
192. E. Mena, R. Owenius, B. Turkbey, R. Sherry, G. Bratslavsky, S. Macholl, M. Miller, E. Somer, L. Lindenberg, S. Adler, J. Shih, P. Choyke and K. Kurdziel, *Eur. J. Nucl. Med. Mol. Imaging*, 2014, **41**, 1879-1888.
193. L. M. Kenny, R. C. Coombes, I. Oulie, K. B. Contractor, M. Miller, T. J. Spinks, B. McParland, P. S. Cohen, A. Hui and C. Palmieri, *J. Nucl. Med.*, 2008, **49**, 879-886.
194. A. Iagaru and S. S. Gambhir, *Am. J. Roentgenol.*, 2013, **201**, W183-191.
195. E. Chang, S. Liu, G. Gowrishankar, S. Yaghoubi, J. P. Wedgeworth, F. Chin, D. Berndorff, V. Gekeler, S. S. Gambhir and Z. Cheng, *Eur. J. Nucl. Med. Mol. Imaging*, 2011, **38**, 722-730.
196. A. Iagaru, C. Mosci, B. Shen, F. T. Chin, E. Mittra, M. L. Telli and S. S. Gambhir, *Radiology*, 2014, **273**, 549-559.
197. R. Minamimoto, A. Karam, M. Jamali, A. Barkhodari, S. Gambhir, O. Dorigo and A. Iagaru, *Eur. J. Nucl. Med. Mol. Imaging*, 2015, 1-9.
198. M. S. Morrison, S. Ricketts, J. Barnett, A. Cuthbertson, J. Tessier and S. R. Wedge, *J. Nucl. Med.*, 2009, **50**, 116-122.
199. R. Sharma, K. G. Kallur, J. S. Ryu, R. V. Parameswaran, H. Lindman, N. Avril, F. V. Gleeson, J. D. Lee, K. H. Lee, M. J. O'Doherty, A. M. Groves, M. P. Miller, E. J. Somer, C. R. Coombes and E. O. Aboagye, *J. Nucl. Med.*, 2015, **56**, 1855-1861.
200. W. A. Weber, S. I. Ziegler, R. Thodtman, A. R. Hanauske and M. Schwaiger, *J. Nucl. Med.*, 1999, **40**, 1771-1777.
201. P. Slobbe, A. J. Poot, A. D. Windhorst and G. A. van Dongen, *Drug Discov. Today*, 2012, **17**, 1175-1187.
202. E. Samen, J. O. Thorell, L. Lu, T. Tegnebratt, L. Holmgren and S. Stone-Elander, *Eur. J. Nucl. Med. Mol. Imaging*, 2009, **36**, 1283-1295.
203. L. F. Hennequin, E. S. E. Stokes, A. P. Thomas, C. Johnstone, P. A. Plé, D. J. Ogilvie, M. Dukes, S. R. Wedge, J. Kendrew and J. O. Curwen, *J. Med. Chem.*, 2002, **45**, 1300-1312.
204. E. Samén, L. Lu, J. Mulder, J. O. Thorell, P. Damberg, T. Tegnebratt, L. Holmgren, H. Rundqvist and S. Stone-Elander, *Eur. J. Nucl. Med. Mol. Imaging*, 2014, **4**, 17-27.
205. J. Prabhakaran, V. Arango, V. J. Majo, N. R. Simpson, S. A. Kassir, M. D. Underwood, H. Polavarapu, J. N. Bruce, P. Canoll, J. J. Mann and J. S. Kumar, *Bioorg. Med. Chem. Lett.*, 2012, **22**, 5104-5107.
206. F. Li, S. Jiang, Y. Zu, D. Y. Lee and Z. Li, *J. Nucl. Med.*, 2014, **55**, 1525-1531.

207. A. J. Poot, B. van der Wildt, M. Stigter-van Walsum, M. Rongen, R. C. Schuit, N. H. Hendrikse, J. Eriksson, G. A. van Dongen and A. D. Windhorst, *Nucl. Med. Biol.*, 2013, **40**, 488-497.
208. T. Kniess, R. Bergmann, M. Kuchar, J. Steinbach and F. Wuest, *Bioorg. Med. Chem.*, 2009, **17**, 7732-7742.
209. M. M. Abouzied, E. S. Crawford and H. A. Nabi, *J. Nucl. Med. Technol.*, 2005, **33**, 144-155.
210. N. Larson, *J. Nucl. Med.*, 2006, **47**, 31N-32N.
211. J. W. Hicks, H. F. VanBrocklin, A. A. Wilson, S. Houle and N. Vasdev, *Molecules*, 2010, **15**, 8260-8278.
212. C. Nanni, L. Fantini, S. Nicolini and S. Fanti, *Clin. Radiol.*, 2010, **65**, 536-548.
213. M. A. Pantaleo, M. Nannini, A. Maleddu, S. Fanti, V. Ambrosini, C. Nanni, S. Boschi and G. Biasco, *Cancer Treat. Rev.*, 2008, **34**, 103-121.
214. A. Iagaru, Y. Wang, C. Mari, A. Quon, M. L. Goris, S. Horning and S. S. Gambhir, *Hell. J. Nucl. Med.*, 2008, **11**, 153-156.
215. S. Novello, T. Vavala, M. G. Levra, F. Solitro, E. Pelosi, A. Veltri and G. V. Scagliotti, *Clin. Lung Cancer*, 2013, **14**, 230-237.
216. A. F. Shields, J. R. Grierson, B. M. Dohmen, H. J. Machulla, J. C. Stayanoff, J. M. Lawhorn-Crews, J. E. Obradovich, O. Muzik and T. J. Mangner, *Nat. Med.*, 1998, **4**, 1334-1336.
217. A. Salskov, V. S. Tammisetti, J. Grierson and H. Vesselle, *Semin. Nucl. Med.*, 2007, **37**, 429-439.
218. L. Kenny, R. C. Coombes, D. M. Vigushin, A. Al-Nahhas, S. Shousha and E. O. Aboagye, *Eur. J. Nucl. Med. Mol. Imaging*, 2007, **34**, 1339-1347.
219. O. S. Tehrani and A. F. Shields, *J. Nucl. Med.*, 2013, **54**, 903-912.
220. H. Wang, J. Zhang, J. Tian, B. Qu, T. Li, Y. Chen, J. Liu and S. Wang, *J. Nucl. Med.*, 2009, **50**, 1857-1864.
221. X. Bao, M. W. Wang, Y. P. Zhang and Y. J. Zhang, *Biomed. Res. Int.*, 2014, **2014**, 218578.
222. I. N. Fleming, R. Manavaki, P. J. Blower, C. West, K. J. Williams, A. L. Harris, J. Domarkas, S. Lord, C. Bladry and F. J. Gilbert, *Br. J. Cancer*, 2015, **112**, 239-250.
223. K. A. Krohn, J. M. Link and R. P. Mason, *J. Nucl. Med.*, 2008, **49 Suppl 2**, 129S-148S.
224. V. Kersemans, B. Cornelissen, R. Hueting, M. Tredwell, K. Hussien, P. D. Allen, N. Falzone, S. A. Hill, J. R. Dilworth, V. Gouverneur, R. J. Muschel and S. C. Smart, *PLoS ONE*, 2011, **6**, e25911.

225. J. G. Rajendran, D. C. Wilson, E. U. Conrad, L. M. Peterson, J. D. Bruckner, J. S. Rasey, L. K. Chin, P. D. Hofstrand, J. R. Grierson, J. F. Eary and K. A. Krohn, *Eur. J. Nucl. Med. Mol. Imaging*, 2003, **30**, 695-704.
226. L. M. Cher, C. Murone, N. Lawrentschuk, S. Ramdave, A. Papenfuss, A. Hannah, G. J. O'Keefe, J. I. Sachinidis, S. U. Berlangieri, G. Fabinyi and A. M. Scott, *J. Nucl. Med.*, 2006, **47**, 410-418.
227. N. Kawai, W. Lin, W. Cao, D. Ogawa, K. Miyake, R. Haba, Y. Maeda, Y. Yamamoto, Y. Nishiyama and T. Tamiya, *Eur. J. Nucl. Med. Mol. Imaging*, 2014, **41**, 1870-1878.
228. S. Vallabhajosula, L. Solnes and B. Vallabhajosula, *Semin. Nucl. Med.*, 2011, **41**, 246-264.
229. H. H. C. Ernst, *Schering Res Found Workshop*, 2007, **62**, 15-50.
230. M. G. Campbell and T. Ritter, *Chem. Rev.*, 2015, **115**, 612-633.
231. R. E. Ehrenkauf, J. F. Potocki and D. M. Jewett, *J. Nucl. Med.*, 1984, **25**, 333-337.
232. M. Constantinou, F. I. Aigbirhio, R. G. Smith, C. A. Ramsden and V. W. Pike, *J. Am. Chem. Soc.*, 2001, **123**, 1780-1781.
233. N. Vasdev, B. E. Pointner, R. Chirakal and G. J. Schrobilgen, *J. Am. Chem. Soc.*, 2002, **124**, 12863-12868.
234. S. Lu and V. W. Pike, *J. Fluor. Chem.*, 2010, **131**, 1032-1038.
235. H. J. Wester, *Pharmaceutical Radiochemistry*, SCINTOMICS, Furstenfeldbruck, Germany, 2010.
236. S. Yu, *Biomed. Imag. Interv. J.*, 2006, **2**, e57-67.
237. A. F. Brooks, J. J. Topczewski, N. Ichiishi, M. S. Sanford and P. J. H. Scott, *Chem. Sci.*, 2014, **5**, 4545-4553.
238. F. Claessens, C. Helsen, S. Prekovic, T. Van den Broeck, L. Spans, H. Van Poppel and S. Joniau, *Nat. Rev. Urol.*, 2014, **11**, 712-716.
239. M. I. Walton, P. D. Eve, A. Hayes, A. T. Henley, M. R. Valenti, A. K. D. H. Brandon, G. Box, K. J. Boxall, M. Tall, K. Swales, T. P. Matthews, T. McHardy, M. Lainchbury, J. Osborne, J. E. Hunter, N. D. Perkins, G. W. Aherne, J. C. Reader, F. I. Raynaud, S. A. Eccles, I. Collins and M. D. Garrett, *Oncotarget*, 2015, **7**, 2329-2342.
240. S. Preshlock, M. Tredwell and V. Gouverneur, *Chemical Reviews*, 2016, **116**, 719-766.
241. T. Liang, C. N. Neumann and T. Ritter, *Angew. Chem. Int. Ed. Engl.*, 2013, **52**, 8214-8264.

242. M. Huiban, M. Tredwell, S. Mizuta, Z. Wan, X. Zhang, T. L. Collier, V. Gouverneur and J. Passchier, *Nat. Chem.*, 2013, **5**, 941-944.
243. M. S. Yusbov, D. Y. Svitich, M. S. Larkina and V. V. Zhdankin, *Arkivoc*, 2013, 364-395.
244. J. Cardinale, J. Ermert, S. Humpert and H. H. Coenen, *RSC Adv.*, 2014, **4**, 17293-17299.
245. B. H. Rotstein, N. A. Stephenson, N. Vasdev and S. H. Liang, *Nat. Commun.*, 2014, **5**, 4635-4641.
246. N. Ichiishi, A. F. Brooks, J. J. Topczewski, M. E. Rodnick, M. S. Sanford and P. J. Scott, *Org. Lett.*, 2014, **16**, 3224-3227.
247. N. Ichiishi, A. J. Canty, B. F. Yates and M. S. Sanford, *Organometallics*, 2014, **33**, 5525-5534.
248. Y. Ye, S. D. Schimler, P. S. Hanley and M. S. Sanford, *J. Am. Chem. Soc.*, 2013, **135**, 16292-16295.
249. M. Tredwell, S. M. Preshlock, N. J. Taylor, S. Gruber, M. Huiban, J. Passchier, J. Mercier, C. Genicot and V. Gouverneur, *Angew. Chem. Int. Ed. Engl.*, 2014, **53**, 7751-7755.
250. A. V. Mossine, A. F. Brooks, K. J. Makaravage, J. M. Miller, N. Ichiishi, M. S. Sanford and P. J. Scott, *Org. Lett.*, 2015, **17**, 5780-5783.
251. Z. Gao, Y. H. Lim, M. Tredwell, L. Li, S. Verhoog, M. Hopkinson, W. Kaluza, T. L. Collier, J. Passchier, M. Huiban and V. Gouverneur, *Angew. Chem. Int. Ed. Engl.*, 2012, **51**, 6733-6737.
252. C. Wang, J. Dong, J. Zhang, C. Wang, H. Gao, P. Li, C. Wang and J. Zhang, *Med. Chem. Comm.*, 2013, **4**, 1434-1438.
253. E. M. Dokla, A. H. Mahmoud, M. S. A. Elsayed, A. H. El-Khatib, M. W. Linscheid and K. A. Abouzid, *PLoS ONE*, 2012, **7**.
254. B. Pignataro, *New Strategies in chemical synthesis and catalysis*, Wiley-VCH, 2012.
255. N. Volz and J. Clayden, *Angew. Chem. Int. Ed.*, 2011, **50**, 12148-12155.
256. C. Wang, H. Gao, J. Dong, Y. Zhang, P. Su, Y. Shi and J. Zhang, *Bioorg. Med. Chem.*, 2014, **22**, 277-284.
257. K. Nakamura, E. Taguchi, T. Miura, A. Yamamoto, K. Takahashi, F. Bichat, N. Guilbaud, K. Hasegawa, K. Kubo, Y. Fujiwara, R. Suzuki, K. Kubo, M. Shibuya and T. Isae, *Cancer Res.*, 2006, **66**, 9134-9142.
258. H. C. Toh, P. Chen, B. I. Carr, J. J. Knox, S. Gill, P. Ansell, E. M. McKeegan, B. Dowell, M. Pedersen, Q. Qin, J. Qian, F. A. Scappaticci, J. L. Ricker, D. M. Carlson and W. P. Yong, *Cancer*, 2013, **119**, 380-387.

259. N. M. Tannir, Y. Wong, C. K. Kollmannsberger, M. S. Ernstoff, D. J. Perry, L. J. Appleman, E. M. Posadas, D. Cho, T. K. Choueiri, A. Coates, N. Gupta, R. Pradhan, J. Qian, J. Chen, F. A. Scappaticci, J. L. Ricker, D. M. Carlson and M. D. Michaelson, *Eur. J. Cancer*, 2011, **47**, 2706-2714.
260. D. H. Albert, P. Tapang, T. J. Magoc, L. J. Pease, D. R. Reuter, R. Wei, J. Li, J. Guo, P. F. Bousquet, N. S. Ghoreishi-Haack, B. Wang, G. T. Bukofzer, Y. Wang, J. A. Stavropoulos, K. Hartandi, A. L. Niquette, N. Soni, E. F. Johnson, J. O. McCall, J. J. Bouska, Y. Luo, C. K. Donawho, Y. Dai, P. A. Marcotte, K. B. Glaser, M. R. Michaelides and S. K. Davidsen, *Mol. Cancer Ther.*, 2006, **5**, 995-1006.
261. F. A. L. M. Eskens, M. J. A. de Jonge, P. Bhargava, T. Isoe, M. M. Cotreau, B. Esteves, K. Hayashi, H. Burger, M. Thomeer, L. van Doorn and J. Verweij, *Clin. Cancer Res.*, 2011, **17**, 7156-7163.
262. K. Sanphanya, S. K. Wattanapitayakul, S. Phowichit, V. V. Fokin and O. Vajragupta, *Bioorg. Med. Chem. Lett.*, 2013, **23**, 2962-2967.
263. M. McTigue, B. W. Murray, J. H. Chen, Y. Deng, J. Solowiej and R. Kania, *Proc. Natl. Acad. Sci. USA*, 2012, **109**, 18281-18289.
264. K. Lee, K. W. Jeong, Y. Lee, J. Y. Song, M. S. Kim, G. S. Lee and Y. Kim, *Eur. J. Med. Chem.*, 2010, **45**, 5420-5427.
265. N. Miyamoto, Y. Oguro, T. Takagi, H. Iwata, H. Miki, A. Hori and S. Imamura, *Bioorg. Med. Chem.*, 2012, **20**, 7051-7058.
266. S. Huang, R. Li, K. R. LaMontagne, L. M. Greenberger and P. J. Connolly, *Bioorg. Med. Chem. Lett.*, 2011, **21**, 1815-1818.
267. D. Carnaroglio, K. Martina, G. Palmisano, A. Penoni, C. Domini and G. Cravotto, *Beilstein J. Org. Chem.*, 2013, **9**, 2378-2386.
268. O. Kreye, H. Mutlu and M. A. R. Meier, *Green Chem.*, 2013, **15**, 1431-1455.
269. M. V. Zabalov and R. P. Tiger, *J. Mol. Struct: Theochem*, 2010, **962**, 15-22.
270. K. J. Padiya, S. Gavade, B. Kardile, M. Tiwari, S. Bajare, M. Mane, V. Gaware, S. Varghese, D. Harel and S. Kurhade, *Org. Lett.*, 2012, **14**, 2814-2817.
271. P. A. Duspara, M. S. Islam, A. J. Lough and R. A. Batey, *J. Org. Chem.*, 2012, **77**, 10362-10368.
272. E. Broughton, *Environmental Health*, 2005, **4**, 6-6.
273. K. Shibatomi, F. Kobayashi, A. Narayama, I. Fujisawa and S. Iwasa, *Chem. Comm.*, 2012, **48**, 413-415.
274. M. Constantinou, S. L. Waters, C. J. Steel, K. G. Poole, P. S. Marino, P. W. Ind, C. G. Rhodes, F. L. Aigbirhio, A. Moore, V. W. Pike and S. K. Luthra, *J. Label. Compd. Radiopharm.*, 2004, **47**, 55-70.

275. G. Smith, Y. Zhao, J. Leyton, B. Shan, Q. Nguyen, M. Perumal, D. Turton, E. Årstad, S. K. Luthra, E. G. Robins and E. O. Aboagye, *Nucl. Med. Biol.*, 2011, **38**, 39-51.
276. W. Qu, M. Kung, C. Hou, S. Oya and H. F. Kung, *J. Med. Chem.*, 2007, **50**, 3380-3387.
277. D. W. Kim, D. Ahn, Y. Oh, S. Lee, H. S. Kil, S. J. Oh, S. J. Lee, J. S. Kim, J. S. Ryu, D. H. Moon and D. Y. Chi, *J. Am. Chem. Soc.*, 2006, **128**, 16394-16397.
278. D. W. Kim, Jeong, S. T. Lim, M. Sohn, J. A. Katzenellenbogen and D. Y. Chi, *J. Org. Chem.*, 2008, **73**, 957-962.
279. T. H. Witney, I. S. Alam, D. R. Turton, G. Smith, L. Carroll, D. Brickute, F. J. Twyman, Q. D. Nguyen, G. Tomasi, R. O. Awais and E. O. Aboagye, *Clin. Cancer Res.*, 2012, **18**, 1063-1072.
280. N. K. Kaushik, N. Kaushik, P. Attri, N. Kumar, C. H. Kim, A. K. Verma and E. H. Choi, *Molecules*, 2013, **18**, 6620-6662.
281. J. R. Weng, C. H. Tsai, S. K. Kulp and C. S. Chen, *Cancer Lett.*, 2008, **262**, 153-163.
282. R. Dhani, A. Avinash, S. K. Salenaagina, M. V. S. Teja, P. Masthanaiah, P. R. Rathnam and V. C. Silpa, *J. Chem. Pharm. Res.*, 2011, **3**, 519-523.
283. R. Tripathy, A. Reiboldt, P. A. Messina, M. Iqbal, J. Singh, E. R. Bacon, T. S. Angeles, S. X. Yang, M. S. Albom, C. Robinson, H. Chang, B. A. Ruggeri and J. P. Mallamo, *Bioorg. Med. Chem. Lett.*, 2006, **16**, 2158-2162.
284. G. D. Kim, O. J. Cheong, S. Y. Bae, J. Shin and S. K. Lee, *Mar. Drugs*, 2013, **11**, 1087-1103.
285. S. Saraswati and S. S. Agrawal, *Cancer Lett.*, 2013, **332**, 83-93.
286. S. R. Wedge, J. Kendrew, L. F. Hennequin, P. J. Valentine, S. T. Barry, S. R. Brave, N. R. Smith, N. H. James, M. Dukes, J. O. Curwen, R. Chester, J. A. Jackson, S. J. Boffey, L. L. Kilburn, S. Barnett, G. H. P. Richmond, P. F. Wadsworth, M. Walker, A. L. Bigley, S. T. Taylor, L. Cooper, S. Beck, J. M. Jurgensmeier and D. J. Ogilvie, *Cancer Res.*, 2005, **65**, 4389-4400.
287. H. Fu, L. Yu, M. Cui, J. Zhang, X. Zhang, Z. Li, X. Wang, J. Jia, Y. Yang, P. Yu, H. Jia and B. Liu, *Bioorg. Med. Chem.*, 2013, **21**, 3708-3714.
288. F. Sobrio, M. Amokhtari, F. Gourand, M. Dhilly, F. Dauphin and L. Barré, *Bioorg. Med. Chem.*, 2000, **8**, 2511-2518.
289. H. Wadsworth, P. A. Jones, W. Chau, C. Durrant, N. Fouladi, J. Passmore, D. O'Shea, D. Wynn, V. Morisson-Iveson, A. Ewan, M. Thaning, D. Mantzilas, I. Gausemel, I. Khan, A. Black, M. Avory and W. Trigg, *Bioorg. Med. Chem. Lett.*, 2012, **22**, 1308-1313.

290. V. Morisson-Iveson, H. Wadsworth, J. Passmore, A. Ewan, S. Nilsen, M. Thaning and W. Trigg, *Tetrahedron Lett.*, 2014, **55**, 5141-5143.
291. M. Laube, C. Gassner, S. K. Sharma, R. Günther, A. Pigorsch, J. König, M. Köckerling, F. Wuest, J. Pietzsch and T. Kniess, *J. Org. Chem.*, 2015, **80**, 5611-5624.
292. P. J. Connolly, S. Huang, G. Xu, J. Butler, A. R. Fuentes-Pesquera, L. M. Greenberger, K. R. L. Montagne and R. Li, *Substituted pyrimidine kinase inhibitors*, WO2007/109783, 2007.
293. R. Roskoski, Jr., *Biochem. Biophys. Res. Comm*, 2008, **375**, 287-291
294. A. F. Nassar, A. M. Kamel and C. Clarimont, *Drug Discov. Today*, 2004, **9**, 1020-1028.
295. F. F. Fleming, L. Yao, P. C. Ravikumar, L. Funk and B. C. Shook, *J. Med. Chem.*, 2010, **53**, 7902-7917.
296. L. Carroll, H. L. Evans, A. C. Spivey and E. O. Aboagye, *Chem. Commun.*, 2015, **51**, 8439-8441.
297. B. Robinson, *Chem. Rev.*, 1963, **63**, 373-401.
298. M. Inman and C. J. Moody, *Chem. Sci.*, 2013, **4**, 29-41.
299. J. J. Li, in *Name Reactions: A Collection of Detailed Mechanisms and Synthetic Applications*, Springer Berlin Heidelberg, Berlin, Heidelberg, 2009, DOI: 10.1007/978-3-642-01053-8_216, pp. 463-464.
300. Y. Xia, X. Song, D. Li, T. Ye, Y. Xu, H. Lin, N. Meng, G. Li, S. Deng, S. Zhang, L. Liu, Y. Zhu, J. Zeng, Q. Lei, Y. Pan, Y. Wei, Y. Zhao and L. Yu, *Sci. Rep.*, 2014, **4**, 6031.
301. S. Chatterjee, L. C. Heukamp, M. Siobal, J. Schöttle, C. Wieczorek, M. Peifer, D. Frasca, M. Koker, K. König, L. Meder, D. Rauh, R. Buettner, J. Wolf, R. A. Brekken, B. Neumaier, G. Christofori, R. K. Thomas and R. T. Ullrich¹, *J. Clin. Invest.*, 2013, **123**, 1732-1740.
302. I. K. Dev, R. E. Dornsife, T. M. Hopper, J. A. Onori, C. G. Miller, L. E. Harrington, K. M. Dold, R. J. Mullin, J. H. Johnson, R. M. Crosby, A. T. Truesdale, A. H. Epperly, K. W. Hinkle, M. Cheung, J. A. Stafford, D. K. Luttrell and R. Kumar, *Br. J. Cancer*, 2004, **91**, 1391-1398.
303. E. A. Kuczynski, A. M. Vilorio-Petit and B. L. Coomber, *Cancer*, 2011, **117**, 5601-5611.

304. P. Sini, I. Samarzija, F. Baffert, A. Littlewood-Evans, C. Schnell, A. Theuer, S. Christian, A. Boos, H. Hess-Stumpp, J. A. Foekens, B. Setyono-Han, J. Wood and N. E. Hynes, *Cancer Res.*, 2008, **68**, 1581-1592.
305. H. Gao, P. Su, Y. Shi, X. Shen, Y. Zhang, J. Dong and J. Zhang, *Eur. J. Med. Chem.*, 2015, **90**, 232-240.
306. C. Kremer, G. Breier, W. Risau and K. H. Plate, *Cancer Res.*, 1997, **57**, 3852-3859.
307. M. V. Berridge, P. M. Herst and A. S. Tan, in *Biotechnology Annual Review*, Elsevier, 2005, vol. 11, ch. Tetrazolium dyes as tools in cell biology: New insights into their cellular reduction pp. 127-152.
308. M. L. Barcellona and E. Gratton, *Biophys. J.*, 1996, **70**, 2341-2351.
309. S. Elmore, *Toxicol. Pathol.*, 2007, **35**, 495-516.
310. M. Mariani, R. Karki, M. Spennato, D. Pandya, S. He, M. Andreoli, P. Fiedler and C. Ferlini, *Gene*, 2015, **563**, 109-114.
311. A. Fourest-Lieuvin, L. Peris, V. Gache, I. Garcia-Saez, C. Juillan-Binard, V. Lantez and D. Job, *Mol. Biol. Cell*, 2006, **17**, 1041-1050.
312. M. Kimura, T. Yoshioka, M. Siao, Y. Banno and H. Nagaoka, *Cell Death Dis.*, 2013, **4**, e603-612.
313. T. Wittmann, A. Hyman and A. Desai, *Nat. Cell Biol.*, 2001, **3**, E28-E34.
314. A. A. Nagle, F. F. Gan, G. Jones, C. L. So, G. Wells and E. H. Chew, *PLoS ONE*, 2012, **7**, e50125.
315. T. Peng, J. Wu, L. Tong, M. Li, F. Chen, Y. Leng, R. Qu, K. Han, Y. Su, Y. Chen, W. Duan, H. Xie and J. Ding, *Acta Pharmacol. Sin.*, 2014, **35**, 916-928.
316. A. Kamal, Y. V. V. Srikanth, T. B. Shaik, M. N. A. Khan, M. Ashraf, M. K. Reddy, K. A. Kumar and S. V. Kalivendi, *Med. Chem. Comm.*, 2011, **2**, 819-823.
317. A. Brancale and R. Silvestri, *Med. Res. Rev.*, 2007, **27**, 209-238.
318. V. Háda, Z. Dubrovay, Á. Lakó-Futó, J. Galambos, Z. Gulyás, A. Aranyi and C. Szántay Jr, *J. Pharm. Biomed. Anal.*, 2013, **84**, 309-322.
319. P. J. Ferguson, J. R. Phillips, M. Selner and C. E. Cass, *Cancer Res.*, 1984, **44**, 3307-3312.
320. F. Mollinedo and C. Gajate, *Apoptosis*, 2003, **8**, 413-450.
321. P. Singh, K. Rathinasamy, R. Mohan and D. Panda, *IUBMB Life*, 2008, **60**, 368-375.
322. R. Alvarez, P. Puebla, J. F. Diaz, A. C. Bento, R. Garcia-Navas, J. de la Iglesia-Vicente, F. Mollinedo, J. M. Andreu, M. Medarde and R. Pelaez, *J. Med. Chem.*, 2013, **56**, 2813-2827.
323. G. La Regina, R. Bai, A. Coluccia, V. Famigliani, S. Pelliccia, S. Passacantilli, C. Mazzoccoli, V. Ruggieri, A. Verrico, A. Miele, L. Monti, M. Nalli, R. Alfonsi, L. Di

- Marcotullio, A. Gulino, B. Ricci, A. Soriani, A. Santoni, M. Caraglia, S. Porto, E. Da Pozzo, C. Martini, A. Brancale, L. Marinelli, E. Novellino, S. Vultaggio, M. Varasi, C. Mercurio, C. Bigogno, G. Dondio, E. Hamel, P. Lavia and R. Silvestri, *J. Med. Chem.*, 2015, **58**, 5789-5807.
324. M. Asif, *Int. J. Med. Chem.*, 2014, 395637.
325. G. Marzaro, A. Guiotto and A. Chilin, *Expert Opin. Ther. Patents*, 2012, **22**, 223-252.
326. J. Blanc, R. Geney and C. Menet, *Anticancer Agents Med. Chem.*, 2013, **13**, 731-747.
327. J. A. Barltrop, T. C. Owen, A. H. Cory and J. G. Cory, *Bioorg. Med. Chem. Lett.*, 1991, **1**, 611-614.
328. S. R. Wedge, D. J. Ogilvie, M. Dukes, J. Kendrew, R. Chester, Janet A. Jackson, S. J. Boffey, P. J. Valentine, J. O. Curwen, H. L. Musgrove, G. A. Graham, G. D. Hughes, A. P. Thomas, E. S. E. Stokes, B. Curry, G. H. P. Richmond, P. F. Wadsworth, A. L. Bigley and L. F. Hennequin, *Cancer Res.*, 2002, **62**, 4645-4655.
329. J. James, B. Ruggeri, R. C. Armstrong, M. W. Rowbottom, S. Jones-Bolin, R. N. Gunawardane, P. Dobrzanski, M. F. Gardner, H. Zhao, M. D. Cramer, K. Hunter, R. R. Nepomuceno, M. Cheng, D. Gitnick, M. Yazdanian, D. E. Insko, M. A. Ator, J. L. Apuy, R. Faraoni, B. D. Dorsey, M. Williams, S. S. Bhagwat and M. W. Holladay, *Mol. Cancer Ther.*, 2012, **11**, 930-941.
330. F. Solca, G. Dahl, A. Zoephel, G. Bader, M. Sanderson, C. Klein, O. Kraemer, F. Himmelsbach, E. Haakma and G. R. Adolf, *J. Pharmacol. Exp. Ther.*, 2012, **343**, 342-350.
331. C. E. Whittles, T. M. Pocock, S. R. Wedge, J. Kendrew, L. F. Hennequin, S. J. Harper and D. O. Bates, *Microcirculation*, 2002, **9**, 513-522.
332. H. Zhong, D. Wang, N. Wang, Y. Rios, H. Huang, S. Li, X. Wu and S. Lin, *Cell Res.*, 2011, **21**, 1080-1087.
333. A. Endo, S. Fukuhara, M. Masuda, T. Ohmori and N. Mochizuki, *J. Recept. Signal Transduct. Res.*, 2003, **23**, 239-254.
334. K. Urschel, C. D. Garlich, W. G. Daniel and I. Cicha, *Atherosclerosis*, **219**, 499-509.
335. H. Su, Y. Seimbille, G. Ferl, C. Bodenstein, B. Fueger, K. Kim, Y.-T. Hsu, S. Dubinett, M. Phelps, J. Czernin and W. Weber, *Eur. J. Nucl. Med. Mol. Imaging*, 2008, **35**, 1089-1099.
336. E. Mishani, G. Abourbeh, M. Eiblmaier and C. J. Anderson, *Curr. Pharm. Des.*, 2008, **14**, 2983-2998.

337. G. Ortu, I. Ben-David, Y. Rozen, N. M. Freedman, R. Chisin, A. Levitzki and E. Mishani, *Int. J. Cancer*, 2002, **101**, 360-370.
338. A. Pal, J. A. Balatoni, U. Mukhopadhyay, K. Ogawa, C. Gonzalez-Lepera, A. Shavrin, A. Volgin, W. Tong, M. M. Alauddin and J. G. Gelovani, *Mol. Imaging Biol.*, 2011, **13**, 853-861.
339. D. O'Hagan, *Chem. Soc. Rev.*, 2008, **37**, 308-319.
340. L. He, H. Li, J. Chen and X. Wu, *RSC. Adv.*, 2014, **4**, 10265-10277.
341. M. Kidwai, S. Rastogi and R. Mohan, *Croat. Chem. Acta*, 2003, **76**, 365-369.
342. F. Alexandre, A. Berecibar and T. Besson, *Tetrahedron Lett.*, 2002, **43**, 3911-3913.
343. A. G. Nerkar, D. Pawale, M. R. Ghante and S. D. Sawant, *Int. J. Pharm. Pharm. Sci.*, 2013, **5**, 564-566.
344. Z. Wan, S. Wacharasindhu, C. G. Levins, M. Lin, K. Tabei and T. S. Mansour, *J. Org. Chem.*, 2007, **22**, 10194-10210.
345. V. Chandregowda, G. Venkateswara Rao and G. Chandrasekara Reddy, *Org. Process Res. Dev.*, 2007, **11**, 813-816.
346. D. Asgari, A. Aghanejad and J. S. Mojarrad, *Bull. Korean Chem. Soc.*, 2011, **32**, 909-914.
347. W. Liu, X. Huang, M. Cheng, R. J. Nielsen, W. A. Goddard and J. T. Groves, *Science*, 2012, **337**, 1322-1325.
348. W. Liu, X. Huang and J. T. Groves, *Nat. Protoc.*, 2013, **8**, 2348-2354.
349. Y. Jia, C. M. Quinn, S. Kwak and R. V. Talanian, *Curr. Drug Discov. Technol.*, 2008, **5**, 59-69.
350. J. C. Uitdehaag, F. Verkaar, H. Alwan, J. de Man, R. C. Buijsman and G. J. Zaman, *Br. J. Pharmacol.*, 2012, **166**, 858-876.
351. H. Ma, S. Deacon and K. Horiuchi, *Expert Opin. Drug Discov.*, 2008, **3**, 607-621.
352. P. Held, *Z'-LYTE® Kinase Assay from Invitrogen™ on Synergy™ 4*, BioTek, Invitrogen, 2015^
353. J. Spencer, A. P. Mendham, A. K. Kotha, S. C. W. Richardson, E. A. Hillard, G. Jaouen, L. Male and M. B. Hursthouse, *Dalton Transactions*, 2009, **6**, 918-921.
354. N. Vasdev, P. N. Dorff, A. R. Gibbs, E. Nandan, L. M. Reid, J. P. O'Neil and H. F. VanBrocklin, *J. Label Compd. Radiopharm.*, 2005, **48**, 109-115.
355. N. Vasdev, P. N. Dorff, J. P. O'Neil, F. T. Chin, S. Hanrahan and H. F. VanBrocklin, *Bioorg. Med. Chem.*, 2011, **19**, 2959-2965.
356. P. Slobbe, A. D. Windhorst, M. Stigter-van Walsum, R. C. Schuit, E. F. Smit, H. G. Niessen, F. Solca, G. Stehle, G. A. van Dongen and A. J. Poot, *Nucl. Med. Biol.*, 2014, **41**, 749-757.

357. R. A. Hartz, K. K. Nanda, C. L. Ingalls, V. T. Ahuja, T. F. Molski, G. Zhang, H. Wong, Y. Peng, M. Kelley, N. J. Lodge, R. Zaczek, P. J. Gilligan and G. L. Trainor, *J. Med. Chem.*, 2004, **47**, 4741-4754.
358. M. A. Peterson, H. Shi and P. Ke, *Tetrahedron Lett.*, 2006, **47**, 3405-3407.
359. R. Davis, *J. Chem. Soc.*, 1957, 2420.
360. M. K. Nielsen, C. R. Ugaz, W. Li and A. G. Doyle, *J. Am. Chem. Soc.*, 2015, **137**, 9571-9574.
361. X. Xiao, S. Antony, G. Kohlhagen, Y. Pommier and M. Cushman, *Bioorg. Med. Chem.*, 2004, **12**, 5147-5160.
362. P. C. Prabhakaran, N. Woo, P. S. Yorgey and S. J. Gould, *J. Am. Chem. Soc.*, 1988, **110**, 5785-5791.
363. S. K. Thompson, R. A. Smith, S. Reddy, T. M. John, V. K. Nyavanadi, H. Subramanya, V. Potluri, S. K. Panigrahi, P. R. Nadipalli and S. Sengupta, *Quinazolines and azaquinazolinone as dual inhibitors of RAS/RAF/MEK/ERK and PI3K/AKT/PTEN/MTOR pathways*, WO2014169167, 2014.
364. A. Damont, F. Hinnen, B. Kuhnast, M. Schöllhorn-Peyronneau, M. James, C. Luus, B. Tavitian, M. Kassiou and F. Dollé, *J. Label. Compd. Radiopharm.*, 2008, **51**, 286-292.
365. W. D. Emmons and A. F. Ferris, *J. Am. Chem. Soc.*, 1953, **75**, 2257-2257.
366. Z. Zhang, K. Kil, P. Poutiainen, J. Choi, H. Kang, X. Huang, B. Roth and A. Brownell, *Bioorg. Med. Chem. Lett.*, 2015, **25**, 3956-3960.
367. L. Hennequin, *Chemical Compounds*, US20030207878, 2003.
368. J. Pesti, T. LaPorte, J. Thornton, L. Spangler, F. Buono, G. Crispino, F. Gibson, P. Lobben and C. Papaioannou, *Org. Process Res. Dev.*, 2014, **18**, 89-102.
369. R. Bhide, J. Fan, L. Parlanti, S. Barbosa, L. Qian, Z. Cai and F. Gibson, *Process for preparing certain pyrrolotriazine compounds*, WO2004009542, 2004.
370. R. D. Dillard, N. J. Bach, S. E. Draheim, D. R. Berry, D. G. Carlson, N. Y. Chirgadze, D. K. Clawson, L. W. Hartley, L. M. Johnson, N. D. Jones, E. R. McKinney, E. D. Mihelich, J. L. Olkowski, R. W. Schevitz, A. C. Smith, D. W. Snyder, C. D. Sommers and J. Wery, *J. Med. Chem.*, 1996, **39**, 5119-5136.
371. L. F. A. Hennequin, D. Mckerrecher, P. Ple and E. S. E. Stokes, *Quinazoline derivatives as angiogenesis inhibitors*, WO2000047212, 2001.
372. A. Fiumana and K. Jones, *Chem. Comm.*, 1999, **17**, 1761-1762.
373. I. Borza, S. Kolok, G. Ignácz-Szendrei, I. Greiner, G. Tárkányi, K. Galgóczy, C. Horváth, S. Farkas and G. Domány, *Bioorg. Med. Chem. Lett.*, 2005, **15**, 5439-5441.

374. N. M. Heron, G. R. Pasquet, A. A. Mortlock and F. H. Jung, *Quinazoline derivatives for treatment of cancer*, WO2004094410, 2004.
375. R. M. R. Sarmiento, A. W. Thomas and R. Wyler, *3H-Quinazolin-4-one derivatives*, WO2004054985, 2004.
376. A. Foucourt, C. Dubouilh-Benard, E. Chosson, C. Corbière, C. Buquet, M. Iannelli, B. Leblond, F. Marsais and T. Besson, *Tetrahedron*, 2010, **66**, 4495-4502.
377. S. Tasler, O. Müller, T. Wieber, T. Herz, S. Pegoraro, W. Saeb, M. Lang, R. Krauss, F. Totzke, U. Zirrgiebel, J. E. Ehlert, M. H. G. Kubbutat and C. Schächtele, *Bioorg. Med. Chem.*, 2009, **17**, 6728-6737.
378. T. Wang, A. S. Lui and I. S. Cloudsdale, *Org. Lett.*, 1999, **1**, 1835-1837.
379. A. H. Davison, S. J. Davies and D. F. C. Moffat, *Quinoline and Quinoxaline derivatives as inhibitors of kinase enzymatic activity*, WO2004094410, 2006.
380. F. Liu, X. Chen, A. Allali-Hassani, A. M. Quinn, G. A. Wasney, A. Dong, D. Barsyte, I. Kozieradzki, G. Senisterra, I. Chau, A. Siarheyeva, D. B. Kireev, A. Jadhav, J. M. Herold, S. V. Frye, C. H. Arrowsmith, P. J. Brown, A. Simeonov, M. Vedadi and J. Jin, *J. Med. Chem.*, 2009, **52**, 7950-7953.
381. N. M. Heron, J. H. Jung, G. R. Pasquet and A. A. Mortlock, *Phosphonoxy quinazoline derivatives and their pharmaceutical use*, WO2004058781, 2004.
382. F. H. Jung, G. R. Pasquet, C. Lambert-van der Brempt, J. M. Lohmann, N. Warin, F. Renaud, H. Germain, C. De Savi, N. Roberts, T. Johnson, C. Dousson, G. B. Hill, A. A. Mortlock, N. M. Heron, R. W. Wilkinson, S. R. Wedge, S. P. Heaton, R. Oedra, N. J. Keen, S. Green, E. Brown, K. Thompson and S. Brightwell, *J. Med. Chem.*, 2006, **49**, 955-970.
383. A. A. Mortlock, *Quinazoline Compounds*, WO2004058752, 2004.
384. A. Galan, J. Chen, H. Du, T. Forsyth, T. P. Huynh, H. W. B. Johnson, P. Kearney, J. W. Leahy, M. S. Lee, G. Mann, B. H. Ridgway, C. S. Takeuchi and P. Zhou, *Jak-2 modulators and methods of use*, WO2008042282, 2008.
385. M. Gao, C. M. Lola, M. Wang, K. D. Miller, G. W. Sledge and Q. Zheng, *Bioorg. Med. Chem. Lett.*, 2011, **21**, 3222-3226.
386. F. Li, S. Jiang, Y. Zu, D. Y. Lee and Z. Li, *J. Nucl. Med.*, 2014, **55**, 1525-1531.
387. A. Wang, L. Zhou, K. Fang, L. Zhou, Y. Lin, J. Zhou and S. Wei, *Eur. J. Med. Chem.*, 2012, **58**, 12-21.

8.2 Appendices

8.2.1. Appendix One

Appendix One describes the optimisation conditions, in full, for the fluorination of **51**.

Table 32: Identification of successful conditions. (^amicrowave heating)

Entry	Eq of F source	F Source	Solvent	Temp (°C)	Conversion	Notes	
a	1	TBAF	MeCN	75	NR	All these reactions conducted for 24 hours in the given solvent and temperature. Aliquots taken for LC-MS analysis at 1,2 and 24 hrs. The final reaction concentrated/freeze dried to remove the solvent and NMR analysis undertaken	
b	1.1	TBAF	MeCN	75	NR		
c	1.5	TBAF	MeCN	75	NR		
d	2	TBAF	MeCN	75	NR		
e^a	2	TBAF	MeCN	110	NR		
f^a	5	TBAF	MeCN	110	NR		
g^a	1	TBAF	THF	110	NR		
h^a	1.1	TBAF	THF	110	NR		
i^a	1.5	TBAF	THF	110	NR		
j^a	2	TBAF	THF	110	NR		
k^a	5	TBAF	THF	110	NR		
l^a	2	CsF	MeCN	110	<10%		
m^a	5	CsF	MeCN	110	<10%		
n	1	CsF	MeCN	75	NR		
o	1.1	CsF	MeCN	75	NR		
p	1.5	CsF	MeCN	75	NR		
q	2	CsF	MeCN	75	NR		
r	1	CsF	DMF	120	pTsF		
s	1.1	CsF	DMF	120	pTsF		
t	1.5	CsF	DMF	120	pTsF		
u	2	CsF	DMF	120	pTsF		
v	1	CsF	DMSO	120	NR		
w	1.1	CsF	DMSO	120	NR		
x	1.5	CsF	DMSO	120	NR		
y	2	CsF	DMSO	120	NR		
z	2	CsF	DMF [^]	120	pTsF		
aa	2	CsF	DMSO [^]	120	NR		
ab	3	CsF	t-BuOH	80	<25%		
ac	3	CsF	t-amyl alcohol	80	>50%		[^] anhydrous

Table 33: Use of a phase transfer catalyst for the fluorination of **51** with KF with a reaction time of one hour

Entry	Eq of KF	Eq of PTC	PTC	Solvent	Temp (°C)	Conversion
a	1.5	1.4	K ₂₂₂	MeCN	110	<15%
b	1.5	1.5	18-C-6	MeCN	110	NR

Table 34: Time course conversion of **51** to **52** using differing equivalents of CsF using *t*-amyl alcohol whilst heating at 100 °C. Aliquots taken at the allotted time, solvent removed and conversion judged by ¹⁹F NMR

Entry	Time (hour)	Product Conversion % using different equivalents of			
		CsF (average)			
		1	2	5	10
a	0	0	0	0	0
b	1	5	50	95	97
c	2	8	68	94	99
d	3	10	77	96	97
e	4	10	85	97	98
f	5	16	87	97	100

8.2.2 Appendix Two

Appendix Two highlights IC_{50} curves obtained from the cellular proliferation assay described in Chapter Three (3.4.2.1). Data is presented with A549 at the top and HCT116 at the bottom.

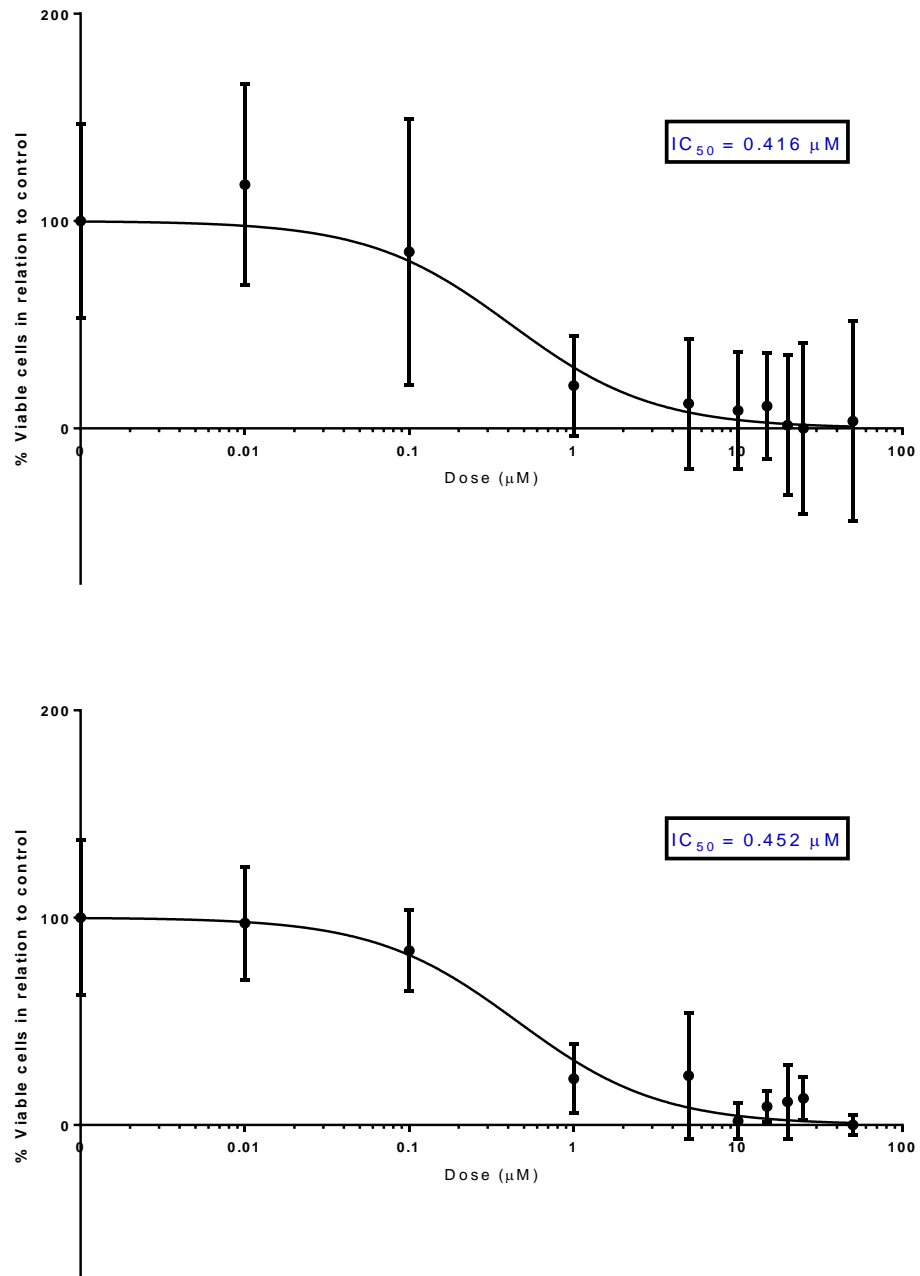


Figure 109: IC_{50} curves for 78a

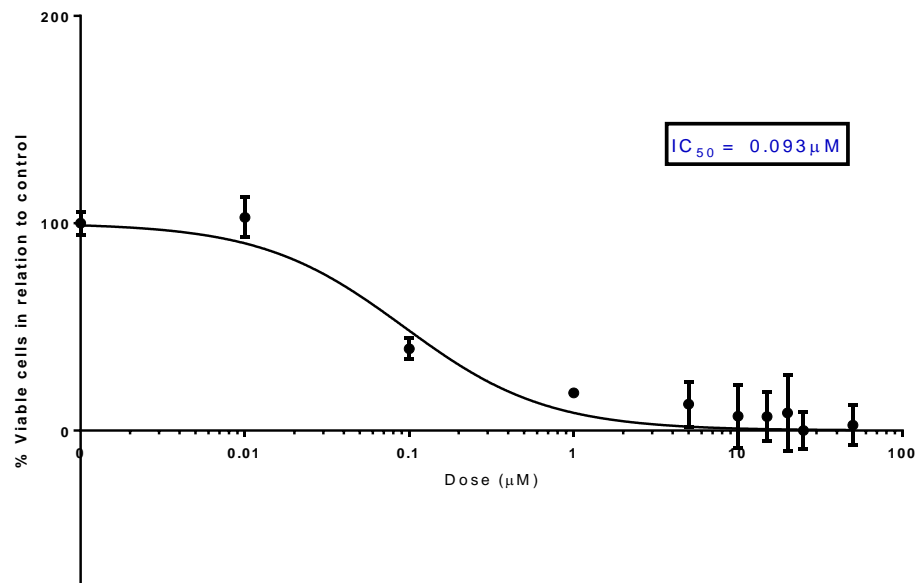
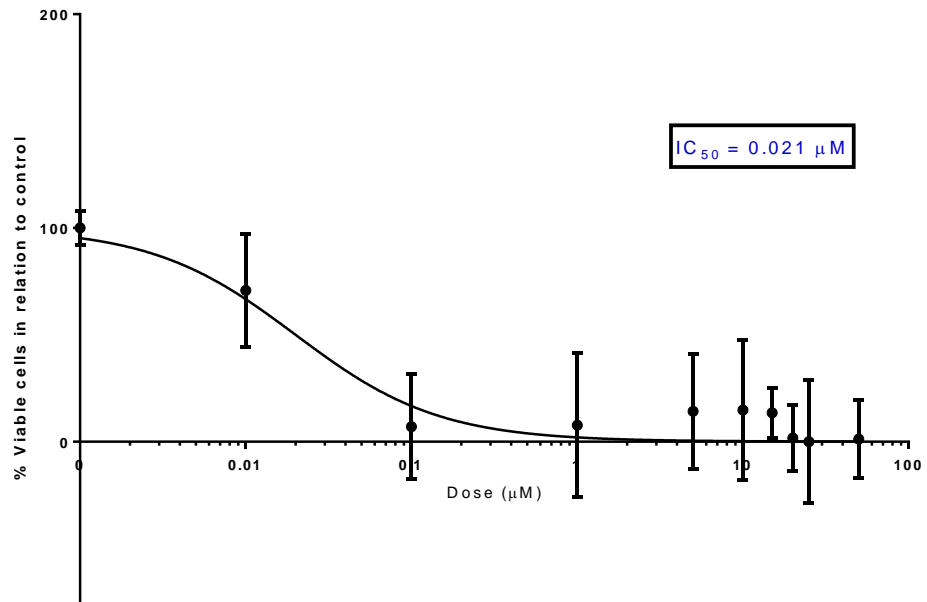


Figure 110: IC₅₀ curves for 78b

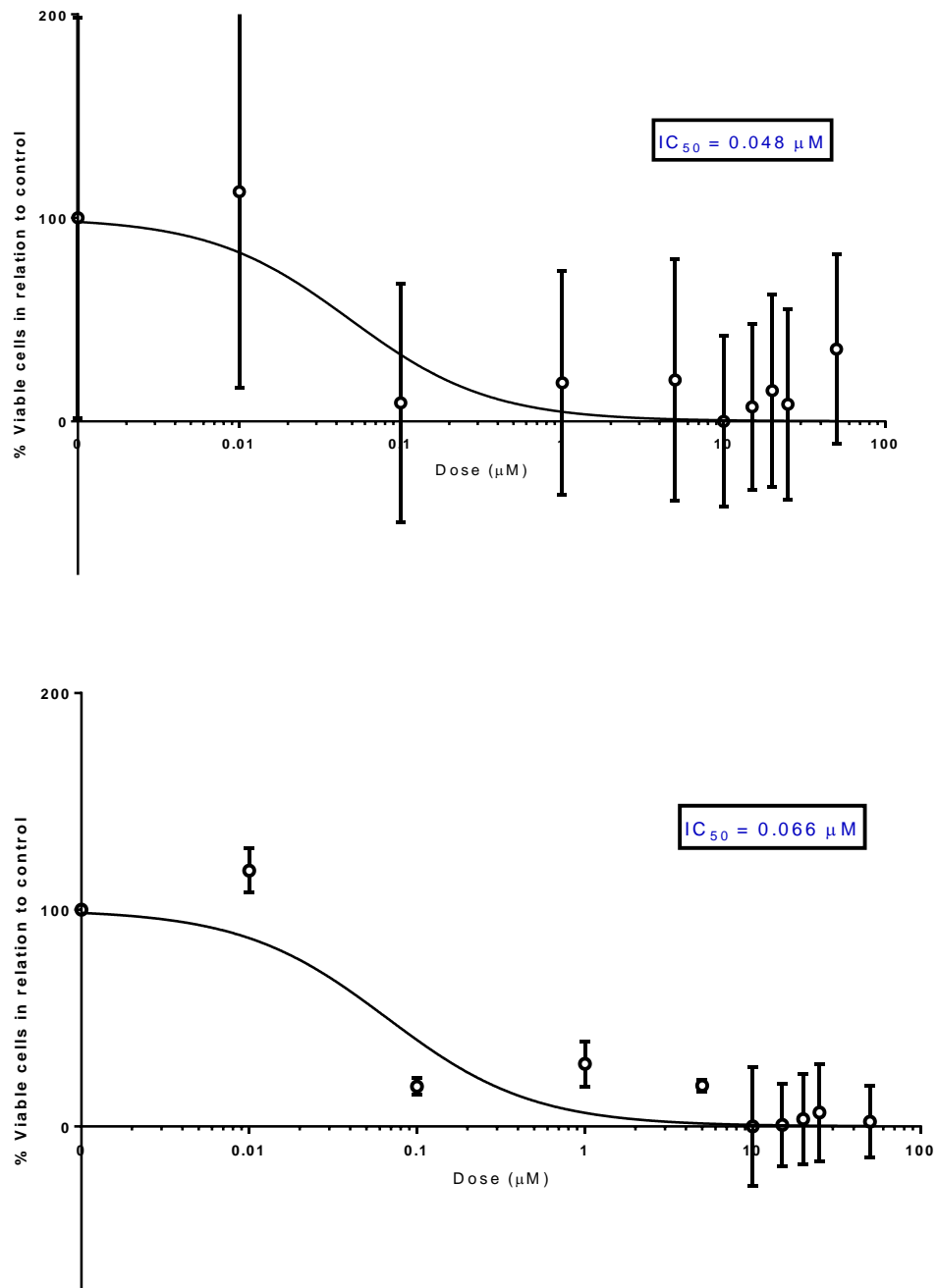


Figure 111: IC_{50} curves for 78c

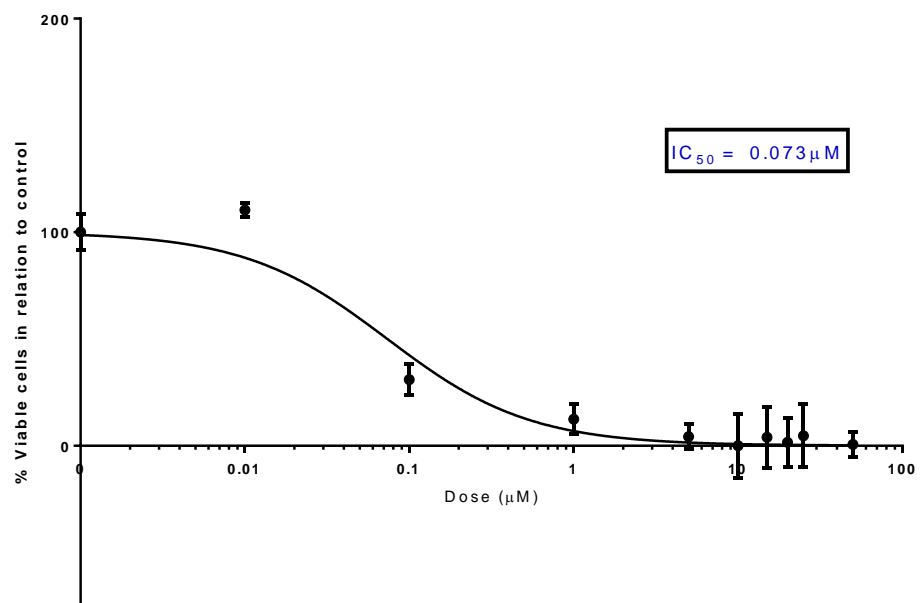
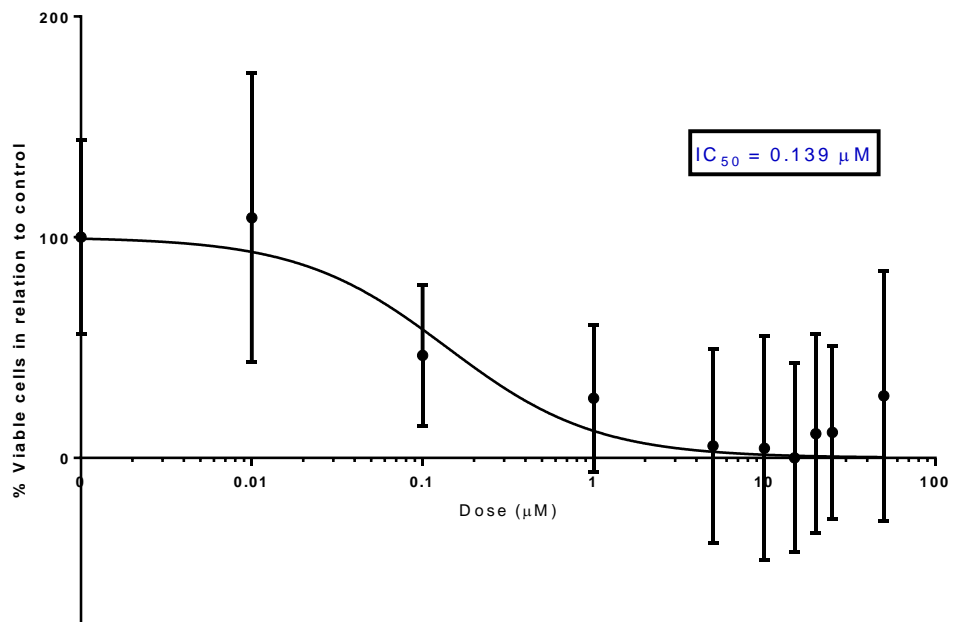


Figure 112: IC₅₀ curves for 78d

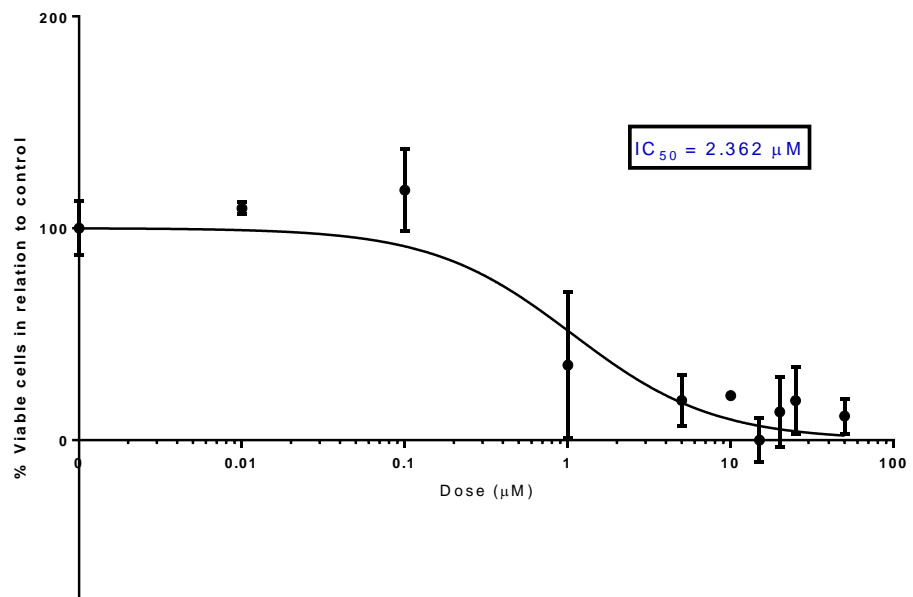
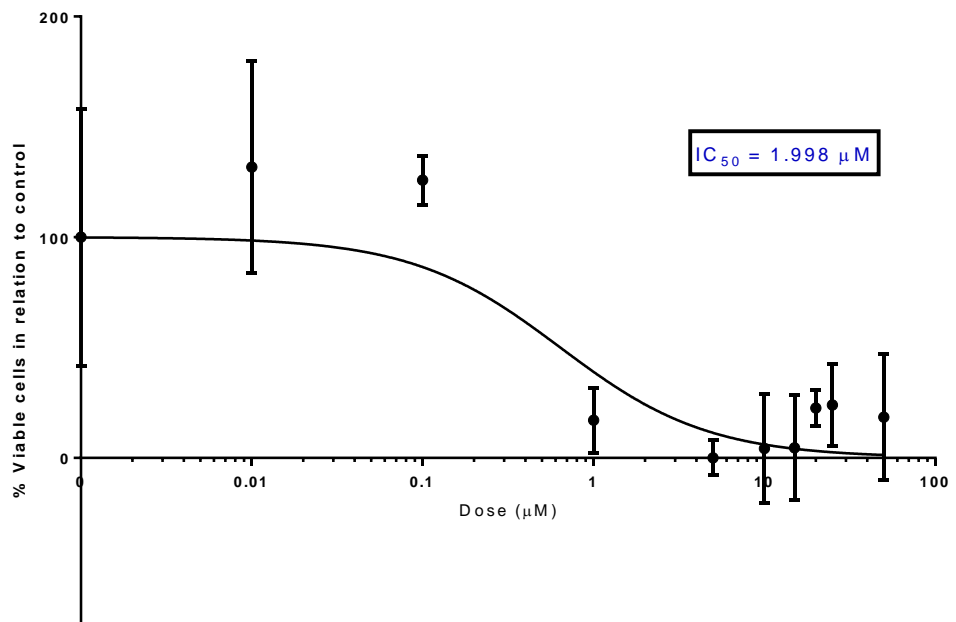


Figure 113: IC_{50} curves for 78e

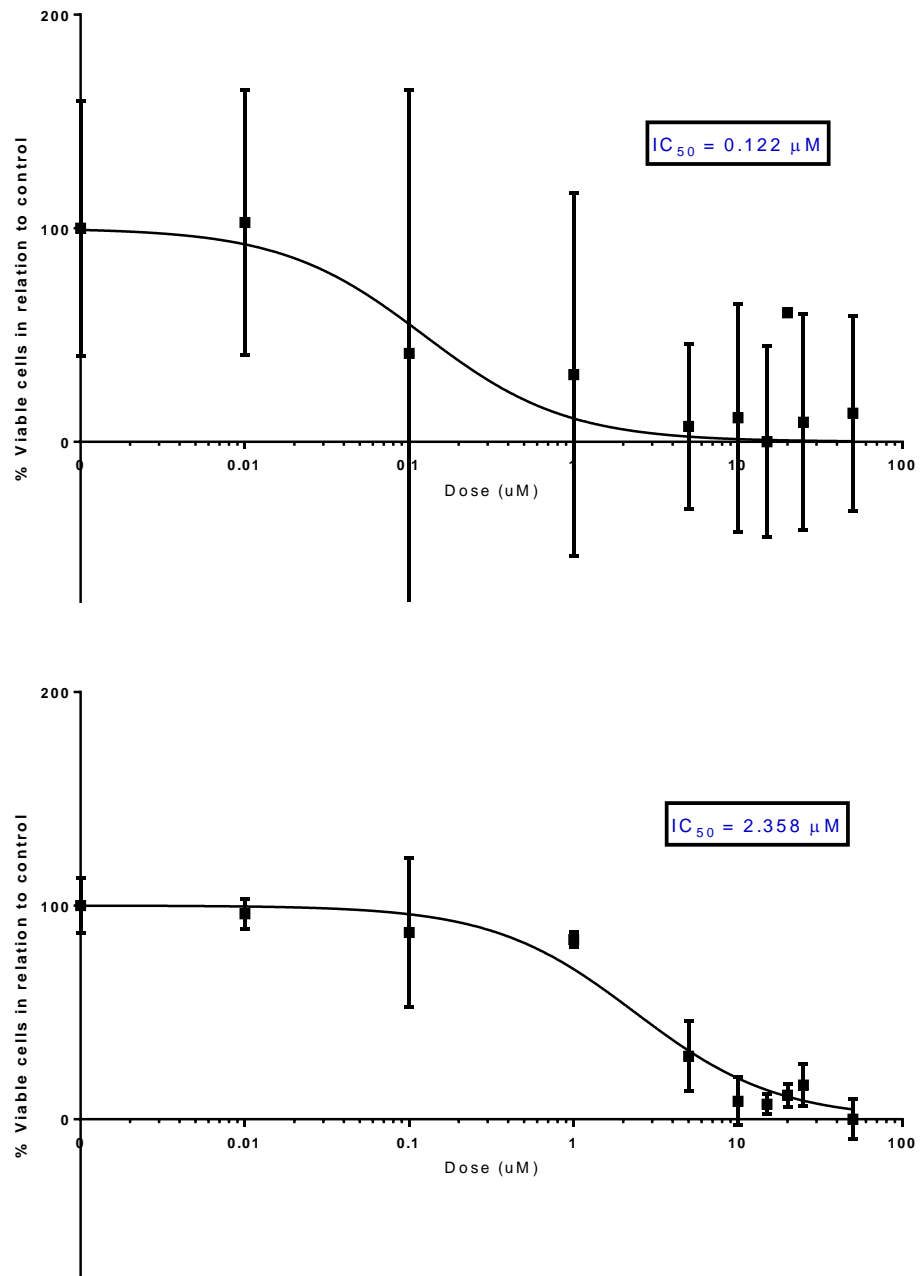


Figure 114: IC_{50} curves for 78f

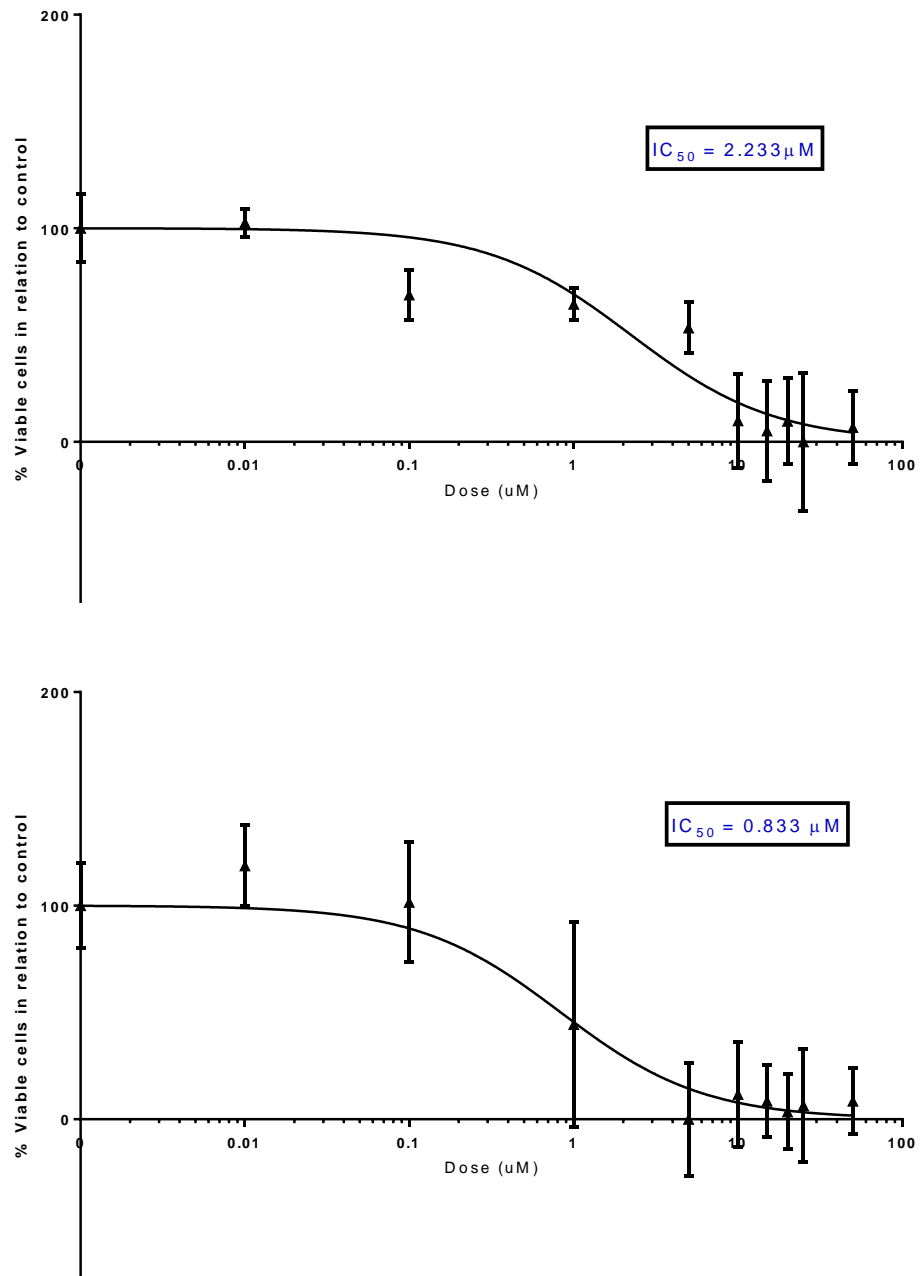


Figure 115: IC₅₀ curves for 78g

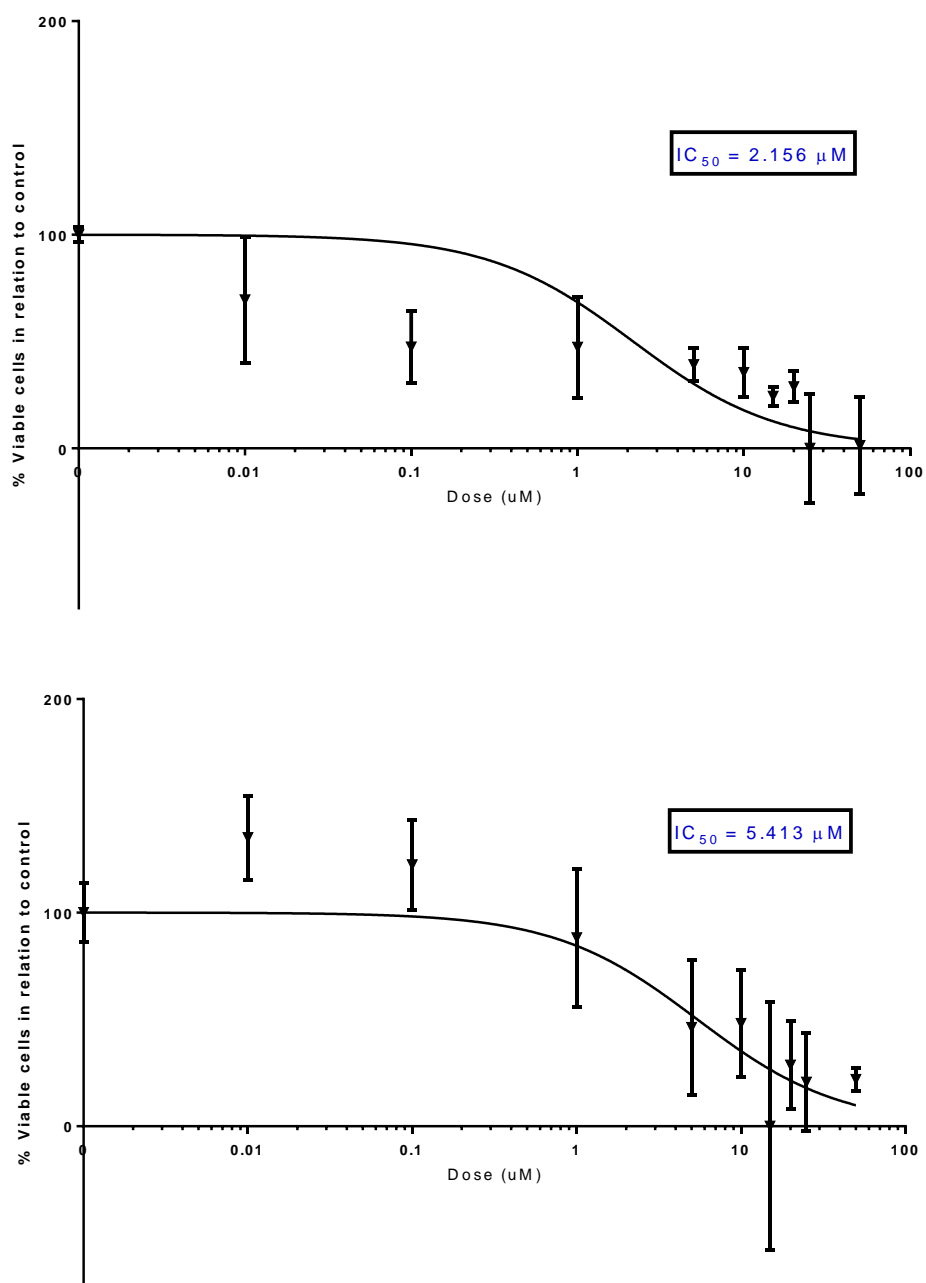


Figure 116: IC_{50} curves for 78h

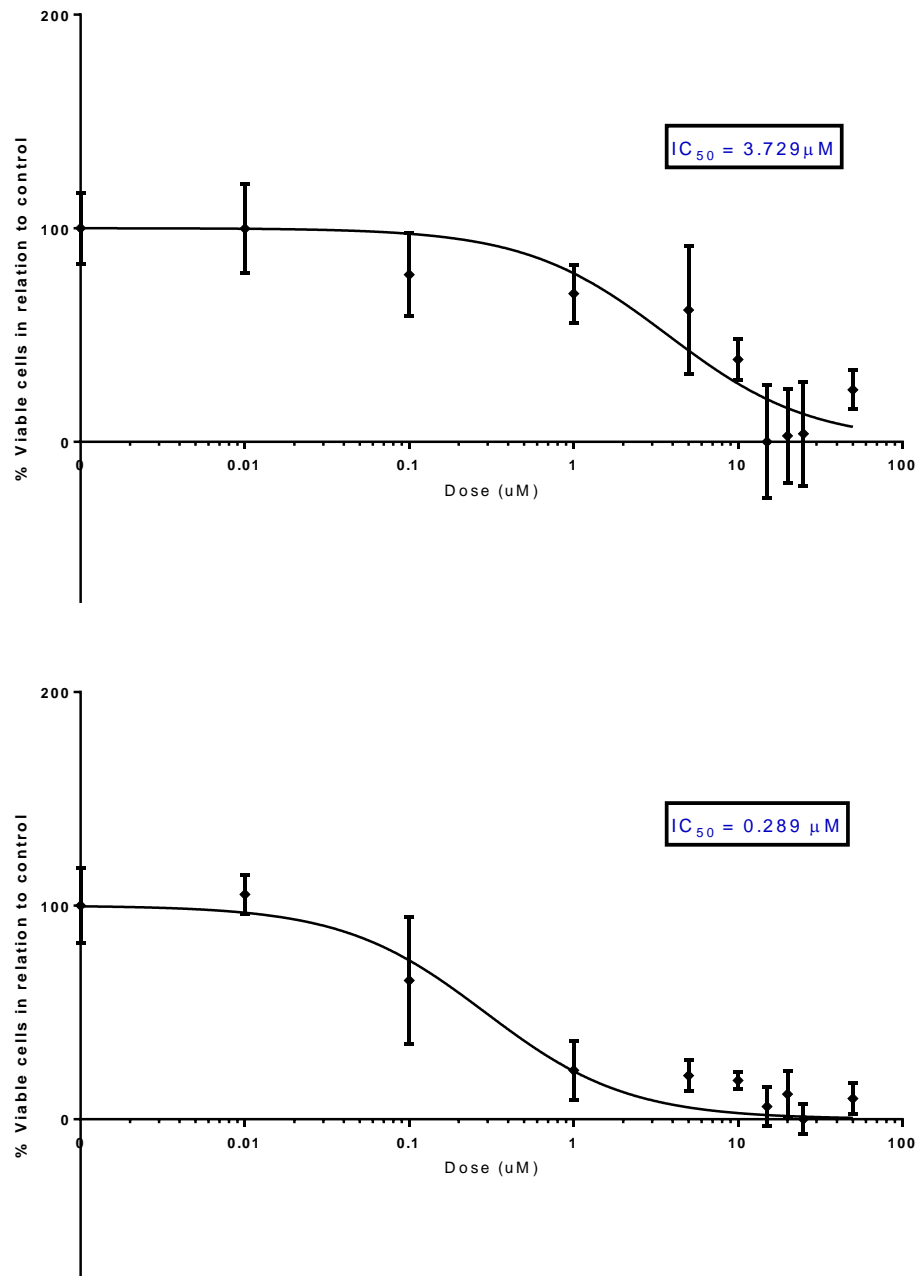


Figure 117: IC₅₀ curves for 78i

8.2.3. Appendix Three

Appendix Three describes the activity data obtained for **98**, **101** and **123** using the Z-LYTE assay platform from Chapter Four (4.2.2.2). The data is presented in the form of IC₅₀ curves.

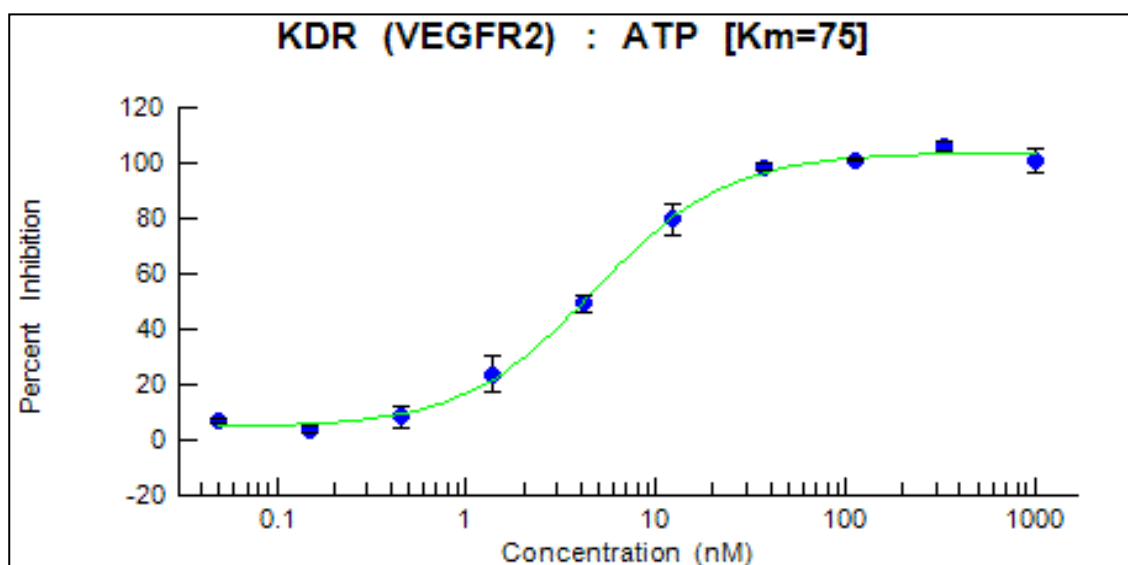


Figure 118: VEGFR₂ IC₅₀ curve for **98**

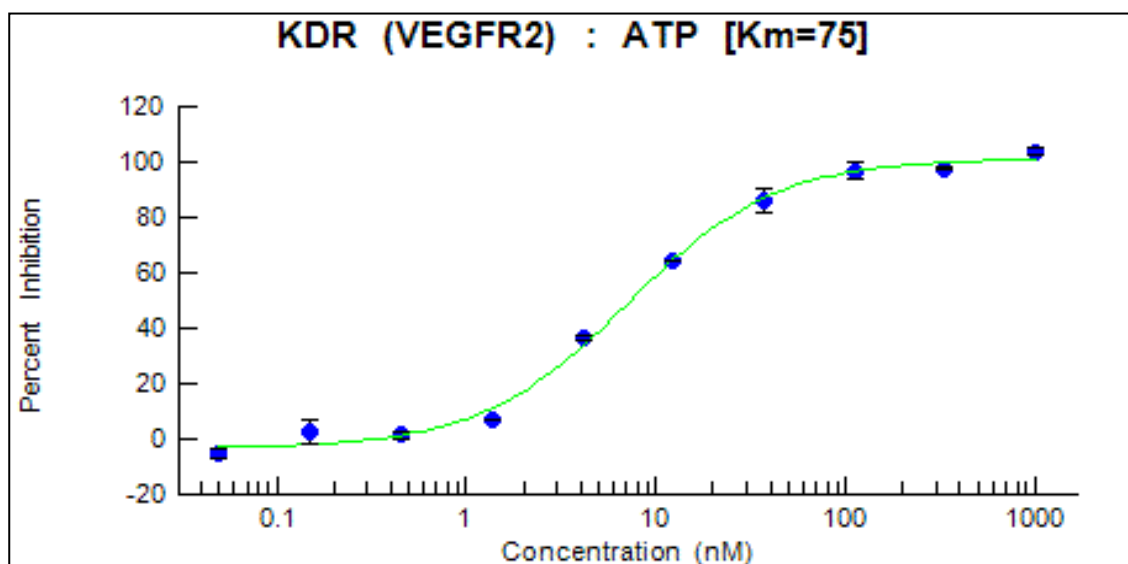


Figure 119: VEGFR₂ IC₅₀ curve for **101**

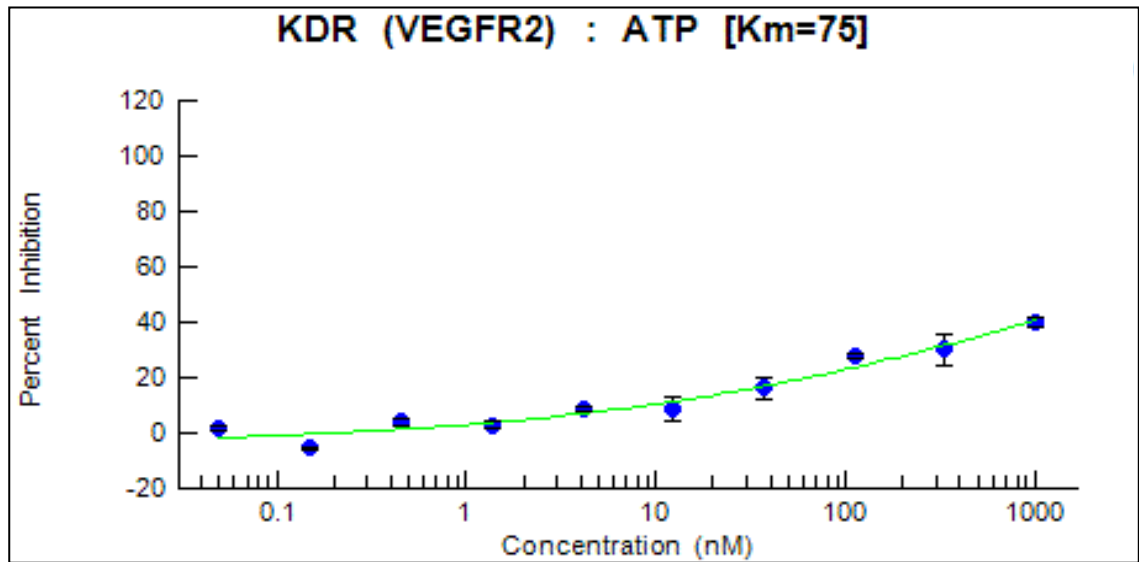


Figure 120: VEGFR₂ IC₅₀ curve for **123**

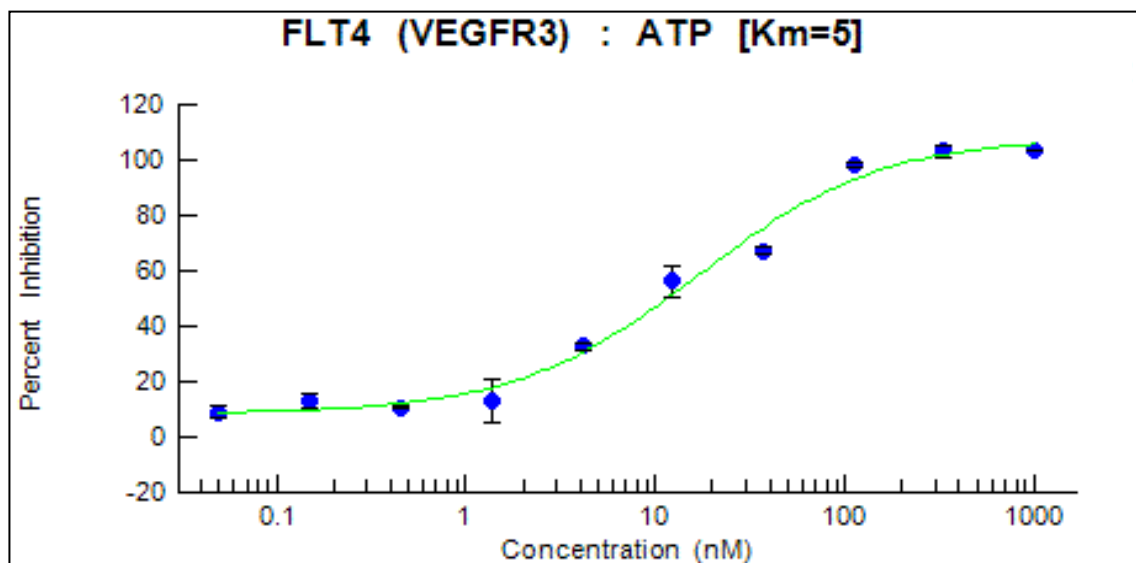


Figure 121: VEGFR₃ IC₅₀ curve for **101**

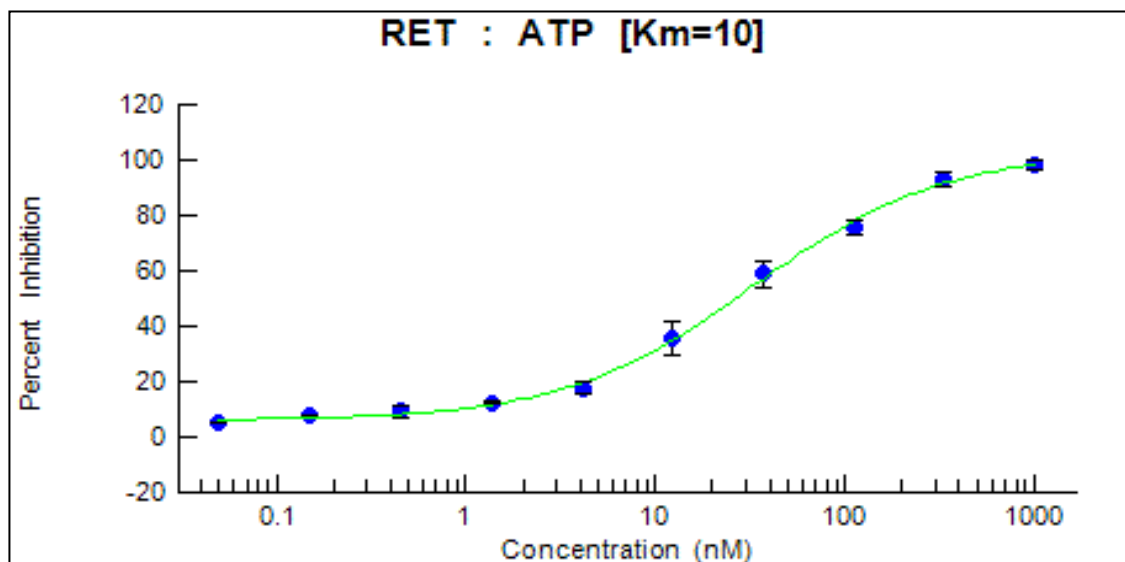
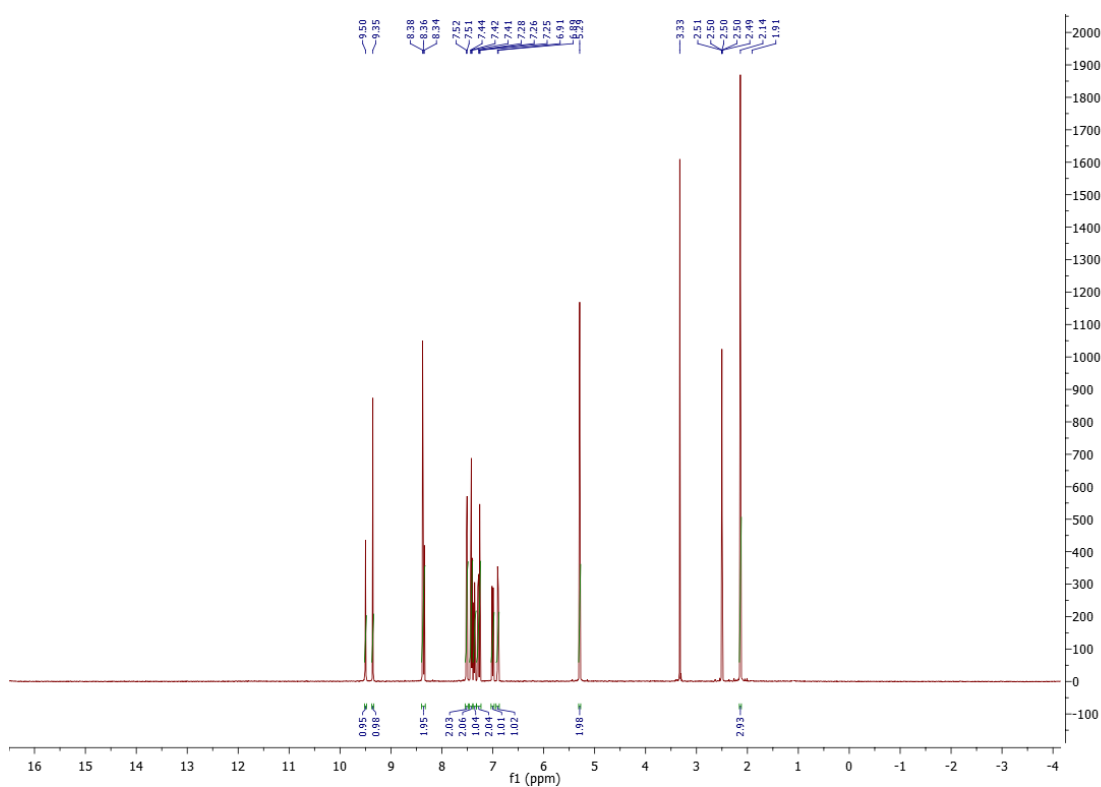


Figure 122: RET IC₅₀ curve for **101**

8.2.4. Appendix Four

Appendix Four highlights the ^1H NMR's and HPLC chromatograms for final compounds **98**, **101**, **123**, **136** and **166** from Chapters Four and Five.



Name	Start (mm:ss)	End (mm:ss)	Retention (mm:ss)	Area (mAU·s)	%ROI (%)
Region 1	6:01	6:12	6:06	73.2	0.17
Region 2	7:31	8:20	7:42	43634.9	98.92
Region 3	22:38	23:06	22:44	403.7	0.92
3 Peaks				44111.8	100.00

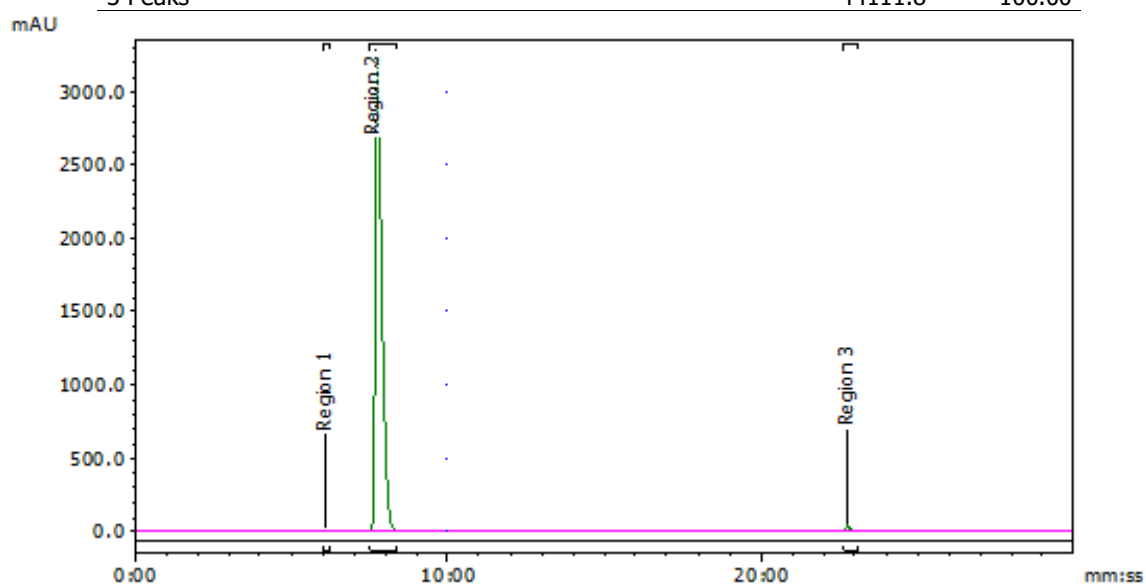
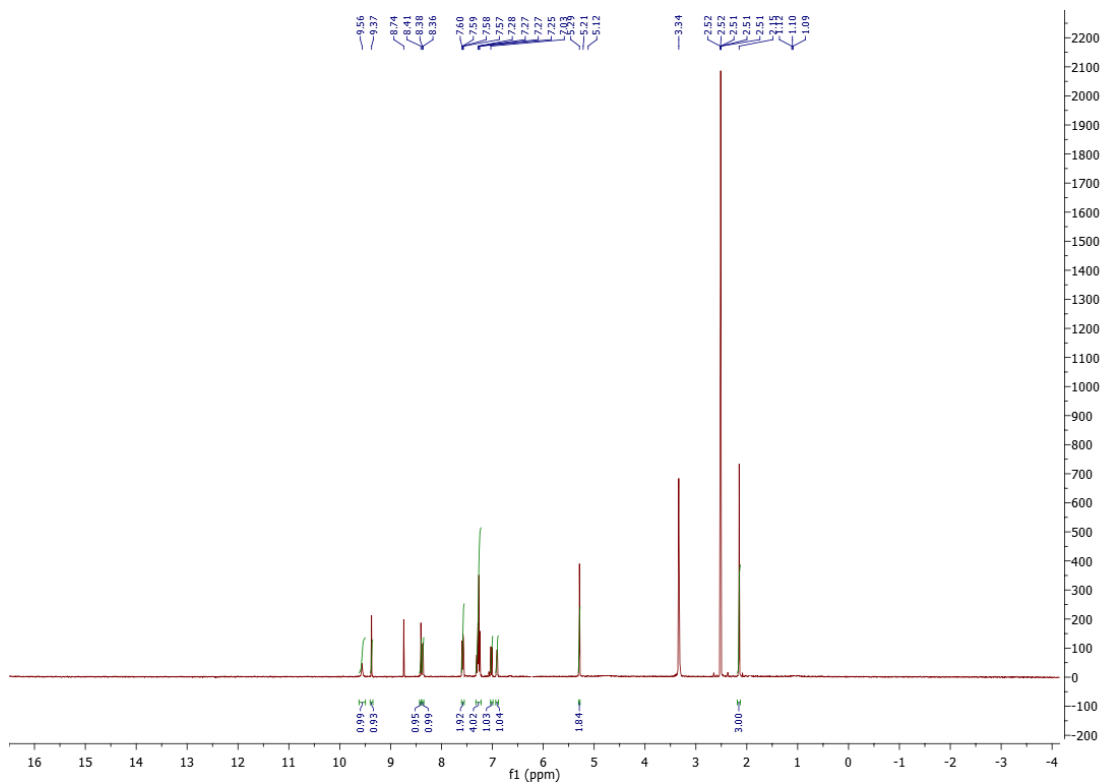


Figure 123: ^1H NMR and HPLC chromatogram for **98**



Name	Start (mm:ss)	End (mm:ss)	Retention (mm:ss)	Area (mAU·s)	%ROI (%)
Region 1	7:09	7:37	7:18	56922.9	98.42
Region 2	8:44	8:54	8:49	111.3	0.19
Region 3	9:01	9:15	9:08	113.9	0.20
Region 4	9:16	9:30	9:23	335.9	0.58
Region 5	22:42	23:01	22:47	351.2	0.61
5 Peaks				57835.1	100.00

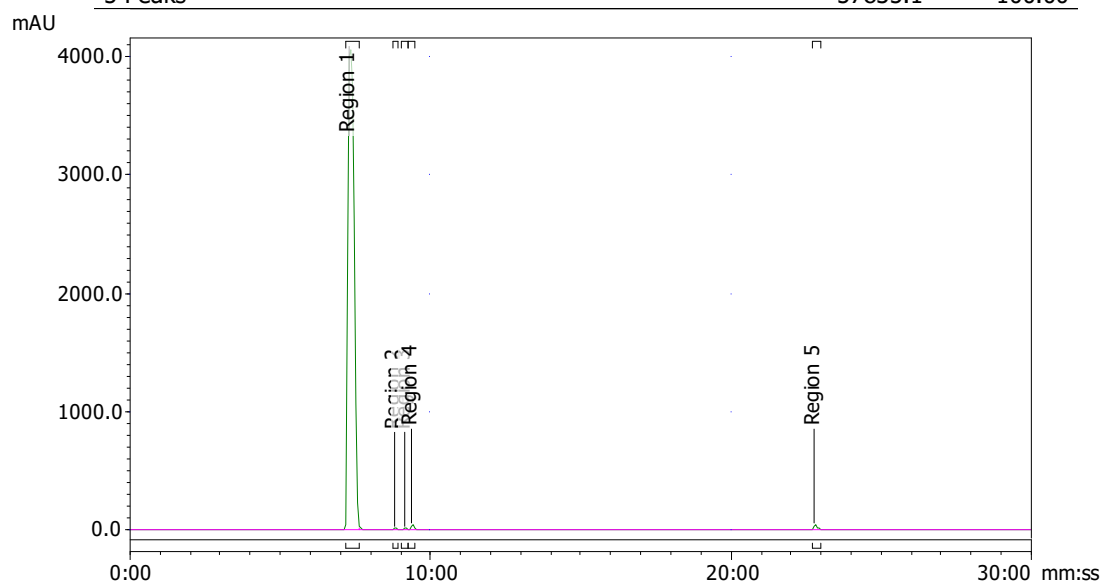
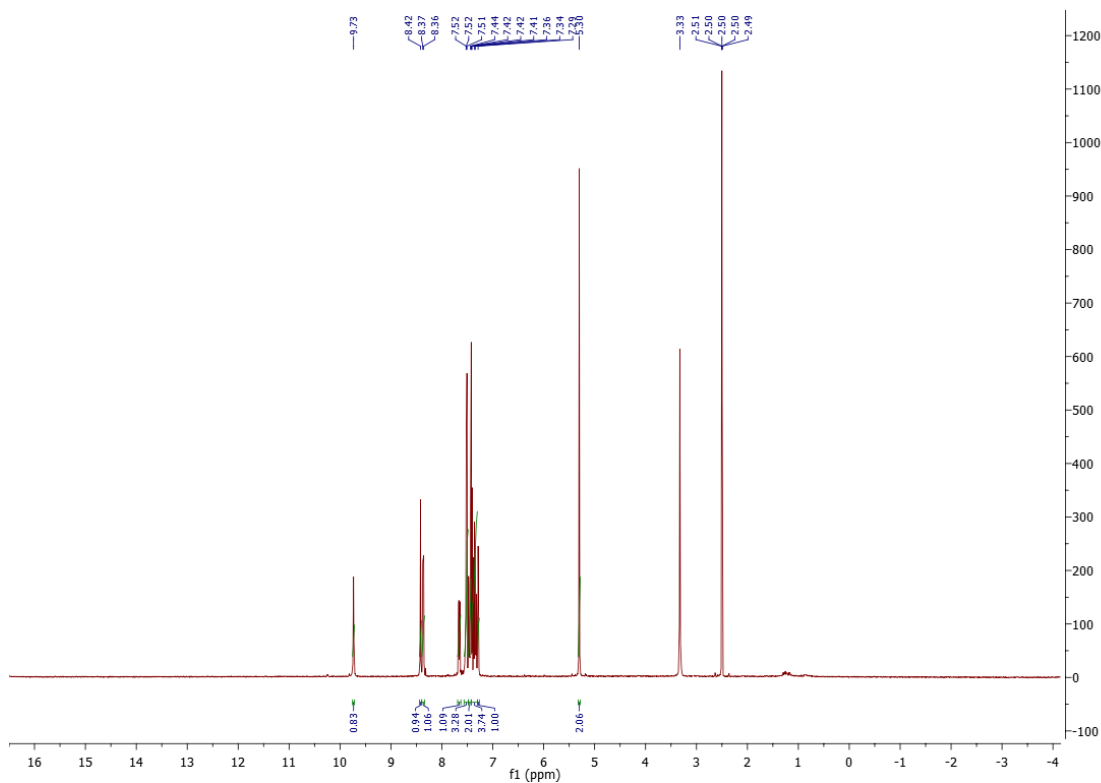


Figure 124: ^1H NMR and HPLC chromatogram for **101**



Name	Start (mm:ss)	End (mm:ss)	Retention (mm:ss)	Area (mAU·s)	%ROI (%)
Region 1	6:48	7:06	6:56	625.4	0.88
Region 2	8:07	8:26	8:17	211.6	0.30
Region 3	8:47	9:35	8:59	70106.3	98.24
Region 4	9:35	10:22	10:12	296.1	0.41
Region 5	11:24	11:29	11:24	11.8	0.02
Region 6	22:40	22:50	22:43	110.4	0.15
6 Peaks				71361.6	100.00

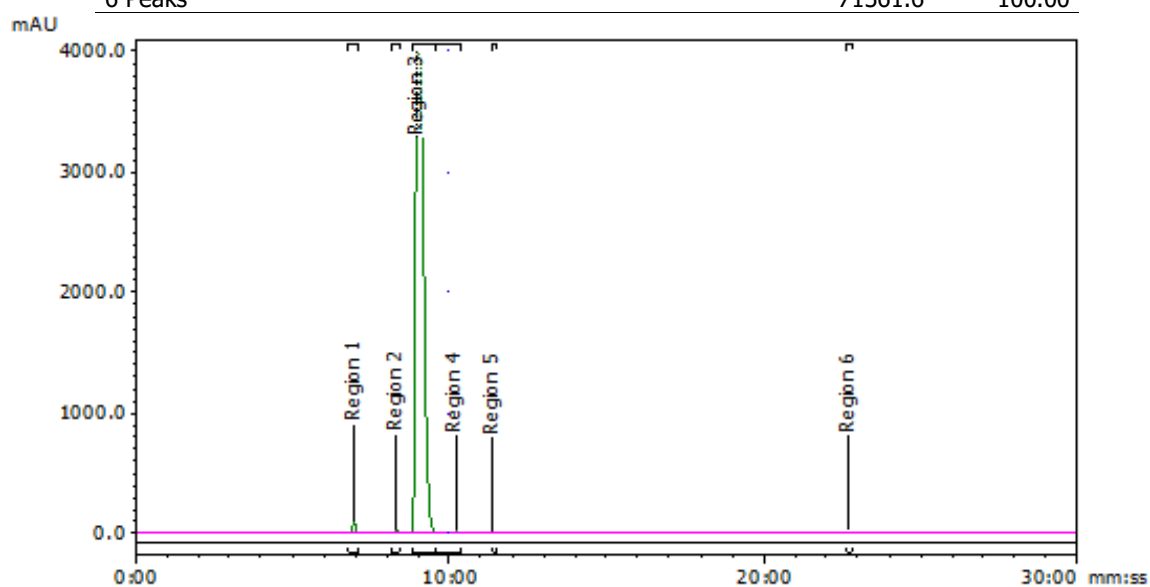
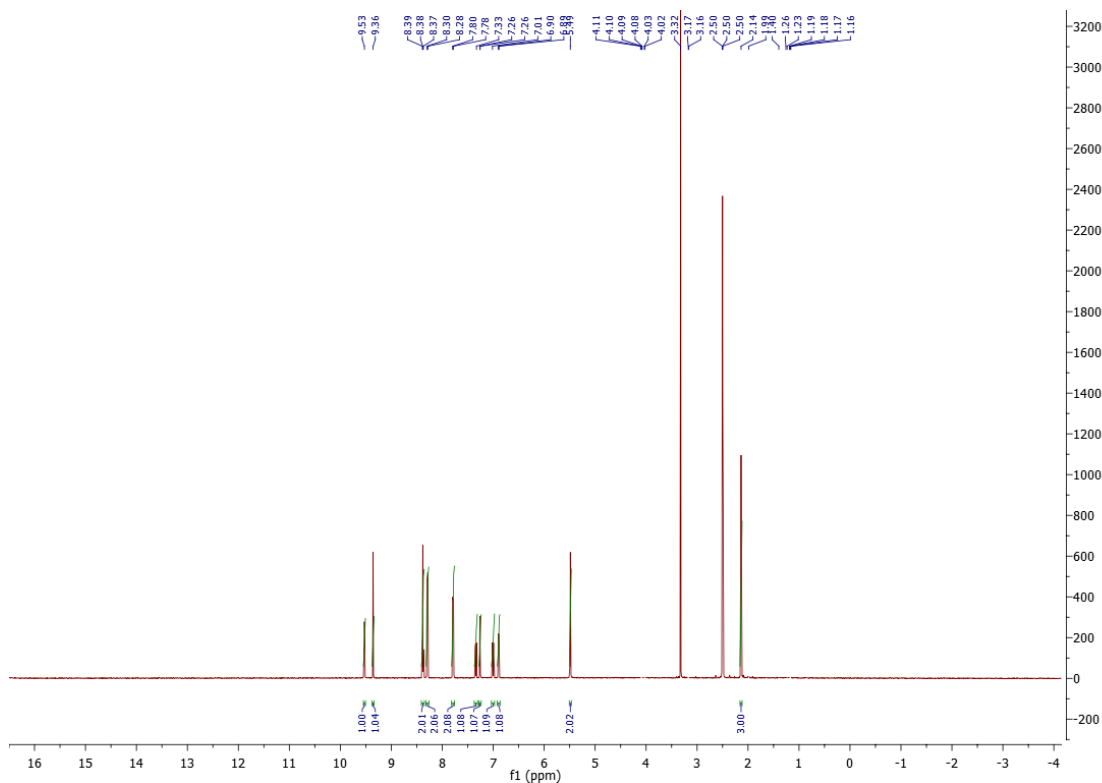


Figure 125: ^1H NMR and HPLC chromatogram for **123**



Name	Start (mm:ss)	End (mm:ss)	Retention (mm:ss)	Area (mAU·s)	%ROI (%)
Region 1	7:13	7:42	7:22	42924.2	97.48
Region 2	9:09	9:21	9:16	230.6	0.52
Region 3	9:22	9:38	9:30	228.8	0.52
Region 4	22:38	23:02	22:45	649.1	1.47
4 Peaks				44032.7	100.00

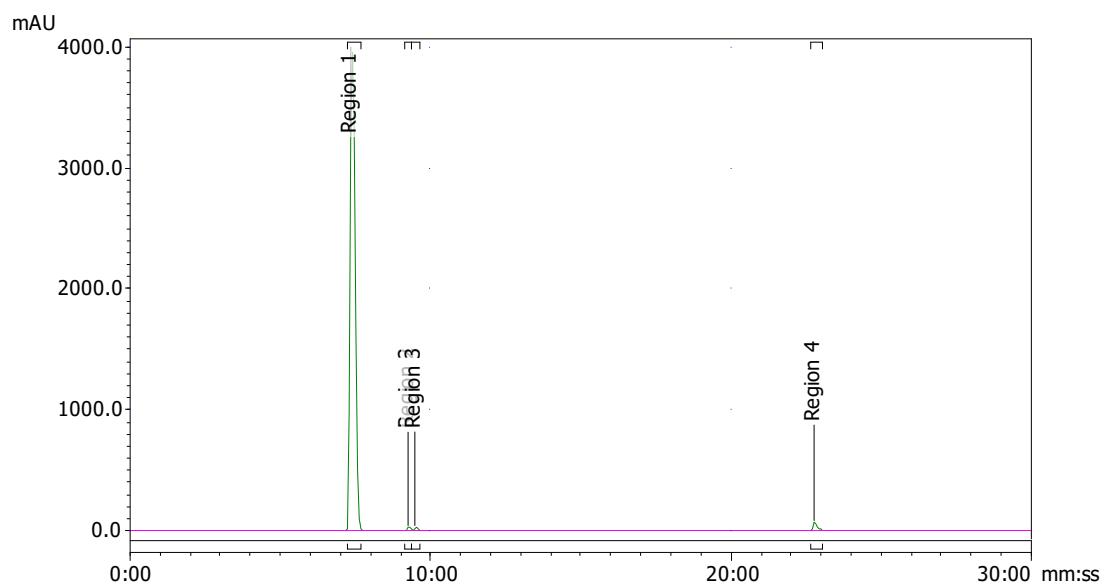
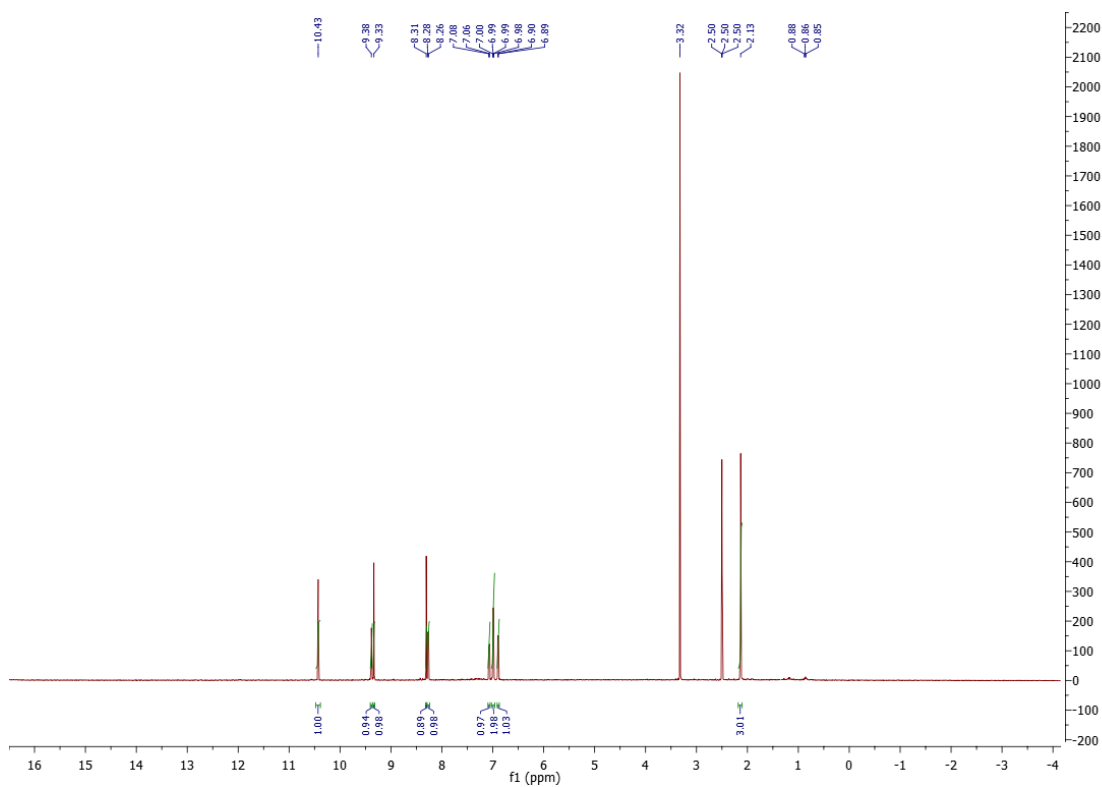


Figure 126: ^1H NMR and HPLC chromatogram for **136**



Name	Start (mm:ss)	End (mm:ss)	Retention (mm:ss)	Area (mAU·s)	%ROI (%)
Region 1	3:36	4:10	3:58	18494.9	97.84
Region 2	5:00	5:21	5:11	407.9	2.16
2 Peaks				18902.8	100.00

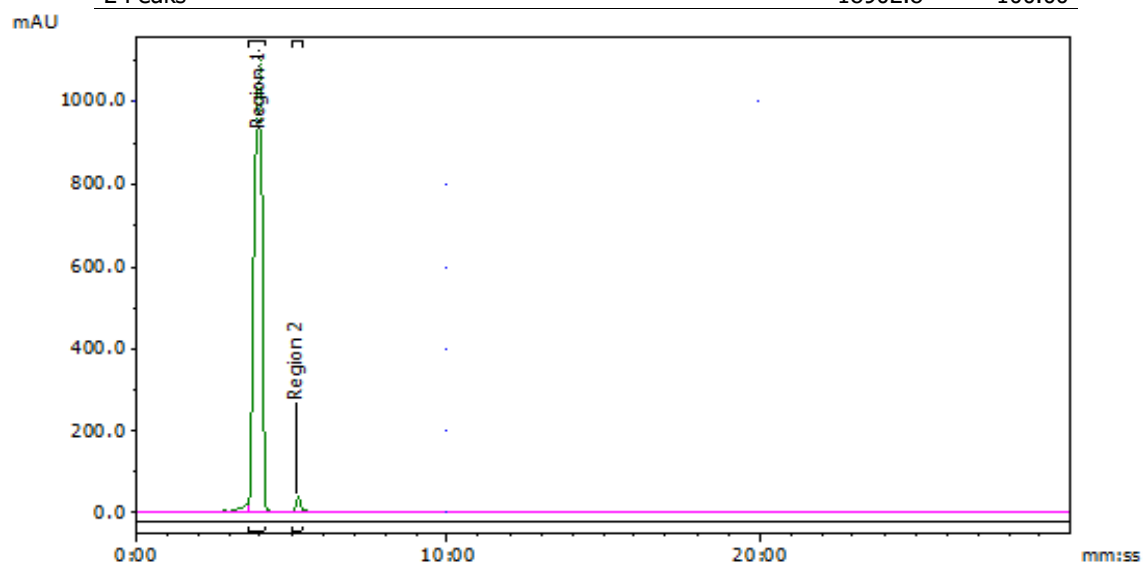


Figure 127: ^1H NMR and HPLC chromatogram for **166**